Establishment and Systematic Benchmarking of Innovative Methods for Quantitative Interactome Mapping in Mammalian Cells

Inaugural-Dissertation

to obtain the academic degree

Doctor rerum naturalium (Dr. rer. nat.)

submitted to the Department of Biology, Chemistry and Pharmacy

of Freie Universität Berlin

by

PHILIPP TREPTE

from Zwenkau

January 2016

The work was conducted from January 2011 until January 2016 under supervision of Prof. Dr. Erich E. Wanker at the Max Delbrueck Center for Molecular Medicine in the Helmholtz-Association.

I hereby confirm that I have written the thesis independently using solely the aids mentioned and without illicit assistance from third parties.

1. Reviewer: Prof. Dr. Erich E. Wanker
2. Reviewer: Prof. Dr. Fritz G. Rathjen

Thesis defense on 29.04.2016

Table of Contents

1. Summary

Protein-protein interactions (PPIs) play a key role in probably all biological processes. Disease-causing missense mutations act through complicated genotype-to-phenotype associations often resulting in the perturbation of PPIs. Thus, the systematic discovery of PPIs is an important goal of network biology to understand the fundamental mechanisms of cellular function and dysfunction in health and disease.

My aim was to establish and benchmark a new set of innovative mammalian cell-based PPI detection assays, DULIP and BRIP, that generate quantitative interaction scores and allow the identification of interactions at medium to high throughput. DULIP is a **du**al **l**uminescence-based co-**i**mmuno**p**recipitation assay for interactome mapping in mammalian cells. In DULIP assays the bait and prey proteins are co-produced as *Renilla* and firefly luciferase fusions. In addition, the bait protein harbors a protein A tag that allows the precipitation of bait/prey protein complexes in microtiter plates. Through the use of two luciferase tags, bait and prey fusion protein expression can be quantified, as can the success of bait and prey precipitation. This enables the calculation of quantitative interaction scores for all tested protein pairs and allows for the generation of quantitative PPI data sets.

In contrast, BRIP is a **b**ioluminescence **r**esonance energy transfer (BRET) and co-**i**mmuno**p**recipitation (co-IP)-based PPI detection assay for quantitative interactome mapping. For BRIP assays, the proteins of interest are co-produced as NanoLuc luciferase and protein A-mCitrine fusion proteins in mammalian cells. Interactions are detected sequentially in one experiment by two distinct PPI-detection principles. In intact cells, PPIs are quantified by BRET, followed by a luminescence-based detection of protein complex formation after co-IP. Protein expression can be detected in intact cells and cell lysates by measuring the luminescence and fluorescence activities of the NanoLuc and mCitrine fusion tags. Hence, the BRIP assay allows the calculation of two independent quantitative interaction scores, one in intact cells and the other after co-IP.

Both assays were established and benchmarked on positive and random PPI reference sets. While the DULIP assay displayed a comparable sensitivity and specificity to other available PPI methods, the BRIP assay significantly detected more interactions of the positive reference set due to the combination of two interaction detection principles in one assay. Furthermore, the analysis of a reference set containing PPIs with known binding affinities demonstrated that both low- and

high-affinity interactions can be detected with DULIP and BRIP assays. While both assays preferentially detected high-affinity interactions, the BRET read-out of the BRIP assay showed a higher sensitivity to detect low-affinity interactions compared to either the co-IP read-out of the BRIP or the DULIP assays.
In studies using the interaction between the synaptic proteins Munc18 and Syntaxin-1, the effect of point mutations on interaction strength could be detected with both assays. However, only the in-cell BRET read-out of the BRIP assay allowed a quantitative assessment of the effects of single point mutations on the binding strength of the Munc18-Syntaxin-1 interaction.

Taken together, my studies demonstrate that the DULIP and BRIP assays are innovative methods that are suitable for quantitative interactome research. They can be applied to generate comprehensive and quantitative PPI data sets in mammalian cells. Moreover, both assays are suitable for studying the effects of point mutations on interaction strength and allow the investigation of the influence of small-molecules on protein-protein interactions.

2. Zusammenfassung

Protein-Protein-Interaktionen (PPIs) spielen eine entscheidende Rolle in vermutlich allen biologischen Prozessen. Krankheitsrelevante Mutationen agieren über komplizierte Genotyp-zu-Phänotyp-Zusammenhänge, welche oft gestörte PPIs zur Folge haben. Entsprechend ist die systematische Untersuchung von PPIs ein wichtiges Ziel der Netzwerkbiologie, um fundamentale Mechanismen zellulärer Funktionen und Dysfunktionen in Gesundheit und Krankheit aufzuklären.

Mein Ziel war es, neue und innovative Methoden – DULIP und BRIP – zur Detektion von PPIs in Säugertierzellen zu etablieren und zu benchmarken. Beide Methoden erlauben die Bestimmung quantitativer Interaktionsscores und die Detektion von PPIs im mittleren bis hohen Maßstab. DULIP ist ein **du**aler, **L**umineszenz-basierter Co**i**mmun**p**räzipitazions-Assay für die Interaktombestimmung in Säugertierzellen. Im DULIP Assay werden Köder und Beuteprotein als *Renilla*- und Firefly-Fusionsproteine koproduziert. Zusätzlich verfügt das Köderprotein über einen Protein A-Tag, welcher die Präzipitation von Proteinkomplexen in Mikrotitierplatten erlaubt. Durch die Verwendung von zwei Luciferase-Tags, kann die Köder- und Beuteproteinproduktion, sowie der Erfolg der Präzipitazion quantifiziert werden. Das erlaubt die Berechnung von quantitativen Interaktionsscores für alle getesteten Proteinpaare und die Generierung von quantitativen PPIs-Datensätzen.

Im Gegensatz dazu ist der BRIP-Assay ein **B**iolumineszenz-**R**esonanzenergietransfer (BRET) und Co**i**mmun**p**räzipitazions (co-IP)-basierter PPI-Detektions-Assay für die quantitative Interaktombestimmung. Für BRIP-Assays werden die Proteine von Interesse als NanoLuc-Luciferase- und Protein A-mCitrine-Fusionsproteine in Säugertierzellen koproduziert. Die Interaktionen werden sequenziell in einem Experiment durch zwei unterschiedliche PPI-Detektionsprinzipien detektiert. In intakten Zellen werden PPIs über BRET quantifiziert, worauf die Lumineszenz-basierte Detektion von Proteinkomplexen nach der co-IP erfolgt. Die Proteinproduktion von Köder- und Beuteproteinen kann in intakten Zellen und Zelllysaten durch die Messung von Lumineszenz- und Fluoreszenz-Aktivitäten der NanoLuc- und mCitrine-Tags erfolgen. Demzufolge eignet sich der BRIP Assay zur Berechnung von zwei unabhängigen quantitativen Interaktionsscores, einer in intakten Zellen und der andere nach der co-IP.

Beide Assays wurden mit ähnlichen positiven und zufälligen PPIs-Referenzsets etabliert und gebenchmarkt. Während der DULIP-Assay eine vergleichbare Sensitivität und Spezifität zu bereits verfügbaren Methoden zeigte, detektierte der BRIP-Assay eine signifikant größere Anzahl

an Interaktionen des positiven Referenzsets, aufgrund der Kombination von zwei PPIs-Detektionsprinzipien. Des Weiteren zeigte die Analyse eines PPIs-Referenzsets mit bekannten Affinitäten, dass sowohl gering-affine, als auch hoch-affine Interaktionen mit dem DULIP- und dem BRIP-Assay detektiert werden können. Während beide Assays vorzugsweise hoch-affine Interaktionen detektierten, zeigte die BRET-Komponente im Vergleich zur co-IP-Komponente des BRIP-Assays oder zum DULIP-Assay eine höhere Sensitivität bei der Detektion von gering-affinen Interaktionen.

In Studien über die Interaktion zwischen Munc18 und Sytaxin-1 konnten die Effekte von Punktmutationen, welche die Interaktionsstärke beeinflussen, mit beiden Assays detektiert werden. Allerdings konnte nur mit der BRET Komponente des BRIP-Assay ein quantitativer Unterschied zwischen den Effekten der unterschiedlichen Punktmutationen auf die Interaktionsstärke der Munc18-Syntaxin-1-Interaktion aufgezeigt werden.
Zusammengefasst konnte ich in meinen Studien zeigen, dass DULIP- und BRIP-Assays innovative Methoden sind, welche sich für quantitative Interaktomstudien eignen. Diese können angewandt werden, um umfassende und quantitative PPIs-Datensätze in Säugerzellen zu generieren. Weiterhin eignen sich beide Assays zur Messung der Effekte von Punktmutationen auf die Interaktionsstärke und zur Untersuchung von Einflüssen niedermolekularer Substanzen auf PPIs.

3. Introduction

The human genome contains ~20,000 protein-coding genes with an average of four splice variants per gene, suggesting that the human proteome consists of at least 80,000 protein variants that are differentially produced depending on the developmental state, tissue and cell type[1,2]. Proteins are key to all cellular processes including metabolism, cell signaling, gene expression regulation, structural organization and transport processes. They accomplish their cellular functions by interacting directly with other molecules like lipids, metabolites, nucleic acids and proteins[3]. Among those, protein-protein interactions (PPIs) play a crucial role in all cellular functions by sensing and transmitting information, regulating enzymatic activities, maintaining cellular homeostasis and acting as molecular machines. Previous estimations suggest that the human interactome (HI), which is the whole set of possible PPIs within all human cells, consists of 130,000 – 650,000 PPIs[4,5]. However, such estimations assume that each of the ~20,000 protein-coding genes encodes only one isoform. Consequently the actual size of the human interactome is likely to be significantly larger.

Many human diseases are associated with deregulated protein pathways or missense mutations that affect the interaction patterns (edgotypes) of the respective disease proteins[6]. Today, over 100,000 genetic variations are associated with human diseases highlighting the need of a human disease interactome (HDI)[7]. When considering all differences between individuals due to human genetic variation the personal interactome seems an unreachable task. A typical human genome differs from a reference genome by 4.1 to 5.0 million sites (single nucleotide polymorphisms, insertions/deletions, copy number variations, etc.) whereby only a fraction are in the protein coding regions[8]. Consequently, the identification and characterization of PPIs is considered as an important step towards elucidating the function of complex biological systems and the understanding of pathobiological mechanisms in diseases.

Current approaches to generate large-scale PPI maps successfully applied yeast two-hybrid and affinity-purification followed by mass spectrometry (AP-MS)[9-15]. Both types of methods yield reliable, largely complementary PPI data sets, which allow the creation of interactome networks involving whole proteomes or particular cellular pathways and disease processes of interest[9,16-20]. However, most of the generated interaction data contains only qualitative information (yes or no). The development and application of methods that allow the quantification of PPIs has become more prominent only recently[21-24]. Quantifying PPIs is not only an important step towards understanding the molecular basis and significance of interactions, it is even more crucial when it comes to analyzing the impact of disease associated mutations on the perturbation of cellular pathways[7].

3.1. On the binding affinity of protein-protein interactions

If a protein-protein interaction is formed in the cell relies on the encounter of two interacting proteins in space (cellular compartment, cell type) and time (co-expression) as well as on their unoccupied, but compatible interaction surfaces[25]. PPIs can be classified by their function, localization, binding interface or simply by their strength[25]. When characterizing PPIs according to their strength, they are subdivided in transient or permanent associations (Fig. 1a)[26]. Permanent interactions are often considered obligate where the single molecule cannot exist outside its complex and is therefore suggested to be irreversible[27]. An example of a permanent interaction is cytochrome c' which exists only as a homodimer and is part of the electron transport chain in mitochondria[26,28]. In contrast to permanent interactions, most protein complexes constantly associate and dissociate, thus they are transient of nature. Transient interactions can be either weak or strong and the interaction strength is described by the binding affinity that is defined by the equilibrium dissociation constant (K_D)[29]. To experimentally determine the K_D the relative amount of the formed protein complex [AB] is measured at constant concentrations of one interaction partner [A] and increasing amounts of the second protein [B] (Fig. 1b). Hence, the equilibrium dissociation constant K_D is defined as:

$$K_D = \frac{k_{off}}{k_{on}} = \frac{[A] \cdot [B]}{[AB]} = \frac{1}{K_A} \quad (1)$$

where the K_D represents the concentration of the free protein [B] which occupies half of the binding sites of its interaction partner [A] at equilibrium[29]. Protein complexes [AB] will form and separate at a constant rate of association (k_{on}) and dissociation (k_{off})[29]. Binding affinities can also be analyzed in physical terms as the Gibbs free energy of association (ΔG_A)[29,30]:

$$\Delta G_A = -RT\ln(K_A) \quad (2)$$

where R is the gas constant, T the absolute temperature and K_A the equilibrium association constant, which is inverse to the K_D ($1/K_D$). The more negative the value, the more favorable is the interaction. When molecules or proteins associate, heat is evolved or absorbed and the order of the system increased[31]. Therefore PPIs are characterized by changes in enthalpy (ΔH) and entropy (ΔS), which reflect the exact magnitude and nature of the interaction[30]:

$$\Delta G = \Delta H - T\Delta S \quad (3)$$

where ΔH (enthalpy) is the thermodynamic potential, T the absolute temperature (in Kelvin) and ΔS (entropy) the measure of disorder during the reaction. Together, the binding affinity is determined by the local concentration of the protein components and the biochemical and structural properties of the protein binding interfaces[25]. The binding interface of transient interactions is usually smaller (~1000 Å^2) than for permanent interactions (>1000 Å^2), slightly enriched in polar uncharged amino acids but the proportion of hydrophobic residues is usually

the same as for the rest of the protein surface[25,27,32]. Often proteins undergo conformational changes when engaging in PPIs, in some cases even from an unfolded/disordered to a folded/ordered conformation[33]. Interactions that are characterized by a disorder to order transition are highly dynamic and very specific but usually of low affinity[34,35].

Weak transient interactions often have a short lifetime and dissociation constants (K_D) in the micro- to millimolar range, which makes them difficult to detect and are therefore less commonly studied[36]. They are formed continuously to facilitate the regulation of complex biological systems, which is critical for many aspects of cellular function[27]. Examples for transient interactions are between kinases and their substrate or between ubiquitin-conjugating enzymes and ubiquitin ligases[36,37]. As an example, the interaction between the E2 ubiquitin-conjugating enzyme UBE2T (Ubiquitin-conjugating enzyme E2 T) and the E3 ubiquitin ligase FANCL (Fanconi anemia group L protein) has an affinity in the micromolar range (0.45 µM)[37]. FANCL acts in the fanconia anemia (FA) pathway in the nuclear FA complex that mediates the monoubiquitination of FANC2D (Fanconi anemia group D2 protein), a protein that is necessary to activate the DNA damage repair. The interaction was originally identified in a yeast two-hybrid (Y2H) screen and the affinity determined by isothermal titration calorimetry (ITC). Even, the crystal structure was solved, which required, however, the direct fusion of the two proteins[37-39]. Still, the detection of this interaction in living mammalian cells remained unsuccessful until the recent development of a PPI platform that allows the detection of weak PPIs[36].

Strong transient interactions have a K_D in the nano- to femtomolar range and are often regulated by effector proteins like kinases or by bound molecules like GTP. For example, the interaction between the SM (Sec1/Munc18-like) protein Munc18 and the SNARE (soluble N-ethylmaleimide sensitive factor adaptor protein receptor) protein Syntaxin-1 has a relatively high affinity (~10 nM)[40]. SNARE proteins initiate membrane fusion between the synaptic vesicles and the plasma membrane (exocytosis) by forming tight SNARE complexes[41,42]. Especially in neurons, the SNARE complex assembly needs to be tightly regulated as exocytosis results in neurotransmitter release which is crucial for synaptic transmission. Dysfunction of this process can lead to cognitive impairments and neurodegeneration[43,44]. Munc18 is a regulatory protein of the SNARE complex that tightly binds to the inactive, closed conformation of the SNARE protein Syntaxin-1, preventing it thereby to enter the SNARE complex[45,46]. This interaction again is regulated by the protein kinase C (PKC), which is activated after depolarization of the synaptic membrane and Ca^{2+} influx into the presynaptic terminal. Subsequently, PKC phosphorylates several targets like potassium channels but also Munc18. Munc18 is phosphorylated by PKC at two major sites (Serine 306 and 313), which results in a significantly reduced affinity to Syntaxin-1 (840 nM) and an enhanced neurotransmitter release[40,47].

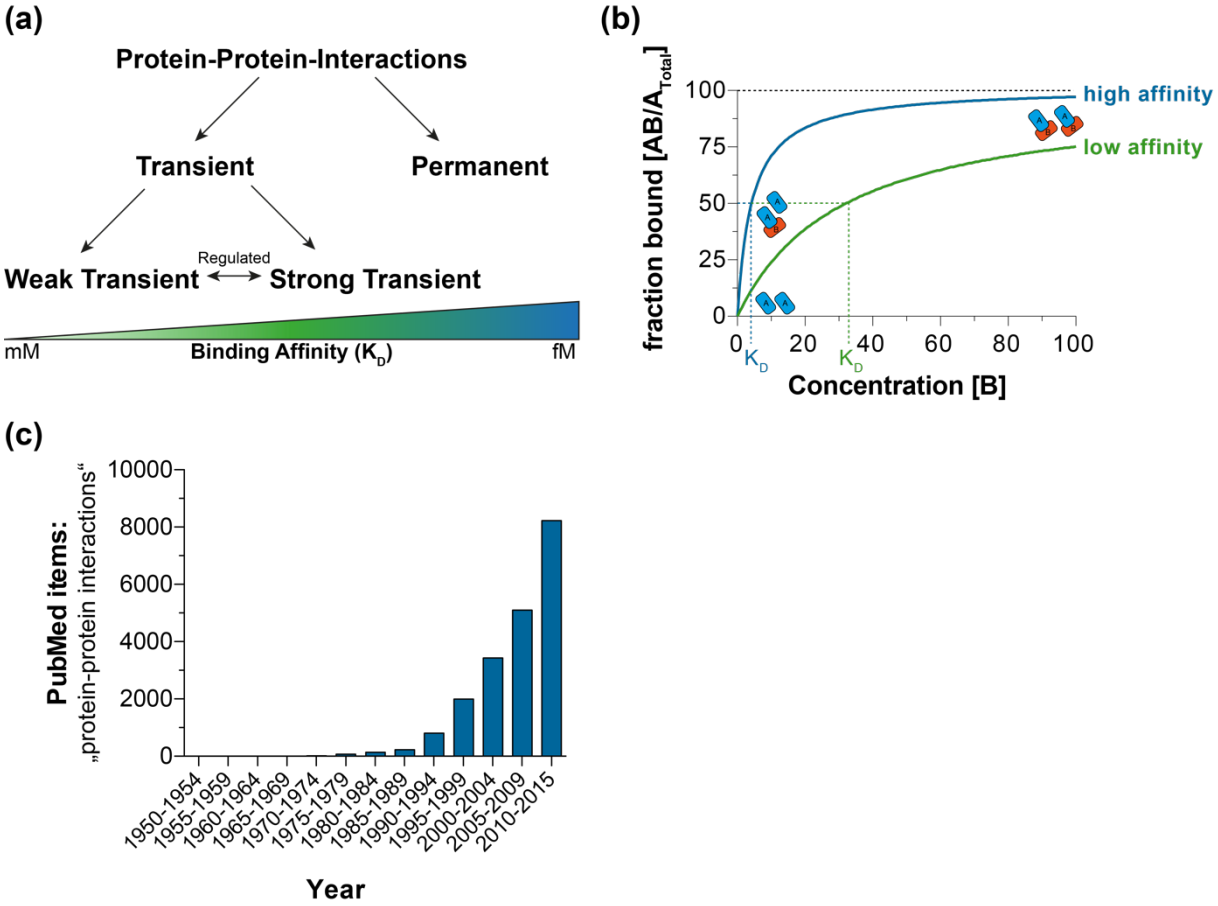

Fig. 1: Protein-Protein Interactions are defined by their affinity. (**a**) Binding affinities are described by the equilibrium dissociation constant (K_D). Permanent interactions usually have a K_D within the femtomolar range, while transient interactions are distinguished between weak transient (milli- and micromolar) and strong transient (nanomolar) interactions. Transient interactions are often regulated by an effector protein, posttranslational modification or conformational change. Adapted from Perkins *et al.* 2010[9] (**b**) Equilibrium dissociation constants can be determined experimentally. Protein [B] is added in increasing amounts to the system, while the quantity of [A] is kept constant. The K_D is the amount of [B] that is necessary so that 50% of the protein complex [AB] forms. Thus lower K_Ds represent higher affinity interactions, whereas high K_Ds are an indication of lower affinity interactions. (**c**) Number of publications found on PubMed between 1950-2015 in 5-year cycles on the search term "protein-protein-interactions".

Taken together, proteins can form permanent protein complexes or transiently interact with other proteins to regulate their activity or transmit information. Transient interactions can be of low or high affinity, with weak interactions being especially difficult to detect.

3.2. Quantitative detection of protein-protein interactions *in vitro* and in cells

PPIs have been studied for more than a century[3,48]. But only with the development of the yeast-two hybrid (Y2H) method and improvements in mass-spectrometry (MS) techniques at the end of the 1980s, appropriate techniques were available to study PPIs systematically, which led to a dramatic increase in publications concerning PPIs (Fig. 1c)[49-51]. With the genomic revolution and the sequencing of genomes the first high-throughput PPI studies became possible[10,11,52-58].

However, Y2H and MS assays typically yield qualitative information without providing information about the strengths of interactions. Today, the diversity of methods to detect PPIs ranges from purely *in vitro* to cell-based approaches, to methods detecting PPIs in whole organisms (*in vivo*)[59]. The following overview presents some of the most important available methods to detect PPIs and their potential to quantitatively measure PPIs is discussed. Thereby, I will use the terms qualitative, semi-quantitative and quantitative interaction scores as follows:

1) qualitative interaction scores provide only yes or no answers and no information on the abundance of the interacting proteins is available;
2) semi-quantitative interaction scores provide a quantitative data output (e.g. raw fluorescence data measured in a microplate reader) and in some cases also information on the relative abundance of one of the interacting proteins;
3) quantitative interaction scores provide at least one quantitative data output and information on the relative abundance of both interacting proteins that can in some cases be used to calculate relative or even absolute binding strengths.

Here, absolute binding affinities are defined by K_D values that are determined *in vitro* where the absolute number of molecules (in mol/l) introduced is known. Such are distinguished from relative binding strengths that are e.g. determined in intact cells. In cells, the absolute number of molecules present is usually unknown and only relative protein and protein-complex quantities can be estimated[60].

3.2.1. Available methods to detect protein-protein interactions *in vitro*

In vitro methods used to detect PPIs rely on recombinant proteins that are usually purified from bacteria or insect cells[61]. Hence, such proteins often lack potentially important posttranslational modifications, have to be purified without their transmembrane domains or exist in intact cells usually only in stable protein complexes[61]. Until today almost only methods that use recombinant proteins allow to determine the thermodynamic parameters of an interaction (e.g. rate of association, dissociation, equilibrium dissociation constant, enthalpy, entropy)[29].

3.2.1.1. Isothermal titration calorimetry (ITC)

The formation of a PPI in solutions results in a change in enthalpy and entropy of the system. The change of enthalpy (heat released or absorbed) can be measured by using isothermal titration calorimetry (ITC), which allows a direct thermodynamic characterization of a PPI. An isothermal titration calorimeter consists of two identical thermal conducting cells, one reference and one sample cell. The cells are surrounded by an adiabatic jacket, which prevents the transfer of heat from the cells to their surrounding. Heaters hold the cells at a constant temperature, and both cells are attached to sensitive thermopile/thermocouple circuits that detect temperature

differences between the reference and the sample cell (Fig. 2a)[62]. During an experiment the sample cell is filled with one of the proteins at a defined concentration, followed by the titration of its interacting partner (ligand). Through the binding of the two proteins heat is released or absorbed depending on the nature of the interaction[31]. During an exothermic reaction the temperature in the sample cell will increase, while it will decrease in an endothermic reaction. As the ligand is titrated into the reaction, its amount increases and therefore also the produced or absorbed heat. Once the interaction is saturated due to ligand excess, less heat is released or absorbed. The amount of power that is necessary to keep the temperature in the sample cell constant is directly measured and plotted against the time (Fig. 2b). The area under each peak corresponds directly to the heat produced or absorbed, which again is directly proportional to the quantity of bound ligand. For data analysis each peak is therefore integrated, normalized to the amount (in mol) of injected ligand and plotted against the molar ratio of the two interacting proteins (Fig. 2b). The equilibrium association constant (K_A), enthalpy (ΔH_A) and binding stoichiometry (n) can be estimated through non-linear regression. Using equations (2) and (3) the Gibbs free energy (ΔG_A) and entropy changes (ΔS_A) can be calculated[29]. Consequently, ITC is a quantitative *in-vitro* method to determine the thermodynamic parameters of an interaction.

3.2.1.2. Surface Plasmon Resonance (SPR)

Another *in vitro* method that is commonly used to detect and quantify PPIs is surface plasmon resonance (SPR). In contrast to ITC, SPR is an optical detection method for which one of the interaction partners is immobilized on a thin gold film. Its binding partner (ligand) is continuously passed over it through a flow cell in an aqueous solution. Polarized light is generated by a laser and directed at a critical angle through a prism to the bottom surface of the gold film in order to excite surface plasmons (Fig. 2c)[63]. Surface plasmons (SPs) are delocalized electrons that propagate as electromagnetic waves along a metal surface. When an SP is excited by a photon, the photons energy is transferred to the electromagnetic wave and thus the reflected light decreases. The angle of the polarized light used is critical to excite an SP and depends on the refractive index within 300 nm of the gold surface. This changes when a ligand binds to the immobilized protein on the gold film. Consequently, the change in the refractive index results in an increase in light intensity as less energy is transferred from the photons to the electromagnetic wave[64]. This increase in light is described by the resonance/response unit (RU) where 1 RU is equal to a 0.0001 degree change of the critical angle.

At the beginning of the experiment, the immobilized proteins have not yet been exposed to their interaction partner. Once the ligand is injected into the flow cell, the association rate (k_{on}) is measured as a function of RU over time (Fig. 2c and d). When the immobilized protein is saturated with ligand, the RU reaches a maximal plateau that can be used to determine the K_D

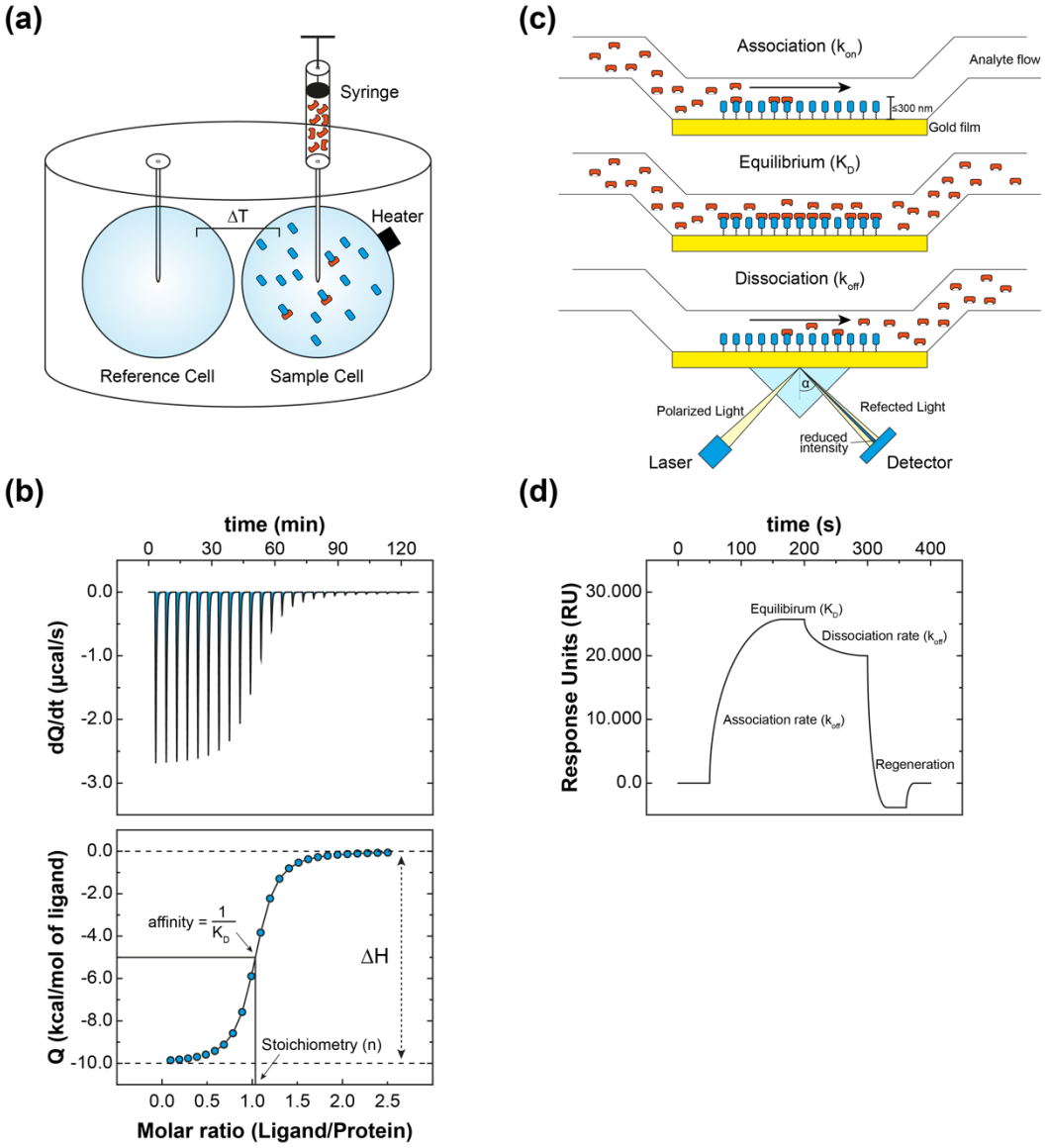

Fig. 2: Quantitative *in vitro* methods to determine binding affinities. (**a**) For isothermal titration calorimetry (ITC) a reference and sample cell are surrounded by an adiabatic jacket. The sample cell contains a purified protein, to which its ligand is titrated. (**b**) The energy which is necessary to keep the sample and the reference cell at a constant temperature is recorded, and by integrating the area under the curve it can be plotted against the molar ratio of the interacting proteins. Through non-linear regression the thermodynamic parameters enthalpy (ΔH), molecular stoichiometry (n) and the equilibrium dissociation constant (K_D) can be estimated. (**c**) Schematic representation of a basic surface plasmon resonance (SPR) experiment. A protein is immobilized on a gold film that creates the bottom of a flow chamber, through which a ligand is passed in an aqueous solution. Ligand binding to the immobilized proteins results in a change of the refractive index that can be detected optically as a change in light intensity (**d**). Initially, the addition of ligand is used to measure the association which reaches an equilibrium when all proteins are saturated with ligand. Next, the ligand flow is stopped, wherefore bound ligands dissociate. The flow chamber can be regenerated by removing all ligand so that it can be used repeatedly.

(Fig. 2c and d). Finally, the ligand is removed from the solution in the flow cell and the rate of dissociation (k_{off}) of the bound ligand from the immobilized protein measured (Fig. 2c and d)[65]. Interestingly, SPR can be coupled with mass spectrometry (SPR-MS) to capture, quantify and identify binding partners of a protein of interest from a protein solution (cell or tissue lysate)[66].

In contrast to other methods, detection of PPIs by SPR is non-destructive, does not require the use of specific antibodies and interacting proteins can be directly analyzed via MS[64,67]. Thus SPR is a quantitative method that can even be adapted to identify PPIs in high-throughput[64].

3.2.2. Available methods to detect protein-protein interactions in cells

Even though *in vitro* methods are indispensable to determine kinetic and thermodynamic parameters of a PPIs, they also have their drawbacks due to the purification of proteins from bacteria, insect cells or by cell-free systems[61]. Furthermore, such methods are often carried out in low-throughput and can thus not be used to map PPIs on a proteome-wide scale. In contrast, methods to detect PPIs in yeast or mammalian cells can be performed in high-throughput and, at the same time, have the advantage that the proteins are present in a more native environment. However, such techniques often require high over expression, the use of protein tags and quantification of interactions or the calculation of binding strengths is difficult. Therefore, *in vitro* and in-cell methods are complementary to each other and can be used to determine all parameters of a given interaction. Hereinafter, an introduction to a fraction of the wide variety of available PPI methods in yeast and mammalian cells is given.

3.2.2.1. Yeast two-hybrid (Y2H)

The yeast two-hybrid (Y2H) was invented in 1989 by Stanley Fields and Ok-kyu Song[49]. It laid the basis for high-throughput interactome research which started 10 years later. Today, the Y2H is still a flourishing technique for binary interaction mapping[12,53,68].

The Y2H is based on the reconstitution of a transcription factor that results when two proteins interact and the subsequent transcriptional activation of a reporter gene. Traditionally, the yeast native transcription factor GAL4 is split into its two domains, the N-terminal DNA binding domain (DBD) and the C-terminal transcriptional activation domain (TAD), each genetically fused to a protein of interest[49]. The DBD binds to the upstream activating sequence (UAS) but cannot activate transcription independently. Only when the two hybrid proteins interact in the nucleus of a yeast cell, the TAD is recruited to the UAS, resulting in the transcriptional activation of a reporter gene (Fig. 3a). Typical reporter genes can be auxotrophic markers encoding for an essential enzyme in an amino acid synthesis pathway (e.g. *HIS3*, *URA3*) or other reporters like the β-galactosidase enzyme. Hence, PPIs are monitored in yeast cell growth assays or by quantifying the enzymatic activity of the β-galactosidase. Nowadays multiple variants of the Y2H system are available, ranging from different DBD/TAD combinations to split-ubiquitin systems and mammalian based two-hybrid approaches[10,69-71].

Until today, the Y2H system has been used to identify thousands of interactions in various species, being currently the most efficient method to map binary PPIs[10-12,53,72,73]. Despite constant

criticisms of the Y2H assay, which suggest that the method has a relatively high false-positive rate, experimental benchmarking approaches with a random reference set have shown that different Y2H variants exhibit excellent false-positive detection rates of only 1.0-4.5%, which is comparable to other commonly used methods[74-77]. Nevertheless, interactions are not discovered in their native environment and have to occur in the yeast nucleus. Thus, interactions with potentially no biological relevance can be discovered. Hence, the validation of Y2H identified PPIs in mammalian cells is an important step towards increasing the confidence of such interactions. This needs adequate methods that provide a high sensitivity and specificity to validate particularly Y2H interactions[71].

In a typical Y2H experiment yeast colony growth assays are used to provide qualitative information about an interaction[78]. A semi-quantitative read-out can be achieved by measuring the size of a colony or by determining the enzymatic activity of the β-galactosidase[79-81]. Such interaction scores can be used to quantitatively compare the effect of point mutations on interaction strength when studying the same protein pair, assuming that the point mutations do not influence protein stability or production[82]. Still, as absolute protein-levels of hybrid fusion proteins cannot be easily measured, quantitative interaction scores that allow a comparison of different interactions cannot be determined.

3.2.2.2. Bimolecular fluorescence/luminescence complementation assay (BiFC/BiLC)

Protein complementation assays (PCAs) have a long history of being used to study PPIs in yeast or mammalian cells[83-86]. Typically, in protein complementation assays a fluorescent protein or an enzyme is split into two parts, each of which is fused to the N- or C-terminal parts of the proteins of interest. Different variants of PCAs have been used in small- or genome-scale experiments to identify novel PPIs or to validate PPIs that were initially identified e.g. in a Y2H screen[12,69,87-89].

Besides the Y2H system, one of the most common PCAs is the bimolecular fluorescence complementation (BiFC) assay, which is based on the reconstitution of a fluorescent protein (Fig. **3**b). It was first described in the year 2000 for the green fluorescent protein (GFP), which was split into an N- and a C-terminal fragment that contains the first 157 (NGFP) or the terminal 81 amino acids (CGFP)[85]. The fragments did not reconstitute a functional GFP protein independently, which is why both were fused to peptides that assembled into antiparallel leucine zippers. Following, the GFP reassembled into an active fluorescent protein exhibiting a single excitation maximum at 475 nm and an emission maximum at 506 nm[85]. By now, BiFC assays have been developed for many of the available fluorescent proteins (FPs), ranging from the enhanced cyan, green and yellow fluorescent proteins (ECFP, EGFP, EYFP) over Venus, Citrine, Cerulean to mCherry and many more (reviewed in Miller *et al.* 2015)[90]. However, all these variants suffer from spontaneous self-assembly of the protein fragments, which results in a relatively high

background fluorescence and therefore in a low signal-to-background ratio. To overcome this limitation, specific variants of the Venus-based BiFC system were developed with improved signal-to-background ratios[91,92]. Furthermore, once the intact fluorophore has formed it is irreversible, which limits the method's use in studying PPI dynamics, leads to false-positive results and contributes to the high background fluorescence[93].

A related PCA is the bimolecular luminescence complementation (BiLC), which uses a luciferase instead of a fluorescent protein (Fig. 3c). Similar to BiFC, BiLC has been developed in different flavors, using either the Firefly[94], *Renilla*[95], *Gaussia princeps*[96] or more recently the NanoLuc[97] luciferase. It is important that the reconstitution of the luciferase fragments is reversible, therefore allowing to detect associations and dissociations of PPIs in living cells in real-time[96,98]. Thus, the BiLC offers a high signal-to-background ratio, which is, together with its reversibility, its main advantage over the BiFC system. Even though BiLC has been used to provide subcellular information on the localization of a studied PPI[99], detecting luminescence by bioluminescence imaging remains challenging due to the relatively low number of emitted photons[100]. In contrast, BiFC approaches have the advantage that protein complexes can be directly visualized in living cells on a subcellular scale at a spatial resolution of ~200 nm, using conventional fluorescence microscopy. With the recent combination of BiFC and super-resolution microscopy (BiFC-PALM) it has become possible to increase the spatial resolution to about 20 nm[101,102]. Nowadays, multiple variants of BiFC/BiLC methods are available, approaching different challenges. The simultaneous visualization of multiple protein interactions in individual cells was accomplished through the combination of fragments from different fluorescent proteins, which results in the formation of distinct fluorescent protein assemblies with different spectral characteristics[103]. More recently, Cabantous and colleagues circumvented the common problem of large protein tags necessary to study PPIs in intact mammalian cells by generating a tripartite split-GFP method[104]. Instead of splitting GFP in two, they generated three fragments: two distinct twenty amino-acid long tags (GFP10 and GFP11) that are each fused to the proteins of interest and one GFP detector (GFP1-9) comprised of the residual protein. When the proteins of interest interact and GFP10/GFP11 form an intact fragment, the GFP detector binds to this complex reconstituting a functional fluorescent protein[104].

A great advantage of BiFC/BiLC methods is their potential to detect weak transient interactions due to their high sensitivity that results from the new fluorescent/luminescent signal produced only upon interaction. For example, the interaction between the c-Abl-SH3 domain and the poly-proline peptide p41 (K_D=1.5 µM) can be detected with the YFP-based BiFC variant in intact cells[105]. In a different approach, a Cre-recombinase mediated cassette exchange was combined with the firefly luciferase-based BiLC system (ReBiL) to generate stable, inducible cell lines with which the low affinity PPI between FANCL and UBE2T (K_D=0.454 µM) could be validated in

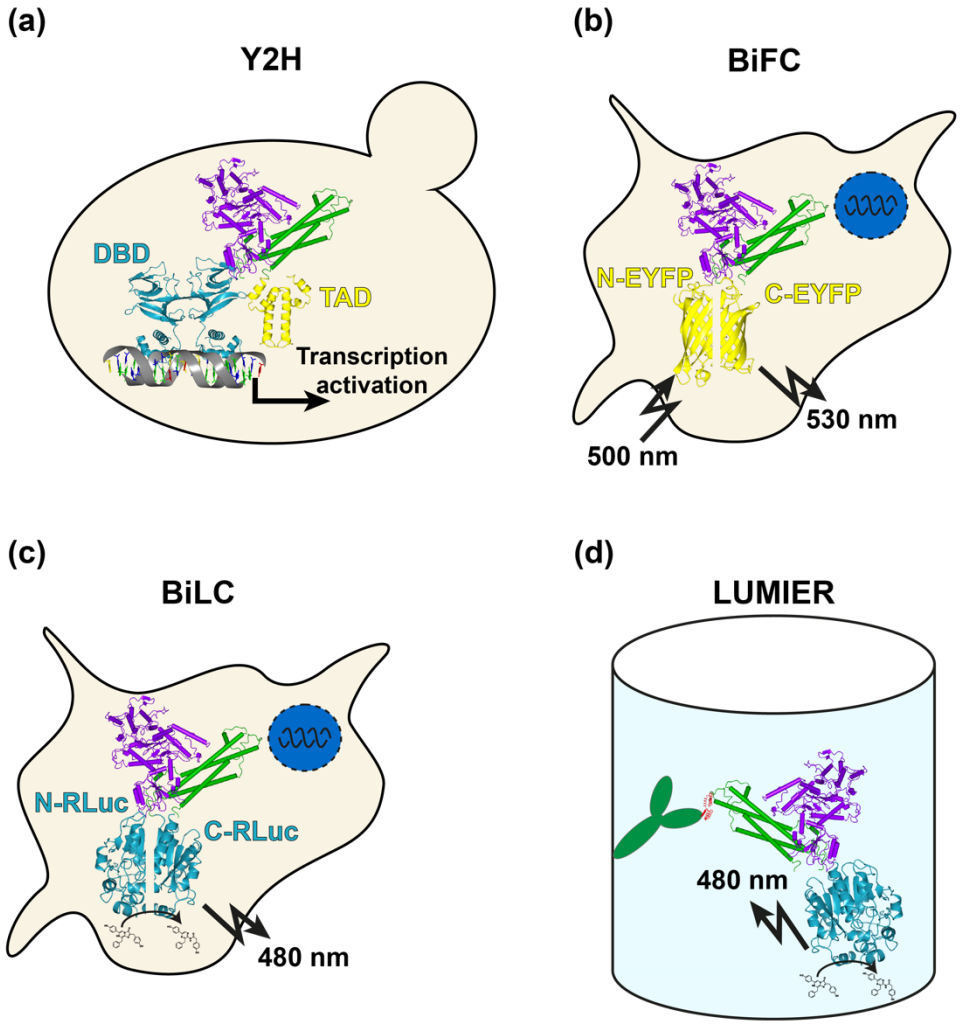

Fig. 3: **Methods to detect protein-protein interactions in yeast and mammalian cells.** (**a**) The yeast two-hybrid (Y2H) system is based on the reconstitution of a DNA binding domain (DBD) and a transcriptional activation domain (TAD) when two proteins interact, leading to the transcriptional activation of a reporter gene. (**b**) Bimolecular fluorescence complementation assay (BiFC). Cells produce the proteins of interest that are fused to a N- or C-terminal fragment of a fluorescent protein (e.g. EYFP). Upon interaction, the fluorescent protein is reconstituted which then emits light after excitation. (**c**) Bimolecular luminescence complementation (BiLC) assay. Cells produce the proteins of interest that are fused to a N- or C-terminal fragment of a luciferase (e.g. *Renilla*). Upon interaction, the luminescent protein is reconstituted which then emits light after substrate conversion. (**d**) Luminescent-based mammalian interactome mapping (LUMIER). Cells produce proteins of interest, where one is fused to a FLAG-tag and the other to the *Renilla* luciferase. After cell lysis, immunoprecipitation is performed with α-FLAG antibody coated microtiter plates and the luminescence as a measure of co-IP efficiency determined after substrate addition.

mammalian cells for the first time[36]. A disadvantage of BiFC/BiLC methods is their incapability to directly determine protein expression levels of the individual fusion proteins, as the protein-fragment tags are non-functional when not reconstituted. Thus it is impossible to determine the fraction of proteins engaged in a PPI compared to the total protein amount. Consequently, the quantification of PPIs using BiFC/BiLC is difficult as only semi-quantitative interaction scores can be obtained. Even though it was suggested that BiFC/BiLC are suitable for the quantitative analysis of PPIs because the fluorescence or luminescence emitted is dependent on the amount of protein-complex formation, this assumption neglects that the total protein amount has an important influence on the emitted fluorescence/luminescence as well[106]. Still, a reasonable first attempt

was undertaken to perform quantitative BiFC experiments in *Saccharomyces cerevisiae* by using strains that express one of the interacting proteins under the control of three different promoters resulting accordingly in different protein levels. At the same time, the interaction partner was expressed under the control of the same promoter ensuring constant protein levels. Consequently, the relative amount of the two interacting proteins was different in the individual strains, resulting in different fluorescence intensities[106]. Adaptation of this approach to achieve a higher diversity in protein expression (e.g. through an inducible expression system) would likely allow the generation of quantitative interaction scores. Nevertheless, the application of this approach to systematic PPI studies is impractical, as the number of relative proteins would have to be detected by Western-blotting or ELISAs (Enzyme Linked Immunosorbent Assays) which are both dependent on antibodies.

BiFC and BiLC approaches are highly variable, allow for the localization of a PPI at subcellular resolution, and are highly sensitive to detect low affinity interactions. However, in BiFC and BiLC approaches, the quantification of protein levels is tedious and both methods are thus not suited to generate quantitative interaction score, despite their quantitative data output (measured fluorescence/luminescence). Furthermore, the missing information of protein levels can impede trouble-shooting about undetected PPIs and consequently lead to high false-negative results.

3.2.2.3. Luminescence-based Mammalian Interactome Mapping (LUMIER)

In traditional co-immunoprecipitation (co-IP) assays, the co-IP-efficiency is determined by Western-blotting, which limits assay-throughput and quantifiability of interactions[107]. With the development of the LUMIER (luminescence-based mammalian interactome mapping) assay, high-throughput screening and quantification of interactions after immunoprecipitation (IP) have become possible[108]. Consequently, among the currently available mammalian cell-based interaction detection methods, only the LUMIER method has been applied repeatedly in systematic, large-scale PPI screening efforts[7,13,22,69,74,108-115]. The LUMIER assay is a luminescence-based co-IP assay, in which the *Renilla* luciferase (RL) is fused to proteins of interest (prey). These RL-tagged preys are co-produced with individual FLAG-tagged bait proteins, and interactions are detected by measuring the RL enzymatic activity after cell lysis and IP (Fig. 3d). Importantly, the LUMIER assay does not only provides qualitative information about an interaction, but also yields a semi-quantitative read-out[108]. However, with the initial set-up bait protein quantity cannot easily be measured, which is why the calculation of quantitative interaction scores or relative binding strengths is not possible[108]. To overcome this limitation, different approaches have been undertaken: Taipale *et al.* established a LUMIER method with bait control (LUMIER with BACON) where bait protein quantification is achieved through ELISAs. ELISAs are performed after the initial luminescence measurement and include additional washing steps and incubation with an

HRP (horseradish peroxidase)-coupled FLAG antibody[22]. Through the application of LUMIER with BACON, a large number of novel client proteins interacting with the molecular chaperone Hsp90 have been identified and more recently a comprehensive quantitative chaperone interaction network revealing the architecture of protein homeostasis pathways has been generated[22,114]. Furthermore, in a collaborative approach from the labs of Marc Vidal, Albertha Walhout and Susan Lindquist, the first large-scale characterization on the effects of disease mutations on PPIs was performed[7].

In an alternative approach, Jia *et al*. developed a dual luciferase reporter pull-down (DLR-PD) assay, which uses two luciferase-tagged fusion proteins. The bait is tagged to the firefly luciferase that contains an additional HAVI-tag (6xHis and Avi-tag) while the prey is fused to the *Renilla* luciferase. In contrast to the LUMIER, streptavidin beads are utilized for the precipitation of biotinylated bait protein. Biotinylation is achieved through the additional co-expression of a biotin-protein ligase (BirA) which specifically adds a biotin covalently to a 14-mer peptide, the Avi-tag[116,117]. Thus, the DLR-PD assay allows the easy quantification of both bait and prey proteins in cell lysates and after immunoprecipitation. However, the additional co-production of the BirA ligase and the dependency of the immunoprecipitation on the biotinylation efficiency introduces an additional variable that is difficult to control and that is likely to have have a strong impact on reproducibility.

In total, with the advancements of the initial LUMIER assay two closely related methods are available that allow the generation of systematic, large-scale and quantitative interaction maps.

3.2.2.4. Fluorescence/Bioluminescence Resonance Energy Transfer (FRET/BRET)

The concept of resonance energy transfer (RET) was first described more than 80 years ago by James Franck and Günther Cario, who discovered the energy transfer between two atoms, mercury and thallium, in vapor[118,119]. Almost 30 years later Theodor Förster studied the mechanisms of fluorescence resonance energy transfer (FRET, often also referred to as Förster resonance energy transfer) between fluorescein and chlorophyll and proposed that the transfer efficiency (E) is inversely correlated to the sixth power of the distance (r) between the two molecules[120]:

$$E = \frac{1}{1 + \left({}^{r}/_{R_0}\right)^6} \qquad (4)$$

where R_0 is describing the Förster radius, which is the critical distance of the two molecules at which the RET efficiency is 50%. Hence, during FRET, energy from an excited donor (D) fluorophore is transmitted to an acceptor (A) molecule only when the two are within 1-10 nm of each other[121]. If the acceptor is also a fluorophore the transmitted energy is emitted as a photon with a longer wavelength. The transfer is non-radiative, meaning that the donor does not actually

emit a photon and the acceptor does not absorb one. Förster proposed that this radiation free energy transfer occurs via a long-range dipole-dipole resonance interaction between the donor and acceptor chromophores and that this is dependent on the relative dipole orientation (κ) of their dipoles (Fig. 4c):

$$\kappa = \frac{1}{\tau_D}\left(\frac{R_0}{r}\right)^6 \quad (5)$$

where τ_D is the donor life-time and R_0 again the Förster radius. The Förster radius is specific for different pairs of molecules as it depends not only on the orientation (κ) of the dipols but also on the spectroscopic properties of the donor and acceptor:

$$R_0^6 = 8.785 \times 10^{-5} \frac{\kappa^2 \varphi_D J}{n^4} \quad (6)$$

where κ is the dipole orientation factor, ϕ_D the quantum yield of the donor (ratio of emitted photons to absorbed photons), *n* the refractive index of the medium and *J* the overlap integral between the donor emission and acceptor excitation spectra. Thereby the overlap integral *J* also accounts for the molar extinction coefficient of the acceptor, which describes the capacity of the acceptor to absorb a photon.

One of the initial applications of FRET was its use as a spectroscopic ruler as it was early discovered that the energy transfer is dependent on the distance separating the fluorophores[122]. However, only with the identification of the green fluorescent protein (GFP) and the possibility to use it as a genetically encoded tag in 1994, the basis to systematically study PPIs by FRET was created[123,124]. Already, within the next three years multiple variants of the wild-type GFP protein were developed that exhibited a wide range of spectral properties and today the whole spectrum of visible light is covered by different types of fluorescent proteins, making FRET accessible for a broad application in cell-based assays[125,126]. One of the first applications of FRET using variants of the GFP was as biological sensor for calcium and to monitor the activity of proteases[127-129]. At the same time, the exceptional suitability of FRET to study protein-protein interactions was recognized and the method was applied to study the interaction between the apoptotic proteins Bcl-2 and Bax[130]. When studying PPIs, one protein is genetically fused to a donor (e.g. ECFP) and the other to an acceptor (e.g. EYFP) fluorescent protein, with FRET generally being detected only when the two labeled proteins interact directly (Fig. 4a)[131]. Commonly, FRET can be determined by measuring the fluorescence intensities or the donor lifetime with a microscope or a fluorescence microplate reader, because as a consequence of an interaction, i) the emission of the donor is quenched, ii) the emission of the acceptor increases, and iii) the lifetime of the donor in its excited state is reduced, all of which can be used for the calculation of the FRET efficiency[132]. Donor quenching can be detected by acceptor photobleaching experiments where

the acceptor is photochemically destroyed, which leads to dequenching and hence to an increased emission of the donor that can be quantified and used to calculate FRET efficiencies[133]. Alternatively, the increased acceptor emission after an energy transfer can be quantified directly in sensitized emission (SE) measurements, which requires more complicated normalization procedures[134]. One requirement for FRET is that donor emission and acceptor excitation overlap significantly. Yet, imperfections in the spectroscopic properties of both fluorophores also result in overlapping donor and acceptor excitation and emission spectra (Fig. 4d). Hence, excitation of the donor with an external light source leads to a direct acceptor excitation that is not the result of a resonance energy transfer (acceptor cross-excitation, Fig. 4d). Furthermore, the energy that is not transferred onto the acceptor after donor excitation is emitted as light, which is also detectable at the acceptor emission wavelength (donor bleedthrough) and cannot be easily distinguished from the actual acceptor emission (Fig. 4d). Several algorithms to correct for acceptor cross-excitation and donor bleedthrough have been developed, being very similar and often base on the same mathematical principles[135]. To correct for both, two reference measurements are performed in which only donor or only acceptor fluorophores are present. The donor only sample allows to correct for the donor bleedthrough whereas the acceptor only sample makes it possible to correct the acceptor cross-excitation. However, as not all donor and acceptor molecules participate in a FRET interaction the total concentration of donor or acceptor, or the concentration of both needs to be taken into account[134,135]. Caution should be exercised at high levels of free donor or acceptor protein, as this can mask a positive interaction.

Lastly, the lifetime of the excited donor, which is reduced in the presence of an energy transfer can be determined using fluorescence lifetime imaging microscopy (FLIM). A great advantage here is that donor bleedthrough and acceptor cross-excitation are irrelevant as they do not modify the lifetime. The lifetime is independent of the concentration of the fluorophores, excitation light intensity and detector sensitivity. Hence, FLIM-FRET is the most straightforward method to determine FRET, and it has been suggested just recently that by using multichannel FLIM-FRET (MC-FLIM-FRET) even relative binding strengths on a single-cell scale can be determined[136].

However, acceptor photobleaching and FLIM measurements cannot be performed easily in systematic screening approaches as they require special microscopic setups. In contrast, sensitized emission can be calculated from fluorescence values detected with a fluorescence microplate reader and is therefore more suitable for large scale screening approaches.

Interestingly, resonance energy transfer between proteins is a natural phenomenon occurring in marine animals, such as in the jellyfish *Aequorea victoria* or in the sea pans *Renilla reniformis*. However, the energy transfer in such animals does not occur between two fluorescent proteins but rather between a luciferase (donor) and a fluorescent protein (acceptor). This process is

termed bioluminescence resonance energy transfer (BRET). It occurs in the same organism from which the green fluorescent protein (GFP) was first isolated in 1961, but the phenomenon of BRET remained unrecognized at the time[123]. Osamu Shimomura and his colleagues noticed that the greenish luminescence of *Aequorea* shifted to a blue color when disrupting the animals with cytolytic agents or analyzing the purified luciferase (aequorin) solution. Still, they documented that the green light emanating in the living animals was likely a result of a fluorescence produced by the "green protein". Only 10 years later Morin and Hastings noticed that the green fluorescence indeed involved an energy transfer similar to FRET from aequorin to GFP[123,137,138]. Despite the early discovery of BRET as a natural phenomenon, the first time that it was used to study a PPI was in 1999, one year after FRET was first applied to study a PPI with genetically encoded fluorescent fusion proteins[130,139]. Accordingly, for BRET experiments the two studied proteins have to be fused to a luciferase and a fluorescent protein. The first luciferase-fluorescent protein combination was between the *Renilla* luciferase and the yellow fluorescent protein (YFP), but nowadays numerous different combinations are used (Fig. 4b)[139,140]. Similar to FRET, the donor emission and acceptor excitation have to overlap significantly for an efficient energy transfer to occur (Fig. 4e). However, unlike a fluorescent donor, which has to be excited with monochromatic light at its specific excitation wavelength, the luciferase uses a chemical substrate that is oxidized to produce light at a luciferase-substrate-complex specific wavelength (Fig. 4b)[141]. For example, the *Renilla* luciferase has its emission (Em) maximum at 480 nm when using coelenterazine h[139], but at 395 nm when using the substrate derivative DeepBlueC[142]. Consequently, BRET assays do not suffer from acceptor cross-excitation, which simplifies data analysis (Fig. 4e). Not only the *Renilla* luciferase, but also the firefly[143], *Gaussia*[144] or NanoLuc[145] luciferase have been used as energy donors for BRET assays. Accordingly a wide range of acceptor fluorescent proteins with compatible excitation spectra, like GFP, EGFP, DsRed and different YFP proteins, such as EYFP and Venus have been utilized in various BRET versions[146,147]. In addition to genetically encoded fluorescent proteins, quantum dots (QD) or fluorescent dyes can be used as acceptors[145,148,149]. However, both cannot be encoded genetically and hence the labeling has to occur in the case of QDs *in vitro* and for fluorophores via a chloroalkene linker, which irreversibly binds to the HaloTag through the formation of a covalent bond[145]. The HaloTag is a 36 kDa large protein tag that can be genetically fused to proteins of interest, which therefore allows to label HaloTag fusion proteins with fluorophores also in living cells[150]. An overview of the most popular BRET systems can be found in Table 1.

While the underlying physical mechanisms of resonance energy transfer (RET) are identical for the bioluminescence and fluorescence-based transfer, BRET assays offer several advantages over FRET: i) the donor is not excited with monochromatic light excluding acceptor cross-excitation and donor photobleaching, ii) reduced auto-fluorescence emitted from endogenous cell

Table 1: Overview of the most popular BRET systems. Em: emission; Ex: excitation.

System	Donor	Substrate	Em [nm]	Acceptor	Ex [nm]	Em [nm]	Oligomers
BRET1[139]	*Renilla*	Coelenterazine	480	EYFP	514	527	Weak Dimer
BRET2[142]	*Renilla*	DeepBlueC	395	GFP2/10	395	510	Weak Dimer
BRET3[151]	*Renilla8*	Coelenterazine	480	mOrange	548	562	Monomer
BRET4[143]	Firefly	Luciferine	565	DsRed	556	586	Monomer
BRET5[144]	*Gaussia*	Coelenterazine	467	EYFP	514	527	Weak Dimer
BRETn[152]	NanoLuc	Furimazine	460	Venus	515	528	Weak Dimer
eBRET[153]	*Renilla*	EnduRen	480	EYFP	514	527	Weak Dimer
enhanced BRET2[154]	*Renilla8*	DeepBlueC	395	GFP2/10	395	510	Weak Dimer
QD-BRET[155]	*Renilla8*	Coelenterazine	480	QD65	300-650	655	Oligomers
NanoBRET[145]	NanoLuc	Furimazine	460	HaloTag-NCT	595	635	Monomer

compartments after excitation with an external light source, iii) luciferases provide a higher sensitivity due to increased signal-to-background ratios and iv) lower donor and acceptor protein levels are sufficient due to the signal amplification of the luminescence reaction, which reduces unspecific encounters between donor- and acceptor-fused hybrid proteins[140,156].

However, in contrast to traditional BRET assays, FRET can be readily used to monitor PPIs in living cells at subcellular resolution by fluorescence microscopy[157]. This is achieved by the higher brightness of fluorescent proteins when excited by an external light source. Thereby, the brightness of a fluorescent protein is defined as the product of the molar extinction coefficient (efficiency for the absorption of a photon) and the quantum yield (probability of photon emission per absorbed photon)[126]. Similarly, the brightness of a luciferase is defined as the product of the enzymatic rate and the quantum yield, while the quantum yield of a luciferase is the probability of photon emission per consumed substrate molecule[158,159]. Even though the quantum yield of luciferases is comparable to fluorescent proteins, e.g. firefly has a quantum yield of 0.44 and the enhanced cyan fluorescent protein (ECFP) of 0.40, luminescent assays typically yield lower light intensities due to slower rates by which the excited state is reached[158,160]. Therefore, for techniques in which the brightness is the limiting parameter, like flow cytometry or microscopy where individual cells are studied, fluorescence-based approaches are favored[158]. As a consequence, imaging by bioluminescence microscopy is rarely used to detect PPIs with BRET at subcellular resolution as it requires ultra-sensitive cameras and long detection times[159]. However, when studying whole cell populations, for example in a microplate reader, luminescence offers a greater sensitivity to fluorescence as no optical filters or monochromators are needed[158].

With the recent development of the NanoLuc luciferase, which is a structurally optimized derivative of the small subunit of the *Oplophorus gracilorostris* luciferase, and the co-development of a new substrate (furimazine), a luciferase-substrate complex was generated with increased brightness and the potential to overcome the limitations in bioluminescence imaging[161-163]. The NanoLuc is only 19 kDa in size, shows a ~150-fold higher activity than the *Renilla* or firefly luciferases, and exhibits improved biochemical and physical characteristics (pH-,

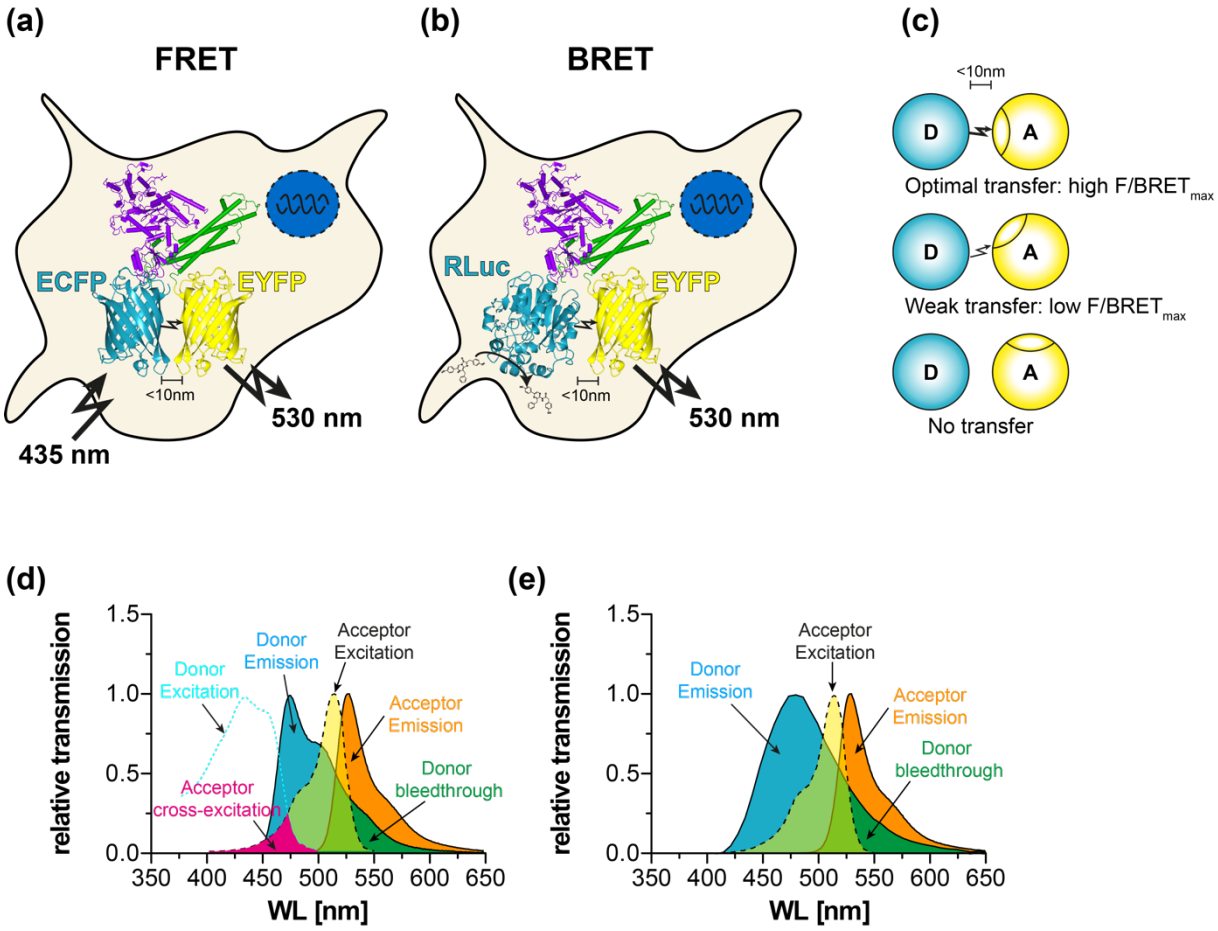

Fig. 4: Resonance energy transfer based methods to monitor protein-protein interactions in mammalian cells. (**a**) Fluorescence resonance energy transfer (FRET). Cells produce proteins of interest that are fused to a donor fluorescent protein (e.g. ECFP) or an acceptor fluorescent protein (e.g. EYFP). Upon interaction and excitation of the donor, the energy is transferred radiation-free via long-range dipol-dipol interactions from the donor onto the acceptor. For an efficient energy transfer to occur, the fluorophores have to be within 10 nm of each other. (**b**) Bioluminescence resonance energy transfer (BRET). Cells produce proteins of interest that are fused to a donor luciferase (e.g. *Renilla*) or an acceptor fluorescent protein (e.g. EYFP). Upon interaction and substrate conversion of the donor, the energy is transferred radiation-free via long-range dipol-dipol interactions from the donor-substrate complex onto the acceptor. For an efficient energy transfer to occur, donor and acceptor have to be within 10 nm of each other. (**c**) The prerequisite for a resonance energy transfer (RET) are the close proximity of donor and acceptor (<10 nm) and the proper orientation of the dipols. If the donor emission dipol and acceptor absorption dipol form a 90° angle, no RET can occur. (**d**) Excitation and emission spectra of donor (e.g. ECFP) and acceptor (e.g. EYFP) fluorescent proteins were generated from raw data available from Chroma Technology Group®. Acceptor cross-excitation results from direct excitation of the acceptor with the wavelength used to excite the donor. Donor bleedthrough is the donor emission overlapping with the acceptor emission. (**e**) Emission spectrum of the donor luciferase (e.g. *Renilla*, in-house measurement) and excitation and emission spectra of the acceptor fluorescent protein (e.g. EYFP, raw data from Chroma Technology Group®). Donor bleedthrough is the donor emission overlapping with the acceptor emission.

temperature-, urea resistance)[163]. Furthermore, its relatively narrow emission spectrum, peaking at 460 nm, and its overlap with the excitation spectrum of green and yellow fluorescent proteins, make it a popular choice as a donor luciferase in recent BRET assays[145,152,164,165].

Compared to FRET, where various approaches can be used to determine the transfer efficiency, the calculation of BRET is easier and mostly consistent[166]. The emitted luminescence is commonly detected at the short wavelength of the donor (e.g. at 480 nm for *Renilla*) and at the long wavelength of the acceptor (e.g. at 530 nm for YFP). The ratio of the long to the short wavelength

(BRET ratio) gives a direct estimation of the BRET efficiency, which has to be only corrected for the donor bleedthrough[156].

While FRET and BRET efficiencies give quantitative values that are mostly dependent on the donor-acceptor distance and not on the affinity of the interacting proteins, saturation experiments where the quantity of one interaction partner is kept constant while increasing amounts of the other are produced allow the estimation of relative in-cell binding strengths[167]. From such experiments, the parameters $BRET_{50}$ and $BRET_{max}$ or respectively, $FRET_{50}$ and $FRET_{max}$ can be extracted, where $B/FRET_{max}$ represent the maximal B/FRET efficiency at which the protein that is kept constant is completely saturated with its binding partner[168,169]. In contrast, the $B/FRET_{50}$ value, which represents the stoichiometric ratio of donor to acceptor at which the half-maximal B/FRET efficiency is reached, gives a direct readout of relative in-cell binding strengths that can be compared between different PPIs (compare to Fig. 1b)[168].

Consequently, of the presented in-cell methods to monitor PPIs, BRET and FRET assays provide the most reliable quantitative interaction scores, which even allow to determine $B/FRET_{50}$ values that correlate to relative binding strengths.

3.3. Unraveling the challenges of interactome-research.

The genomic revolution that started with the sequencing of the human genome in the year 2001 and continued with the development of targeted genome editing technologies have a broad application in basic biomedical and clinical research[55,56,170]. By now, the genomic sequences of at least 2,504 humans as well as of multiple organisms such as the mouse, chimpanzee and zebrafish have been solved[171-174]. However, the phenotypic characterization of genetic differences between organisms or individuals is a challenging task and lacks far behind the genomic progress.

Proteins, for example, are difficult to study as they are very diverse in their abundance, localization and half-life. Their interactions with other macromolecules are dynamic and hence difficult to map in their entity over time and space. Previous approaches to decipher the human interactome mainly focused on Y2H and AP-MS technologies, and a first “complete” human interactome seems to be reachable at least for the Y2H system (Fig. 5a)[10-12,18,68,175,176]. While both approaches have their advantages and disadvantages, both methods provide mainly static and qualitative information without providing information on interaction dynamics or binding strengths. However, such parameters are crucial for understanding complex biological processes and the strength of an interaction informs us on the stability and lifetime of a protein complex. Binding affinities allow for a direct prioritization in protein interaction networks and can

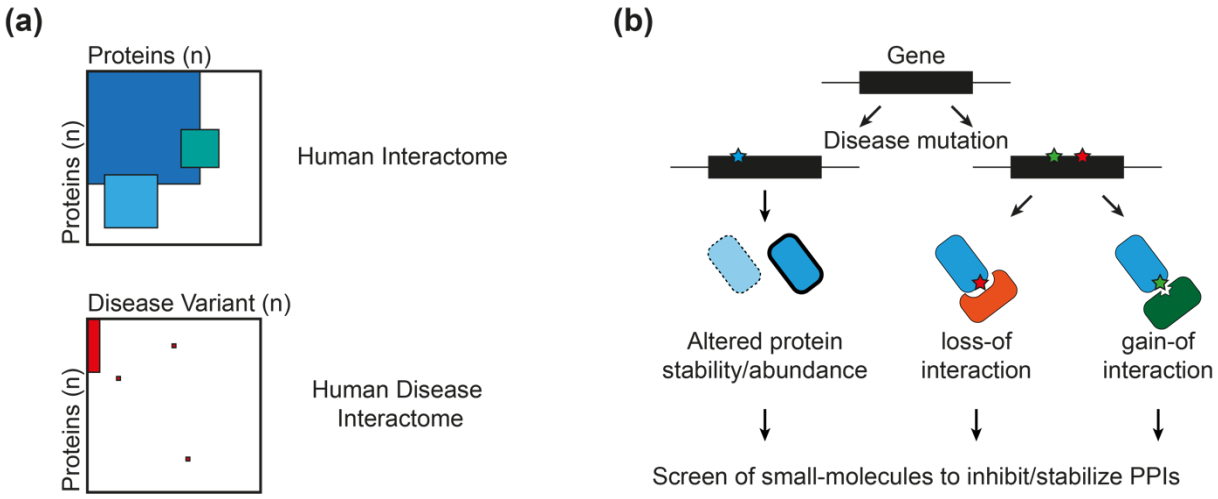

Fig. 5: The human interactome (**a**) Schematic representation of the screening completeness of the human interactome and the human disease interactome. Colored boxes are presented exemplary and represent the fraction of pairwise protein combinations tested. (**b**) Missense disease mutations can effect encoded proteins in their stability or abundance, or can lead to loss or gain of PPIs. Small molecule screens can help to identify compounds that inhibit or stabilize protein or their interactions. Adapted from Sahni *et al.* 2015

furthermore help to understand the biological relevance of an interaction. Therefore, quantitative PPI methods in mammalian cells that are easy to implement in different laboratories and provide reproducible and comparable results are urgently needed.

This becomes even more prominent when considering the influence of disease mutations on interaction strength. In a study by Sahni *et al.* in 2015, a first systematic characterization of the influence of disease-associated missense mutations on macromolecular interactions was provided[7]. The authors suggest that ~60% of such mutations perturb PPIs of which half lead to a complete loss of the interactions and the other to the selective perturbation of particular PPIs. While a complete loss of interactions is mostly associated with reduced protein abundance or stability, the selective perturbation of PPIs likely results from missense mutations within protein interaction domains (Fig. 5b)[7]. Whereas most missense mutations perturb PPIs, some studies reported also gain-of-interactions (Fig. 5b)[6]. The cancer-associated R273H mutation within p53 (TP53, cellular tumor antigen p53) results in a gain-of-function in which cells show an aberrant polarity and increased invasiveness. This gain-of-function is at least partially caused by the gain-of-interaction of p53-R273H with nardilysin (NRD1) as this interaction promotes cell invasion[6,177]. Screening approaches to identify small-molecules that stabilize or inhibit disease-associated PPIs have been undertaken in the past 20 years with some success[178]. Especially cancer related interactions have been studied intensively and multiple compounds such as Navitoclax are now in clinical trials (Fig. 5b)[178,179].

However, it is unlikely that missense mutations either result in a complete loss-of-interaction or have no effect on an interaction. It is more likely that binding affinities are “dynamically” influenced by such mutations. Hence, methods that allow the quantitative analysis of interaction

strength are key to unravel the influence of disease mutations on PPIs. As there are today already over 100,000 disease associated disease variants known[7], the step towards understanding the influence of all disease-associated missense mutations on the interaction pattern remains a distant goal, as ongoing research has just started to decipher the human disease interactome (Fig. 5a).

4. Aims of the study

The aim of my study was to establish new and innovative methods to detect PPIs in mammalian cells. The goal was to develop methods that allow to quantify the production of both interacting proteins independently as well as to generate a quantitative PPI data output that can be used to calculate quantitative interaction scores that potentially correlate to binding affinities.

New PPI-detection methods should be benchmarked on reference sets containing known positive and negative PPIs that allow the direct comparison to existing assays[74]. Furthermore, I wanted to systematically determine the sensitivity of the assays to detect PPIs with different binding affinities. Especially low-affinity interactions should be tested as they are difficult to detect but play an essential role in probably all cellular processes[27].

Additionally, proof-of-principle experiments with point-mutations that influence the binding strength should be conducted, as such changes should also be detectable with PPI-detection methods. Assays that detect the effect of mutations on PPIs are of great importance for disease research as recent studies indicate that the majority of disease-associated missense mutations perturb PPIs[7].

Taken together, the goal of my work was to establish and systematically benchmark PPI-detection methods that are high-throughput applicable and suitable for quantitative interactome mapping in mammalian cells.

5. Results

5.1. DULIP: A Dual Luminescence-based Co-Immunoprecipitation Assay for Interactome Mapping in Mammalian Cells*

Mapping of protein–protein interactions (PPIs) is critical for understanding protein function and complex biological processes. Here, I present DULIP, a **du**al **l**uminescence-based co-**i**mmuno**p**recipitation assay, for systematic PPI mapping in mammalian cells (Fig. 6). DULIP is a second-generation luminescence-based PPI screening method for the systematic and quantitative analysis of co-immunoprecipitations using two different luciferase tags. Benchmarking studies with positive and negative PPI reference sets revealed that DULIP allows the detection of interactions with high sensitivity and specificity. Furthermore, the analysis of a PPI reference set with known binding affinities demonstrated that both low- and high-affinity interactions can be detected. Finally, using the well-characterized interaction between Syntaxin-1 and Munc18, I found that DULIP is capable of detecting the effects of point mutations on interaction strength. Taken together, the here presented studies demonstrate that DULIP is a sensitive and reliable method of great utility for systematic interactome research. It can be applied for interaction screening and validation of PPIs in mammalian cells. Moreover, DULIP permits the specific analysis of mutation-dependent binding patterns.

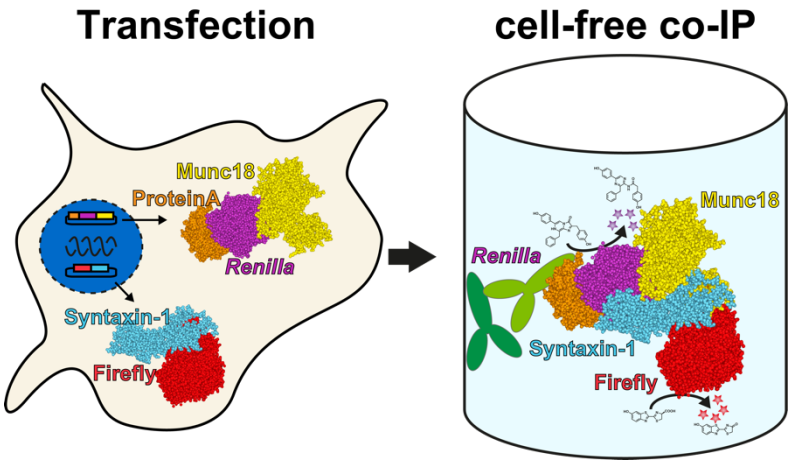

Fig. 6: Overview of the DULIP procedure. Transfection: Mammalian cells are transfected with plasmids encoding the fusion proteins to be analyzed for interaction screening. Here, a protein A-*Renilla* luciferase-Munc18 hybrid fusion protein is co-produced with a firefly luciferase tagged to Syntaxin-1 protein in HEK293 cells. **Cell-free co-IP:** After cell lysis, the lysate is transferred to an IgG-coated well of a 384-well plate, and after extensive washing the luciferase activities of the *Renilla* and firefly luciferase are quantified.

* The text and figures under section 5.1 have been reused with modifications from the published version: Trepte, P. *et al.* DULIP: A Dual Luminescence-Based Co-Immunoprecipitation Assay for Interactome Mapping in Mammalian Cells. *Journal of Molecular Biology* 427, 3375–3388 (2015).

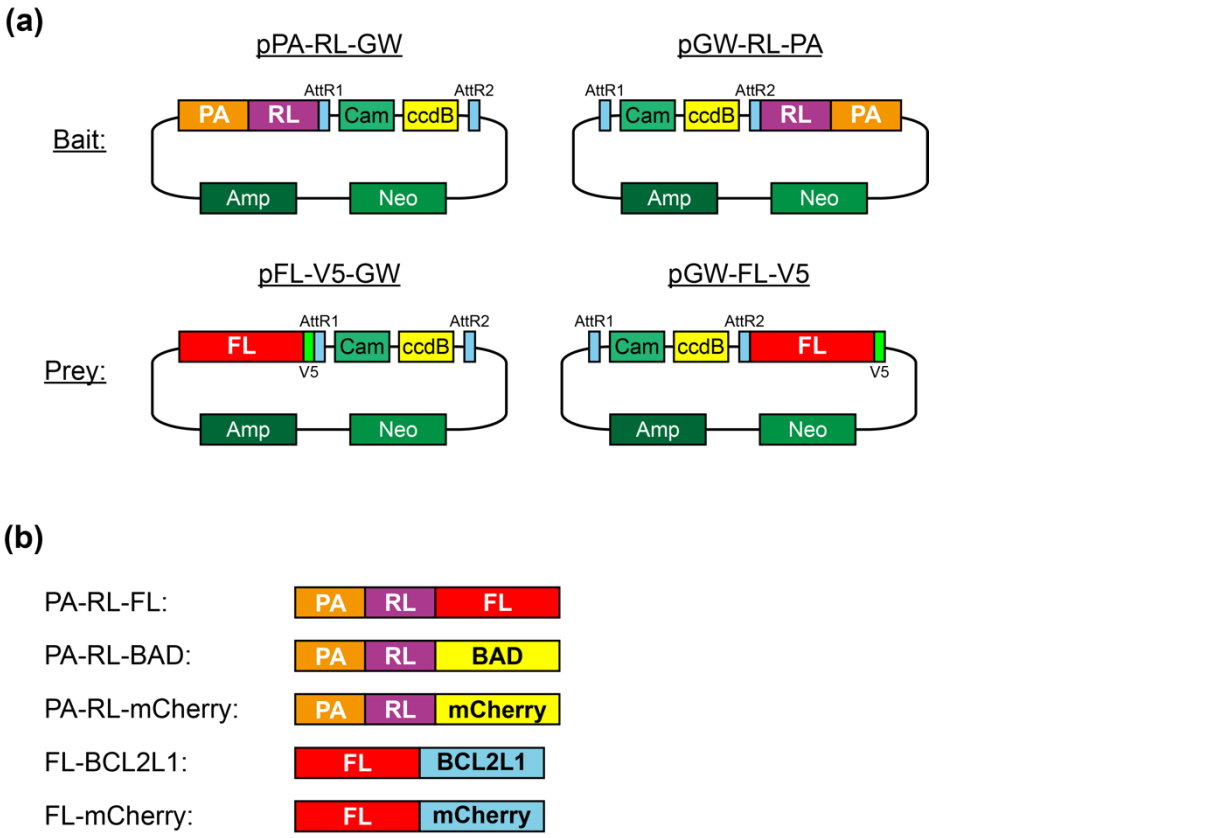

Fig. 7: DULIP vectors and proteins utilized for PPI testing. (**a**) Scheme of Gateway compatible plasmids for expression of bait and prey hybrid proteins. AttR sites flank the gateway cassette (GW) and allow the introduction of open-reading frames via LR recombination reaction. Bait vectors enable the expression of N- or C-terminally tagged RL fusions harboring also a protein A (PA) tag. The PA tag facilitates the efficient immunoprecipitation of bait proteins. Prey vectors encode N- or C-terminally tagged FL fusion proteins. The prey proteins additionally harbor a V5 epitope tag for their detection on immunoblots. RL: *Renilla* luciferase; FL: firefly luciferase; PA: Protein A; V5: V5-tag; Amp: ampicillin resistance; Neo: neomycin resistance; Cam: chloramphenicol resistance; ccdB: ccdB gene; AttR1/AttR2: Gateway® recombination sites; GW: Gateway® cassette. (**b**) Schematic depiction of hybrid fusion proteins utilized to study the published interaction between BAD and BCL2L1 with DULIP assays.

5.1.1. Generation of Gateway-compatible vectors suitable for systematic DULIP interaction screening

To establish a dual luminescence-based co-immunoprecipitation (DULIP) interaction detection assay, Gateway-compatible plasmids pPA-RL-GW and pGW-RL-PA were constructed, from which bait proteins with N- or C-terminal protein A-*Renilla* luciferase (PA-RL) tags are produced (Fig. 7a). Similarly, pFL-V5-GW and pGW-FL-V5 plasmids for the production of prey proteins harboring N- or C-terminal firefly luciferase (FL) tags were constructed. The Gateway technology allows shuttling of genes that are available as entry vectors into gateway-compatible destination vectors via site-specific recombination[180]. This technology is the basis for genetic high-throughput PPI screening approaches as it provides the necessary efficiency in the cloning procedure.

Using this technology, cDNA fragments encoding bait or prey fusion proteins were inserted in the available plasmids for systematic interaction testing. For proof-of-principle experiments, I selected the proteins BAD and BCL2L1 because these proteins were previously shown to interact

in various PPI detection assays[74]. Using the Gateway cloning technology, plasmids encoding the proteins PA-RL-BAD (bait) and FL-BCL2L1 (prey) were generated (Fig. 7b; Table 2 in the supplementary information). Additionally, to account for false-positive interactions I constructed plasmids encoding the fusion proteins PA-RL-mCherry and FL-mCherry for control experiments (Fig. 7b). I hypothesized that an unrelated monomeric protein like mCherry should not specifically interact with BAD or BCL2L1 in co-immunoprecipitation experiments. Therefore, fusions with mCherry might be generally useful to assess non-specific interactions of tested bait and prey fusion proteins. The lack of data normalization in luminescence-based PPI assays accounts for a high variability between experimental replicates. To compensate for variables like expression levels, temperature, plate order and timing of substrate addition I additionally generated a tandem construct (TC) that encodes a PA-RL-FL hybrid protein (Fig. 7b). In this fusion protein FL is connected via a short peptide linker to the PA-RL fragment. I expect that the molar ratio of FL to RL is constant for the TC wherefore it can be used to normalize luciferase activities detected in different plates and experiments. The identities of the generated plasmids as well as their encoded hybrid proteins are summarized in Table 2 (supplementary information).

5.1.2. DULIP assays facilitate the detection of the known interaction between BAD and BCL2L1

To study the interaction between the apoptotic regulators BAD (Bcl2-associated agonist of cell death; pro-apoptotic) and BCL2L1 (Bcl-2-like protein 1; anti-apoptotic), four independent transfections of HEK293 cells in 96-well microtiter plates were performed (Fig. 8a). This included the analysis between the protein pairs PA-RL-BAD and FL-BCL2L1, PA-RL-BAD and FL-mCherry (control 1), PA-RL-mCherry and FL-BCL2L1 (control 2) as well as the investigation of the hybrid protein PA-RL-FL (control 3). Transfected cells were lysed after 48 h and both RL and FL enzymatic activities (RL_{IN} and FL_{IN}) were quantified in crude protein extracts. I was able to measure RL and FL activities in all four cell lysates (Fig. 8b), suggesting that the expected recombinant hybrid proteins were indeed produced in the cells. Next, the PA-tagged bait proteins were immunoprecipitated from cell lysates using IgG-coated 384-well microtiter plates. After extensive washing the enzymatic activities of both RL and FL were quantified (RL_{OUT} and FL_{OUT}) in precipitated protein complexes. In this step, the measured RL activities indicate the successful immunoprecipitation (IP) of PA-tagged bait proteins, while the measured FL activities are indicative of the co-precipitated prey proteins (co-IP, Fig. 8c). In all four experiments, which were performed in parallel, the expected PA-tagged bait proteins were immunoprecipitated. However, high FL_{OUT} activities were only measured for the tandem construct PA-RL-FL and the prey protein

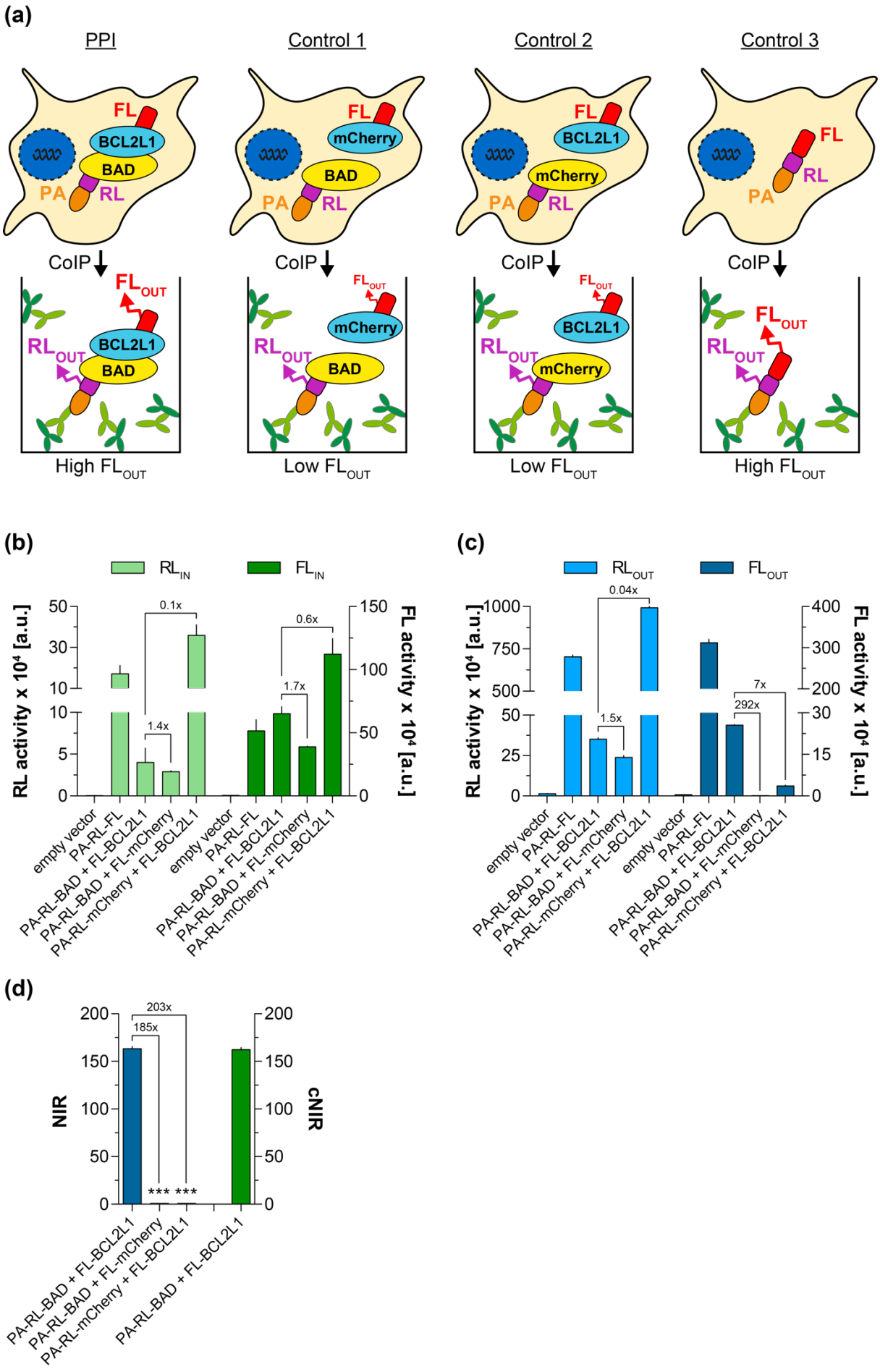

Fig. 8 (legend on next page)

Fig. 8: Investigating the interaction between BAD and BCL2L1 with DULIP assays. (**a**) Schematic representation of the DULIP approach. To assess the interaction between the proteins BAD (bait) and BCL2L1 (prey) the fusion proteins PA-RL-BAD/FL-BCL2L1 (PPI), PA-RL-BAD/FL-mCherry (Control 1) and PA-RL-mCherry/ FL-BCL2L1 (Control 2) were co-produced in HEK293 cells. In addition, cells were analyzed expressing the fusion protein PA-RL-FL (Control 3). (**b**) Analysis of protein expression through quantification of RL and FL luminescence activities in cell lysates. Cell lysates were investigated 48 h post transfection (**c**) Analysis of co-immunoprecipitates through quantification of RL and FL luciferase activities. The PA-tagged bait proteins were immunoprecipitated in IgG-coated microtiter plates. (**d**) Calculation of normalized interaction ratios (NIRs) for tested PPIs. The NIR for the interaction PA-RL-BAD/FL-BCL2L1 was significantly higher than the NIRs for the control PPIs PA-RL-BAD/FL-mCherry, PA-RL-mCherry/FL-BCL2L1. Finally, for the PPI of interest PA-RL-BAD/FL-BCL2L1 a background corrected normalized interaction ratio (cNIR) was calculated. All values are means of two independent experiments performed in triplicates each ± SEM. Two-tailed unpaired t-test; ***p<0.001.

FL-BCL2L1 that was co-precipitated with the bait protein PA-RL-BAD (Fig. 8c). For the interaction of interest between PA-RL-BAD and FL-BCL2L1 in comparison to the control interactions PA-RL-BAD and FL-mCherry as well PA-RL-mCherry and FL-BCL2L1, a ~292- and ~7-fold higher luciferase activity (FL_{OUT}) was obtained, indicating that the method is suitable to distinguish between a proven PPI (BAD and BCL2L1) and negative control PPIs (e.g. PA-RL-BAD and FL-Cherry). These results also confirm mCherry as a useful control protein that can be applied more generally in DULIP assays to investigate non-specific background binding.

As the co-immunoprecipitation efficiency of prey proteins depends on the immunoprecipitation efficiency of PA-tagged bait proteins, I calculated the luciferase activity ratios (FL_{OUT}/RL_{OUT}) for the interactions PA-RL-BAD and FL-BCL2L1, PA-RL-mCherry and FL-BCL2L1 as well as for PA-RL-BAD and FL-mCherry. In addition, the FL_{OUT}/RL_{OUT} ratio was determined for the control protein PA-RL-FL. This ratio - termed luciferase immunoprecipitation ratio (LIR) of control 3 - can be approximated as being 1:1 since the number of RL and FL molecules in the tandem construct are equivalent. Subsequently, the LIR was utilized to normalize the luciferase activity ratios of the tested bait/prey combinations (interaction of interest and controls 1 and 2, see Fig. 8a) revealing the **n**ormalized luminescence-based **i**nteraction **r**atios (NIRs, Fig. 8d and Fig. 9). Consequently, NIRs indicate the success of prey protein co-immunoprecipitation in relation to the efficacy of bait protein immunoprecipitation and give an indication of the molecular ratio of the interacting complex. Thus, a NIR of 100 would suggests that all bait protein is saturated with prey protein in a 1:1 stoichiometry. As shown in Fig. 8d, the calculated NIR for the interaction between PA-RL-BAD and FL-BCL2L1 is 185- and 203-fold higher than the NIRs for the control interactions PA-RL-BAD/FL-mCherry and PA-RL-mCherry/FL-BCL2L1, respectively. Thus, the normalization step significantly increases the specificity of PPI detection, allowing a clear distinction between positive and negative PPIs. Furthermore, a NIR of over 100 suggests that more than one BCL2L1 molecule is bound to BAD, which is in accordance with previous observations that BCL2L1 exists as a homodimer[181].

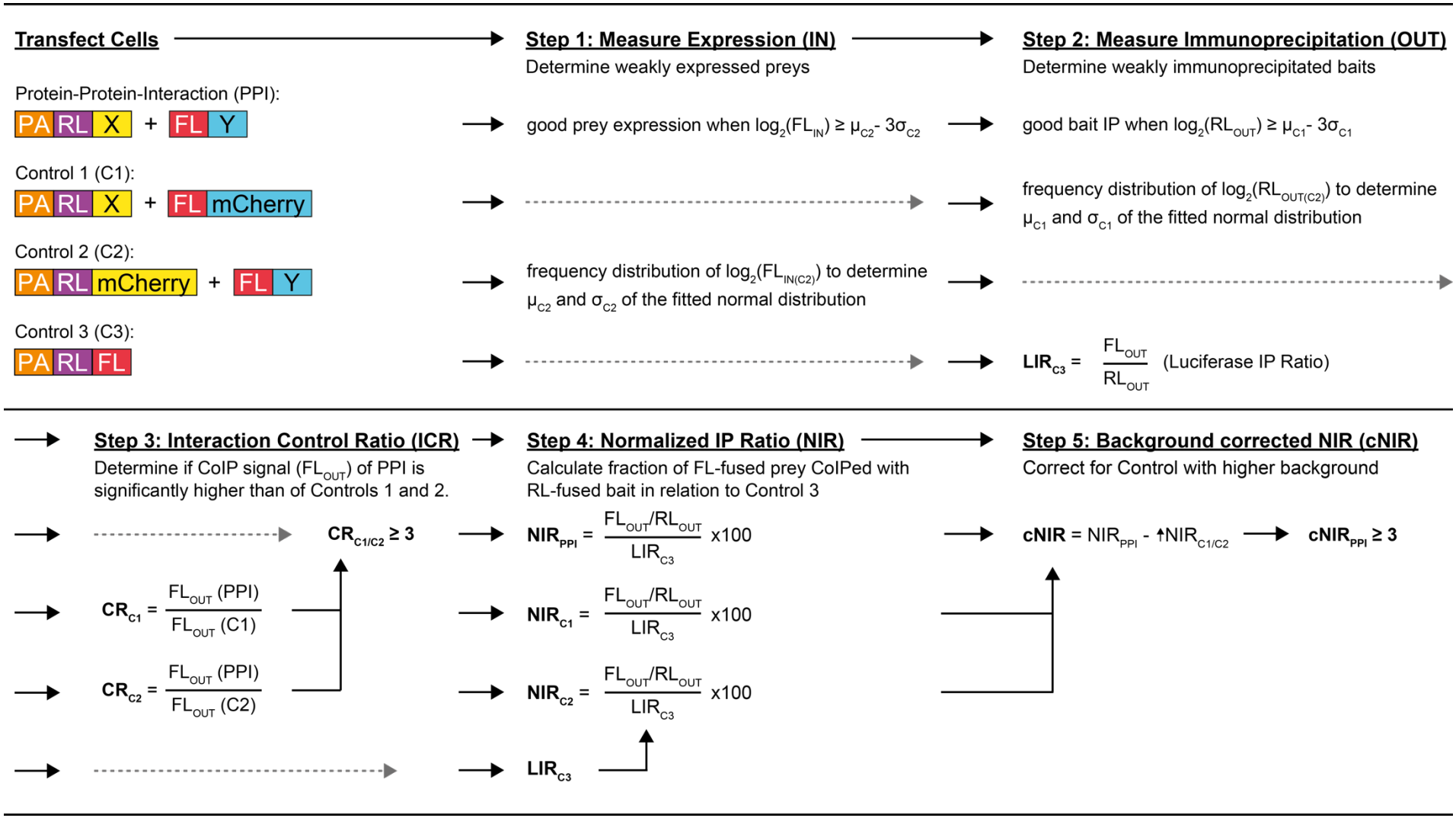

Fig. 9 (legend on next page)

Fig. 9: Step-by-step instructions for DULIP data analysis. Step 1: Measure Expression (IN). Transfected cells are lysed and the expression of bait and prey proteins was measured through quantification of luminescence activities. Preys with significantly weaker firefly activity (FL_{IN}) than the FL_{IN} mean signals of all control 1 preys are excluded from further data analysis. **Step 2: Measure Immunoprecipitation (OUT).** Cell lysates are subjected to immunoprecipitation and the RL_{OUT} and FL_{OUT} luciferase activities in the immunoprecipitates are finally measured. Baits that are insufficiently immunoprecipitated are excluded from further data analysis if their measured RL_{OUT} activities are significantly lower than the mean RL_{OUT} signals of all Control 2 baits. **Step 3: Interaction Control Ratios (ICRs).** FL_{OUT} values of PPIs of interest were divided by FL_{OUT} values of control PPIs (control 1 and 2, see Fig. 8a and this figure). This revealed luminescence-based interaction control ratios (ICRs) for each PPI of interest, which were used for quality assessment of PPIs. Only PPIs of interest with ICRs ≥ 3 were further analyzed. **Step 4: Normalized Immunoprecipitation Ratios (NIRs).** The normalized immunoprecipitation ratio (NIR) is determined as the relative amount of FL-X that is bound to PA-RL-Y in relation to the PA-RL-FL tandem construct (Control 3). **Step 5: Background corrected NIRs (cNIRs).** The relative background binding of each tested bait or prey protein to the luciferase fused to an unrelated protein (mCherry) is determined. The protein (bait or prey) that gives the higher background is subtracted from the calculated NIR of each protein of interest. More detailed information is also provided in the materials and methods section.

Finally, I calculated a background **c**orrected **n**ormalized luminescence-based **i**nteraction ratio (cNIR, Fig. 8d) for PA-RL-BAD and FL-BCL2L1. I first compared the NIRs obtained for the control PPIs (control 1 and control 2) and identified the interaction with the higher value. Next, this value, here the NIR for the interaction between PA-RL-BAD and FL-mCherry, was subtracted from the NIR of the interaction of interest, PA-RL-BAD and FL-BCL2L1. In the following systematic investigations of PPIs with the DULIP assay cNIRs will be utilized as a quantitative measure in order to compare interaction data (see below). A detailed step-by-step description of the calculations that lead to cNIRs can be found in the Fig. 9 and section 7.7.

5.1.3. Y2H and FRET assays confirm the interaction between BAD and BCL2L1

To confirm that the interaction between BAD and BCL2L1 is suitable for method establishment and can be detected consistently with independent methods, the interaction was validated with an established yeast two-hybrid (Y2H) interaction-mating assay and a cell-based FRET assay. First, MATa yeast strains producing the bait proteins LexA-BAD or LexA-mCherry were generated and subsequently mated on YPD plates with MATα strains expressing the prey proteins Gal4-BCL2L1 or Gal4-mCherry. Next, the generated diploid yeast strains were spotted onto selective plates and PPIs were identified through monitoring of yeast colony growth (Fig. 10a). For each tested interaction, 12 independent matings and three technical replicates were performed. The interaction between LexA-BAD and Gal4-BCL2L1 was detected in all mating experiments (100%, Fig. 10b), confirming the results of the DULIP assay (Fig. 8d). In strong contrast, the control PPIs LexA-BAD/Gal4-mCherry and LexA-mCherry/Gal4-BCL2L1 were detected with significantly lower frequency (Fig. 10b), indicating that the Y2H method is capable of distinguishing between specific and non-specific PPIs.

Next, the interaction between BAD and BCL2L1 was also examined in mammalian cells using a ECFP/EYFP-based FRET assay (Fig. 10c). For these experiments HEK293 cells were co-transfected with cDNAs encoding BAD fused to ECFP (ECFP-BAD) as donor and BCL2L1 fused to EYFP as

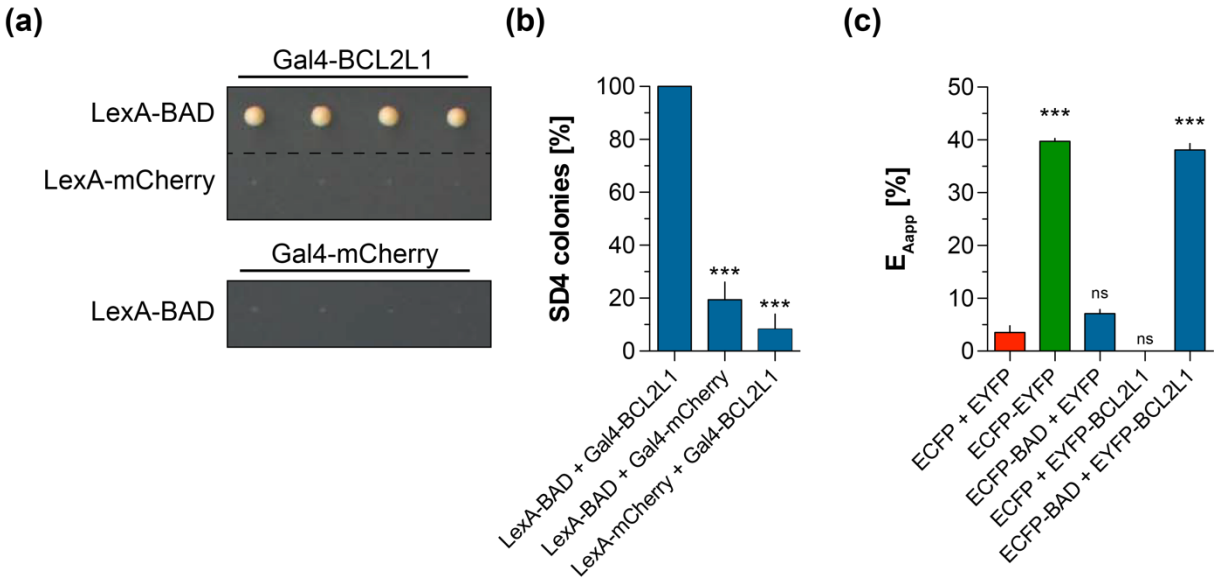

Fig. 10: Investigating the interaction between BAD and BCL2L1 using Y2H and FRET assays. (**a**) Representative interaction mating experiment. Diploid yeast strains co-expressing the proteins LexA-BAD/Gal4-BCL2L1, LexA-mCherry/Gal4-BCL2L1 or Gal4-LexA/Gal4-mCherry were analyzed. (**b**) Quantification of yeast colony growth. 12 independent mating experiments with three technical replicates each were analyzed. Bars represent mean ± SEM. Two-sided Fisher's exact test; ***p<0.001. (**c**) Analysis of the interaction between BAD and BCL2L1 using FRET assays. HEK293 cells were assessed 24 h post transfection using a fluorescence plate reader. FRET values for tested protein combinations were calculated using the sensitized emission method. FRET efficiencies are the mean values of three independent experiments performed in triplicates each ± SEM (Statistical significance was assessed by one-way ANOVA; ns: non-significant, ***p<0.001).

acceptor (EYFP-BCL2L1). The cells were fixed 24 hours after transfection; the fluorescence signals measured and FRET efficiencies calculated using the sensitized emission method[182]. For data comparison the hybrid fusion protein ECFP-EYFP was used as a positive control, which showed FRET efficiencies of ~40% indicating the close proximity of the two fluorophores (Fig. 10c). In strong contrast, in cells co-producing the individual control proteins ECFP and EYFP, only very low FRET values (3.6%) were obtained. However, relatively high FRET efficiencies (~38%) were detected in cells co-producing the proteins ECFP-BAD and EYFP-BCL2L1 (Fig. 10c), revealing the close binding of BAD and BCL2L1. As additional controls, the interactions between ECFP-BAD and EYFP or respectively with ECFP and EYFP-BCL2L1 were examined (Fig. 10c). These combinations did not result in a significant FRET signal indicating that the fluorescent proteins EYFP and ECFP do not unspecifically interact with the tested proteins of interest. Thus, I confirmed that the interaction between BAD and BCL2L1 can be used more generally to establish PPI detection assays as it can be detected with various methods.

5.1.4. Assessment of assay quality

To assess assay quality parameters such as sensitivity (known interactions recovered) and specificity (negative interactions identified as such) reference sets of positive and negative interacting pairs are required. To compile a positive reference set at the Max-Delbrueck-Center

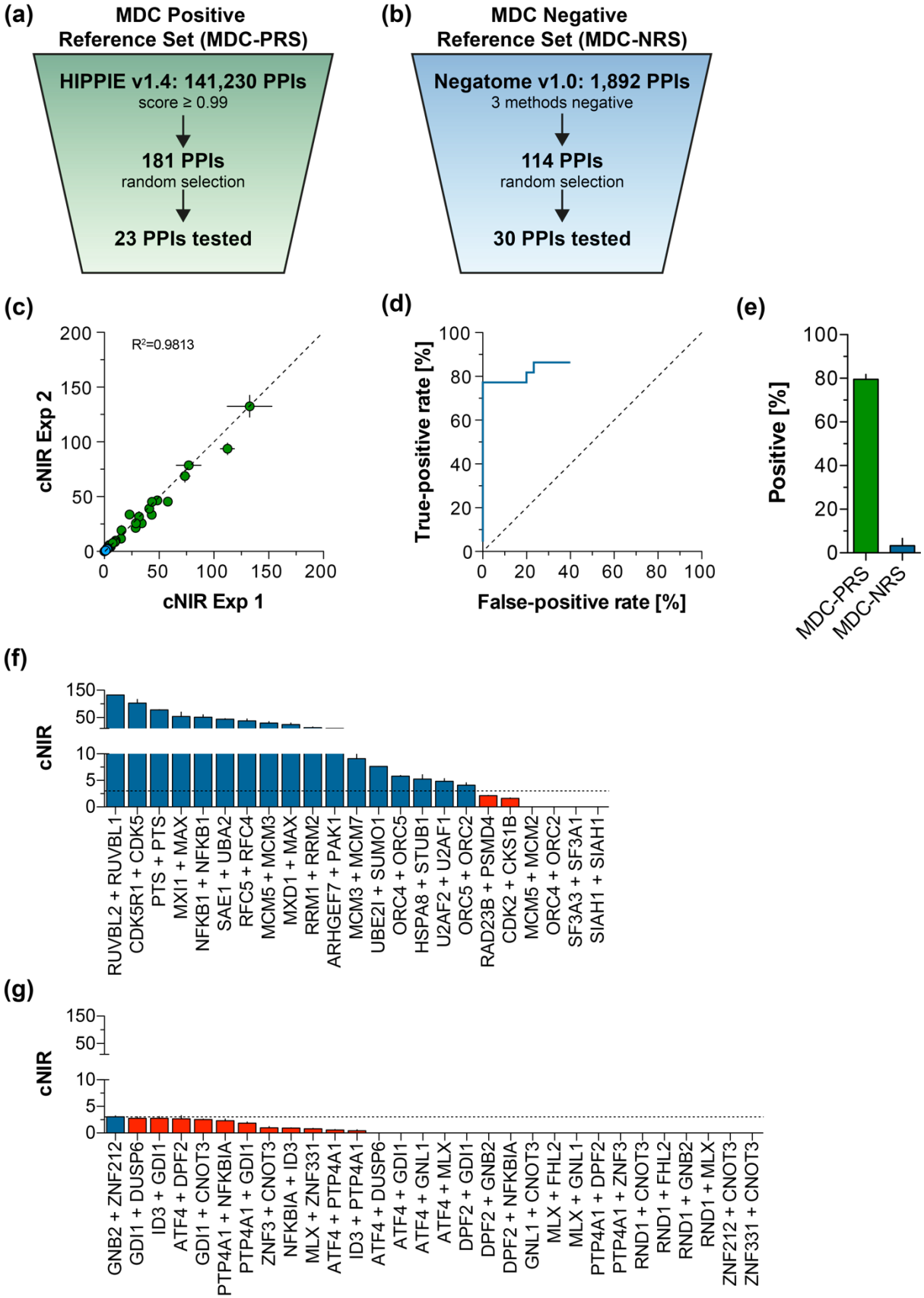

Fig. 11: Systematic analysis of positive and negative interaction reference sets using DULIP assays. (**a**) Selection strategy for interaction pairs compiled in the MDC positive reference set (MDC-PRS). From 181 PPIs with a confidence score ≥0.99 (HIPPIE database) 25 protein pairs were randomly selected, of which 23 were examined in DULIP assays. (**b**) Selection scheme for PPIs compiled in the MDC negative reference set (MDC-NRS). I selected 30 PPIs from the Negatome database (v1.0) for systematic interaction testing in DULIP assays. (**c**) Investigation of the reproducibility of DULIP PPI mapping experiments. cNIR values were calculated for all interactions of the MDC-PRS and the MDC-NRS.

The scatter plot shows the mean cNIRs of three technical replicates from two independent experiments (Exp1 and Exp2). Error bars are SEM of three technical replicates. (**d**) Estimation of assay sensitivity through receiver operating characteristic (ROC) analysis. A cNIRof ≥3 was optimal to separate positive and negative PPIs with DULIP assays. (**e**) With a benchmarked DULIP assay high-confidence human PPIs were detected with a sensitivity of 79.5% and a specificity of 96.7% in the MDC-generated reference sets. In the previously published CCSB reference sets hPRS and hRRS PPIs were recovered with a success rate of 34.8 and 3.7%, respectively. (**f**) and (**g**) Interactions from the MDC PPI reference sets with the higher luminescence-based interaction ratios of the two orientations (set a or set b) are shown. Values are displayed as a bar diagram (means ± SEM of two biological replicates). PPIs surpassing the cNIR threshold (dotted line) are considered positive and are colored blue. Negative PPIs are indicated by red color.

(MDC-PRS) of human PPIs I started with 181 interactions that possess a PPI confidence score of ≥0.99 in the HIPPIE database[183]. PPIs with such scores are considered as high confidence interactions, because they were previously shown to be detectable with multiple independent methods in various experiments. From this PPI set, 25 protein pairs were randomly selected, of which 23 were finally examined in interaction tests (Fig. 11a and Table 3). To compile a negative reference set at the Max-Delbrueck-Center (MDC-NRS) I started with 114 PPIs from the Negatome database (v1.0)[184]. These interactions were not detectable with at least three independent methods in previous studies, suggesting that they should also be negative in DULIP assays. I randomly selected 30 protein pairs from this data set for systematic PPI analysis in mammalian cells (Fig. 11b and Table 3).

Next, two expression plasmids were constructed for each selected protein, enabling its investigation either as a bait (PA-RL-tagged fusion) or as a prey (FL-tagged fusion) in DULIP assays. Thus, all selected protein pairs were systematically analyzed as bait/prey (set a) and prey/bait combinations (set b) in mammalian cells (Table 3). In total, 95 protein pairs (PRS and NRS) were systematically tested in two independent experiments (experiment 1 and 2) in DULIP assays (Fig. 12 and Table 3).

As described above for the interaction between BAD and BCL2L1 (Fig. 8a-d), four independent transfections were performed in order to analyze a PPI of interest. In all these experiments, after cell lysis, both RL and FL activities were systematically quantified in protein extracts before and after co-immunoprecipitation of protein complexes. For a true interaction, the amount of co-immunoprecipitated prey correlates directly to the amount of immunoprecipitated bait depending on the affinity of the interaction. For unknown interactions, one assumes when calculating the NIR that this is the only parameter influencing the co-immunoprecipitation of the prey. However, preys can also bind unspecifically to the *Renilla* luciferase, the protein A-tag, the antibodies or the microtiter plate. Therefore, at this stage the obtained FL_{OUT} values for all PPIs of interest, which indicate the efficiency of the co-immunoprecipitation, were divided by FL_{OUT} values of the control PPIs (controls 1 and 2, see Fig. 8a and Fig. 9) in order to obtain FL_{OUT}-based interaction control ratios (ICRs). An ICR of ~1 would therefore indicate that equal amounts of prey were co-immunoprecipitated for the interaction of interest and a control PPI. We defined,

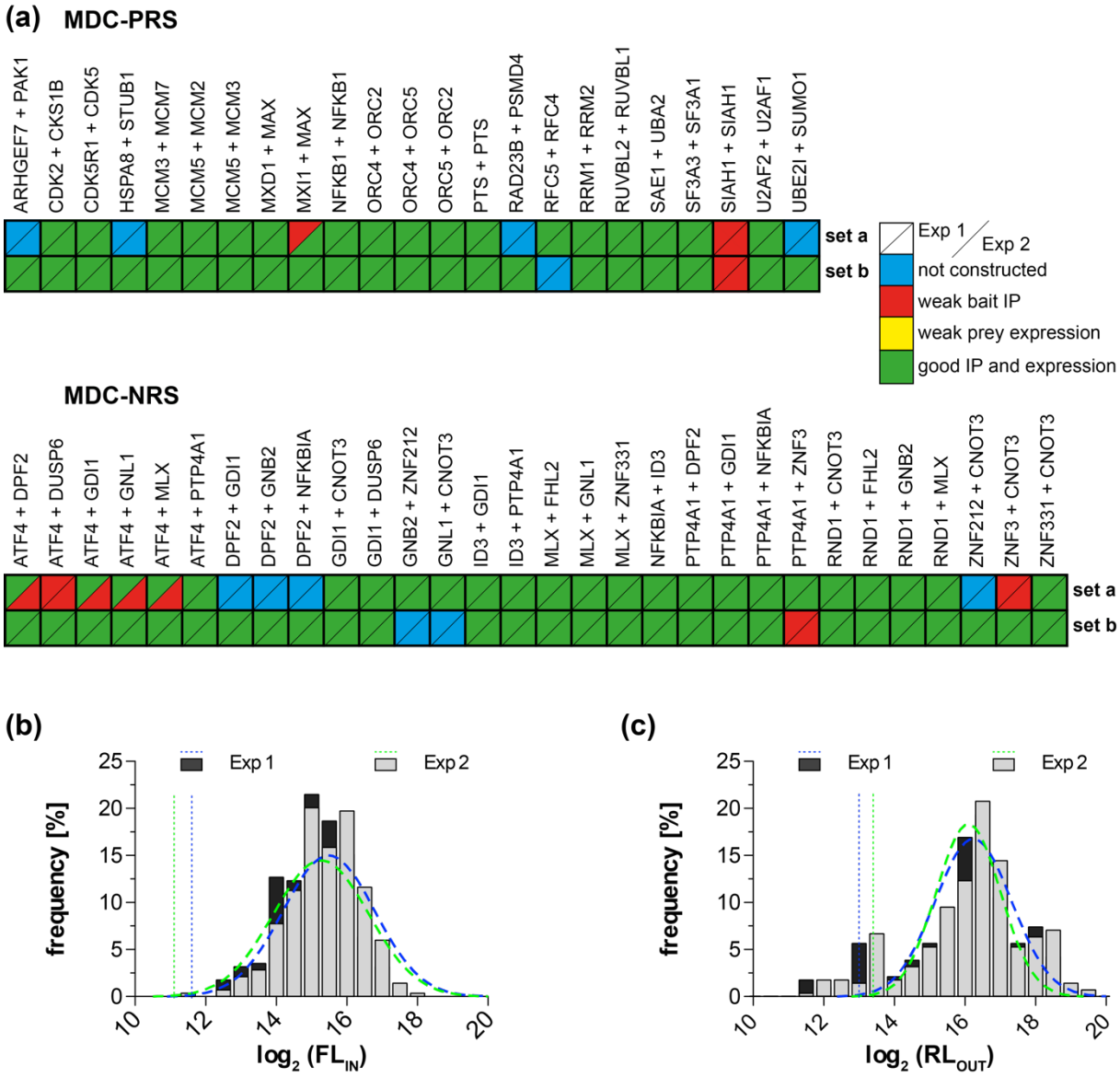

Fig. 12: Overview of selected PPIs for DULIP benchmarking studies. (**a**) Schematic representation of tested PPIs from the PRS and the NRS generated at the MDC. PPIs were assessed in both configurations (set a and b) in two independent experiments (Exp 1 and 2). Green color indicates PPIs that were successfully screened with DULIP assays. PPIs for which cloning failed (blue triangles), prey proteins were not expressed (yellow triangles) or bait proteins were insufficiently immunoprecipitated (red triangles) were excluded from further analysis. (**b**) Estimation of prey protein expression. FL signals (FL_{IN}) obtained for preys are presented as a frequency distribution. Data from two biological replicates (Exp 1 and 2) were log_2-transformed prior to analysis. Based on the log_2-transformed FL signals of PPIs examined in control 1 experiments (Fig. 2d), a Gaussian fit was applied to identify non-expressed prey proteins (broken lines). (**c**) Estimation of the success of bait immunoprecipitation. Bait RL signals (RL_{OUT}) from experiments 1 and 2 were log_2-transformed and presented as a frequency distribution. Based on the log_2-transformed RL signals of PPIs examined in control 2 experiments, a Gaussian fit was applied to identify bait proteins that are insufficiently immunoprecipitated (broken lines).

that only PPIs with ICRs of ≥3 (see step 3 in Fig. 9) were considered for further analysis. This selection criterion was applied for systematic large-scale PPI detection studies to ensure that the FL_{OUT} values for all tested PPIs of interest are significantly higher than the FL_{OUT} values of the respective control PPIs (controls 1 and 2). Through this selection strategy from the 95 protein pairs tested in set a and b, 30 interactions in the NRS and 7 in the PRS were excluded from further

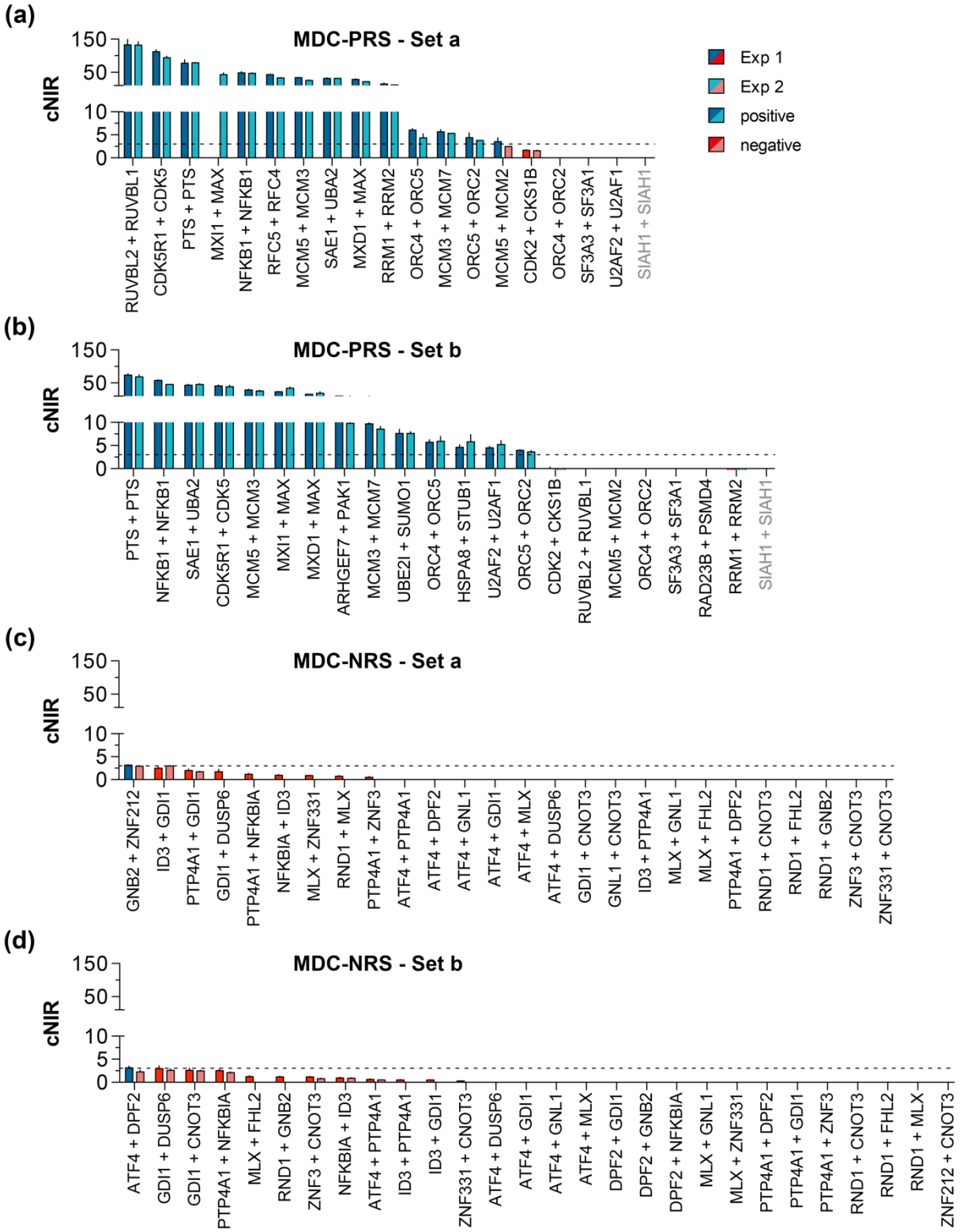

Fig. 13: Comparison of biological replicates of DULIP tested PPIs. (**a**) and (**b**) Representation of PPIs from the MDC-PRS (sets a and b). Positive PPIs are shown in dark (Exp 1) or light blue (Exp 2) colors. Negative PPIs are presented in red (Exp 1 and 2) colors. (**c**) and (**d**) Representation of PPIs from the MDC-NRS; cNIRs calculated for PPIs from the sets a and b are shown using the same color code as in a and b. Data (cNIRs) are displayed as means ± SEM from three technical replicates each for experiments 1 and 2.

analysis and hence no cNIR values calculated. As the production of prey proteins is critical for the success of co-immunoprecipitation experiments, I next assessed the abundance of these proteins (FL fusions) in all prepared protein extracts. I used the frequency distribution and a fitted Gaussian function of all measured FL_{IN} values to identify prey proteins that are not sufficiently produced in HEK293 cells (Fig. 12b). Prey proteins with FL_{IN} values $<\mu-3\sigma$ were defined as not expressed and not considered for further data analysis. With this strategy, all of the interactions in the reference interaction sets (PRS and NRS) were considered for benchmarking studies (Fig. 12a).

Next, I used a similar strategy to assess the immunoprecipitation of bait proteins (PA-tagged fusions) as a prerequisite for the successful co-immunoprecipitation of prey proteins. Thus, PPIs with bait proteins that are not sufficiently precipitated should not be considered for further data analysis. Using a fitted Gaussian function I defined three bait proteins with RL_{OUT} values $<\mu-3\sigma$ as not immunoprecipitated (Fig. 12c). Thereby, five PPIs harboring these bait proteins were excluded from further benchmarking studies (Fig. 12a).

For the remaining 53 PPIs the corrected normalized luminescence-based interaction ratios (cNIRs), a quantitative measure of the potential interaction strength of proteins, were calculated (Fig. 11f and g). I found that the cNIRs for the tested PPIs were highly reproducible in two independent experiments (r^2 = ~0.98; Fig. 11c and Fig. 13a-d). Moreover, they covered a broad range of values, suggesting that the method detects PPIs with different binding affinities (Table 3). I next used the ROC (receiver operating characteristic) analysis (Fig. 11d) to define the cutoff for the identification of "true" positive PPIs. Using a cNIR of ≥3, I observed a clear separation between known positive and potential false-positive PPIs, which was used to estimate the assay's sensitivity. Under these conditions, 79.5% of the PPIs in the MDC-PRS were detected with the DULIP assay (Fig. 11e), while 3.3% of the PPIs in the MDC-NRS were identified. The results of the benchmarking studies are summarized in Fig. 11f and g.

To more comprehensively evaluate the performance of DULIP, I next examined the assay's detection rate of PPIs in the established *Homo sapiens* reference sets hPRS and hRRS, which were successfully applied previously to benchmark various PPI detection methods[4,70,74]. From the complete 184 PPIs of the hPRS (92 PPIs) and hRRS (92 PPIs) 164 were tested with the DULIP assay (Fig. 14a and b). As before, all selected protein pairs were systematically analyzed as bait/prey (set a) and prey/bait (set b) combinations in mammalian cells (Fig. 14d and e and Table 4). In these experiments, I detected PPIs in the positive reference set hPRS and the random reference set hRRS with a success rate of 35.4% and 3.7%, respectively (Fig. 14c), which is in good agreement with previous benchmarking results (Fig. 15a and b)[70,74]. Thus, I confirmed that the established DULIP assay is a robust method, which allows the detection of PPIs with high sensitivity and specificity.

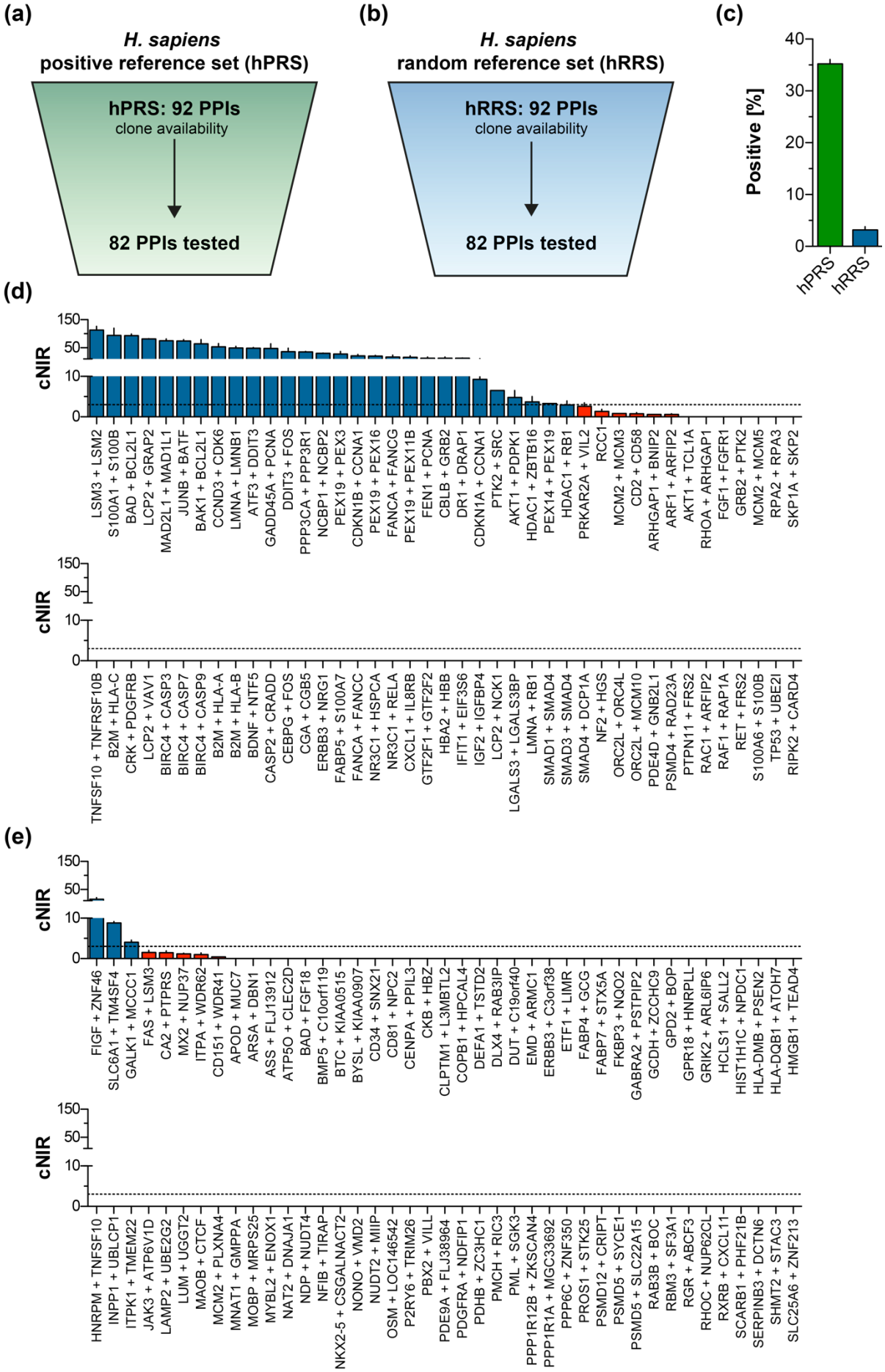

Fig. 14 (legend on next page)

Fig. 14: Systematic analysis of PPIs in hPRS and hRRS reference sets using DULIP assays. (**a**) and (**b**) From 92 PPIs in the published hPRS and hRRS reference sets 82 PPIs were selected in each case and examined in DULIP assays. (**c**) Recovery rate of PPIs in the hPRS and hRRS with the DULIP assay. (**d**) and (**e**) Data display from both orientations (set a or b) the higher cNIRs for the hPRS (**d**) and hRRS (**e**) PPIs as a bar diagram (means ± SEM of two biological replicates). PPIs surpassing the cNIR threshold (dotted line) are considered positive and are colored blue. Negative PPIs are indicated by red color.

5.1.5. DULIP is suitable to validate interactions detected with the Y2H

Systematic PPI mapping on genome scale is mostly performed with the Y2H assay wherefore suitable validation methods are needed. Several methods, like the LUMIER or BiFC have been widely used to validate Y2H interactions. While these methods have been benchmarked on reference sets that contain interactions detected with different methods, their ability to recover specifically interactions that have been identified with the Y2H is unknown[12,13,74]. To estimate a methods sensitivity and specificity to explicitly validate Y2H interactions I generated custom reference sets to address this question. The Y2H positive reference set (Y2H-PRS) was created from the HIPPIE database (v1.6)[183] by filtering for interactions that have been exclusively detected with the Y2H method (26,192 PPIs) and described in at least two publications (3,038 PPIs). From those, 167 PPIs were randomly selected and tested with the DULIP assay (Fig. 16a). Additionally, I randomly selected from the 13,944 Y2H-PPIs described in the *h*uman *i*nteractome data set covering Space *II* and reported in 20*14* (HI-II-14)[12], 76 PPIs (HI-PRS) to validate them with the DULIP assay (Fig. 16b). Finally, to generate a Y2H relevant random reference set (Y2H-RRS) I selected from all potential gene combinations available in the MDC cDNA bank (~14,000 genes = 1.96×10^8 PPIs) randomly 139 PPIs from which I had subtracted known interactions described in HI-II-14 or in the HIPPIE database (Fig. 16c). Importantly, 94% of the tested protein-combinations in the Y2H-RRS were covered by the HI-II-14 search space where they showed no interactions[12].

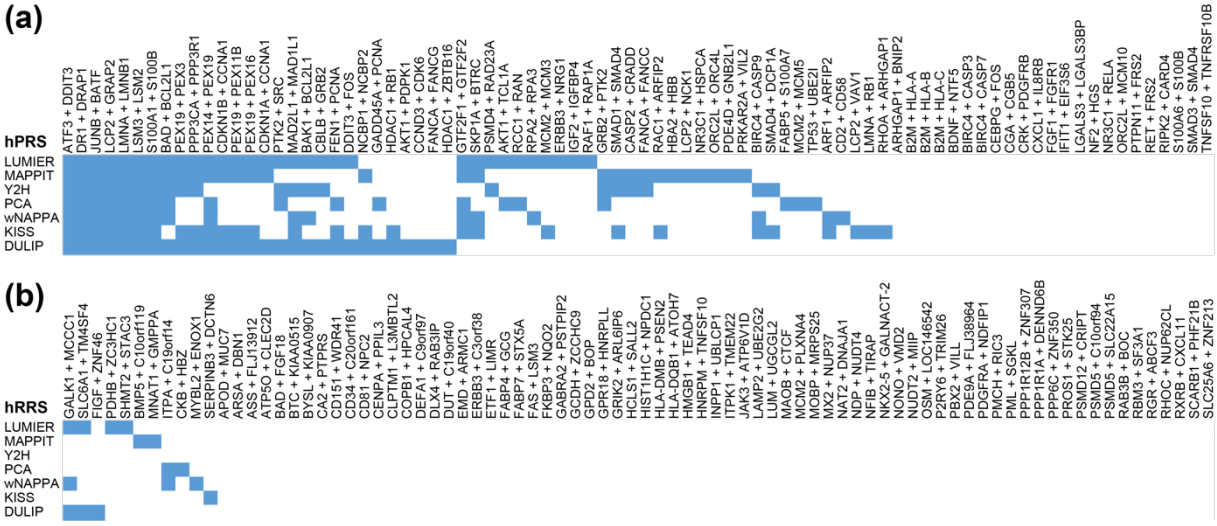

Fig. 15: Benchmarking result of the DULIP assay against other methods. Overview of the PPIs detected with the DULIP assay and other published methods for the hPRS (**a**) and hRRS (**b**). Displayed are only the PPIs screened with the DULIP assay.

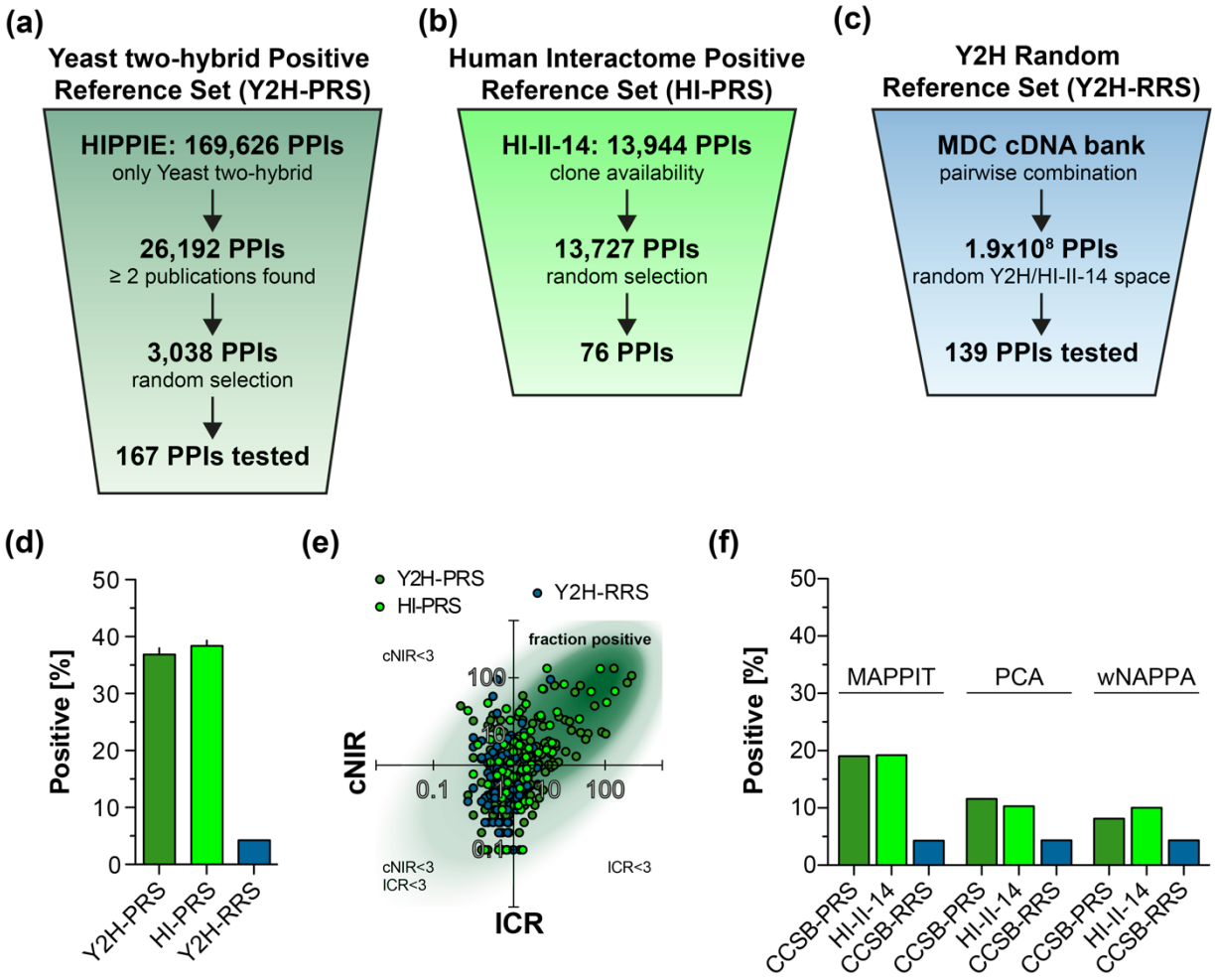

Fig. 16: Systematic analysis of Y2H-based positive and random reference sets with the DULIP assay. (**a**) For the Y2H positive reference set (Y2H-PRS), I selected from the 169,626 PPIs in the HIPPIE database (v1.6) interactions identified exclusively with the Y2H assay. From the remaining 26,192 PPIs I selected interactions reported in two studies resulting in 3,038 high-confident Y2H PPIs. From those I randomly selected 167 PPIs that were systematically tested with the DULIP assay. (**b**) For the human interactome positive reference set (HI-PRS) I selected from the 13,944 Y2H-PPIs reported in the HI-II-14 dataset all interactions for which cDNA clones for both interacting proteins were available (13,727 PPIs). From those, 76 PPIs were randomly selected and tested in the DULIP assay. (**c**) For the Y2H random reference set (Y2H-RRS) I aligned all available cDNA clones to obtain ~1.9x10^8 potential PPIs. From those, I randomly selected 139 PPIs containing only genes that had been used previously in Y2H screens, of which 94% were actually covered by the HI-II-14 search space. (**d**) Recovery rates of the Y2H-PRS (36.9±1.6), HI-PRS (38.4±1.4) and Y2H-RRS (4.3±0.0) with the DULIP assay (means ± SEM of two biological replicates). (**e**) Scatter plot of the ICR (x-axis) against the cNIR (y-axis) of the Y2H-PRS (dark green), HI-PRS (light-green) and Y2H-RRS (blue). The x- and y-axis intersect at x = 3.0 and y = 3.0. Positive interactions are in the upper right quadrant. Displayed are means of two biological replicates. (**f**) Analysis of the raw data for the MAPPIT, PCA and wNAPPA datasets published in Rolland *et al.* 2014 of custom positive (CCSB-PRS) and random (CCSB-RRS) reference sets as well as of selected PPIs from the HI-II-14 PPIs. Interaction cutoffs for each assay were chosen so that a recovery rate of 4.3% in the CCSB-RRS was obtained.

To screen the Y2H-PRS (167 PPIs), HI-PRS (76 PPIs) and Y2H-RRS (139 PPIs) with the DULIP assay, cDNAs encoding the interaction partners were cloned into the respective expression plasmids. Systematic interaction screening was performed as described above using the same cut-offs for the ICR (≥3.0) and cNIR (≥3.0), which resulted in comparable recovery rates to the hPRS and hRRS. I detected 36.9% and 38.4% of interactions in the Y2H-PRS and HI-PRS, respectively, while only 4.3% in the Y2H-RRS (Fig. 16d and e). The results of the Y2H-based reference sets are summarized in Table 5.

Interestingly, Rolland *et al.* used three independent assays, namely MAPPIT (mammalian protein-protein interaction trap), PCA (YFP-based BiFC) and wNAPPA (Nucleic acid programmable protein array) to validate ~800 of the ~14,000 PPIs described in the HI-II-14 dataset[12]. They benchmarked their assays against custom Center for Cancer Systems Biology (CCSB) positive and random reference sets (CCSB-PRS and CCSB-RRS) to define thresholds that could be used to determine specific recovery rates for the three assays. To compare the recovery rates obtained with the MAPPIT, PCA and wNAPPA to the benchmarking results with the DULIP assay, I reanalyzed the publicly available raw data (Table S2 under http://dx.doi.org/10.1016/j.cell.2014.10.050). I selected interaction thresholds for the three methods (MAPPIT: >1.876; PCA: >1.485; wNAPPA: >1.501) in which the recovery rate of the CCSB-RRS would correspond to the 4.3% observed with the DULIP assay in the Y2H-RRS. When doing so, MAPPIT, PCA and wNAPPA validated between 10-19% of the interactions from the HI-II-14 dataset (Fig. 16f). As the DULIP assay showed a recovery rate twice as high (38.4%) as their best performing method - MAPPIT, I suggest that DULIP assays are more suitable to validate PPIs detected with Y2H than currently used methods. Furthermore, as the recovery rates for the Y2H-specific reference sets (Y2H-PRS and Y2H-RRS) showed similar validation rates to the hPRS and hRRS I believe that the quality of Y2H interactions is comparable to PPIs detected with other methods.

5.1.6. DULIP allows the detection of both low- and high-affinity interactions

To address the question whether DULIP can detect both low- and high-affinity PPIs, I additionally created an affinity-based interaction reference set (AIRS). It exclusively consists of interactions with known dissociation constants (K_{Ds}). To generate the AIRS, I selected PPIs from PDBbind[185] as well as from the PPI Affinity Database 2.0[186] and subsequently subcloned cDNAs encoding potential bait and prey fusion proteins into DULIP expression plasmids. In total, 57 affinity-based interactions were selected which were systematically tested as bait/prey (set a) and prey/bait (set b) combinations in DULIP assays (Fig. 17a). As shown in Fig. 17b, the selected interactions in the AIRS indeed covered a broad spectrum of binding affinities, including both low- (59% of PPIs with a K_D >100 nM) and high-affinity (41% of PPIs with a K_D <100 nM) interactions. Using assay conditions identical to the ones applied before, I detected interactions in the AIRS with a success rate of 29.8% (17 of 57 tested PPIs). Strikingly, besides strong PPIs (K_D values in the nanomolar range), also relatively weak interactions (K_D values in the micromolar range) could be readily detected (Fig. 17c and d), supporting the hypothesis that both high- and low-affinity interactions can be identified with the DULIP assay. However, my experiments clearly demonstrate that DULIP is more likely to detect higher affinity than lower affinity PPIs (Fig. 17c and d), substantiating previous observations that co-immunoprecipiation-based PPI detection methods have a certain bias for stronger interactions[27].

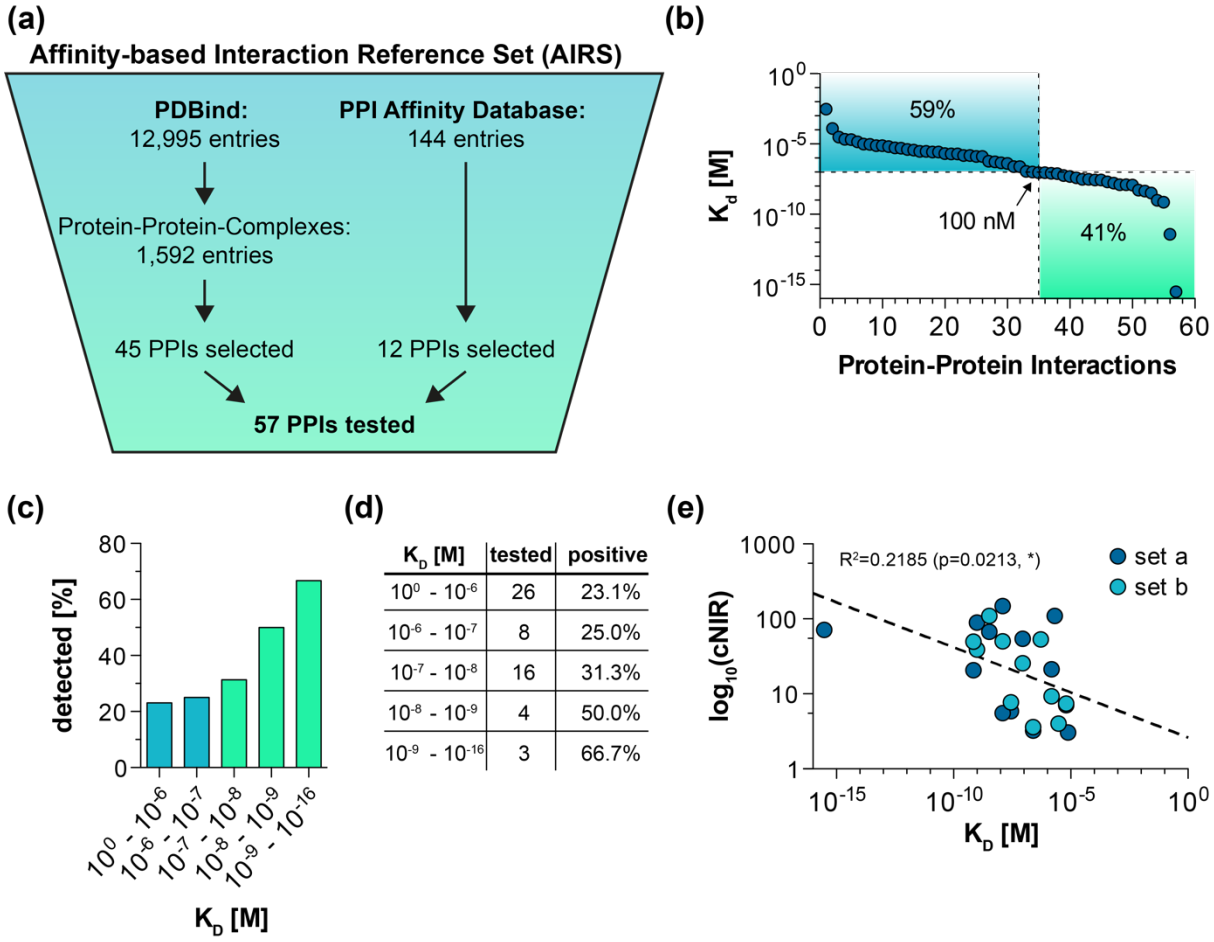

Fig. 17: Systematic analysis of interactions with known binding affinities using the DULIP assay. (**a**) Selection strategy for interaction pairs compiled in the affinity-based interaction reference set (AIRS). I selected 57 PPIs from PDBbind and the Protein-Protein-Interaction Affinity Database 2.0 and systematically tested them in DULIP assays. (**b**) The selected 57 PPIs in the AIRS span a broad range of binding affinities. (**c**) Detection rate of PPIs with DULIP assays in relation to their published binding affinities. (**d**) Number of tested PPIs for the respective binding affinity-range and fraction of interactions detected with DULIP assays. (**e**) Published dissociation constants of DULIP positive interactions plotted against luminescence-based cNIR values. Linear regression plotted as dashed line. Pearson correlation: *p<0.05.

Next, I examined whether the published binding affinities (defined through K_D values) of PPIs in the AIRS correlate with calculated cNIR values obtained with DULIP assays (Table 6). As shown in Fig. 17e, I found a significant correlation between published K_D values and luminescence-based cNIRs, supporting the hypothesis that high cNIRs are an indication of strong interactions.

5.1.7. Point mutations influence the detection of PPIs with DULIP assays

Previous studies indicated that missense mutations in proteins influence their binding affinities, which can be monitored with Y2H assays or other interaction detection methods[7]. Therefore, I examined whether the DULIP assay can detect the effect of mutations on the well-described interaction between the synaptic proteins Munc18 and Syntaxin-1. Previous studies have demonstrated that single point mutations in Munc18 (K46E and E59K) reduce its binding affinity for the protein Syntaxin-1, whereas the double mutant (K46E/E59K) abolishes the binding

completely (Fig. 18a and b)[82,187]. To address if the DULIP assay can detect the influence of point mutations on interaction strength the bait protein PA-RL-Syntaxin-1 with the prey proteins FL-Munc18 wt or the mutant proteins FL-Munc18 K46E, FL-Munc18 E59K or FL-Munc18 K46E/E59K were co-produced in HEK293 cells and cNIRs for these PPIs determined. I found that the interaction between PA-RL-Syntaxin-1 and FL-Munc18 wt can be readily detected with DULIP assays (Fig. 18c), confirming previously published results. However, the interactions between PA-RL-Syntaxin-1 and the mutant proteins were not identifiable. This demonstrates that the effects of both single and double point mutations on the interaction strength can be monitored using standard DULIP assays.

Next, I examined whether the point mutations in Munc18 influence its association with Syntaxin-1 in an established Y2H interaction assay (Fig. 18d and e). I observed that the hybrid proteins Gal4-Syntaxin-1 and LexA-Munc18 wt, LexA-Munc18 K46E or LexA-Munc18 E59K interact in Y2H assays. However, the interaction between Gal4-Syntaxin-1 and LexA-Munc18-K46E/E59K was not detected. This suggests that Y2H colony growth assays are less sensitive for the detection of subtle changes in affinity due to single point mutations than DULIP assays. However, more comprehensive studies with multiple mutant proteins are necessary to further substantiate these results.

Finally, the cell based FRET assay was used to compare these findings in an independent assay. HEK293 cells co-expressing the ECFP-tagged Munc18 variants (wt, K46E, E59K or K46E/E59K) together with EYFP-tagged Syntaxin-1 were fixed, the fluorescence measured and the FRET efficiencies calculated. I detected a strong interaction between ECFP-Munc18 wt and EYFP-Syntaxin-1 (26.3%) while no interaction could be detected between ECFP-Munc18 K46E/E59K and EYFP-Syntaxin-1 (1.8%) reflecting the results from the DULIP and Y2H assays. However, in contrast to the DULIP and Y2H results both Munc18 single point mutants (12.3% for K46E and 13.2% for E59K) showed reduced but still significant FRET efficiencies, demonstrating a remaining binding affinity of Munc18 to Syntaxin-1 in intact cells. Together, this demonstrates that the effects of both single and double point mutations on interaction strength can be monitored using standard DULIP assays but that cell lysis potentially disrupts PPIs with lower affinity. However, additional studies that compare interactions in intact cells and after cell lysates are necessary to confirm these findings.

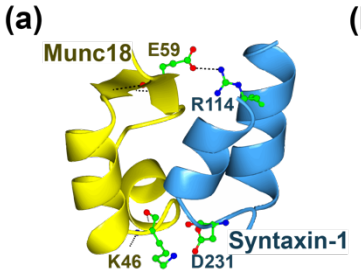

(b)

Interaction	K_d (nM)[1]	K_d (nM)[2]
Syntaxin-1 + Munc18 wt	1.4±0.3	23.3±11.1
Syntaxin-1 + Munc18 K46E	nd	181.2±46.4
Syntaxin-1 + Munc18 E59K	48.1±5.6	83.9±34.3
Syntaxin-1 + Munc18 K46E/E59K	nd	-

[1]Meijer et al., 2012; [2]Han et al., 2011

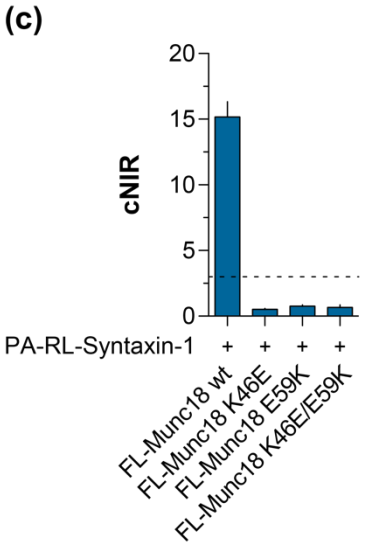

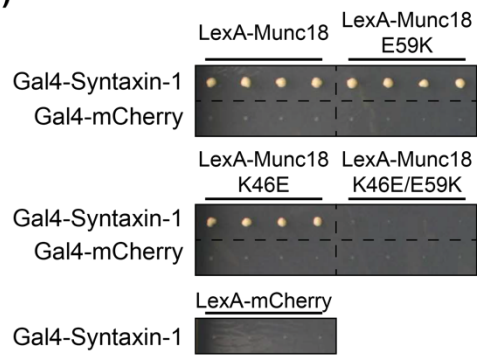

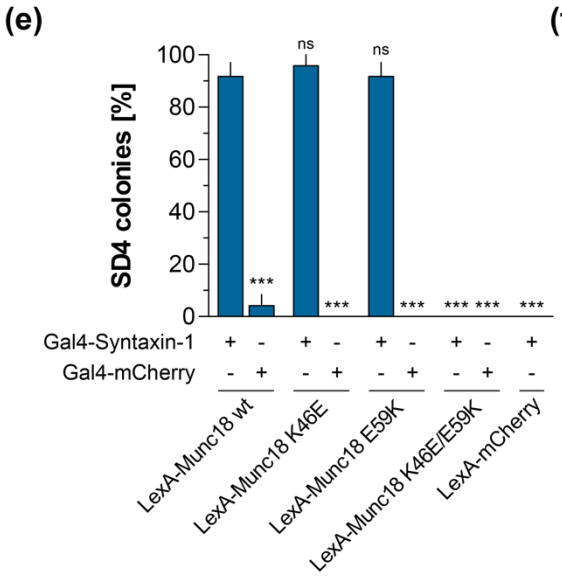

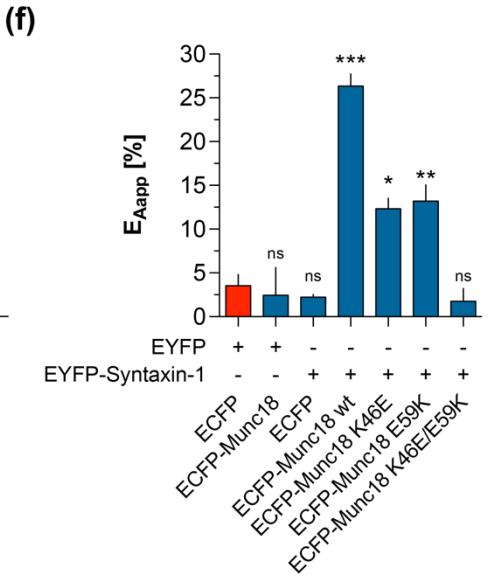

Fig. 18: Point mutations influence the association between Munc18 and Syntaxin-1 in interaction detection assays. (**a**) High resolution structure depicting the binding interface of the Syntaxin-1 (amino acids 110-121 and 222-240) and Munc18 (amino acids 30-61) protein complex (PDB: 3C98). Point mutations in Munc18 that influence the interaction strength are highlighted. (**b**) Previously published studies indicate that point mutations influence the binding affinity of the interacting proteins Munc18 and Syntaxin-1; nd: not determined; -: no interaction detected. (**c**) Analysis of the effects of point mutations on the interaction between Munc18 and Syntaxin-1 with DULIP. For all tested protein pairs cNIRs were determined. Values are the means of two independent experiments performed in triplicates each ± SEM. The dotted line indicates the threshold (cNIR ≥3) above which PPIs are scored positive with DULIP assays. (**d**) Analysis of the effects of point mutations on the interaction between Munc18 and Syntaxin-1 with Y2H interaction assays. Representative interaction mating experiments on selective agar plates are shown. (**e**) Quantification of data from Y2H interaction mating experiments. The data from eight mating experiments with three technical replicates each were analyzed. Bars represent mean values ± SEM. Statistical significance compared to the LexA-Munc18 wt and Gal4-Syntaxin-1 interaction was assessed by two-sided Fisher's exact test; ***p<0.001. (**f**) Analysis of the effect of point mutations on the interaction between Munc18 and Syntaxin-1 using FRET assays. HEK293 cells were assessed 24 h post transfection using a fluorescence plate reader. FRET values for tested protein combinations were calculated using the sensitized emission method. FRET efficiencies are the mean values of three independent experiments performed in

triplicates each ± SEM (Statistical significance compared to the unfused ECFP and EYFP expressing cells was assessed by one-way ANOVA; ns: non-significant, *p<0.05, **p<0.01, ***p<0.001).

5.2. BRIP: A Bioluminescence Resonance Energy Transfer (BRET) and Co-Immunoprecipitation (IP)-based PPI detection Assay for Quantitative Interactome Mapping in Mammalian Cells

Transient and permanent protein-protein interactions participate in all biological processes but their detection can be challenging. Especially weak, transient interactions are difficult to detect and currently available cell-based methods provide only limited quantitative information. I developed BRIP, a two-component PPI detection assay that combines the principles of **b**ioluminescence **r**esonance energy transfer (BRET) and co-**i**mmunoprecip**i**tation (IP) and can be used for quantitative interactome mapping in mammalian cells (Fig. 19). Using the improved brightness of the NanoLuc luciferase allows minimal protein production while providing a high signal-to-background ratio. Benchmarking studies against positive and random reference sets revealed an exceptional sensitivity and specificity of the BRIP assay. Importantly, the BRIP assay was able to detect both weak and strong PPIs and could be used to determine relative binding strengths in cells. Furthermore, I show that BRIP can be applied for the detection of small-molecules that increase or decrease the association of proteins. By combining two PPI detection methods I created an innovative methodology that in the long run can be applied for systematic investigation of PPIs on a proteome-wide scale. Due to the fact that the BRIP assay reveals a quantitative PPI interaction score it will be useful to analyze the effects of disease-causing missense mutations on the strengths of interactions.

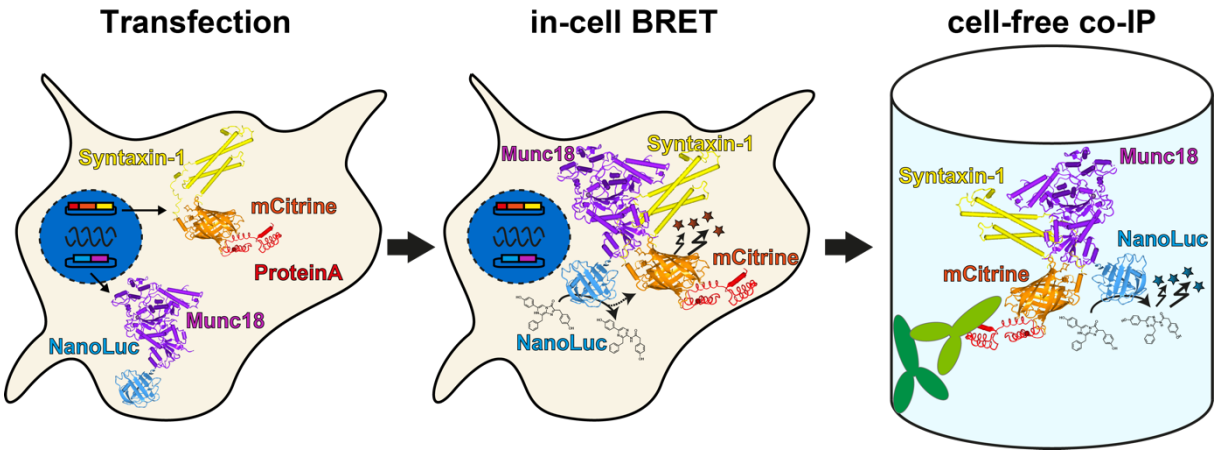

Fig. 19: Overview of the BRIP procedure. Transfection: Mammalian cells are co-transfected with vectors e.g. encoding the fusion proteins NanoLuc-Munc18 (donor protein) and a protein A-mCitrine-Syntaxin-1 (acceptor). **In-cell BRET:** Typically, 48h after transfection, substrate is added to the living cells and the luminescence at the short (~460 nm) and long (~530 nm) wavelengths detected using a microplate reader or a microscope with appropriate filters. **Cell-free co-IP:** After the in-cell BRET measurements, the cells are lysed and the lysate is transferred to IgG-coated 384-well plates for immunoprecipitation. After extensive washing, the fluorescence and luminescence activities of the co-immunoprecipitated proteins are quantified in a microplate reader.

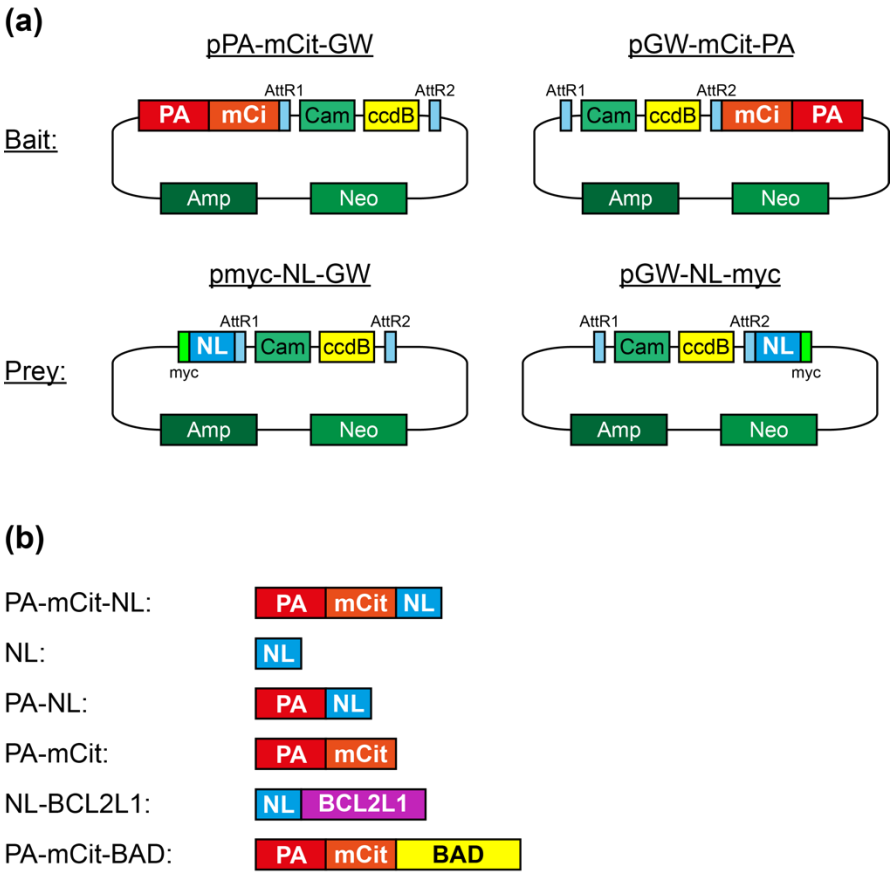

Fig. 20: BRIP vectors and proteins used for assay establishment. (**a**) Gateway compatible destination vectors for donor and acceptor fusion protein production in mammalian cells. The Gateway (GW) cassette containing a chloramphenicol resistance (cam) and the ccdB survival gene is flanked by AttR sites. LR recombination allows gene transfer from an entry plasmid into the BRIP destination vectors. Donor vectors enable the expression of N- or C-terminally tagged NanoLuc luciferase (NL) fusion proteins. Additionally, the donor vectors encode a myc-tag for the detection of proteins by immunoblotting and immunocytochemistry. Acceptor vectors facilitate the expression of N- or C-terminally tagged protein A (PA)-mCitrine (mCit) fusion proteins. Amp: ampicillin resistance; Neo: neomycin resistance; Cam: chloramphenicol resistance; ccdB: ccdB gene; AttR1/AttR2: Gateway® recombination sites; GW: Gateway® cassette. (**b**) Schematic presentation of control proteins used for the establishment of the BRIP assay and for the investigation of the published interaction between BAD and BCL2L1.

5.2.1. Generation of control and Gateway-compatible vectors suitable for quantitative BRIP interaction screening

Initially, I generated Gateway-compatible vectors suitable for PPI screening using the bioluminescence resonance energy transfer and co-immuoprecipitation (BRIP) assay. I constructed the vectors pNL-GW and pGW-NL for expression of proteins with N- or C-terminal NanoLuc (NL) luciferase tags (Fig. 20a). Similarly, I generated the vectors pPA-mCit-GW and pGW-mCit-PA for the production of proteins with N- or C-terminal protein A (PA) and mCitrine (mCit) tags (Fig. 20a). Due to the sequential detection of PPIs with two assay-principles, the NanoLuc-fusion proteins serve as energy donor in the in-cell BRET assay and as preys in the cell-free co-IP read-out. On the other hand, protein A-mCitrine fusion proteins function as energy acceptor in the in-cell BRET assay and they act as baits through their protein A-tag in the cell-free co-IP assay. To test a PPI with the BRIP assay, cDNA fragments encoding the proteins of

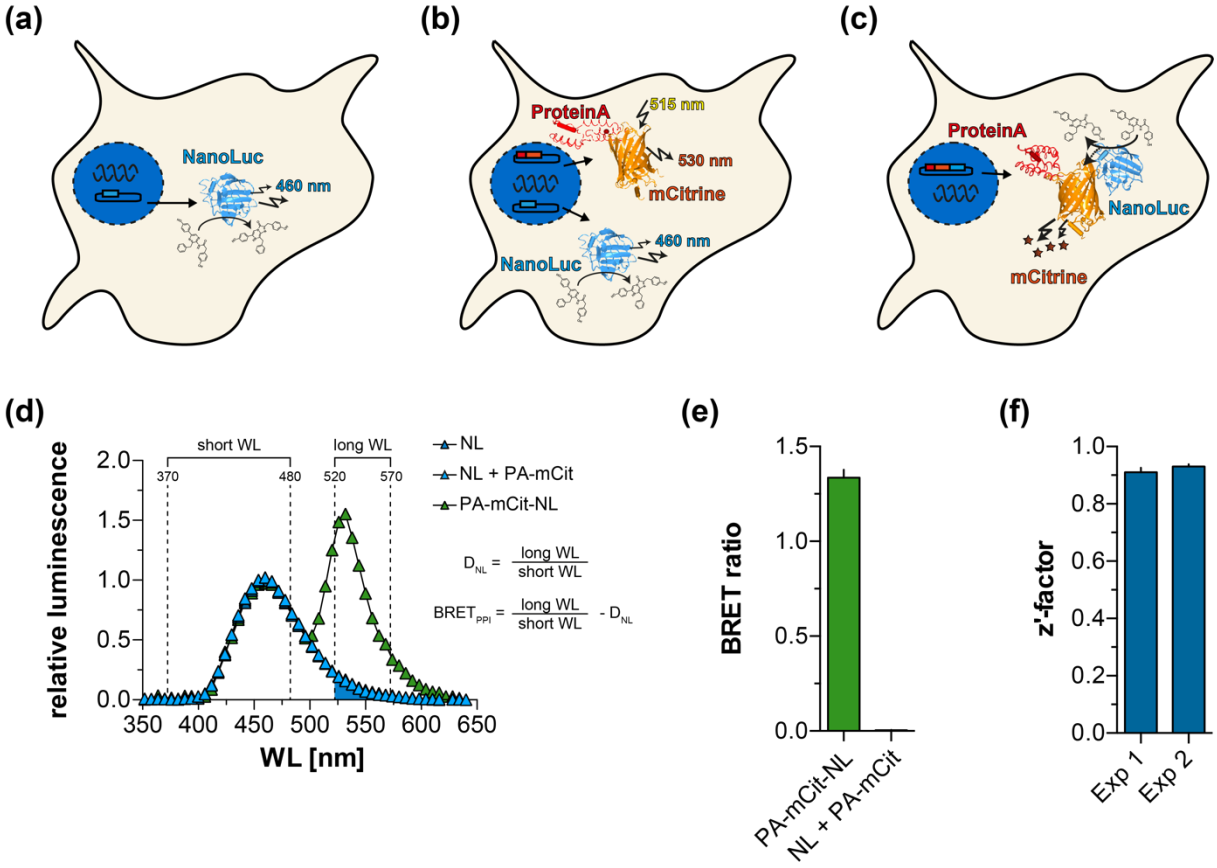

Fig. 21: Determination of basic parameters of the in-cell BRET component. Mammalian cells (HEK293) were transfected with vectors encoding the NanoLuc (NL) alone (**a**), the NanoLuc and the fusion protein protein A-mCitrine (**b**, PA-mCit) or a fusion construct of protein A-mCitrine-NanoLuc (**c**, PA-mCit-NL). Furimazine is depicted as the substrate for the NanoLuc, which is converted upon oxidation into furimamide as the product. (**d**) Normalized luminescence scan measurements where the luminescence emission at different wavelengths of the NL (dark blue), the NL co-produced with PA-mCit (light blue) or the fusion construct of PA-mCit-NL (green) was recorded in HEK293 cells. The emission spectrum of the PA-mCit-NL shows two emission peaks at ~460 and ~530 nm indicating an efficient resonance energy transfer from the substrate-donor complex (NL) onto the acceptor (mCit). In contrast, the NL alone or co-produced with PA-mCit show identical spectra with one emission peak at ~460 nm. Indicated are the luminescence filters at the short wavelength (WL) from 370-480 nm and at the longer WL from 520-570 nm that were used in standard BRIP measurements. BRET ratios were calculated as the luminescence emission of the long WL divided by the short WL. Donor bleed-through (D_{NL}; blue area under the curve) was calculated from the NL alone and subtracted from all BRET ratios. (**e**) BRET ratios calculated for PA-mCit-NL or NL and PA-mCit from two independent experiments with n=16 each. Each n was performed in triplicates. Bars represent mean values ± SEM. (**f**) Z'-factors calculated from two independent experiments with n=16 each. Each n was performed in triplicates. Bars represent mean values ± SEM.

interest are inserted into the respective expression plasmids by Gateway recombination cloning[188]. Additionally, as positive control I constructed a tandem construct (TC) encoding a PA-mCit-NL hybrid protein, where the PA-tagged mCitrine fluorescent protein is directly connected via a short peptide linker to the NanoLuc luciferase (Fig. 20b). Further control plasmids needed for BRIP assays are expression plasmids encoding for the proteins NanoLuc (NL), PA-tagged NanoLuc (PA-NL) and PA-mCitrine (PA-mCit, Fig. 20b). The untagged and PA-tagged NanoLuc proteins are necessary to determine the BRET in intact cells or if necessary also after co-IP. In contrast to the tandem construct, cells co-producing unfused NanoLuc and PA-mCit protein are used as negative control to determine unspecific background binding between the two proteins.

5.2.2. Establishment of a BRIP assay suitable for high-throughput PPI mapping

To establish the BRIP assay, HEK293 cells were transfected with plasmids encoding the NanoLuc alone (Fig. 21a), the NanoLuc and PA-mCit (Fig. 21b) or the tandem construct PA-mCit-NL (Fig. 21c). Initially, luminescence scan measurements were performed. The substrate was added to living cells and the luminescence emission recorded at different wavelengths (Fig. 21d). Cells producing only the NanoLuc showed an emission spectrum with a maximum at 460 nm similar to cells co-producing the NanoLuc together with PA-mCit, indicating that the NanoLuc does not unspecifically bind to the PA-tag or mCit. However, the emission spectrum of the PA-mCit-NL fusion construct showed a second maximum at ~530 nm, resulting from fluorescence emitted by mCitrine as a consequence of an energy transfer from the luciferase-substrate complex onto the acceptor (Fig. 21d). The two emission peaks showed a spectral separation of ~70 nm, which results in a reduced donor bleed-through and is preferable compared to the *Renilla* luciferase[145]. Luminescence scans are inefficient due to long measurement times and the BRET is more difficult to quantify. For quantification of BRET, the luminescence emission of cells producing the NanoLuc (Fig. 21a), the NanoLuc and PA-mCit (Fig. 21b) or the PA-mCit-NL hybrid fusion protein (Fig. 21c), was detected at different wavelengths (WLs) using a short (370-480 nm) and a long (520-570 nm) band-pass filter (Fig. 21d). Initially, the donor bleed-through (D_{NL}), which is the donor emission into the long WL filter from cells producing the NanoLuc alone, was calculated as the ratio of the luminescence emission at the long to the short WL. Following, the BRET ratios for the unfused NanoLuc and PA-mCit as well as for the tandem construct PA-mCit-NL were calculated accordingly with the additional subtraction of the D_{NL} (Fig. 21d). I calculated for the cells co-producing the NanoLuc and PA-mCit a BRET ratio of 0.004±0.001 and for the hybrid fusion PA-mCit-NL of 1.335±0.043 indicating a high reproducibility of the assay and a large range to distinguish between positive and negative interactions (Fig. 21e). To determine the statistical effect size as a measure for high-throughput applications, I transfected 16x 96-well plates with the vectors encoding the NanoLuc alone, the unfused NanoLuc and PA-mCit and the tandem construct PA-mCit-NL. I calculated BRET ratios as described and calculated z'-factors of 0.91 and 0.93 from two biological replicates (Fig. 21f).

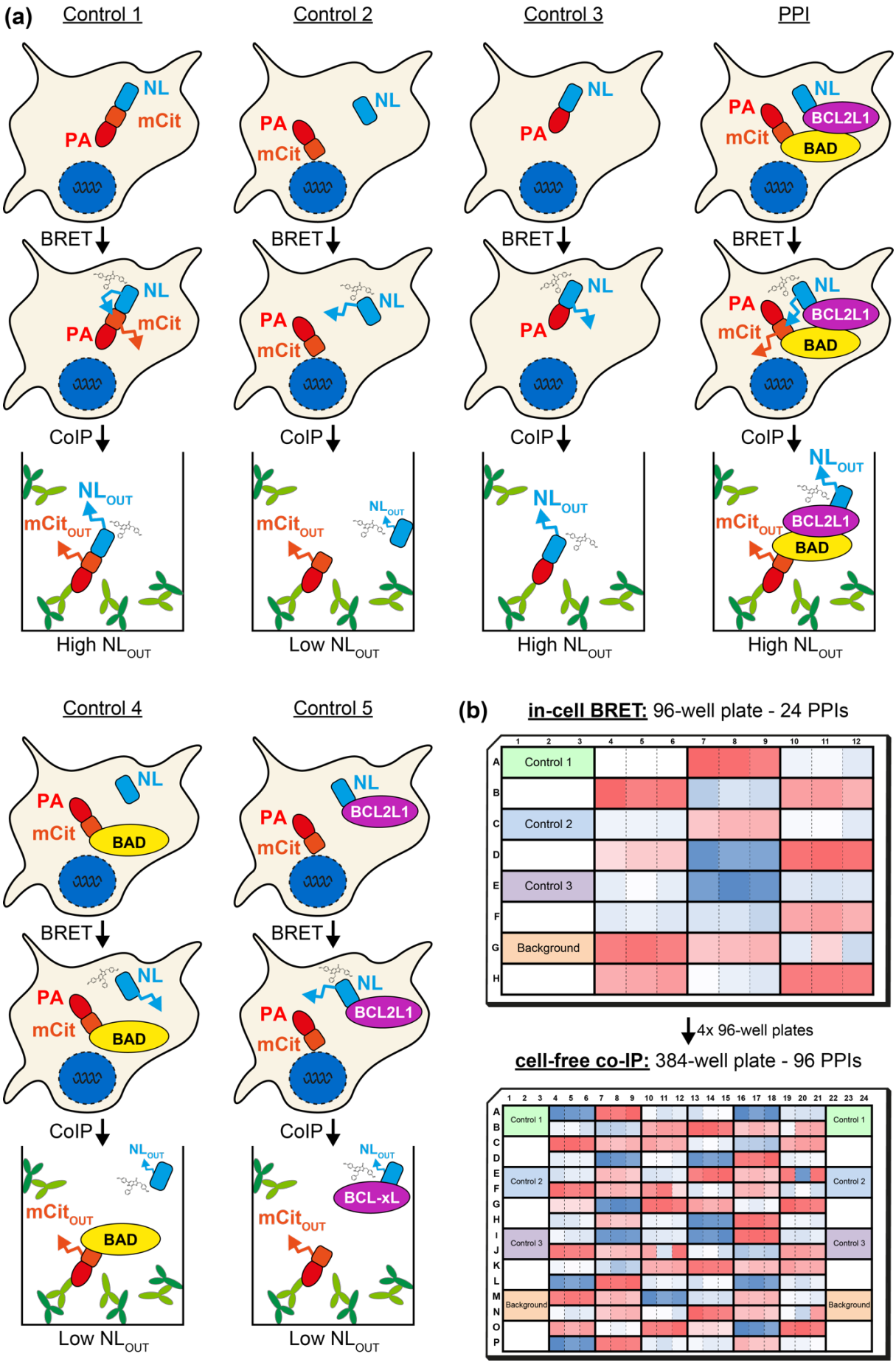

Fig. 22 (legend on next page)

Fig. 22: High-throughput procedure for detecting PPIs with the BRIP assay. (**a**) For all BRIP assays are three controls transfected encoding for PA-mCit-NL as positive control (Control 1), NL + PA-mCit as negative control (Control 2) and PA-NL (Control 3) to determine the donor bleed-through in BRET calculations. To study the interaction between BAD and BCL2L1, PA-mCit-BAD and NL-BCL2L1 (PPI) were co-produced in mammalian cells. Unspecific background binding of the NL to PA-mCit-BAD (Control 4) and of the NL-BCL2L1 to PA-mCit (Control 5) was determined. After transfection, cells were incubated for 48h before substrate was added and in-cell BRET measurements were performed. Afterwards, cells were lysed and immunoprecipitations were performed using IgG-coated 384-well plates. (**b**) Typical layout of a white 96-well plate used for high-throughput BRIP screening suitable to fit 24 PPIs per plate. In-cell BRET is performed in white 96-well plates, of which four are transferred after lysis to one white IgG-coated 384-well plate for the cell-free co-IP assay.

5.2.3. Detection of known interactions with the BRIP assay

As the PPI between BAD and BCL2L1 has been shown to be suitable for PPI assay development[74], the cDNAs encoding BAD and BCL2L1 were cloned into the respective vectors pPA-mCit-GW and pNL-GW, generating expression plasmids encoding for PA-mCit-BAD and NL-BCL2L1 (Fig. 20b). Next, the protein pairs NL-BCL2L1 and PA-mCit-BAD (PPI), NL and PA-mCit-BAD (Control 4) as well as NL-BCL2L1 and PA-mCitrine (Control 5) were produced in HEK293 cells (Fig. 22a). Additionally, the above-described control plasmids encoding PA-mCit-NL (Control 1), NL and PA-mCit (Control 2) and the PA-NL alone (Control 3) were transfected routinely in all following experiments (Fig. 22a). Transfections were performed in triplicates in white 96-well plates and the BRET measurements were performed in intact cells (in-cell BRET), followed by cell lysis and co-IP of protein complexes in white 384-well plates (cell-free co-IP; Fig. 22b).

To confirm the BRET from NL-BCL2L1 to PA-mCit-BAD, I performed a luminescence scan measurement that revealed the characteristic second emission peak at 530 nm, indicating the close proximity of donor and acceptor (Fig. 23a). This result was further substantiated when calculating the BRET ratio for the interactions between NL-BCL2L1 and PA-mCit-BAD, which was significantly higher than for the negative controls NL + PA-mCit-BAD (control 4) and NL-BCL2L1 + PA-mCit (control 5) indicating that the in-cell BRET assay can distinguish between positive and negative PPIs (Fig. 23b).

For the cell-free co-IP, the cells were lysed and the mCitrine fluorescence ($mCit_{IN}$) measured in a microtiter plate reader. Afterwards, substrate was added to the lysate and the emitted luminescence was detected (NL_{IN}). Indeed, in all samples fluorescence and luminescence activity was measurable indicating the production of the respective fusion proteins (Fig. 23c). Furthermore, BRET measurements indicated that the interaction between NL-BCL2L1 and PA-mCit-BAD was still intact after cell lysis, whereas no significant BRET could be measured for the controls 4 and 5 (Fig. 23b). Next, the cell lysates were incubated in IgG- coated 384-well microtiter plates to precipitate the PA-mCit tagged bait proteins, which were quantified after extensive washing by measuring the fluorescence ($mCit_{OUT}$; Fig. 23d). Finally, the enzymatic activity of the NL-tagged prey proteins was determined (NL_{OUT}), which indicates the successful co-precipitation of the prey protein (Fig. 23d). Importantly, while all proteins could be

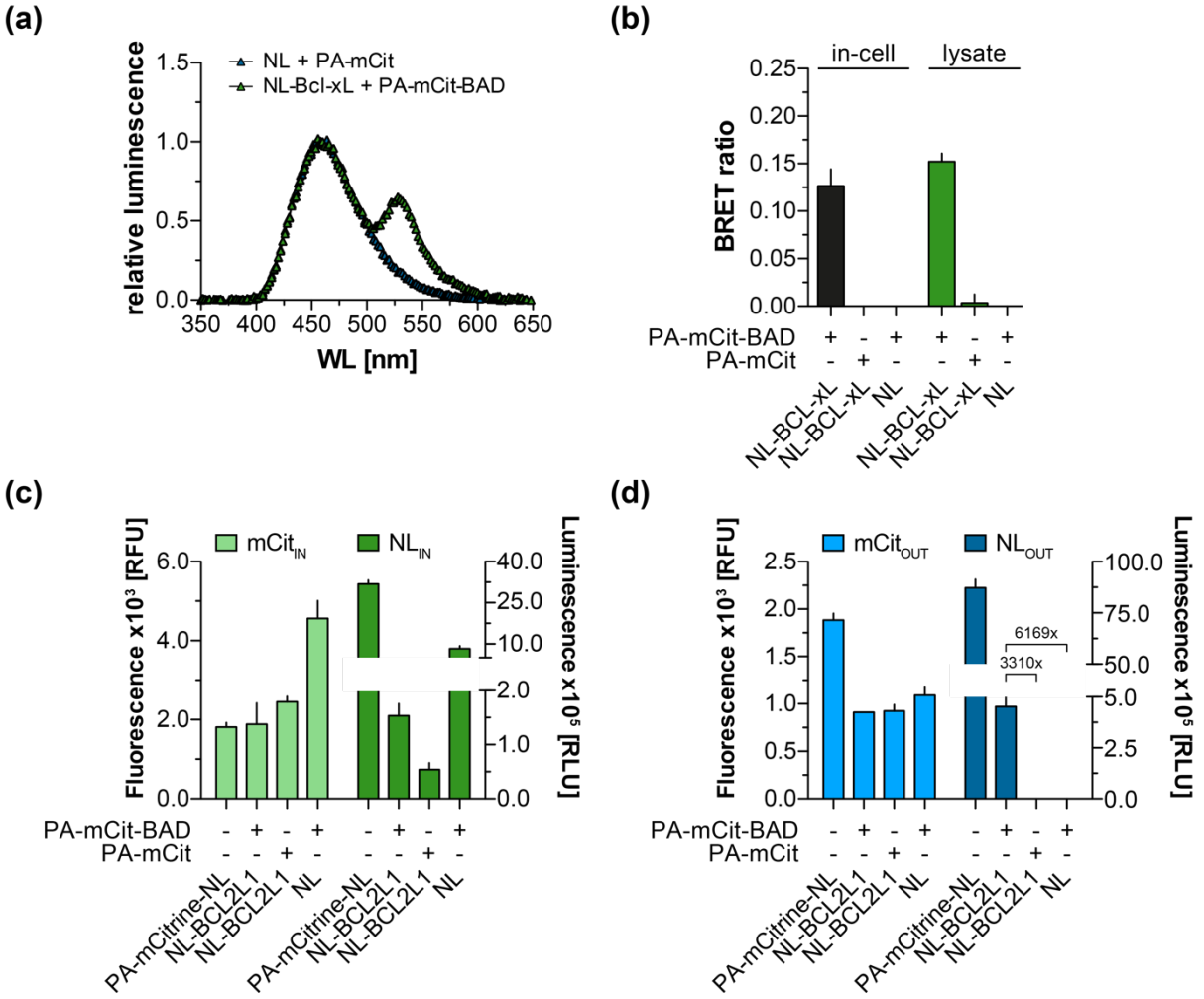

Fig. 23: Detecting the known-interaction between BAD and BCL2L1 using the BRIP assay. (**a**) Only in cells co-producing NL-BCL2L1 and PA-mCit-BAD a resonance energy transfer from donor to acceptor is visible in luminescence scan measurements, indicated by the mCit fluorescence emission maximum at 530 nm. (**b**) BRET ratios were determined in intact cells and in cell lysates. Cells co-producing NL-BCL2L1 and PA-mCit-BAD show both in intact cells and in cell lysates significant BRET ratios of 0.1265±0.0307 and 0.1522±0.0152. No BRET was observable for the respective controls. (**c**) Expression analysis in lysates by quantification of mCit fluorescence (mCit$_{IN}$) and NL luminescence (NL$_{IN}$). (**d**) Quantification of bait precipitation (mCit$_{OUT}$) and prey co-IP (NL$_{OUT}$) by measuring fluorescence and total luminescence activities after co-IP. All experiments were performed three times and the results from one are displayed representatively. The bar diagrams display the mean ± SD from triplicate values. RLU: relative luminescence units; RFU: relative fluorescence units.

immunoprecipitated (as indicated by the measurement of fluorescence, mCit$_{OUT}$), a significant luminescence (NL$_{OUT}$) was only detected for PA-mCit-NL (control 1) and for the interaction between NL-BCL2L1 and PA-mCit-BAD (Fig. 23d). For the interaction of interest between NL-BCL2L1 and PA-mCit-BAD, I detected a 3,331- and 6,169-fold higher luciferase activity in comparison to the controls NL-BCL2L1 and PA-mCit or NL and PA-mCit-BAD, respectively, indicating the high specificity with which positive and negative PPIs can be distinguished in cell-free co-IP experiments (Fig. 23d).

Next, I performed competitive binding and donor saturation experiments using the established BRIP assay. In the competition assay, an unlabeled competitor was co-produced, which resulted in the inhibition of the investigated interaction and a reduction of the BRET ratio[189]. To simplify

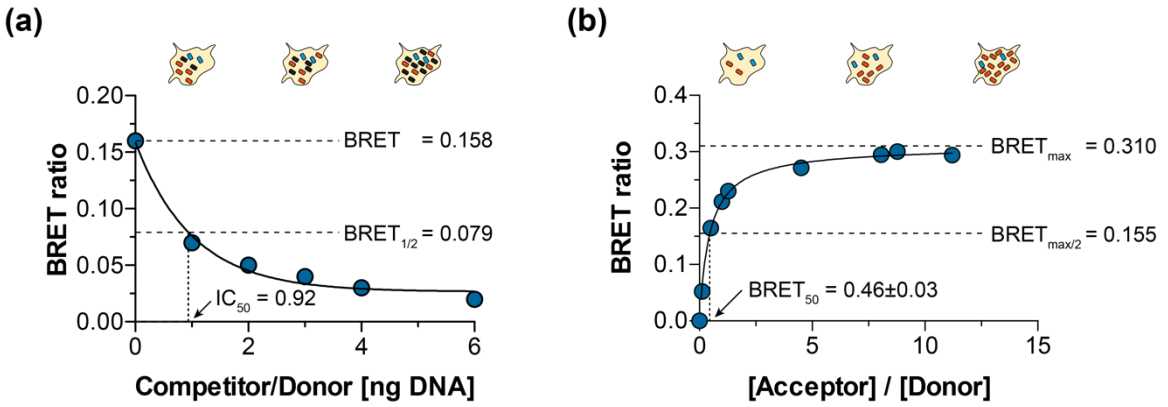

Fig. 24: Assessing the specificity and binding strength for the interaction between BAD and BCL2L1. (**a**) BRET ratios from cells transfected with the same quantities of DNA encoding NL-BCL2L1 and PA-mCit-BAD. Additionally, increasing amounts of myc-BCL2L1 as competitor were co-produced. Non-linear curve fitting to determine competitor/donor DNA ratio for a half-maximal inhibition. Equal production of NL-BCL2L1 and PA-mCit-BAD was confirmed by measuring the fluorescence and luminescence activities. (**b**) For donor saturation experiments, constant amounts of NL-BCL2L1 were co-produced with increasing amounts of PA-mCit-BAD. The approximate acceptor to donor molecular ratio was calculated as described in the methods. Non-linear curve fitting allows to determine the maximal BRET ($BRET_{max}$) and the acceptor to donor stoichiometry at which the half-maximal BRET ($BRET_{50}$) is reached. All experiments were performed three times and the results from one are displayed representatively. Graphs display the mean ± SD from triplicate values from one experiment.

the approach, I produced constant quantities of NL-BCL2L1 and PA-mCit-BAD, while co-producing increasing amounts of the competitor, in this case myc-epitope tagged BCL2L1 (myc-BCL2L1). With increasing concentrations of myc-BCL2L1 a decrease in BRET between NL-BCL2L1 and PA-mCit-BAD was observed indicating that cmyc-BCL2L1 replaces NL-BCL2L1 as the binding partner of PA-mCit-BAD. By non-linear curve-fitting, the half-maximal inhibition of the PPI was reached at a competitor (cmyc-BCL2L1) to donor (NL-BCL2L1) DNA ratio of almost 1:1 (IC_{50}=0.92). Under the assumption that both proteins are produced in similar amounts when the same quantities of DNA are transfected, the produced proteins NL-BCL2L1 and cmyc-BCL2L1 would bind with similar affinity to PA-mCit-BAD (Fig. 24a). Consequently, competition binding assays are suitable to determine the specificity and selectivity of an interaction compared to a third protein.

Importantly, the BRET component of the BRIP assays can also be used to determine relative binding strengths in donor saturation experiments[168,190]. Therefore, I co-produced constant amounts of NL-BCL2L1 with increasing quantities of PA-mCit-BAD in HEK293 cells and determined the corresponding in-cell BRET ratios as described before. The fluorescence and luminescence activities of the tandem construct PA-mCit-NL (control 1) can be estimated to correspond to a 1:1 molecular stoichiometry of donor and acceptor. Thus, it can be used to calculate the approximate molecular ratio of NL-BCL2L1 to PA-mCit-BAD, which was plotted against the obtained BRET ratios (Fig. 24b). With increasing amounts of acceptor (PA-mCit-BAD) to donor (NL-BCL2L1) an increase in BRET was observed that reached its maximum at an ~8x excess of acceptor to donor. By nonlinear regression curve fitting the maximal BRET ($BRET_{max}$)

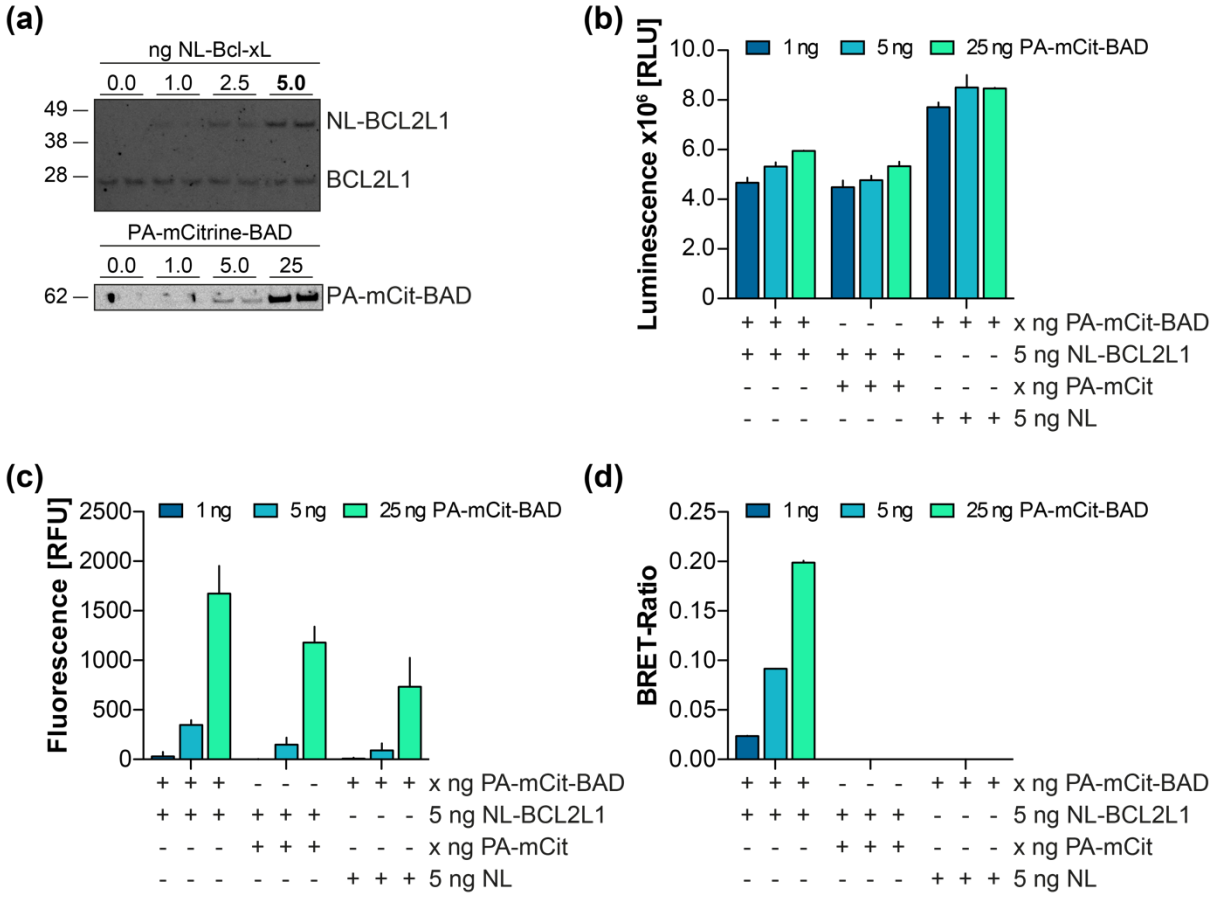

Fig. 25: The BRIP assay allows the detection of PPIs a sub-endogenous protein levels. (**a**) HEK293 cells are transfected with 1.0, 2.5 or 5.0 ng of NL-BCL2L1, or respectively with 1.0, 5.0 or 25.0 ng of PA-mCit-BAD encoding vector. After lysis, equal protein amounts were loaded on a 4-12% gradient SDS-Page, transferred on a nitrocellulose membrane and immunoblotted with an anti-BCL2L1 or anti-BAD antibody. No endogenous BAD could be detected (not shown). (**b**) Total Luminescence emitted from cells transfected with 5.0 ng of NL-BCL2L1 or NL encoding DNA. (**c**) Fluorescence emitted from cells transfected with 1.0, 5.0 or 25.0 ng of PA-mCit-BAD or PA-mCit encoding DNA. (**d**) BRET ratios determined in cells co-producing NL-BCL2L1 or NL together with increasing amounts of PA-mCit-BAD or PA-mCit. All experiments were performed two times and the results from one are displayed representatively. Bar diagrams display the mean ± SD from triplicate values from one experiment. RLU: relative luminescence units; RFU: relative fluorescence units.

was determined, and the molecular ratio at which the half-maximal BRET ($BRET_{50}$) was obtained could be calculated, which is a measure of binding strength (Fig. 24b).

Finally, with the extremely high brightness of the NanoLuc, I wanted to determine whether I can also detect interactions when the fusion proteins are produced at endogenous or at even lower than endogenous levels. Hence, I transfected HEK293 cells with different amounts of the plasmids that encode both NL-BCL2L1 and PA-mCit-BAD. By Western blotting the amounts of transiently produced protein in relation to the endogenous protein levels were determined. For NL-BCL2L1 5 ng of transfected plasmid per well in a 96-well plate corresponded roughly to the endogenous amounts of BCL2L1 in HEK293 cells (Fig. 25a). Cells producing the respective amounts of NL-BCL2L1 showed a luciferase activity of ~5x10^6 RLU (relative luminescence units, Fig. 25b). In contrast to BCL2L1, no endogenous levels of BAD cells could be detected in HEK293 cells. Therefore, a direct comparison to exogenously expressed PA-mCit-BAD protein was not possible

(Fig. 25a). However, from cells transfected with only 1 ng of DNA, the protein PA-mCit-BAD was neither detectable by Western blotting (Fig. 25a) nor by measuring the fluorescence activity (Fig. 25c). Still, even at very low protein amounts, I could detect an interaction between NL-BCL2L1 and PA-mCit-BAD by quantification of BRET. In comparison, in control cells co-producing NL-BCL2L1 and PA-mCit or NL and PA-mCit-BAD no BRET could be measured (Fig. 25d).
Thus, I showed that the BRIP assay can be used to distinguish between positive and negative PPIs. Furthermore, I found that the method is suitable to calculate $BRET_{50}$ values and allows the detection of PPIs even when proteins are expressed at very low levels.

5.2.4. Estimating the sensitivity and specificity to detect PPIs with the BRIP assay

Assay performance is best evaluated by systematic benchmarking using positive and negative PPI reference sets. I have used the available *H. sapiens* positive and random reference sets (hPRS, hRRS) to estimate the sensitivity and specificity of the BRIP assay to detect PPIs[74]. For the originally described 92 PPIs in both the hPRS and hRRS, I generated expression vectors to test 78 and 79 PPIs from the respective reference sets in the BRIP assay (Fig. 26a and b). For each protein to be tested, I constructed two plasmids allowing the investigation of the protein of interest either as donor (NL-tagged fusion) or as acceptor (PA-mCit-tagged fusion) in BRIP assays. Thus, each PPI was analyzed as donor/acceptor (set a) and acceptor/donor combination (set b) in BRIP assays. Transfections were performed as described before, which included that cells producing the three controls PA-NL alone, NL and PA-mCit as well as PA-mCit-NL were present on each screening plate. However, for the screening approach I did not include the controls NL and PA-mCit-Protein-X (control 4) and NL-Protein-Y and PA-mCit (control 5) for each interaction as this reduces assay throughput.
The BRIP assay was performed as before. The luminescence was measured 48 h after transfection in living cells and the in-cell BRET was calculated (Table 8). Following, the cells were lysed and the mCitrine fluorescence and NL activities determined in cell lysates and after co-IP of protein complexes. At this stage, I calculated the co-IP efficiencies, which correspond to the fraction of prey co-precipitated from the lysate (Table 8). This calculation was performed as the control interactions NL and PA-mCit-Protein-X (control 4) and NL-Protein-Y and PA-mCit (control 5) were excluded in the benchmarking approach and thus, a comparison between each interaction and its respective controls not applicable. As each interaction was tested in both directions, I selected the BRET ratios and co-IP efficiencies with the higher value and used these as final interaction scores that were used for further analysis (Fig. 28a and b). The calculated BRET ratios in the cells are highly reproducible in two independent experiments (r^2=0.88; Fig. 26c), whereas more variation was observed after the co-IP suggesting that further optimizations are necessary (r^2=0.68; Fig. 26e). Next, I conducted a receiver operating characteristic (ROC) analysis on both

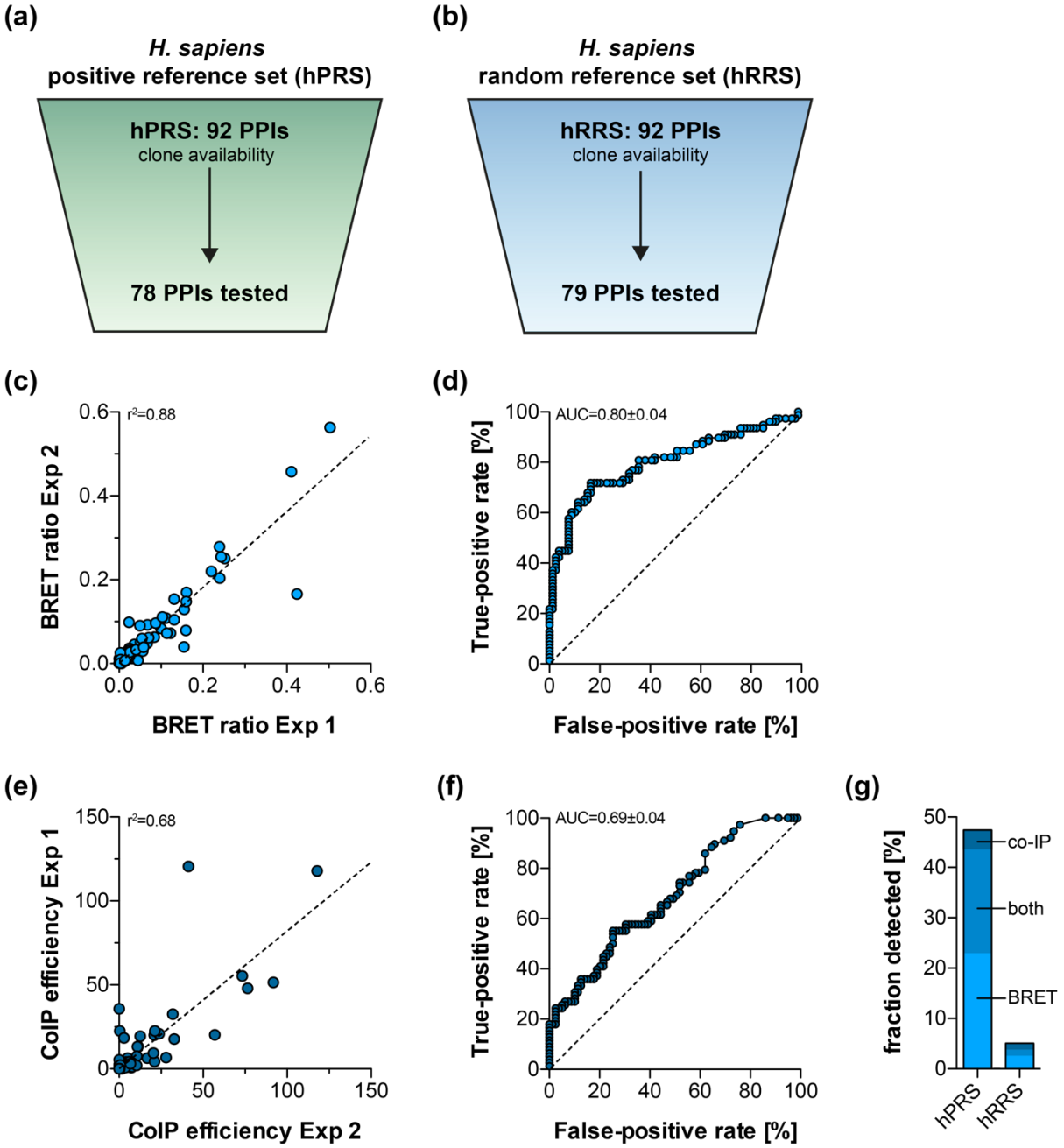

Fig. 26: Systematic benchmarking of positive and random reference sets with the BRIP assay. Due to clone availability or shuttling success, 78 out of the 92 PPIs in the hPRS (**a**) and 79 out of 92 PPIs in the hRRS (**b**) were screened with the BRIP assay. (**c**) Reproducibility of the benchmarking results of the in-cell BRET. The scatter plot shows the mean of the BRET ratio and the calculated correlation from two independent experiments (Exp 1 and Exp 2), each performed in technical triplicates. (**d**) Receiver operating characteristic (ROC) analysis of the in-cell BRET data to determine the threshold for the separation of true and potentially false-positive PPIs. A BRET ratio of ≥0.03 results in a sensitivity and specificity of 42.3% and 96.2%. (**e**) Reproducibility of the cell-free co-IP experiments of PPIs from the hPRS and hRRS from two independent experiments (Exp 1 and Exp 2). The scatter plot shows the mean of two independent experiments, each performed in technical triplicates and the correlation calculated. (**f**) Receiver operating characteristic (ROC) analysis of the co-IP data facilitated the definition of a threshold for the separation of true and potentially false PPIs. A co-IP efficiency of ≥7.0% results in a sensitivity and specificity of 24.4% and 97.5%. (**g**) Fraction of PPIs from the hPRS and hRRS detected when considering both read-outs. A total of 47.4% and 5.1% of the PPIs were recovered from the reference sets (hPRS and hRRS), respectively, using the BRIP assay.

the calculated in-cell BRET ratios as well as for the cell-free co-IP efficiencies to define the cutoff for the identification of true positive PPIs (Fig. 26d and Fig. 26f).

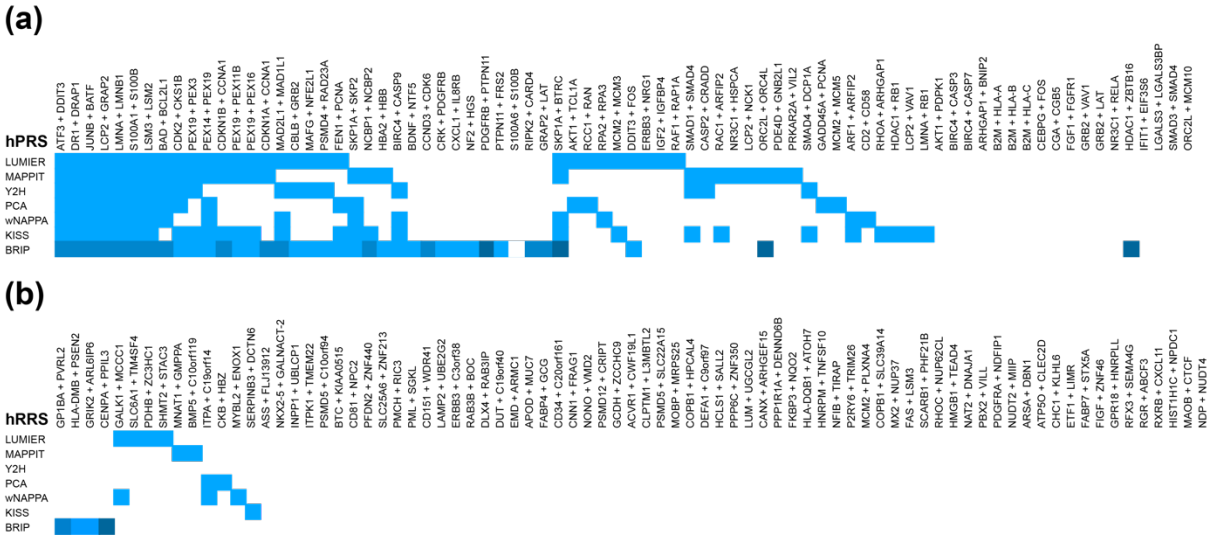

Fig. 27: Benchmarking result of the BRIP assay against other methods. Overview of the PPIs detected with the BRIP assay and other published methods for the hPRS (**a**) and hRRS (**b**). Displayed are only the PPIs screened with the BRIP assay. For the PPIs that were detected with the BRIP assay the in-cell BRET data are colored light blue (■), and the co-IP dark blue (■). PPIs that were detected with both read-outs are indicated in blue (■).

For the in-cell BRET, I defined a BRET ratio of ≥0.03 as a cut-off to distinguish between positive and negative PPIs. Using this cut-off I was able to detect 42.3% of the PPIs in the hPRS and 3.8% in the hRRS (Fig. 26g). Furthermore, the calculated area under the ROC curve (AUC) of ~0.8 indicates a good distinction between true-positive and false-positive PPIs (Fig. 26d).

Similarly, I performed a ROC analysis on the co-IP efficiencies to select a cut-off of ≥7% where I detected 24.4% of PPIs in the hPRS and only 2.5% in the hRRS (Fig. 26f). The reduced assay sensitivity of the co-IP compared to the in-cell BRET is also reflected by the smaller AUC of ~0.7. In total I detected 37 of the 78 screened PPIs in the hPRS (47.4%), of which 15 PPIs were detected with both read-outs (Fig. 26g and Fig. 27a). In contrast, I detected only 4 out of the 79 PPIs in the hRRS (5.1%) of which only one was detected with both read-outs (Fig. 26g and Fig. 27b).

Thus, the BRIP assay detects PPIs with a high sensitivity and specificity and can distinguish between true and false interactions. Interestingly, a clear separation between true and potentially false-interactions could be achieved without the use of the control interactions NL and PA-mCit-Protein-X (control 4) and NL-Protein-Y and PA-mCit (control 5) for each interaction making the assay especially suitable for high-throughput PPI screening in mammalian cells.

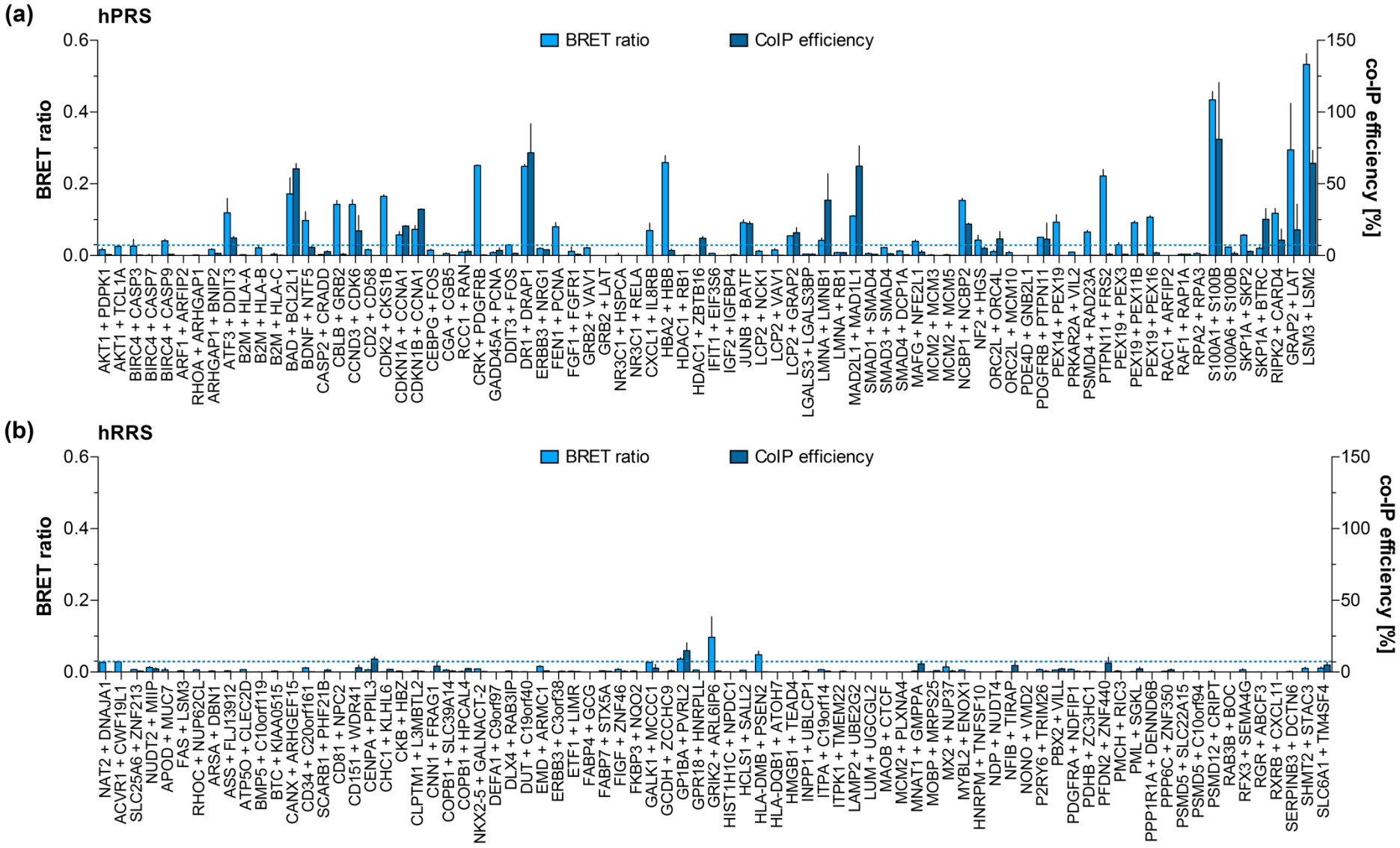

Fig. 28: Systematic analysis of PPIs in the hPRS and hRRS using the BRIP assay. BRET ratios and co-IP efficiencies for all 78 PPIs of the hPRS (**a**) and 79 PPIs of the hRRS (**b**). All interactions were tested as donor/acceptor (set a) and acceptor/donor (set b) orientation. The higher values from set a or set b are displayed as mean ± SEM from two biological replicates.

5.2.5. Detecting interactions with known binding affinities in intact cells and after co-immunoprecipitation

With the establishment of an assay that provides a dual PPI read-out, I had the unique opportunity to compare the recovery rate of interactions with known affinities before and after cell lysis. Therefore, the available affinity-based interaction reference set (AIRS) was used, to which additional 14 PPIs were added to obtain a total of 71 PPIs with known *in vitro* dissociation constants (Fig. 28a). This AIRSv2 covered a wide spectrum of dissociation constants from low- (K_D > 100 nM) to high affinity (K_D < 100 nM) interactions (Fig. 28b). By doubling the number of interactions in the nano- to picomolar range (10^{-8}-10^{-16}) a greater density of high affinity PPIs was achieved (Fig. 29b and c).

Next, the cDNAs encoding the interacting protein pairs were cloned into BRIP expression vectors as donor/acceptor (set a) and acceptor/donor (set b) combinations. I applied the same assay conditions as for the reference sets (hPRS and hRRS) measuring the luminescence activity in intact cells, cell lysates and after the co-IP. Accordingly, the BRET ratios and co-IP efficiencies were calculated for each interaction in both directions (set a and b, Table 9) and the corresponding higher interaction scores were used for further analyses. Applying the cut-offs as determined with the hPRS and hRRS (BRET ≥0.03; co-IP ≥7.0%), an overall recovery rate in the AIRSv2 of ~37% was achieved (26 of 71 tested PPIs). Importantly, both low- and high-affinity interactions could be readily detected with the BRIP assay (Fig. 29d).

The recovery rate of the in-cell BRET compared to the cell-free co-IP was with ~34% over ~17% significantly higher, mainly due to the higher validation rate of low-affinity interactions in intact cells (Fig. 29e). Only a weak trend between dissociation constant and recovery rate was detectable for the in-cell BRET, suggesting that low-affinity and high-affinity interactions can be detected with a similar sensitivity in intact cells. In contrast, the cell-free co-IP read-out detected strong interactions more readily than weak interactions, supporting the hypothesis that cell-lysis can disrupt particularly weak interactions (Fig. 29e)[27].

Next, I analyzed whether the published *in vitro* dissociation constants directly correlate to the calculated interaction scores of the BRIP assay. As partly expected, the in-cell BRET ratios showed no direct correlation to the K_D values as the parameter influencing the energy transfer most, is the distance between donor and acceptor and hence, not the affinity[120]. However, as demonstrated for the interaction between NL-BCL2L1 and PA-mCit-BAD the donor saturation is decisive of the measured BRET (Fig. 24b). Consequently, the $BRET_{max}$ should be reached in the case of a high-affinity interactions earlier, as lower acceptor levels are sufficient to saturate the donor. Thus, high affinity interactions are expected to have in general higher BRET ratios. Therefore, I analyzed

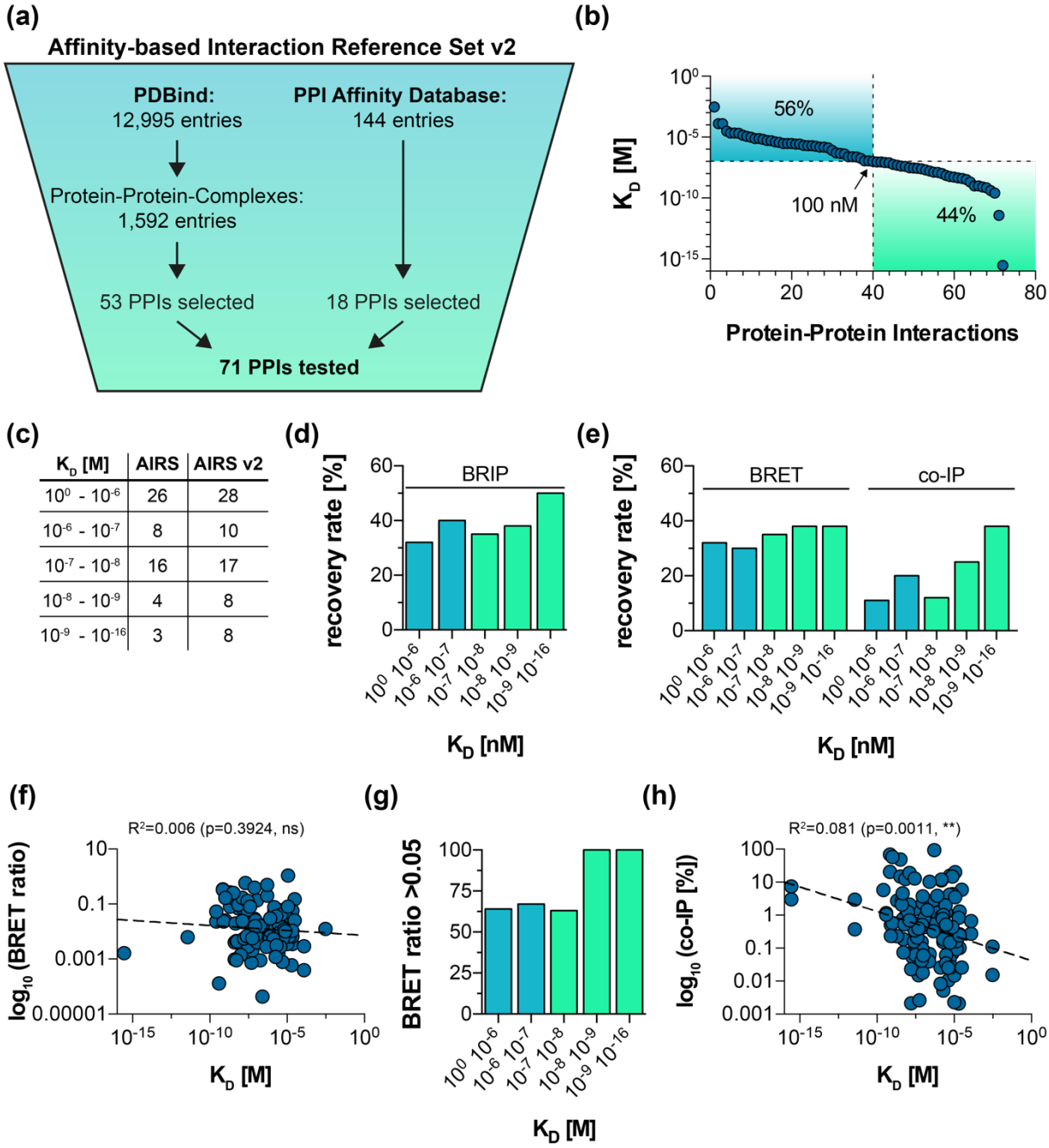

K_D [M]	AIRS	AIRS v2
10^{0} - 10^{-6}	26	28
10^{-6} - 10^{-7}	8	10
10^{-7} - 10^{-8}	16	17
10^{-8} - 10^{-9}	4	8
10^{-9} - 10^{-16}	3	8

Fig. 29: Systematic analysis of PPIs with known affinities using the BRIP assay. (**a**) Selection strategy for interactions with known affinities compiled in the affinity-based interaction reference set v2 (AIRSv2). I selected 71 PPIs from PDBbind and the Protein-Protein-Interaction Affinity Database 2.0 and systematically tested them with the BRIP assay. (**b,c**) The selected 71 PPIs in the AIRSv2 span a broad range of binding affinities, with a particularly higher density of interactions in the nano- to picomolar range compared to the AIRS. (**d**) Recovery rate of the BRIP assay in relation to their published *in vitro* dissociation constants. (**e**) Recovery rate of PPIs with the BRET and co-IP read-out in relation to their published *in vitro* dissociation constants. Recovery rates were determined using the cut-offs as determined with the hPRS and hRRS. (**f, h**) Published dissociation constants plotted against BRET ratio (**f**) or co-IP efficiency (**h**). Linear regression plotted as broken line. Pearson correlation: ns p>0.05, **p<0.01. (**g**) Frequency of interactions with high BRET ratios of >0.05 in relation to their known dissociation constants.

the frequency of positive interactions with low and high-affinities to have relatively high BRET ratios of >0.05. Indeed, the fraction of strong interactions (K_D values in the nanomolar range) with a high BRET ratio (>0.05) is considerably higher than the fraction of weak interactions (K_D values in the micromolar range, Fig. 29g).

In contrast, the calculated co-IP efficiencies for interactions in the AIRSv2 significantly correlate to the published *in vitro* dissociation constants suggesting that high co-IP efficiencies are an indication of strong interactions (Fig. 29h).

5.2.6. Quantification of binding affinities altered by missense mutations

It has been estimated that ~60% of all disease associated missense mutations perturb PPIs, of which half may lead to a complete loss of the interaction[7]. To test whether the BRIP assay can detect the influence of missense mutations on the interaction strength, I utilized similar as before the well characterized interaction between Syntaxin-1 (STX1A) and its binding protein Munc18 (STXBP1, Syntaxin binding protein 1) for proof-of-principle experiments. Several point mutations have been described that result in a reduced binding affinity of Munc18 to Syntaxin-1 (Fig. 30a and b)[82,187]. Hence, I introduced the single mutations K46E and E59K as well as the double mutation K46E/E59K into Munc18 and generated plasmids encoding NL-Munc18 wt, NL-Munc18 K46E, NL-Munc18 E59K and NL-Munc18 K46E/E59K. Additionally, I constructed a plasmid encoding PA-mCit-Syntaxin-1. Next, HEK293 cells were co-transfected with the respective plasmids and both in-cell BRET measurement as well as cell-free co-IP experiments performed. Interestingly, the interaction between NL-Munc18 wt and PA-mCit-Syntaxin-1 was detectable with both read-outs (in intact cells and after co-IP). However, the single point mutations (K46E and E59K) with reduced affinity to Syntaxin-1 could only be detected in intact cells with the BRET assay but not after co-IPs (Fig. 30c and d). Consistently, the interaction between NL-Munc18 K46E/E59K and PA-mCit-Syntaxin-1 was not detected with either read-out demonstrating the ability of the assay to discriminate between strong, weak and negative PPIs. Next, I performed donor saturation experiments to determine $BRET_{50}$ values, which are an indication of relative in-cell binding strengths[156,168]. Hence, constant amounts of the NL-Munc18 variants (wt, K46E, E59K, K46E/E59K) with increasing amounts of PA-mCit-Syntaxin-1 were co-produced in HEK293 cells and in-cell BRET measurements performed. Importantly, I could determine $BRET_{50}$ values for the wt and single point mutants, but not for the double mutant, which reflects the differences in binding strength similar to the described *in vitro* dissociation constants (Fig. 30e)[82]. I also observed a change in the maximal BRET ratio ($BRET_{max}$) between the wt and the single point mutants (Fig. 30e). The $BRET_{max}$ value represents the maximal energy transfer at donor saturation and depends on the distance and orientation between donor and acceptor[168]. Thus, the reduced $BRET_{max}$ values for the single missense mutations in Munc18 indicate that either the distance between donor and acceptor is increased or that the relative orientation of both to one another has changed. Hence, the in-cell BRET assay can be used to determine relative binding strengths, which can be used to analyze the impact of disease associated missense mutations on interaction strength.

With the increased brightness of the luciferase, I aimed to perform live cell imaging to allow the detection of PPIs at subcellular resolution and to analyze the effect of missense mutations more closely. Hence, HEK293 cells were transfected with control constructs encoding the tandem construct PA-mCit-NL or the NL luciferase alone, as well as with constructs encoding PA-mCit-Syntaxin-1 and the different NL-tagged Munc18 variants. Localization of the mCit-tagged fusion proteins was analyzed by fluorescence microscopy (Fig. 30f). After addition of the substrate, luminescence emission was imaged using a short (460 BP, 460±50 nm) and a long wavelength (530 BP, 530±50) emission filter. ImageJ was used to divide the intensities of the long and short wavelength images displayed as BRET ratio images (Fig. 30f). While the NL alone showed the highest signal intensity in the 460 BP filter, which is in accordance to its emission spectrum (Fig. 21d), the tandem construct PA-mCit-NL shows an emission shift towards the longer wavelength (535 BP) indicating the successful resonance energy transfer from the NL onto mCit (Fig. 30f). Similarly, the studied interaction between NL-Munc18 and PA-mCit-Syntaxin-1 shows a relatively high signal at the longer wavelength, which furthermore seems to accumulate at the cell membrane. Accordingly, the calculated BRET is the highest at the edge of the cell, indicating that the interaction indeed occurs at the plasma membrane. In contrast, the negative controls expressing NL-Munc18 and PA-mCit or NL and PA-mCit-Syntaxin-1 look similar to cells expressing the NL alone and thus show no BRET signal. Consistent to the measurements in the luminescent plate reader, the Munc18 double mutant (K46E/E59K) shows no BRET and Munc18 seems to be distributed mainly in the cytosol. However, the single point mutations in Munc18, K46E and E59K show a higher BRET than control cells that accumulates in perinuclear regions. Importantly, PA-mCit-Syntaxin-1 localization seems to be dependent on its interaction with Munc18. Only when co-expressed with NL-Munc18, PA-mCit-Syntaxin-1 travels to the plasma membrane, whereas co-expression of the NL alone or with either of the mutations, PA-mCit-Syntaxin-1 remains at a perinuclear location, which is consistent with previous results in double Munc18 knock-out PC12 cells overexpressing Munc18 variants fused to emerald-GFP[82].
Consequently, the BRIP assay is also suitable for live-cell microscopy allowing the investigation of the subcellular localization of PPIs and the effect of missense mutations or dynamic cellular processes.

(a)

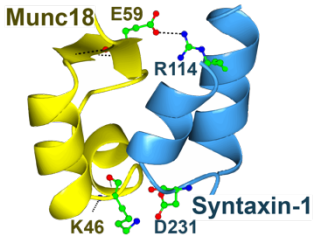

(b)

Interaction	K_d (nM)[1]	K_d (nM)[2]
Syntaxin-1 + Munc18 wt	1.4±0.3	23.3±11.1
Syntaxin-1 + Munc18 K46E	nd	181.2±46.4
Syntaxin-1 + Munc18 E59K	48.1±5.6	83.9±34.3
Syntaxin-1 + Munc18 K46E/E59K	nd	-

[1]Meijer et al., 2012; [2]Han et al., 2011

(c)

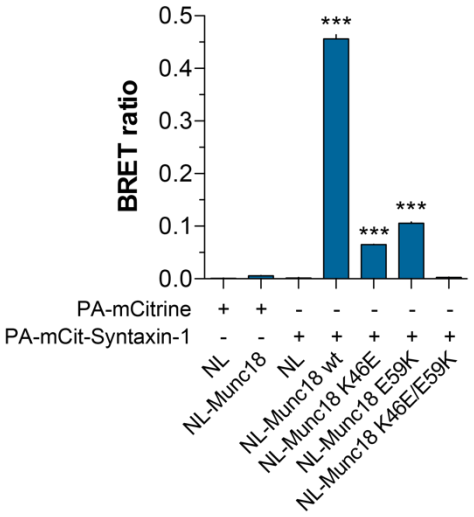

(d)

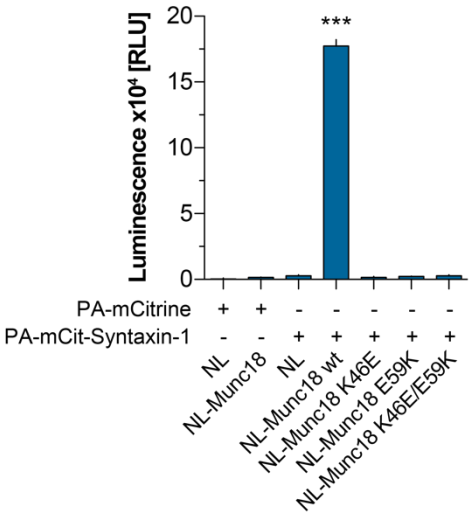

(e)

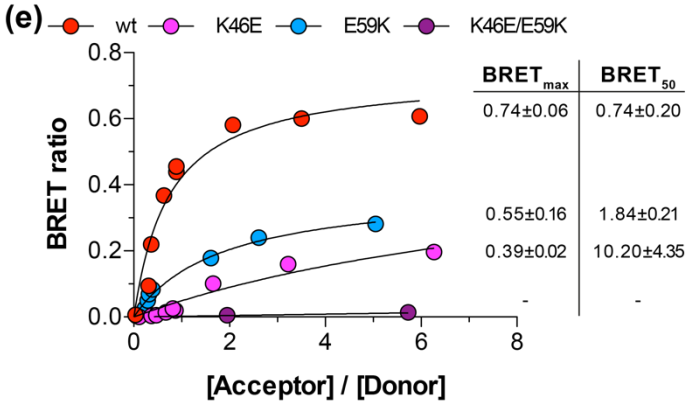

	$BRET_{max}$	$BRET_{50}$
wt	0.74±0.06	0.74±0.20
K46E	0.55±0.16	1.84±0.21
E59K	0.39±0.02	10.20±4.35
K46E/E59K	-	-

(f)

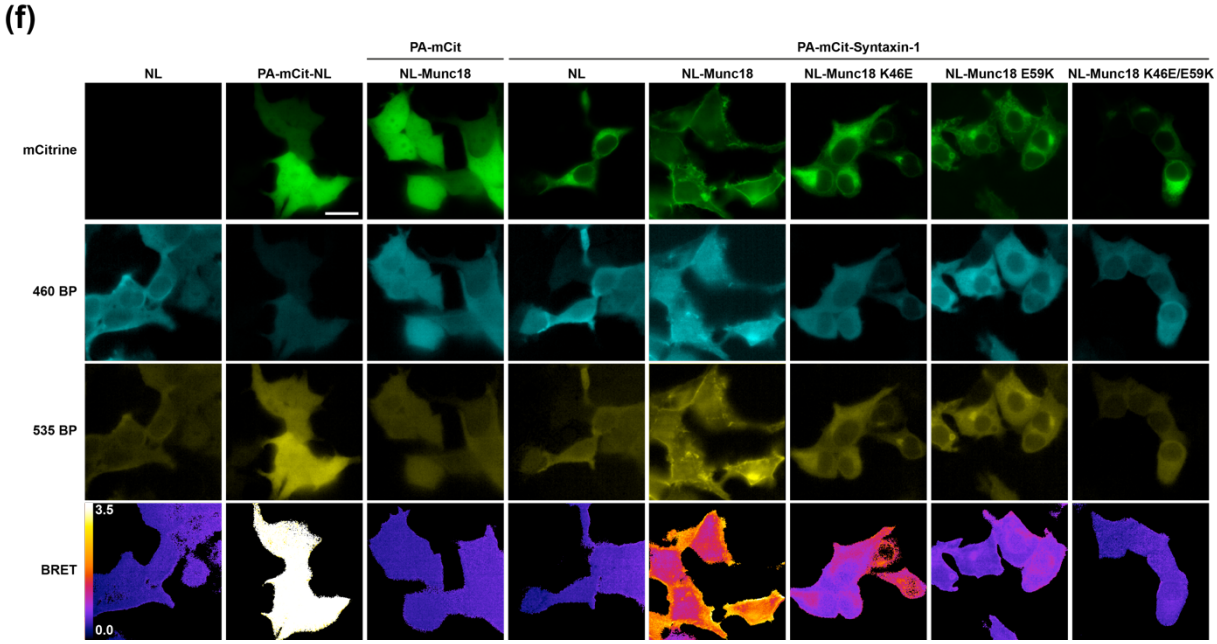

Fig. 30 (legend on next page)

Fig. 30: Quantification of the effects of missense mutations on interaction strength. (**a**) Interaction interface between Munc18 and Syntaxin-1 derived from the crystal structure of the protein complex (PDB: 3C98). Highlighted are crucial amino acids within the interface: K46 and E59 in Munc18, R114 and D231 in Syntaxin-1. (**b**) Overview of previously published missense mutations that influence the equilibrium dissociation constant of the interaction between Munc18 and Syntaxin-1 (nd: not determined; - : no interaction detected)[82,187]. (**c, d**) Analysis of the impact of missense mutations on interaction strength. The effects of missense mutations were monitored with the in-cell BRET (**c**) and after cell-free co-IP (**d**). (**e**) Donor saturation experiments to determine $BRET_{50}$ and $BRET_{max}$ values. Constant amounts of Munc18 fusion proteins were co-produced with increasing quantities of PA-mCit-Syntaxin-1. The approximate acceptor to donor molecular ratio was calculated as described in the methods section. Non-linear curve fitting was performed to obtain $BRET_{max}$ and $BRET_{50}$ values. (**f**) Live-cell imaging of HEK293 cells producing the indicated fusion proteins. mCitrine fluorescence was detected before substrate addition. After substrate addition, a short (460, cyan) and long (535, yellow) band-pass (BP) filter was used to detect the emitted luminescence at the respective wavelengths. BRET images were calculated by adjusting the background to 0, and dividing the 535 BP by the 460 BP images using ImageJ. BRET images were colored with the Fire lookup table (LUT). Scale bar = 20 µm. All experiments were performed three times and the results from one are displayed representatively. The bar diagrams and xy-graph display the mean ± SD from triplicate values.

5.2.7. Detecting the effects of small-molecules on PPIs using the BRIP assay

Modulating PPIs with small-molecules is a promising therapeutic approach to treat various disorders[178]. To assess whether the BRIP assay is suitable to detect the influence of small-molecules on PPIs, I analyzed the known compounds Navitoclax (ABT-263), Nutlin-3 and Rapamycin. Navitoclax, is an inhibitor of the anti-apoptotic Bcl-protein family that was discovered using structure-based design, parallel synthesis and nuclear-magnetic resonance (NMR)[191,192]. The mechanism how Navitoclax binds to BCL2L1 is similar to the interaction between BAD and BCL2L1. It binds to the same hydrophobic hot-spots within the binding surface of BCL2L1 like the BH3 α-helix of BAD, thereby displacing BAD, which induces apoptosis (Fig. 31a)[193]. To test the effect of Navitoclax on the interaction between BAD and BCL2L1 in intact cells, HEK293 cells were transfected with plasmids encoding the proteins NL-BCL2L1 and PA-mCit-BAD. 24 h after transfection, different concentrations of Navitoclax were added and after an additional 24 h incubation in-cell BRET was quantified. I found that the compound Navitoclax can inhibit the interaction between NL-BCL2L1 and PA-mCit-BAD in a concentration dependent manner. Through non-linear curve fitting an IC_{50} value of 735 nM was calculated, which represents the amount of Navitoclax necessary for a half-maximal PPI inhibition in intact cells (Fig. 31b).

Similarly, Nutlin-3 was identified in a screen for small-molecule antagonists of MDM2[194]. MDM2 is a negative regulator of p53 activity, that directly binds to the transactivation domain of p53 and additionally acts as an ubiquitin ligase promoting p53 degradation[195]. MDM2 is overexpressed in several cancer types, suggesting that the interaction with p53 is a promising target for drug intervention studies[196]. Nutlin-3 binds with three of its four hydrophobic side chains into the binding pockets of MDM2 that are normally occupied by p53 (Fig. 31c). To test the effect of Nutlin-3 on the interaction, I first generated plasmids encoding NL-MDM2 and PA-mCitrine-p53. Next, HEK293 cells were transfected with the respective plasmids and 24 h after

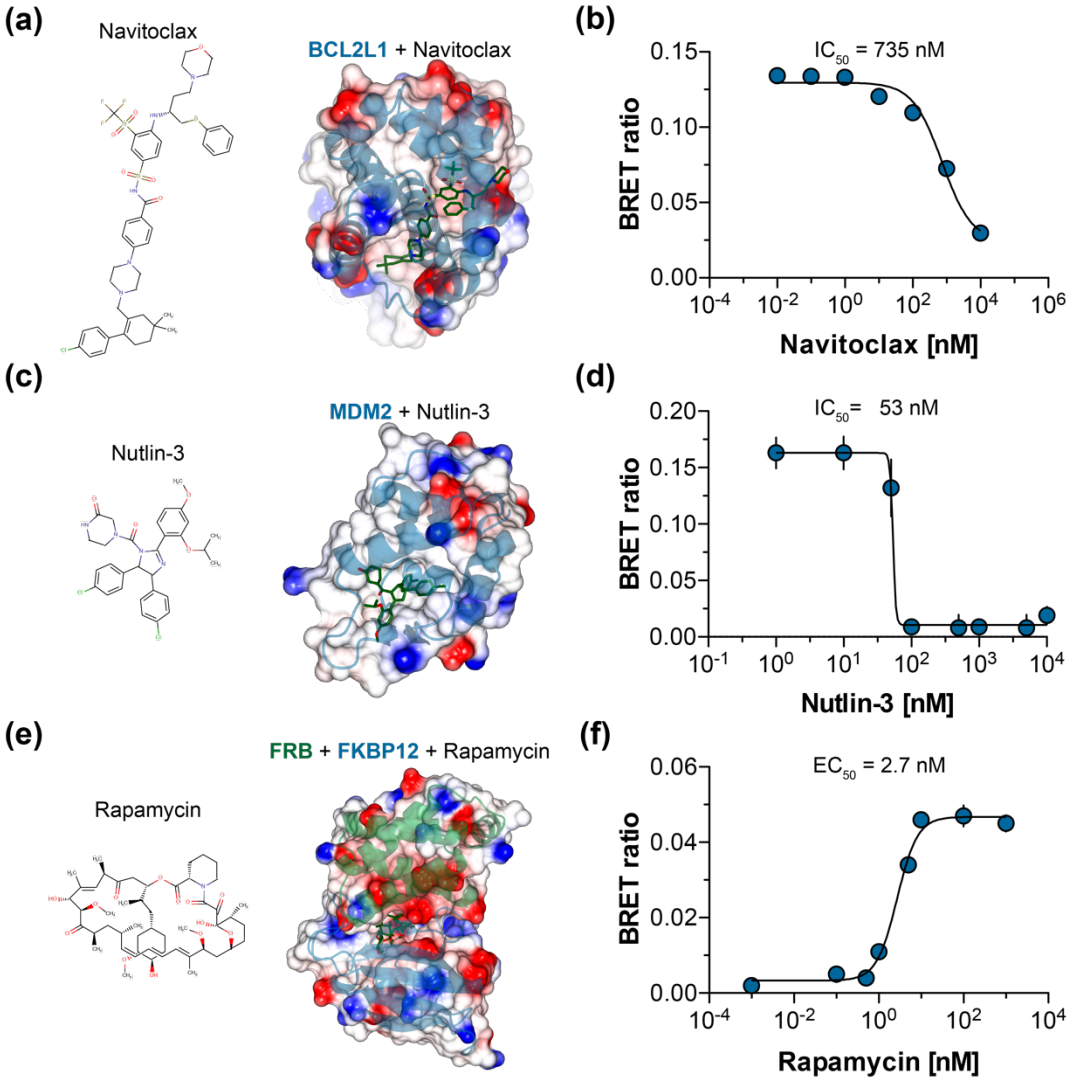

Fig. 31: In-cell BRET assays allow the detection of small-molecules that influence PPIs. (**a**) Chemical structure of Navitoclax (ABT-263) bound to BCL2L1 (PDB: 4LVT). (**b**) Cells were co-transfected with vectors expressing NL-BCL2L1 and PA-mCit-BAD and 24h later treated with indicated amounts of compound. After incubation of additional 24 h substrate was added and luminescence activity was measured. (**c**) Chemical structure of Nutlin-3 and its binding to MDM2 (PDB: 4HG7). (**d**) Cells were co-transfected with vectors expressing NL-MDM2 and PA-mCit-p53 and 24h after transfections treated with indicated amounts of compound. After 6h, substrate was added to the cells and the luminescence activity measured. (**e**) Chemical structure of Rapamycin and its cooperative binding to FKBP12 and the FRB domain of FRAP (PDB: 1NSG). (**f**) Cells were co-transfected with vectors expressing NL-FKBP12 and PA-mCit-FRB and 24h later treated with indicated amounts of compound. After incubation for additional 4h substrate was added and the luminescence activity measured. All experiments were performed three times and the results from one are displayed representatively. Data points are the means ± SD from three technical replicates that were fitted by non-linear regression and the IC_{50} or EC_{50} values calculated. All protein structures are displayed as protein surfaces colored by electrostatic potential and overlayed with the ribbon structure. Protein structures were visualized with CCP4MG™ and chemical structures with MarvinSketch (Chemaxon).

transfection different concentrations of Nutlin-3 were added. After an incubation for 6 h the luminescence was quantified and the BRET ratios were calculated. As before, a concentration dependent inhibition of the interaction between NL-MDM2 and PA-mCit-p53 was observed and the concentration where the half-maximal inhibition was reached determined (IC_{50}=53 nM; Fig. 31d).

Finally, I also tested the well characterized rapamycin-induced interaction between FKBP12 (peptidyl-prolyl cis-trans isomerase FKBP1A) and the FKBP12-rapamycin binding (FRB) domain of mTOR (Serine/threonine-protein kinase mTOR) in the BRIP assay[198,199]. Rapamycin was first identified as an antifungal compound that is naturally produced by the bacterium *Streptomyces hygroscopicus*[200]. Later, it was shown that rapamycin binds directly to FKBP12 and that this complex inhibits mTOR activity by binding to its FRB domain (Fig. 31e)[199,201]. To test the rapamycin-induced association of FKBP12 and the FRB domain of mTOR, I generated plasmids encoding NL-FKBP12 and PA-mCit-FRB that were subsequently transfected into HEK293 cells. 24 h after transfection I added Rapamycin to the cells for an additional 4 h after which I measured the luminescence activity and calculated the BRET ratio. As expected, I observed a concentration dependent induction of the FKBP12-rapamycin-FRB complex formation, for which I calculated a half maximal effective concentration (EC_{50}) of 2.7 nM (Fig. 31f).

Consequently, I could show that the BRET component of the BRIP assays is suitable to detect the effects of small-molecules on PPIs using the known compounds Navitoclax, Nutlin-3 and Rapamycin.

6. Discussion

In this study, I have established two luminescence-based PPI detection methods, DULIP and BRIP. Many cell-based PPI methods provide a quantitative data output when the proteins of interest interact, but lack information on the respective protein levels. Hence, the fraction of proteins actually engaged in an interaction cannot be estimated and therefore no quantitative interaction scores or relative binding strengths can be determined.

Thus, I have focused on the development of methods that generate quantitative interaction scores, which correlate ideally with the strength of an interaction. Both assays were benchmarked on similar PPI reference sets allowing a direct comparison of the two methods among each other as well as to other established PPI assays.

6.1. DULIP assays provide quantitative interaction scores for systematic interactome research[†]

The DULIP assay is a second-generation luminescence-based PPI detection method that is conceptionally similar to the previously described LUMIER method (see section 3.2.2.3)[108]. LUMIER assays have the disadvantage that the bait protein immunoprecipitation cannot be quantified in systematic co-immunoprecipitation experiments[108]. To overcome this limitation a modified LUMIER assay (LUMIER with BACON) was recently developed[22]. It enables the quantification of precipitated FLAG-tagged bait proteins in systematic studies using additional ELISAs. This improved method is clearly superior than the initially described LUMIER assay. Through the application of LUMIER with BACON a large number of novel client proteins interacting with the molecular chaperone Hsp90 have been successfully identified[22]. Furthermore, the method more recently helped to establish a comprehensive quantitative chaperone interaction network revealing the architecture of protein homeostasis pathways[114]. For systematic mapping of PPIs on a proteome-wide scale using LUMIER with BACON, however, the quantification of bait proteins need to be performed in addition to luciferase assays. This is labor intensive and requires additional resources, which is a drawback, especially in high-throughput applications of the procedure.

To overcome these limitations, I have developed DULIP, which enables the quantification of co-immunoprecipitated bait and prey proteins in a single sample. This is achieved through the co-expression of two luciferase-tagged proteins in mammalian cells: a *Renilla* luciferase (RL) fusion

[†] The discussion of the DULIP assay has been reused with modifications from the published version: Trepte, P. *et al.* DULIP: A Dual Luminescence-Based Co-Immunoprecipitation Assay for Interactome Mapping in Mammalian Cells. *Journal of Molecular Biology* 427, 3375–3388 (2015).

(bait) and a firefly luciferase (FL) fusion (prey) protein. Both can be quantified in the same reaction by using chemistries that allow the separate measurement of both luciferase activities.
The quantification of both fusion proteins in precipitated protein complexes allows the calculation of quantitative interaction scores. Normalization of these data using the fusion construct (PA-RL-FL) allows the estimation of relative protein amounts within a protein complex. Thus, DULIP assays are superior when large numbers of PPIs are to be systematically tested in mammalian cells with co-immunoprecipitations and result in the generation of a quantitative interaction score for PPIs.

A limitation of luminescence-based PPI methods like LUMIER is that the data output is often highly variable and that assays performed on different days and in different microtiter plates or laboratories yield inconsistent results. This inter- and intra-assay variability is most probably due to the fact that assay conditions like temperature, incubation time and transfection efficiency cannot be controlled perfectly in repeated experiments and that small changes in the concentrations of transiently transfected plasmids have a high impact on protein expression and therefore on the luminescence activity. To overcome these limitations, it is important to standardize the different steps of the PPI screening procedure and to include controls which can be used for data normalization on each assay plate. I found that the luminescence values, which were obtained with the control protein PA-RL-FL (Fig. 8b and c), are suitable for normalization of the luminescence output of tested PPIs. Through this normalization step and the calculation of background corrected normalized interaction ratios (cNIRs) for all tested PPIs, highly reproducible, quantitative interaction data were obtained (Fig. 11c), which can be directly compared between experiments. I suggest that the control protein PA-RL-FL could be used more generally for normalization of measured luminescence activities in order to produce widely comparable, quantitative PPI data.

In a recently reported study a pull-down PPI detection method with two luciferase tagged fusion proteins has been described[110]. In strong contrast to DULIP, streptavidin beads were utilized in this study for the precipitation of biotinylated HAVI-tagged bait proteins, limiting assay throughput. This has the disadvantage that initially a biotin ligase is required, which needs to be additionally co-produced in mammalian cells. However, this previously reported method has not yet been systematically benchmarked with well-defined PPI reference sets. It remains to be seen whether it is suitable for larger scale application and the generation of quantitative PPI data.

My studies with a positive PPI reference set composed of high-confidence PPIs from the HIPPIE database (selected PPIs with a HIPPIE score of ≥0.99) revealed that benchmarked DULIP assays

(cNIR cutoff ≥3) can detect known human PPIs with a sensitivity of ~80% (Fig. 11e). This was a surprisingly high and unexpected PPI detection rate as many previously published PPI detection assays recovered binary interactions from positive reference sets with success rates of 20-35%[4,70,74]. I therefore performed an additional assessment of the method's sensitivity using the hPRS reference set. The hPRS contains 92 PPIs that are supported by a great number of publications and involved proteins show a broad cellular localization[4]. Importantly, the hPRS has already been applied for the benchmarking of multiple PPI detection methods[70,74]. Interestingly, positive PPIs were recovered from the hPRS with a success rate of ~35% with the DULIP assay (Fig. 11e), which is in good agreement with previously published studies[70,74]. Thus, the benchmarking studies with hPRS and hRRS indicate that DULIP performs similarly well as other described PPI detection methods. The reason for the very high recovery rate of PPIs from the MDC-PRS (Fig. 11e) is still unclear. I suggest that the MDC-PRS compared to the hPRS is enriched for high-affinity interactions, which probably have a higher tendency to yield a positive score in a variety of different PPI detection methods.

Benchmarking studies to determine the specificity of an assay are typically performed using random PPI reference sets with the assumption that from a randomly chosen pool of protein pairs, the likelihood to find true-positive interactions is minimal[74]. Even though this assumption is reasonable, I suggest that reference sets of true-negative interactions are a noteworthy alternative. With the release of the Negatome database[‡] a resource of non-interacting proteins became available that could be used to generate true-negative PPI reference sets[184,202]. I started my project with the idea to generate the MDC negative reference set (MDC-NRS) from the Negatome database, from which I selected only protein pairs that had not been found to interact with at least three methods[184]. From the 30 tested PPIs, I only detected one interaction to be positive with the DULIP assay (Fig. 11g). However, as the initial MDC-NRS contains a limited number of PPIs, I suggest that a more comprehensive NRS based on the Negatome database would provide a meaningful set of negative PPIs that could be used more generally for benchmarking studies.

Systematic interactome mapping studies have been primarily performed with Y2H assays[10-12] wherefore methods are needed that can validate such interactions with high reliability. To estimate the quality of the DULIP assay to specifically validate Y2H interactions, I generated the Y2H-based reference sets Y2H-PRS, HI-PRS and Y2H-RRS. Thereby, the Y2H-PRS set contains 167 interactions that have been detected exclusively with Y2H assays and the HI-PRS was derived directly from the most recent Y2H generated human interactome dataset and contains

[‡] http://mips.helmholtz-muenchen.de/proj/ppi/negatome/

76 PPIs (HI-II-14). I detected in both reference sets interactions with a similar sensitivity (~37% and ~38%), which is comparable to the recovery rate of the hPRS (Fig. 16d). Thus, I suggest that high-quality Y2H interactions are of similar quality than PPIs detected with other methods. Furthermore, compared to recovery rates that were obtained with methods such as MAPPIT, PCA or wNAPPA[12], the DULIP assay yields a ~3-fold higher recovery rate, indicating that it is more suitable to validate Y2H PPIs than other currently used methods (Fig. 16f). However, the PPI detection methods MAPPIT, PCA and wNAPPA have been tested on different Y2H PPI sets than the DULIP assay wherefore a direct comparison of assay performance needs to be considered with caution. Still, it is noteworthy that the DULIP assay is fairly sensitive to recover Y2H PPIs, which are known to comprise of many low-affinity interactions[27,71,203-205], suggesting that the DULIP assay also detects such weak-transient interactions.

6.2. BRIP combines the principles of two mammalian cell-based PPI detection methods in one assay

Probably all PPI detection assays yield complementary, yet also distinct results when screening the same set of interactions[74,75]. In systematic benchmarking studies with the hPRS and hRRS, five distinct methods (LUMIER, MAPPIT, Y2H, PCA and wNAPPA) were used to compare their sensitivity and specificity to detect PPIs. From the 92 screened PPIs, only eight were detected with all five assays while a total of 47 were detected with at least one of the other assays[74]. Similar results were obtained comparing different Y2H systems[75]. Each of the ten Y2H variants used, detected a different subset of interactions in the hPRS and hRRS. Overall, 73 out of 92 PPIs in the hPRS could be detected, whereby none of the interactions could be detected with all ten Y2H variants[75]. These results highlight that PPI detection methods, which are based on very similar principles, can reveal different results when well-defined PPI reference sets are analyzed. Thus, comprehensive and reproducible PPI data sets with high confidence can only be obtained when interactions are detected with multiple methods.

To overcome these limitations, I developed and benchmarked in this study a PPI detection assay that combines the principles of two methods in one sequential assay – termed BRIP. The BRIP assay detects PPIs in mammalian cells using an in-cell bioluminescence resonance energy transfer (BRET) read-out and after lysis in cell extracts a co-immunoprecipitation (co-IP) read-out. It is highly innovative and the two independent read-outs increase sensitivity, flexibility and overall assay quality. This is achieved through the co-production of a NanoLuc luciferase fusion protein together with a protein A-mCitrine fusion protein. The recently development NanoLuc luciferase is an excellent substitute for currently used luciferases such as the *Renilla* luciferase. It

is suitable to increase the detection of BRET signals and to improve luminescence-based co-IP assays[145,163-165,206]. In combination with mCitrine, which is a brighter and monomeric form of the yellow fluorescent protein (YFP), the NanoLuc/mCitrine combination is an excellent donor and acceptor pair for BRET experiments in mammalian cells[126]. Furthermore, the quantification of mCitrine fluorescence and NanoLuc luminescence activity in co-IP experiments can be used to quantify protein complex formation. Thus, BRIP assays are superior to other mammalian cell based methods like BRET, FRET, LUMIER or DULIP, as PPIs are examined with two distinct PPI detection principles in one experiment.

Importantly, I assessed the assay's sensitivity and specificity to detect PPIs using the published hPRS and hRRS reference sets, which have been previously used to benchmark multiple other PPI detection methods[4,70,74]. I achieved a very high sensitivity of ~47% through the combination of two PPI read-outs in one method outperforming all other methods like LUMIER, Y2H, KISS and even DULIP (Fig. 26g, Fig. 27). The distance and orientation between donor (NanoLuc) and acceptor (mCitrine) are of great importance for BRET to occur. For example, the interaction between ORC2L (Origin recognition complex subunit 2) and ORC4L (Origin recognition complex subunit 4) from the hPRS was only detected with the co-IP read-out of the BRIP assay. Both proteins are components of the 270 kDa heterohexameric origin recognition complex (ORC) that is essential for DNA replication initiation[207]. With the recently solved crystal structure of the complex it became questionable whether ORC2L and ORC4L indeed directly interact, as they take up opposite positions in the heterohexameric complex[207]. This agrees with the marginal BRET signal of only 0.01 whereas a co-IP efficiency of ~12% suggests that ORC2L and ORC4L are present in a stable complex and do not interact directly (Fig. 28a). Hence, I suggest that PPIs that are not readily detectable with the in-cell BRET, e.g. as the distance between donor an acceptor is >10 nm or their dipole-dipole orientation is unfavorable, can still be part of a permanent complex that can be recapitulated with the cell-free co-IP read-out.

In total, PPIs within the hPRS that were detected with the BRIP assay contain highly diverse interactions of which some occur in the nucleus (e.g. LMNA and LMNB1)[208], at the mitochondrial membrane (e.g. BAD and BCL2L1)[209,210], the peroxisome (e.g. PEX19 and PEX3)[211], are phosphorylation dependent (CRK and PDGFRB)[212], involve transmembrane proteins (e.g. CXCL1 and IL8RB)[213] or occur between typical PPI domains (SH3-polyProline; SH2-phosphorylated tyrosine; e.g. CBLB and GRB2 as well as CRK and PDGFRB)[212,214]. This demonstrates that the BRIP assay can detect interactions between different classes of proteins occurring under various conditions or in different cellular compartments.

Consequently, under the applied conditions, the BRIP assay shows an excellent performance to discriminate between true and false PPIs. This was also supported by the recovery rate observed

for the AIRSv2, in which I could detect ~37% of the interactions with the BRIP assay. In contrast, only about ~30% of the interactions in the AIRS could be detected with the DULIP assay. However, the sensitivity of the luminescence-based co-IP read-out of the BRIP assay to detect PPIs in the hPRS and the AIRSv2 was with ~24% and ~17%, respectively, significantly lower compared to the DULIP assay, where ~35% and ~30% of interactions were recovered from the corresponding reference sets. This highlights that although the BRIP assay shows a high success rate for the in-cell BRET read-out, the cell-free co-IP component needs further assay optimizations. I suggest that by including the controls interactions NL and PA-mCit-Protein-X (control 4) and NL-Protein-Y and PA-mCit (controls 5) similar to the studies with the DULIP assay, the success rate of the co-IPs in the BRIP assay could be improved. Furthermore, technical parameters like transfected DNA amounts, microtiter plates used for the co-IPs or lysis buffer could be optimized to increase the assay's performance.

6.3. Detection of low-affinity PPIs with the DULIP and BRIP assays

Low-affinity interactions are often of transient nature, as they readily undergo changes in their oligomeric state[25]. They are characterized by equilibrium dissociation constants in the micromolar range and a lifetime of seconds[27]. Such weak transient interactions participate in the regulation of critical cellular functions, for example by phosphorylation of proteins or the ubiquitination of a substrate, thereby changing the activity of a protein[27]. However, their functional relevance is often unclear as such weak interactions are difficult to detect experimentally.

Immunoprecipitation-based methods have been traditionally unable to detect low-affinity PPIs as they are disrupted upon cell lysis or during the necessary washing steps to remove unspecific binding proteins[27]. However, such low-affinity interactions can be preserved by chemically cross-linking of protein complexes[215]. This can, however, also increase background binding of non-specific proteins. Nevertheless, cross-linking combined with affinity purification followed by mass-spectrometry helped to profile ubiquitinated proteins in yeast suggesting that it is a promising technique to detect weak protein complexes[216].

In general, methods like the Y2H, BiFC/BiLC or FRET have been considered more suitable to detect low-affinity PPIs, as the interactions are measured in intact cells[27]. In a systematic Y2H screen transient and permanent interactions were repeatedly tested four-times. While strong interactions were recovered multiple times, weak interactions were only detected once in repeated experiments[205]. Similarly, BiFC/BiLC and FRET assays have been used repeatedly to

detect low-affinity interactions in intact mammalian cells[36,217]. Recently, a modified FRET assay has been published that utilizes weak helper peptide interactions to generate high-efficiency FRET (hiFRET) signal, which allowed the detection of the transient interaction between Raf1 and B-Raf in HeLa cells[217].

To determine the efficacy of the DULIP and BRIP assays to detect low-affinity PPIs compared to high-affinity interactions, I newly generated the affinity-based interaction reference sets AIRS and AIRSv2. Both PPI sets contain a broad spectrum of lower and higher affinity interactions, but the AIRSv2 was broadened to cover 14 additional PPIs (Fig. 17a and Fig. 29a). I found that DULIP assays can detect PPIs in the AIRS with a sensitivity of ~30% (Fig. 17c and d), which is in agreement with the results of the other positive reference sets (MDC-PRS, hPRS, Y2H-PRS) and previously published data[4,70,74]. Even from the lower affinity interactions, I could still validate ~24% of the PPIs substantiating the assumption that the DULIP assay can also recover weak-transient PPIs (Fig. 17d).

In contrast, with the BRIP assay I could detect ~37% of the PPIs in the AIRSv2 highlighting again the higher sensitivity of the BRIP assay compared to the DULIP assay (Fig. 29d). I detected with the in-cell BRET read-out of the BRIP assay 34% of the interactions, while only 17% of the PPIs were obtained with the cell-free co-IP read-out. Interestingly, the difference in detection rate was mostly noticeable for low-affinity PPIs. While such weak interactions could be detected with a similar sensitivity as strong interactions in intact cells using the BRET component, mostly high-affinity interactions could be readily detected using the co-IP read-out (Fig. 29e). Together, the results from the studies with the affinity-based interaction reference sets suggest that low-affinity interactions are likely lost in co-IP experiments due to cell lysis and washing.

The generation of the AIRS, which exclusively contains PPIs with published dissociation constants also allowed me to assess whether the quantitative luminescence-based co-IP output values of DULIP (cNIRs) and BRIP assays (BRET ratio; co-IP efficiency) provide an indication of interaction strength. Using the PPIs from the AIRS, I found a weak correlation between cNIRs and published K_D values (Fig. 17d), indicating that the binding strength of interactions indeed influences the output of DULIP assays. Thus, the detection of PPIs with high cNIRs suggests that relatively stable protein complexes are formed in mammalian cells. However, more detailed validation studies with biochemical and biophysical methods are necessary to further substantiate the results obtained with DULIP assays.

Similarly, I analyzed whether the interaction scores I obtained for PPIs in the AIRSv2 with the BRIP assay correlate to published *in vitro* K_D values. BRET ratios obtained from measurements in intact cells showed no correlation to K_D values, probably because the efficiency of energy transfer is inversely proportional to the sixth power of distance, which has a greater impact on the

detection of PPIs than the interaction affinity (Fig. 29f). In contrast, the calculated co-IP efficiencies showed a weak correlation to the previously reported dissociation constants, indicating that the amount of protein that is co-immunoprecipitated is strongly dependent on the binding affinity, which is in good agreement to the results obtained with the DULIP assay (Fig. 29h). The BRET component of the BRIP assay, on the other hand, has been shown to be suitable to determine $BRET_{50}$ values, which are a measure of relative in-cell binding strengths[168]. However, whether $BRET_{50}$ values indeed correlate more generally to *in vitro* dissociation constants needs to be tested in more comprehensive studies using the AIRSv2.

6.4. Investigation of the effects of missense mutations on binary interactions using DULIP and BRIP assays

Several lines of experimental evidence indicate that mutations changing the amino acid composition of proteins (missense point mutations and in-frame insertions or deletions) can influence their binding affinity[82,218,219]. For example, various point mutations within the DNA mismatch repair protein MLH1 (MutL protein homolog 1) have been reported to cause colorectal cancer[220]. Furthermore, MLH1 is known to bind PSM2 (Mismatch repair endonuclease PMS2) and interestingly, disease mutations within the PMS2-interaction domain of MLH1 disrupt the binding of MLH1 to PMS2. However, disease mutations outside of the interaction interface or non-disease related single nucleotide polymorphisms (SNPs) have no impact on the MLH1-PMS2 interaction[218].

While such changes can be detected with qualitative methods like the Y2H[218], to reliably monitor the magnitude of mutation-dependent effects on the interaction strength quantitative PPI detection methods are required. Here, I examined whether DULIP and BRIP assays are capable of detecting the influence of point mutations on the interaction strength of PPIs. I focused my efforts on the well-characterized interaction between Munc18 and Syntaxin-1, which plays a functional role in synapse communication[82,187,221]. Previous biochemical studies have demonstrated that the point mutations K46E and E59K decrease the binding affinity of this interaction[82], suggesting that such a reduction of binding affinity should also be detectable with quantitative assays like DULIP or BRIP.

Indeed, my studies confirmed the effects of K46E and E59K on the interaction between Munc18 and Syntaxin-1 (Fig. 18c), demonstrating that the methods are well suitable for monitoring the impact of point mutations on interaction strength and have a high potential for the investigation of disease-causing mutations. However, the DULIP assay was not able to distinguish between the effects of the single point mutations (K46E and E59K, reduced affinity) and the double mutation

(K46E/E59K, loss of interaction). Accordingly, the co-IP component of the BRIP assay showed similar results. However, the second component of the BRIP assay, the in-cell BRET read-out was able to detect the differences between the mutations. This is in good agreement with observations that the effects of single point mutations can also be detected in intact yeast or mammalian cells using the Y2H or FRET assays (Fig. 18d, e and f). However, in yeast colony-growth assays the decrease in affinity was not reflected in a reduced growth highlighting the limitations of qualitative methods to detect the effects of mutations on interaction strength (Fig. 18d and e). This suggests that low-affinity interactions are potentially lost during cell lysis supporting my observations with the affinity-based interaction reference sets.

Importantly, the BRET component of the BRIP assay allows us to study the effects of point mutations in greater detail. On the one hand, donor saturation experiments can be performed to determine $BRET_{50}$ values that can be used to quantify the effects of mutations on interaction strength (Fig. 30e). On the other hand, bioluminescence imaging studies can be performed that allow the investigation of the localization of PPIs in cells. For example, I found that Munc18 is necessary for Syntaxin-1 to travel to the plasma membrane, confirming previously published results[82]. In contrast, Munc18 mutants with reduced or absent affinity were unable to support the plasma membrane localization of Syntaxin-1 (Fig. 30f). Importantly, these data highlight the great utility of the BRIP assay to analyze different parameters of an interaction such as the effect of point mutations on the interaction strength and potential changes in subcellular localization.

6.5. Application of the BRET component of the BRIP assay for the investigation of the effects of small molecules on PPIs

Modulating PPIs by small-molecules has emerged as a therapeutic intervention strategy in cancer and other human diseases over the past 20 years[178]. Today, several small-molecules that inhibit PPIs are in clinical trials[196]. Most compounds, however, have been structurally optimized based on the originally discovered small molecules. For example, the small-molecule Nutlin-3 is an inhibitor of the p53-MDM2 interaction that binds competitively to MDM2[194]. The structurally optimized analogue of Nutlin-3, RG7112 leads to cell cycle arrest and apoptosis by activating the p53 pathway and is now in clinical trials[222]. Similarly, ABT-737 was initially identified as an inhibitor of the BAD-BCL2L1 interaction to induce apoptosis[191], but only its analogue ABT-263 is orally available and is now in clinical trials[192,223]. Different to Nutlin-3 and ABT-263, which inhibit their respective interactions, Rapamycin (also known as sirolismus) stimulates the interaction between mTOR and FKBP12[198]. Rapamycin, identified 40 years ago as a fungicide, is

nowadays used as an immunosuppressant to prevent the rejection after organ transplantation[200,224].

The potential of small-molecule inhibitors of PPIs (SMIPPIs) has also been recognized by the pharmaceutical industry and by 2018 sales are already predicted to reach over $800 million per year[225]. However, current high-throughput chemical screening (HTS) approaches face difficulties in recreating complex biological systems in an *in vitro* system. Transmembrane or membrane associated proteins are difficult to isolate and posttranslational modifications or essential cofactors can be missing that are potentially important for an interaction to occur[196]. Therefore, HTS approaches to monitor the efficacy of small-molecules on PPIs in mammalian cells are needed.

To evaluate the effects of compounds on PPIs in intact cells, I tested known small-molecule modifiers with the in-cell BRET component of the BRIP assay. For two of the tested compounds, Nutlin-3 and Rapamycin, I determined IC_{50} or respectively EC_{50} concentrations in the low nanomolar range similarly to previously reported results (Fig. 31b and c)[145,194]. However, the IC_{50} value for Navitoclax (ABT-263) was with 735 nM significantly higher compared to the published *in vitro* data of <0.5 nM (Fig. 31a)[192]. This could be caused either by an inefficient uptake of the small molecule into the cell, or might be the result from relatively high expression levels of the two interacting proteins, wherefore consequently more compound is necessary to inhibit the interaction.

In summary, I could show the applicability of the BRET component of the BRIP assay to detect the effects of small-molecules on PPIs with a potential application for HTS. However, the co-IP read-out of the BRIP assay could also be used to test the efficacy of small-molecules on PPIs and could provide complementary information on the effects of compounds on isolated protein complexes. Such studies could allow the investigation of interactions that are difficult to test with purified proteins *in vitro*.

6.6. The innovative PPI detection methods DULIP and BRIP are suitable for quantitative high-throughput PPI screening

With the development of high-throughput methods to systematically map PPIs, numerous protein interaction networks have been generated and the overall knowledge about PPIs has increased dramatically[3]. According to the BioGrid database over 230,000 PPIs have been reported for ~20,000 unique human proteins, suggesting that for almost every human protein at least one interaction is already known. For the 59 listed species more than 415,000 PPIs connecting 56,000 unique proteins have been reported (BioGrid v3.4.130)[226]. However, most current databases

contain only positive results from proteins that indeed interact, neglecting reports on interactions that do not occur[183,184,226]. Information on non-interacting proteins are, however, important to understand the molecular mechanisms of cellular pathways, to estimate the false-positive rate of PPI-detection methods and to train computational algorithms to predict PPIs[202]. Furthermore, current approaches to filter out the most relevant PPIs for a given question, rely on computational prioritization through integrating a whole array of large-scale datasets[12,227]. This includes expression (RNA, protein) and localization (subcellular, tissue) data as well as data about biological functions and domain compatibility[12,183,228,229]. Even though this computational approach is very valuable, a direct prioritization of PPIs based on an experimentally derived interaction score would increase the molecular understanding of biological processes and allow the establishment of hierarchies between interacting proteins. Therefore, interactome research is demanding for the development of novel tools to map protein-protein interactions[230].

I developed two innovative and quantitative methods, DULIP and BRIP. Both assays were established and benchmarked on positive and negative reference sets in medium-throughput, highlighting their general suitability to detect PPIs in larger-scale studies. DULIP and BRIP assays provide multiple quantitative data outputs (protein amounts produced and protein complexes formed) allowing the calculation of quantitative interaction scores. Hence, both assays are suitable for the quantitative analysis of PPIs, enabling the detection of PPIs with different interaction strengths and the analysis of the impact of mutations, therapeutic molecules or posttranslational modifications on the association of proteins.

I propose that BRIP assays are superior to DULIP assays since the two-component system of the BRIP assay increases sensitivity and flexibility to analyze PPIs. The co-IP component can be used similarly to the DULIP assay, to detect protein complexes. Especially for the detection of two proteins that do not interact directly this is an advantage as they are potentially bridged by endogenous proteins. Furthermore, the co-IP read-out offers a big advantage for interactions where the donor and acceptor have an unfavorable orientation and can therefore not be detected with the in-cell BRET. The BRET component, on the other hand, allows to monitor PPIs in intact cells, which seems to increase the sensitivity to detect low-affinity interactions. Furthermore, the co-localization of fusion proteins can be monitored by bioluminescence and fluorescence imaging, and the calculation of $BRET_{50}$ values provides an indication of binding strengths. The BRIP assay similar to the DULIP assay is applicable for high-throughput screenings as measurements of fluorescence and luminescence activities in cells as well as in cell-extracts and co-immunoprecipitates can be readily automated. However, to perform DULIP and BRIP assays in high-throughput, a robotic assay-platform has to be established, which allows the automated transfection of cells, luminescence measurement and co-immunoprecipitation.

7. Materials and Methods[§]

7.1. Plasmid construction

DULIP vectors pPA-RL-GW and pFL-V5-GW for the production of N-terminal fusions were described previously[231]. For the generation of vectors encoding C-terminal fusion proteins the sequences coding for *Renilla* luciferase (RL) and protein A (PA) were amplified from pPA-RL-GW with primers 5′-GCTGTAAAGCTTATGGCTTCCAAGGTGTACG-3′, 5′-GCTGTAGAATTCCTGC TCGTTCTTCAGCAC-3′ (RL), 5′-GCTGTAGAATTCGGCTCGGGCTCGATGGTGGACAACAAAT TCAAC-3′ and 5′-GCTGTACTCGAGTCACGAGTTCGCGTCTACTTTC-3′ (PA). The resulting PCR fragments were cloned simultaneously in pcDNA3.1(+) (Invitrogen) via HindIII/EcoRI/XhoI restriction sites to obtain pRL-PA. Firefly-V5 cDNA was PCR amplified from pFL-V5-GW with primers 5′-GCTGTAAAGCTTATGGAAGACGCCAAAAACATAAAG-3′ and 5′-GCTGTACTCGA GTCACGTAGAATCGAGACCGAGGAG-3′ and cloned in pcDNA3.1(+) via HindIII/XhoI restriction sites to obtain pFL-V5. Subsequently, the Gateway cassette (GW) was PCR-amplified from pBTM116-D9 and cloned into pReni-PA and pFire-V5 using NheI/HindIII restriction sites, resulting in pGW-RL-PA and pGW-FL-V5. The plasmid pdECFP-C1 was kindly provided by Dr. Stefan Wiemann (DKFZ, Heidelberg). The plasmid pdEYFP-C1 was obtained from a commercial supplier (ImaGenes). As the gateway destination vectors that contain no insert but the gateway cassette show a weak expression in HEK293 cells, I removed the gateway cassette from the vectors pdEYFP-C1 and pdECFP-C1. An oligonucleotide adaptor 5′-ATAAGTGGCCGGCCACT-3′ was self-annealed and cloned into pdEYFP-C1 and pdECFP-C1 via BspEI/XbaI restriction sites to obtain pdEYFP and pdECFP.

N- and C-terminal BRIP destination vectors were generated based on the pcDNA3.1(+) vector (Invitrogen). For acceptor (bait) vectors pPA-mCit-GW, pGW-mCit-PA and pPA-mCit the coding sequences for mCitrine (mCit) and PA were amplified from pmTq2-DVED-mCit (kindly provided by Dr. Raik Grünberg) and pPA-RL-GW, respectively. For N-terminal fusions, PA was amplified using the primers 5′-GCTGTAGCTAGCACCATGGTGGACAACAAATTCAAC-3′ and 5′- GCTGT AGAATTCCGAGTTCGCGTCTACTTTC-3′ and mCit using the primers 5′-GCTGTAGAATTCGGC TCGGGCTCGGTATCGAAAGGTGAAGAGC-3′ and 5′-GCTGTAAAGCTTACCAGCGGCTGTG ACAAATTC-3′. For C-terminal fusions, PA was amplified using the primers 5′-GCTGTAGAATTC

[§] The methods section of the DULIP assay has been reused with modifications from the published version: Trepte, P. *et al.* DULIP: A Dual Luminescence-Based Co-Immunoprecipitation Assay for Interactome Mapping in Mammalian Cells. *Journal of Molecular Biology* 427, 3375–3388 (2015).

GGCTCGGGCTCGGTGGACAACAAATTCAAC-3′ and GCTGTACTCGAGTCACGAGTTCGCGT CTACTTTC-3′ and mCit using the primers 5′-GCTGTAAAGCTTGTATCGAAAGGTGAAGAGC-3′ and 5′-GCTGTAGAATTCACCAGCGGCTGTGACAAATTC-3′. For the control vector pPA-mCit, that contains a stop-codon after the mCit coding sequence the following primers were used to amplify the PA 5′-GCTGTAGCTAGCACCATGGTGGACAACAAATTCAAC-3′ and 5′- GCTGT AGAATTCCGAGTTCGCGTCTACTTTC-3′ and mCit using the primers 5′-GCTGTAGAATTCGGC TCGGGCTCGGTATCGAAAGGTGAAGAGC-3′ and 5′- GCTGTAAAGCTTTCACGCCAGAATG CGTTCG-3′.

For donor/prey vectors pNL-GW, pGW-NL and pNL the NanoLuc coding sequence was amplified from pNL1.1 (Promega). For N-terminal fusions, cmyc-NanoLuc was amplified using the primers 5′-GCTGTAGCTAGCACCATGGAACAGAAACTGATCTCTGAAGAAGACCTGGTCT TCACACTCGAAG-3′ and 5′-GCTGTAAAGCTTCGCCAGAATGCGTTCG-3′ and for C-terminal fusion the primers 5′- GCTGTAAAGCTTGTCTTCACACTCGAAG-3′ and 5′- GCTGTACTCGAGT CACAGGTCTTCTTCAGAGATCAGTTTCTGTTCCGCCAGAATGCGTTCG-3′. For the control vector pNL the following primers were used to amplify the cmyc-NanoLuc 5′-GCTGTAGCTAGC ACCATGGAACAGAAACTGATCTCTGAAGAAGACCTGGTCTTCACACTCGAAG-3′ and 5′-GCT GTAAAGCTTTCACTGCTCGTTCTTCAGCAC-3′.

For all destination vectors, the resulting PCR fragments were cloned simultaneously in pcDNA3.1(+) (Invitrogen) via NheI/EcoRI/HindIII restriction sites for control vectors or N-terminal fusion vectors and via EcoRI/XhoI/HindIII for C-terminal fusion vectors.

Following, the gateway cassette was amplified from pGW-RL-PA for N-terminal fusion vectors pPA-mCit-GW and pNL-GW using the primers 5′-GCTGTAAAGCTTACAAGTTTGTACAAAAAA GCTGAAC-3′ and 5′-GCTGTACTCGAGTTACACCACTTTGTACAAGAAAGCTGA-3′ and for C-terminal fusions vectors pGW-mCit-PA and pGW-NL using the primers 5′-GCTGTAGCTAGCAC AAGTTTGTACAAAAAAGCTGAACGAGAAACG-3′ and 5′- GCTGTAAAGCTTCACCACTTTGTA CAAGAAAGCTGAACGAG-3′. The resulting PCR fragments were cloned in the above generated vectors containing the PA, mCit or NL coding sequences. For N-terminal fusion vectors the restriction sites HindIII/XhoI and for C-terminal fusion vectors NheI/HindIII were used.

To generate the vector pPA-NL, the PA-tag was amplified using the primers 5′- GCTGTAGCTAGC ACCATGGTGGACAACAAATTCAAC-3′ and 5′- GCTGTAGAATTCCGAGTTCGCGTCTACTTTC-3′ and the NanoLuc using the primers 5′- GCTGTAGAATTCACCATGGAACAGAAACTGATCTCT GAAGAAGACCTGGTCTTCACACTCGAAG-3′ and 5′-GCTGTAAAGCTTTCACTGCTCGTTCTT CAGCAC-3′. The resulting PCR products were cloned simultaneously in pcDNA3.1(+) (Invitrogen) via NheI/EcoRI/HindIII restriction sites.

For the following vectors, cDNA inserts were PCR amplified and the resulting fragments inserted into entry vectors by BP recombination reaction. For generation of pPA-RL-mCherry, pFL-

mCherry and pPA-RL-FL, the coding sequence of mCherry was amplified from pmCherryGW (Invitrogen) and the firefly luciferase coding sequence from pFL-V5-GW. For cloning of mCherry the primers 5′-GGGGACAAGTTTGTACAAAAAAGCAGGCTTCATGGTGAGCAAGGGCGAGG AGGATAAC-3′ and 5′-GGGGACCACTTTGTACAAGAAAGCTGGGTCCTTGTACAGCTCGTCC ATGCCG-3′ and for the firefly luciferase the primers 5′-GGGGACAAGTTTGTACAAAAAAGCAG GCTTCGCCACCATGGAAGACGCCAAAAAC-3′ and 5′-GGGGACCACTTTGTACAAGAAAGCT GGGTCCACGGCGATCTTTCCGCCCTTC-3′ were used.

To generate the pPA-mCit-NL fusion construct, the coding sequence of the NanoLuc was amplified using the primers 5′-GGGGACAAGTTTGTACAAAAAAGCAGGCTTCGCCACCATGG TCTTCACACTCGAAG-3′ and 5′- GGGGACCACTTTGTACAAGAAAGCTGGGTCCGCCAGAAT GCGTTCGCAC-3′. The Syntaxin-1 fragment that lacks the Syntaxin-1 transmembrane domain was generated using the primers 5′-GGGGACAAGTTTGTACAAAAAAGCAGGCTTCATGAAGG ACCGAACCCAGGA-3′ and 5′-GGGGACCACTTTGTACAAGAAAGCTGGGTCCGCCTTGCTCT GGTACTTG-3′ for PCR amplification (1-261 aa, Syntaxin-1ΔTM) from the entry clone RZPDo834H065D. The FRB domain encoding the amino acids 2021-2113aa of MTOR was amplified by PCR using the primers 5′-GGGGACAAGTTTGTACAAAAAAGCAGGCTTCACCAT GATCCTCTGGCATGAAATGTG-3′ and 5′- GGGGACCACTTTGTACAAGAAAGCTGGGTGTTT GCTAATGCGACGAAAC-3′ from the vector backbone FR-20-Che~Sp1 that was kindly provided by Dr. Raik Grünberg (Center for Genomic Regulation, Barcelona).

The resulting PCR fragments were shuttled into pDONR221 (Invitrogen) with the BP clonase (Invitrogen) according to the manufacturers instructions to generate entry plasmids (pDONR221-mCherry, pDONR221-FL, pDONR221-NL, pDONR221-Syntaxin-1ΔTM, pDONR221-FRB) that can be used for shuttling into destination plasmids by LR recombination reaction. To introduce the single and double point mutants K46E and E59K into Munc18, the 5′-phosphorylated primers 5′-ATGACAGACATCATGACCGAGG-3′ and 5′-CTCGCAGCAGGAGGACAGCATC-3′ (K46E) as well as 5′-GATATCAACAAGCGCCGAGAGC-3′ and 5′-CTTCACAATTGTGATGCCCTCG-3′ (E59K) were used for PCR amplification of pDONR221-Munc18 entry vector. PCR products were ligated using the T4-ligase (Thermo Scientific). The Munc18 wild-type cDNA from the pENTRZ-Munc18 construct that was kindly provided by Prof. Dr. Matthijs Verhage (Vrije Universiteit, Amsterdam).

Available or newly generated entry vectors utilized to generate expression plasmids, were shuttled into the destination vector pPA-RL-GW, pFL-V5-GW, pBTM116-D9, pACT4-DM, pdEYFP-C1, pdECFP-C1, pPA-mCit-GW, pGW-mCit-PA, pNL-GW or pGW-NL by LR recombination reaction according to the manufacturers instructions (Invitrogen). The obtained expression vectors are summarized in Table 2 and Table 7. Similarly, cDNAs encoding the proteins for the MDC positive and negative reference sets (Table 3), the CCSB reference sets

(Table 4) as well as AIRS (Table 6) were shuttled into the vectors pPA-RL-GW, pGW-RL-PA, pFL-V5-GW or pGW-FL-V5 using the LR clonase. Accordingly, for the BRIP assay the cDNAs encoding the proteins for the CCSB reference sets hPRS and hRRS (Table 8) and the AIRSv2 (Table **9**) were shuttled into the vectors pPA-mCit-GW, pGW-mCit-PA, pNL-GW and pGW-NL.

7.2. Cell culture and transfection

The human embryonic kidney cell line 293 (HEK293) was grown in low-glucose (1g/L) DMEM (Gibco®, ThermoFisher) for DULIP and FRET experiments and in high-glucose (4.5 g/L) for BRIP assays. Both were supplemented with 10% heat inactivated fetal bovine serum (Gibco®, ThermoFisher) and grown at 37°C and 5% CO_2. Cells were subcultured every 3-4 days and transfected with linear polyethyleneimine (25 kDa, Polysciences) using the reverse transfection method according to the manufacturer's instructions. For BRIP transfections, cells were seeded in phenol-red free, high-glucose DMEM media (Gibco®, ThermoFisher) supplemented with 10% heat inactivated fetal bovine serum. Transfections were performed with a total DNA amount of 200 ng per well in a 96-well plate. If expression plasmid concentration was below 200 ng/well, pcDNA3.1(+) was used as carrier DNA to fill the total DNA amount to 200 ng. For FRET and luminescence measurements the cells were examined 24 or 48 h after transfection.

7.3. MDC positive and negative reference set creation

The MDC positive reference set (MDC-PRS) was generated from literature known PPIs using the HIPPIE (*H*uman *I*ntegrated *P*rotein-*P*rotein Interaction r*E*ference) database[183]. HIPPIE provides a scoring algorithm that allows a distinction between higher and lower confidence literature PPIs. For the creation of a positive reference set 25 high confidence PPIs with a HIPPIE score of ≥0.99 were chosen, of which 23 were finally tested in DULIP assays. To compile a MDC negative reference set (MDC-NRS) the Negatome database (v1.0) was searched for PPIs that were investigated with at least 3 independent methods but not detected in either of them. The cDNAs encoding 30 protein pairs were randomly selected and shuttled successfully into DULIP destination plasmids. The CCSB reference sets hPRS and hRRS were previously described[74].

7.4. Yeast two-hybrid based reference set creation

The Y2H positive reference set (Y2H-PRS) was generated from literature known PPIs using the HIPPE database. HIPPIE also allows to filter for interactions according to the methods with which

the interactions were detected and how many publications describe a given PPI. For the Y2H-PRS I selected only PPIs that were identified exclusively with the Y2H and have been described in exactly two publications. For the human interactome positive reference set (HI-PRS), I randomly selected 76 PPIs from the 13,944 PPIs in the HI-II-14 dataset to which I had cDNA clones available[12]. To generate a Y2H-based random reference set (Y2H-RRS) I randomly arranged the cDNA clones available in the Neuroproteomics-MDC cDNA bank to generate ~$1.9x10^8$ potential protein combinations. From those, I selected only genes that have been successfully used in Y2H studies from which I randomly selected 139 PPIs. The cDNAs encoding the proteins pairs for the Y2H-PRS, HI-PRS and Y2H-RRS were shuttled into DULIP destination plasmids for systematic interaction screening using the DULIP assay.

7.5. Affinity-based interaction reference set creation

The affinity-based reference set (AIRS) and AIRSv2 was generated from literature PPIs with known dissociation constants using PDBbind[185] and the Protein-Protein Interaction Affinity Database 2.0 (PPIA, http://bmm.crick.ac.uk/~bmmadmin/Affinity/)[186]. For the AIRS 12 PPIs from PDBbind and 47 PPIs from PPIAD were selected to cover a broad range of protein binding affinities. The cDNAs encoding 57 selected PPIs were shuttled into DULIP expression plasmids and tested in DULIP assays. Similarly, For the AIRSv2 18 PPIs from PDBbind and 53 PPIs from PPIAD were selected to cover a broad range of protein binding affinities. The cDNAs encoding 71 selected PPIs were shuttled into BRIP expression plasmids and subsequently tested in BRIP assays.

7.6. DULIP assay

HEK293 cells were reversely transfected in clear 96 well microtiter plates at a density of $3.75x10^4$ cells per well. 48 h after transfection cells were lysed in 100 µl HEPES lysis buffer (50 mM HEPES, 150 mM NaCl, 10% glycerol, 1% NP-40, 0.5% Deoxycholate, 20 mM NaF, 1.5 mM $MgCl_2$, 1 mM EDTA, 1 mM DTT, 1 U Benzonase, protease inhibitor cocktail (Roche, EDTA free), 1 mM PMSF) for 30 min at 4°C. Production of PA-RL- and FL-tagged fusion proteins was monitored by measuring the respective luciferase activities in crude cell lysates in 384-well microtiter plates. 10 µl of the cell lysate were added to 20 µl PBS (Gibco®, ThermoFisher) and 10 min after the addition of 10 µl Dual-Glo® luciferase reagent (Promega) the firefly activity (FL_{IN}) was measured using an Infinite® M1000 (Tecan) plate reader. To stop the firefly luciferase activity and to measure the *Renilla* luciferase activity (RL_{IN}), 10 µl of the Dual-Glo® Stop & Glow® reagent (Promega) were added and after 15 min of incubation the activity was measured. In parallel,

50 µl of the cell lysate were incubated for 3 hours at 4°C in IgG pre-coated 384-well microtiter plates. Plates were coated with sheep gamma globulin (Jackson ImmunoResearch, 013-000-002), blocked with 1% BSA in carbonate buffer (70 mM $NaHCO_3$, 30 mM Na_2CO_3, pH 9.6) before they were incubated with rabbit anti-sheep IgGs (Jackson ImmunoResearch, 313-005-003) in carbonate buffer overnight. After cell lysate incubation, all wells were washed three times with HEPES lysis buffer before 30 µl of PBS were added to each well. Measurement of firefly (FL_{OUT}) and *Renilla* (RL_{OUT}) luminescence activity was performed using an Infinite® M1000 (Tecan) plate reader.

7.7. DULIP data analysis

To identify weakly expressed preys and weakly immunoprecipitated baits, the measured firefly or *Renilla* luciferase activities were log_2-transformed and the distribution of measured luminescence values for the controls 1 or 2 (Fig. 8a) was binned (Fig. 12b and c). As the expression and immunoprecipitation profiles followed Gaussian distributions, I used a Gaussian curve fit to determine the mean (µ) and standard deviation (σ) of the firefly and *Renilla* luciferase activities (Fig. 12b). Preys were classified as not expressed when the mean luminescence of the three technical replicates was smaller µ-3σ. Similarly, bait immunoprecipitation efficiency was analyzed and proteins were classified as not immunoprecipitated when the mean luminescence of the three technical replicates was smaller µ-3σ (Fig. 12c). To exclude unspecific background binding of prey proteins to antibodies or assay plates, FL_{OUT} values of PPIs of interest were divided by FL_{OUT} values of control PPIs (control 1 and 2, see Fig. 8a and Fig. 9). This revealed luminescence-based interaction control ratios (ICRs) for each PPI of interest, which were used for quality assessment of PPI detection experiments. In systematic interaction detection studies only PPIs of interest with ICRs ≥ 3 were further analyzed. Using the luciferase immunoprecipitation ratios (LIRs) of control 3 (see Fig. 8a) the normalized immunoprecipitation ratios (NIRs) of PPIs of interest were calculated. The NIR is a measure for the success of prey protein co-immunoprecipitation in relation to the success of bait protein immunoprecipitation. Finally, to correct for unspecific background binding, I calculated the background corrected NIRs (cNIRs). The higher NIR value obtained for control 1 or 2 was subtracted from the calculated NIR of the interaction of interest (see also Fig. 8a and Fig. 9).

7.8. FRET assay

HEK293 cells were reversely transfected in black 96-well microtiter plates at a density of 6×10^4 cells per well. 24 h after transfection cells were fixed with 4% paraformaldehyde in PBS and washed twice with PBS. Fluorescence signals were detected with the Infinite® M1000 (Tecan) plate reader: donor channel [excitation (Ex)/emission (Em): 435 nm/475 nm], acceptor channel (Ex/Em: 500 nm/530 nm) and FRET channel (Ex/Em: 435nm/530 nm). For processing of raw data, the fluorescence intensities obtained from cells transfected with empty vector were used. Signals in the FRET channel (DA) were corrected for spectral bleedthrough of the donor (c_D) and acceptor cross-excitation (c_A) using samples expressing only the donor (pdECFP) or acceptor (pdEYFP) constructs. Finally, corrected signals in the FRET channel were normalized to the acceptor signals. In brief, FRET efficiency (E_{Aapp}) in % was calculated as follows:

$$E_{Aapp}=\frac{(DA - c_D \times DD - c_A \times AA)}{AA} \qquad (7)$$

with DD = donor channel signal and AA = acceptor channel signal[134].

7.9. Y2H assay

The Y2H interaction mating assays were performed as previously described[10]. Briefly, bait and prey constructs were transformed into yeast strains L40ccua (MATa) and L40ccα (MATα), respectively. For interaction mating, 100 µl cultures of MATa yeast strains were transferred into 96-well microtiter plates and mixed with 100 µl cultures of MATα yeast strains. The yeast mixtures were then spotted onto YPD agar plates using a spotting robot (KBiosystem). After mating for 48 h at 30°C, the yeast colonies were automatically picked and transferred into 96-well microtiter plates containing selective liquid medium (SDII-Leu-Trp). Finally, for selection of PPIs diploid yeasts were spotted in parallel onto SDIV (-Leu-Trp-Ura-His) and SDII (-Leu-Trp) selective agar plates. After 5-6 days of incubation at 30°C, agar plates were imaged and yeast growth assessed by visual inspection.

7.10. BRIP assay

HEK293 cells were reversely transfected in white 96 well microtiter plates at a density of $4.5\text{x}10^4$ cells per well. In general DNA amounts of donor and acceptor were used at a 1:10 ratio, with 10 ng donor and 100 ng of acceptor. 48 h after transfection mCitrine fluorescence was measured in intact cells (Ex/Em: 500 nm/530 nm) followed by the addition of 5 µM coelenterazine-h

(NanoLight, 301). Cells were incubated for additional 10 min and the total, short-WL and long-WL luminescence measured using no filter, the BLUE1 (370-480 nm) and GREEN1 (520-570 nm) filter at 100-1000 ms integration time. Fluorescence and luminescence were measured using an Infinite® M200, M1000 or M1000Pro (Tecan) microplate reader.

After luminescence measurements in intact cells, the cells were lysed in 80 µl HEPES-phospo lysis buffer (50 mM HEPES, 150 mM NaCl, 10% glycerol, 1% NP-40, 0.5% Deoxycholate, 20 mM NaF, 1.5 mM $MgCl_2$, 1 mM EDTA, 1 mM DTT, 1 U Benzonase, protease inhibitor cocktail (Roche, EDTA free), 1 mM PMSF, 25 mM glycerol-2-phosphate, 1 mM sodium orthovanadate, 2 mM sodium pyrophosphate) for 30 min at 4°C. Production of PA-mCit- and NL-tagged fusion proteins production was monitored by measuring the fluorescence activity ($mCit_{IN}$) or the respective luciferase activity (NL_{IN}) in crude cell lysates in white, small-volume 384-well microtiter plates. To 10 µl of the cell lysate, coelenterazine-h was added to a final concentration of 5 µM and the luminescence activity measured as before in a microplate reader. In parallel, 15 µl of the cell lysates were incubated for 3 hours at 4°C in IgG pre-coated small-volume 384-well microtiter plates. Plates were coated with sheep gamma globulin (Jackson ImmunoResearch, 013-000-002) in carbonate buffer (70 mM $NaHCO_3$, 30 mM Na_2CO_3, pH 9.6) for 3 h at room-temperature, blocked with 1% BSA in carbonate buffer before they were incubated with rabbit anti-sheep IgGs in carbonate buffer (Jackson ImmunoResearch, 313-005-003) overnight at 4°C. Cell-lysates were incubated for 3 h at 4°C, after which, all wells were washed three times with HEPES-phospho lysis buffer and the mCit fluorescence activity measured ($mCit_{OUT}$) as above. Afterwards, 15 µl of PBS containing 5 µM coelenterazine-h were added to each well and the NanoLuc luminescence activity (NL_{OUT}) measured as described above.

For donor saturation experiments, constant amounts of donor were co-transfected with increasing amounts of acceptor DNA at a maximum donor:acceptor ratio of 1:100 (2 ng donor, 200 ng acceptor). The BRIP assay was performed as described above, with the difference that NanoGlo® (Promega) at a concentration of 1:500 was used as the substrate for the NanoLuc. Acceptor to donor ratios were estimated by first calculating the ratio of the fluorescence to luminescence activities of the PA-mCit-NL tandem construct, where the respective activities, correspond to a molecular ratio of 1:1. Next, to estimate the approximate molecular ratio of acceptor to donor for the studied interaction, the ratio of the fluorescence to luminescence activities for the different samples were calculated and normalized to the corresponding tandem construct ratio.

Luminescence scan measurements were performed in a Tecan Infinite® M100Pro from 350-650 nm with 2 or 5 nm step width and an integration time of 100 or 1000 ms. NanoGlo® was used as substrate and all scans were normalized to the emission at 460 nm.

BRIP assays with small-molecules were performed the following: HEK293 cells were co-transfect with NL-BCL2L1 and PA-mCit-BAD, NL-MDM2 and PA-mCit-p53 or NL-FKBP12 and PA-mCit-

FRB. Increasing concentrations of Navitoclax (ABT-263, Selleckchem, S1001), Nutlin-3 (Sigma, N6287) or Rapamycin (Santa Cruz, 3504A) were added to cells 24 h after transfection. Luminescence measurements using 5 µM coelenterazine-h were performed after an additional incubation for 24 h (Navitoclax), 6 h (Nutlin-3) or 4 h (Rapamycin).

7.11. BRIP data analysis

The BRET ratios from in-cell BRET or cell lysate measurements were calculated the following:

$$\text{BRET ratio} = \frac{\text{LWL}}{\text{SWL}} - D_{NL} \tag{8}$$

with LWL and SWL being the detected luminescence at the long (520-570 nm) and the short (370-480 nm) wavelengths, respectively. Thereby, D_{NL} is the donor bleed-through, which is the ratio of the luminescence at the LWL to the SWL determined in cells expressing only the NanoLuc or PA-NanoLuc:

$$D_{NL} = \frac{LWL_{NL}}{SWL_{NL}} \tag{9}$$

For the cell-free co-IP read-out, the co-IP efficiency in % was calculated the following:

$$\text{co-IP efficiency [\%]} = \frac{NL_{OUT}}{1.5 \times NL_{IN}} \times 100 \tag{10}$$

with NL_{OUT} being the total luminescence measured after co-IP and NL_{IN} the luminescence measured in cell lysates. The Z'-factor was calculated from BRET measurements using the parameters mean (µ) and standard deviations (σ) of the positive (p, PA-mCit-NL) and negative controls (n, NL + PA-mCit) the following:

$$\text{Z'-factor} = 1 - \frac{3(\sigma_p+\sigma_n)}{\left|\mu_p-\mu_n\right|} \tag{11}$$

7.12. Western blots

For Western-blotting, cells were lysed for 30 min at 4°C in HEPES-phospho lysis buffer, the protein concentrations determined using the Pierce™ BCA assay (Thermo Scientific) and the same amount of protein loaded on a NuPAGE™ Novex™ 4-12% Bis-Tris precast polyacrylamide gel (ThermoFisher) according to the manufacturer's instructions. Following, proteins were transferred onto a nitrocellulose membrane (GE, 10401197) using a wet blotting system from BioRad®. The membrane was blocked in 3%-milk PBS-T (phosphate-buffer saline, 0.05% Tween) for 60 min at room-temperature and incubated with primary antibody in 3%-milk PBS-T over-night at 4°C.

Antibodies were detected with appropriate HRP (horse-radish-peroxidase) coupled secondary anti-rabbit (1:2000, Sigma A0545) antibody by detecting the chemiluminescence after addition of WesternBright Quantum (Advansta, 12042-D20) in a Fujifil LAS-3000. The primary antibodies used were: anti-BCL2L1 (rabbit, 1:1000, Cell Signaling 2764) and anti-BAD (rabbit, 1:1000, Cell Signaling 9268).

7.13. Live-cell imaging

HEK293 cells were seeded at a low-density with $3x10^4$ cells per well in an ibidi® µ-Slide 8-well tissue culture dish using X-tremeGENE (Roche®) according to the manufacturers instructions. 48 h after transfection imaging was performed using an Olympus® inverted microscope IX83 with an Andor Zyla camera and a 60x objective. A Dual-View™ adapter (Optical Insights®) between microscope und camera was equipped with a short (460/50, Chroma®) and long (535/50, Chroma®) wavelength filter. Imaging was performed in tyrodes buffer (100 mM NaCl, 5 mM KCl, 2 mM HEPES, 2 mM $CaCl_2$, 4 mM $MgCl_2$, 33 mM glucose) with 1:50 NanoGlo® (Promega). Before substrate addition, mCitrine was excited with a LED excitation system (CoolLED® pE, 2%) using a YFP-excitation filter (Olympus®, AHF F48-003 ET-Set) and the emitted fluorescence detected with the above mentioned Dual-View™ filter and Andor Zyla camera with an exposure time of 100 ms. Bioluminescence imaging started immediately after substrate addition with an exposure time of 3000 ms.

Images were processed with ImageJ (http://imagej.nih.gov/ij/). Fluorescence images were background corrected and the contrast adjusted for each image individually as relative intensities were not compared between these images but only the localization of mCit-tagged proteins was analyzed. The single bioluminescence image that contains the short (460 BP) and long wavelength (530 BP) signal was split into two separate images. These two images were stacked and aligned using the StackReg plugin for ImageJ[232]. Next, the images were smoothed by median filtering, background subtracted and thresholded on luminescence intensities. To calculate the BRET ratio on a pixel-by-pixel basis, the 530 BP image was divided by the 460 BP using the image calculator and presented in pseudocolor for better visualization.

8. Supplementary Information

Table 2: Constructs used for systematic DULIP interaction screening. PA: ProteinA; RL: *Renilla* luciferase; FL: firefly luciferase; GW: gateway cassette; X: Bait; Y: Prey

Plasmid	Fusion protein	Symbol	Gene ID	Uniprot ID
pPA-RL-GW	ProteinA-*Renilla*-X			
pGW-RL-PA	X-*Renilla*-ProteinA			
pFL-V5-GW	Firefly-Y			
pGW-FL-V5	Y-Firefly			
pPA-RL-FL	ProteinA-*Renilla*-Firefly			
pPA-RL-mCherry	ProteinA-*Renilla*-mCherry			
pFL-mCherry	Firefly-mCherry			
pPA-RL-BAD	ProteinA-*Renilla*-BAD	BAD	572	Q92934
pFL-BCL2L1	Firefly-BCL2L1	BCL2L1	598	Q07817
pPA-RL-Syntaxin-1	ProteinA-*Renilla*-Syntaxin-1	STX1A	6804	Q16623
pFL-Munc18	Firefly-Munc18	STXBP1	25558	P61765
pFL-Munc18 K46E	Firefly-Munc18 K46E	STXBP1	25558	P61765
pFL-Munc18 E59K	Firefly-Munc18 E59K	STXBP1	25558	P61765
pFL-Munc18 K46E/E59K	Firefly-Munc18 K46E/E59K	STXBP1	25558	P61765
pBTM116-D9	LexA-X			
pBTM116-D9-mCherry	LexA-mCherry			
pBTM116-D9-BAD	LexA-BAD	BAD	572	Q92934
pBTM116-D9-Munc18	LexA-Munc18	STXBP1	25558	P61765
pBTM116-D9-Munc18 K46E	LexA-Munc18 K46E	STXBP1	25558	P61765
pBTM116-D9-Munc18 E59K	LexA-Munc18 E59K	STXBP1	25558	P61765
pBTM116-D9-Munc18 K46E/E59K	LexA-Munc18 K46E/E59K	STXBP1	25558	P61765
pACT4-DM	GAL4-Y			
pACT4-DM-mCherry	GAL4-mCherry			
pACT4-DM-BCL2L1	GAL4-BCL2L1	BCL2L1	598	Q07817
pACT4-DM-Syntaxin-1 ΔTM	GAL4-Syntaxin-1 ΔTM	STX1A	6804	Q16623
pdEYFP-C1	EYFP-X			
pdEYFP-C1-BCL2L1	EYFP-BCL2L1	BCL2L1	598	Q07817
pdEYFP	EYFP			
pdECFP-C1	ECFP-Y			
pdECFP-C1-EYFP	ECFP-EYFP			
pdECFP-C1-BAD	ECFP-BAD	BAD	572	Q92934
pdECFP	ECFP			

Table 3: DULIP results from the MDC-PRS and MDC-NRS. ICR: internal control ratio; cNIR: corrected normalized interaction ratio; Exp: Experiment; NA: not available (no expression/immunoprecipitation); PREY: no prey expression; IP: no immunoprecipitation; NC: not constructed; ND: not determined.

	Set a								Set b								Set a+b		
interaction	ICR Exp1	ICR Exp2	mean cNIR Exp1	sem cNIR Exp1	mean cNIR Exp2	sem cNIR Exp2	results Exp1	result Exp2	ICR Exp1	ICR Exp2	mean cNIR Exp1	sem cNIR Exp1	mean cNIR Exp2	sem cNIR Exp2	results Exp1	result Exp2	result Exp1	result Exp2	Set
ARHGEF7 + PAK1							NC	NC	34,7	30,2	10,3	0,3	9,8	0,4	POS	POS	POS	POS	MDC-PRS
CDK2 + CKS1B	11,1	8,5	1,7	0,1	1,6	0,1	NEG	NEG	4,2	3,1	0,0	0,4	-0,3	0,2	NEG	NEG	NEG	NEG	MDC-PRS
CDK5R1 + CDK5	210,6	189,5	112,4	6,3	93,7	5,2	POS	POS	206,0	172,7	41,0	3,2	39,1	4,3	POS	POS	POS	POS	MDC-PRS
HSPA8 + STUB1							NC	NC	9,3	8,9	4,6	0,5	5,8	1,5	POS	POS	POS	POS	MDC-PRS
MCM3 + MCM7	7,4	7,3	5,7	0,5	5,3	0,4	POS	POS	3,9	3,5	9,7	0,4	8,5	0,7	POS	POS	POS	POS	MDC-PRS
MCM5 + MCM2	3,2	2,4	3,6	0,8	ND	ND	POS	NEG	1,2	1,1	ND	ND	ND	ND	NEG	NEG	POS	NEG	MDC-PRS
MCM5 + MCM3	12,1	11,7	34,1	0,9	25,8	1,6	POS	POS	52,9	49,6	28,9	2,4	25,8	2,0	POS	POS	POS	POS	MDC-PRS
MXD1 + MAX	4,8	4,3	28,6	1,6	21,5	0,3	POS	POS	8,0	8,1	15,7	0,2	19,2	4,4	POS	POS	POS	POS	MDC-PRS
MXI1 + MAX	NA	4,5	NA	NA	43,4	4,8	IP	POS	13,6	16,4	23,1	1,2	33,8	3,8	POS	POS	POS	POS	MDC-PRS
NFKB1 + NFKB1	269,7	228,2	48,3	3,7	46,6	1,6	POS	POS	284,1	216,3	58,0	2,0	45,4	0,5	POS	POS	POS	POS	MDC-PRS
ORC4 + ORC2	1,5	1,1	ND	ND	ND	ND	NEG	NEG	0,8	0,7	ND	ND	ND	ND	NEG	NEG	NEG	NEG	MDC-PRS
ORC4 + ORC5	11,4	8,2	6,0	0,3	4,4	0,9	POS	POS	8,8	6,8	5,7	0,6	5,9	1,1	POS	POS	POS	POS	MDC-PRS
ORC5 + ORC2	4,4	3,2	4,4	1,0	3,8	0,4	POS	POS	4,8	4,3	4,0	0,1	3,6	0,3	POS	POS	POS	POS	MDC-PRS
PTS + PTS	59,0	49,9	77,0	11,2	78,6	1,3	POS	POS	82,0	71,3	73,6	4,5	68,8	5,5	POS	POS	POS	POS	MDC-PRS
RAD23B + PSMD4							NC	NC	7,0	5,9	0,0	0,0	0,0	0,0	NEG	NEG	NEG	NEG	MDC-PRS
RFC5 + RFC4	50,7	42,8	43,2	1,1	33,5	0,7	POS	POS							NC	NC	POS	POS	MDC-PRS
RRM1 + RRM2	7,5	6,1	15,2	2,4	11,6	0,7	POS	POS	12,1	9,2	-17,8	0,2	-14,7	0,7	NEG	NEG	POS	POS	MDC-PRS
RUVBL2 + RUVBL1	300,6	233,4	132,6	20,3	132,5	9,9	POS	POS	2,3	2,3	ND	ND	ND	ND	NEG	NEG	POS	POS	MDC-PRS
SAE1 + UBA2	455,3	408,5	31,6	2,0	31,6	4,7	POS	POS	129,3	110,5	43,5	2,8	45,3	2,8	POS	POS	POS	POS	MDC-PRS
SF3A3 + SF3A1	1,3	1,3	ND	ND	ND	ND	NEG	NEG	0,7	0,5	ND	ND	ND	ND	NEG	NEG	NEG	NEG	MDC-PRS
SIAH1 + SIAH1	NA	NA	NA	NA	NA	NA	IP	IP	NA	NA	NA	NA	NA	NA	IP	IP	NA	NA	MDC-PRS
U2AF2 + U2AF1	1,1	1,4	ND	ND	ND	ND	NEG	NEG	9,2	9,8	4,5	0,3	5,2	0,9	POS	POS	POS	POS	MDC-PRS
UBE2I + SUMO1							NC	NC	42,0	29,9	7,6	0,9	7,6	0,4	POS	POS	POS	POS	MDC-PRS
ATF4 + DPF2	2,3	2,0	ND	ND	ND	ND	NEG	IP	9,1	4,5	3,1	0,4	2,3	0,4	POS	NEG	POS	NEG	MDC-NRS
ATF4 + DUSP6	NA	NA	NA	NA	NA	NA	IP	IP	0,7	0,6	ND	ND	ND	ND	NEG	NEG	NEG	NEG	MDC-NRS
ATF4 + GDI1	0,7	0,5	ND	ND	ND	ND	NEG	IP	0,6	0,6	ND	ND	ND	ND	NEG	NEG	NEG	NEG	MDC-NRS
ATF4 + GNL1	0,8	0,7	ND	ND	ND	ND	NEG	IP	0,4	0,2	ND	ND	ND	ND	NEG	NEG	NEG	NEG	MDC-NRS
ATF4 + MLX	0,5	0,5	ND	ND	ND	ND	NEG	IP	2,4	1,7	ND	ND	ND	ND	NEG	NEG	NEG	NEG	MDC-NRS
ATF4 + PTP4A1	1,5	1,3	ND	ND	ND	ND	NEG	NEG	5,5	3,7	0,6	0,2	0,5	0,1	NEG	NEG	NEG	NEG	MDC-NRS
DPF2 + GDI1							NC	NC	1,2	0,8	ND	ND	ND	ND	NEG	NEG	NEG	NEG	MDC-NRS
DPF2 + GNB2							NC	NC	1,3	1,0	ND	ND	ND	ND	NEG	NEG	NEG	NEG	MDC-NRS
DPF2 + NFKBIA							NC	NC	0,9	0,8	ND	ND	ND	ND	NEG	NEG	NEG	NEG	MDC-NRS
GDI1 + CNOT3	2,2	2,0	ND	ND	ND	ND	NEG	NEG	5,4	4,8	2,6	0,5	2,5	0,2	NEG	NEG	NEG	NEG	MDC-NRS
GDI1 + DUSP6	3,2	3,0	1,8	0,5	2,0	0,5	NEG	NEG	4,6	3,7	3,0	0,6	2,6	0,4	NEG	NEG	NEG	NEG	MDC-NRS
GNB2 + ZNF212	6,1	4,5	3,2	0,1	2,9	0,1	POS	NEG							NC	NC	POS	NEG	MDC-NRS
GNL1 + CNOT3	2,9	2,1	ND	ND	ND	ND	NEG	NEG							NC	NC	NEG	NEG	MDC-NRS
ID3 + GDI1	6,0	5,0	2,5	0,2	3,0	0,1	NEG	NEG	3,5	2,6	0,5	0,1	ND	ND	NEG	NEG	NEG	NEG	MDC-NRS
ID3 + PTP4A1	2,8	2,7	ND	ND	ND	ND	NEG	NEG	4,2	2,9	0,5	0,1	ND	ND	NEG	NEG	NEG	NEG	MDC-NRS
MLX + FHL2	2,3	1,7	ND	ND	ND	ND	NEG	NEG	3,4	2,3	1,2	0,2	ND	ND	NEG	NEG	NEG	NEG	MDC-NRS
MLX + GNL1	1,6	1,1	ND	ND	ND	ND	NEG	NEG	2,9	1,9	ND	ND	ND	ND	NEG	NEG	NEG	NEG	MDC-NRS
MLX + ZNF331	4,0	2,6	0,9	0,1	ND	ND	NEG	NEG	0,7	0,8	ND	ND	ND	ND	NEG	NEG	NEG	NEG	MDC-NRS
NFKBIA + ID3	3,1	2,4	1,0	0,1	ND	ND	NEG	NEG	3,6	3,1	1,0	0,2	0,9	0,1	NEG	NEG	NEG	NEG	MDC-NRS
PTP4A1 + DPF2	2,8	1,8	ND	ND	ND	ND	NEG	NEG	1,8	1,4	ND	ND	ND	ND	NEG	NEG	NEG	NEG	MDC-NRS
PTP4A1 + GDI1	4,6	3,2	2,0	0,3	1,7	0,1	NEG	NEG	2,6	2,3	ND	ND	ND	ND	NEG	NEG	NEG	NEG	MDC-NRS
PTP4A1 + NFKBIA	3,3	2,7	1,2	0,3	ND	ND	NEG	NEG	4,1	3,5	2,6	0,3	2,1	0,2	NEG	NEG	NEG	NEG	MDC-NRS
PTP4A1 + ZNF3	3,3	1,9	0,5	0,1	ND	ND	NEG	NEG	NA	NA	NA	NA	NA	NA	IP	IP	NEG	NEG	MDC-NRS
RND1 + CNOT3	1,4	1,2	ND	ND	ND	ND	NEG	NEG	2,6	1,9	ND	ND	ND	ND	NEG	NEG	NEG	NEG	MDC-NRS
RND1 + FHL2	2,2	1,8	ND	ND	ND	ND	NEG	NEG	2,0	1,5	ND	ND	ND	ND	NEG	NEG	NEG	NEG	MDC-NRS
RND1 + GNB2	2,8	2,2	ND	ND	ND	ND	NEG	NEG	3,1	2,4	1,2	0,2	ND	ND	NEG	NEG	NEG	NEG	MDC-NRS
RND1 + MLX	3,3	2,2	0,8	0,1	ND	ND	NEG	NEG	1,7	1,5	ND	ND	ND	ND	NEG	NEG	NEG	NEG	MDC-NRS
ZNF212 + CNOT3							NC	NC	1,7	1,8	ND	ND	ND	ND	NEG	NEG	NEG	NEG	MDC-NRS
ZNF3 + CNOT3	NA	NA	NA	NA	NA	NA	IP	IP	5,0	3,1	1,2	0,2	0,8	0,1	NEG	NEG	NEG	NEG	MDC-NRS
ZNF331 + CNOT3	0,7	0,6	ND	ND	ND	ND	NEG	NEG	3,1	2,3	0,3	0,0	ND	ND	NEG	NEG	NEG	NEG	MDC-NRS

Table 4: DULIP results from the hPRS and hRRS. ICR: internal control ratio; cNIR: corrected normalized interaction ratio; Exp: Experiment; NA: not available (no expression/immunoprecipitation); PREY: no prey expression; IP: no immunoprecipitation; NC: not constructed; ND: not determined.

Interaction	set a								set b								set a+b		Set
	ICR Exp1	ICR Exp2	mean cNIR Exp1	sem cNIR Exp1	mean cNIR Exp2	sem cNIR Exp2	result Exp1	result Exp2	ICR Exp1	ICR Exp2	mean cNIR Exp1	sem cNIR Exp1	mean cNIR Exp2	sem cNIR Exp2	result Exp1	result Exp2	result Exp1	result Exp2	
AKT1 + PDPK1	3,4	3,8	4,9	0,2	4,7	0,2	POS	POS	1,6	1,5	ND	ND	ND	ND	NEG	NEG	POS	POS	hPRS
AKT1 + TCL1A							NC	NC	0,3	0,3	ND	ND	ND	ND	NEG	NEG	NEG	NEG	hPRS
ARF1 + ARFIP2	2,4	2,3	ND	ND	ND	ND	NEG	NEG	4,2	3,6	0,7	0,1	0,5	0,1	NEG	NEG	NEG	NEG	hPRS
ARHGAP1 + BNIP2	3,0	3,1	0,6	0,3	0,6	0,2	NEG	NEG							NC	NC	NEG	NEG	hPRS
ATF3 + DDIT3	31,0	32,5	52,2	8,2	44,1	1,4	POS	POS	NA	NA	NA	NA	NA	NA	PREY	PREY	POS	POS	hPRS
B2M + HLA-A	1,2	1,1	ND	ND	ND	ND	NEG	NEG	2,4	1,8	ND	ND	ND	ND	NEG	NEG	NEG	NEG	hPRS
B2M + HLA-B	0,5	0,7	ND	ND	ND	ND	NEG	NEG	0,5	0,6	ND	ND	ND	ND	NEG	NEG	NEG	NEG	hPRS
B2M + HLA-C	NA	NA	NA	NA	NA	NA	IP	IP	1,2	0,7	ND	ND	ND	ND	NEG	NEG	NEG	NEG	hPRS
BAD + BCL2L1	135,7	136,6	105,1	17,7	81,6	6,1	POS	POS	111,0	129,9	80,0	11,4	76,6	4,5	POS	POS	POS	POS	hPRS
BAK1 + BCL2L1	30,8	33,9	69,5	1,1	59,5	0,6	POS	POS	44,6	48,2	23,9	1,6	23,2	0,8	POS	POS	POS	POS	hPRS
BDNF + NTF5	0,9	1,0	ND	ND	ND	ND	NEG	NEG	0,6	0,5	ND	ND	ND	ND	NEG	NEG	NEG	NEG	hPRS
BIRC4 + CASP3	0,2	0,2	ND	ND	ND	ND	NEG	NEG	NA	NA	NA	NA	NA	NA	IP	IP	NEG	NEG	hPRS
BIRC4 + CASP7	0,7	0,9	ND	ND	ND	ND	NEG	NEG	2,1	2,1	ND	ND	ND	ND	NEG	NEG	NEG	NEG	hPRS
BIRC4 + CASP9	0,5	0,5	ND	ND	ND	ND	NEG	NEG	2,0	2,2	ND	ND	ND	ND	NEG	NEG	NEG	NEG	hPRS
CASP2 + CRADD	1,7	2,3	ND	ND	ND	ND	NEG	NEG	1,9	3,0	ND	ND	1,5	0,1	NEG	NEG	NEG	NEG	hPRS
CBLB + GRB2	2,5	2,6	ND	ND	ND	ND	NEG	NEG	10,7	13,7	14,6	0,1	11,0	1,8	POS	POS	POS	POS	hPRS
CCND3 + CDK6	94,4	95,2	55,7	3,1	51,2	8,6	POS	POS	24,8	45,2	21,2	5,3	21,8	1,8	POS	POS	POS	POS	hPRS
CD2 + CD58	1,6	1,2	ND	ND	ND	ND	NEG	NEG	3,3	2,9	0,9	0,1	ND	ND	NEG	NEG	NEG	NEG	hPRS
CDKN1A + CCNA1	4,4	9,0	6,7	0,4	11,9	1,3	POS	POS							NC	NC	POS	POS	hPRS
CDKN1B + CCNA1	12,9	15,9	5,5	1,9	7,2	1,4	POS	POS	5,4	6,9	20,3	1,8	22,2	0,2	POS	POS	POS	POS	hPRS
CEBPG + FOS	1,0	0,8	ND	ND	ND	ND	NEG	NEG	1,7	1,4	ND	ND	ND	ND	NEG	NEG	NEG	NEG	hPRS
CGA + CGB5	0,2	0,1	ND	ND	ND	ND	NEG	NEG	0,4	0,4	ND	ND	ND	ND	NEG	NEG	NEG	NEG	hPRS
CRK + PDGFRB	NA	NA	NA	NA	NA	NA	PREY	PREY	0,9	0,9	ND	ND	ND	ND	NEG	NEG	NEG	NEG	hPRS
CXCL1 + IL8RB	0,1	NA	ND	ND	NA	NA	NEG	PREY	NA	NA	NA	NA	NA	NA	IP	IP	NEG	NEG	hPRS
DDIT3 + FOS	10,3	19,5	31,5	3,6	40,2	9,4	POS	POS	0,8	1,3	ND	ND	ND	ND	NEG	NEG	POS	POS	hPRS
DR1 + DRAP1	13,6	15,1	13,7	2,0	11,8	1,2	POS	POS							NC	NC	POS	POS	hPRS
ERBB3 + NRG1	1,4	1,4	ND	ND	ND	ND	NEG	NEG	1,8	2,0	ND	ND	ND	ND	NEG	NEG	NEG	NEG	hPRS
FABP5 + S100A7	1,8	1,5	ND	ND	ND	ND	NEG	NEG	2,0	1,5	ND	ND	ND	ND	NEG	NEG	NEG	NEG	hPRS
FANCA + FANCC	1,2	0,9	ND	ND	ND	ND	NEG	NEG	2,0	1,6	ND	ND	ND	ND	NEG	NEG	NEG	NEG	hPRS
FANCA + FANCG	1,9	2,3	ND	ND	ND	ND	NEG	NEG	23,3	23,3	17,7	1,0	16,7	1,0	POS	POS	POS	POS	hPRS
FEN1 + PCNA	4,0	4,4	15,0	3,3	10,6	2,0	POS	POS	0,2	0,2	ND	ND	ND	ND	NEG	NEG	POS	POS	hPRS
FGF1 + FGFR1							NC	NC	0,0	0,0	ND	ND	ND	ND	NEG	NEG	NEG	NEG	hPRS
GADD45A + PCNA	7,4	8,3	49,1	15,0	45,8	4,2	POS	POS	1,9	1,7	ND	ND	ND	ND	NEG	NEG	POS	POS	hPRS
GRB2 + PTK2							NC	NC	0,2	0,2	ND	ND	ND	ND	NEG	NEG	NEG	NEG	hPRS
GTF2F1 + GTF2F2	1,3	0,9	ND	ND	ND	ND	NEG	NEG	0,1	0,2	ND	ND	ND	ND	NEG	NEG	NEG	NEG	hPRS
HBA2 + HBB	0,3	0,4	ND	ND	ND	ND	NEG	NEG	1,0	1,0	ND	ND	ND	ND	NEG	NEG	NEG	NEG	hPRS
HDAC1 + RB1	3,8	5,0	3,1	0,6	2,8	0,7	POS	NEG	2,4	3,2	ND	ND	5,8	0,6	NEG	POS	POS	POS	hPRS
HDAC1 + ZBTB16	3,1	2,3	14,3	1,0	ND	ND	POS	NEG	4,5	4,0	3,6	0,3	3,8	0,2	POS	POS	POS	POS	hPRS
IFIT1 + EIF3S6	1,6	1,8	ND	ND	ND	ND	NEG	NEG	1,1	0,6	ND	ND	ND	ND	NEG	NEG	NEG	NEG	hPRS
IGF2 + IGFBP4	1,0	1,9	ND	ND	ND	ND	NEG	NEG	0,6	0,4	ND	ND	ND	ND	NEG	NEG	NEG	NEG	hPRS
JUNB + BATF	23,2	22,6	74,8	11,6	73,3	15,1	POS	POS	34,5	33,6	70,5	11,4	49,1	1,6	POS	POS	POS	POS	hPRS
LCP2 + GRAP2	NA	NA	NA	NA	NA	NA	PREY	PREY	106,0	119,4	82,8	5,8	79,9	5,7	POS	POS	POS	POS	hPRS
LCP2 + NCK1	0,4	0,5	ND	ND	ND	ND	NEG	NEG	2,9	1,8	ND	ND	ND	ND	NEG	NEG	NEG	NEG	hPRS
LCP2 + VAV1	NA	NA	NA	NA	NA	NA	PREY	PREY	2,1	1,9	ND	ND	ND	ND	NEG	NEG	NEG	NEG	hPRS
LGALS3 + LGALS3BP	0,5	0,5	ND	ND	ND	ND	NEG	NEG							NC	NC	NEG	NEG	hPRS
LMNA + LMNB1	11,8	8,6	37,2	3,4	28,8	5,1	POS	POS	3,5	3,3	48,4	3,5	50,5	2,6	POS	POS	POS	POS	hPRS
LMNA + RB1	0,4	0,8	ND	ND	ND	ND	NEG	NEG	1,1	0,9	ND	ND	ND	ND	NEG	NEG	NEG	NEG	hPRS
LSM3 + LSM2	104,1	70,5	68,4	4,9	79,8	6,8	POS	POS	101,3	123,8	107,8	6,7	117,8	18,0	POS	POS	POS	POS	hPRS
MAD2L1 + MAD1L1	5,6	17,2	47,0	4,5	102,3	10,9	POS	POS	28,6	31,1	76,4	14,6	35,1	4,3	POS	POS	POS	POS	hPRS
MCM2 + MCM3							NC	NC	4,9	3,9	0,9	0,1	0,8	0,0	NEG	NEG	NEG	NEG	hPRS
MCM2 + MCM5							NC	NC	1,0	1,0	ND	ND	ND	ND	NEG	NEG	NEG	NEG	hPRS
NCBP1 + NCBP2							NC	NC	90,4	76,1	28,8	2,5	31,8	2,9	POS	POS	POS	POS	hPRS
NF2 + HGS	1,7	1,9	ND	ND	ND	ND	NEG	NEG	1,5	1,2	ND	ND	ND	ND	NEG	NEG	NEG	NEG	hPRS
NR3C1 + HSPCA	3,1	2,5	1,6	0,5	ND	ND	NEG	NEG	NA	NA	NA	NA	NA	NA	PREY	PREY	NEG	NEG	hPRS
NR3C1 + RELA	0,8	1,0	ND	ND	ND	ND	NEG	NEG	NA	NA	NA	NA	NA	NA	PREY	PREY	NEG	NEG	hPRS
ORC2L + MCM10	0,0	1,4	ND	ND	ND	ND	NEG	NEG	NA	NA	NA	NA	NA	NA	PREY	PREY	NEG	NEG	hPRS
ORC2L + ORC4L	0,0	0,7	ND	ND	ND	ND	NEG	NEG	NA	NA	NA	NA	NA	NA	PREY	PREY	NEG	NEG	hPRS
PDE4D + GNB2L1	1,1	1,1	ND	ND	ND	ND	NEG	NEG	0,4	0,4	ND	ND	ND	ND	NEG	NEG	NEG	NEG	hPRS
PEX14 + PEX19	6,0	8,1	3,3	0,7	3,3	0,6	POS	POS	13,7	13,9	3,1	0,6	3,3	0,4	POS	POS	POS	POS	hPRS
PEX19 + PEX11B	5,5	6,5	1,1	0,1	1,8	0,3	NEG	NEG	13,8	12,9	16,3	4,0	15,8	1,6	POS	POS	POS	POS	hPRS
PEX19 + PEX16							NC	NC	13,9	12,4	16,6	3,0	24,0	2,1	POS	POS	POS	POS	hPRS
PEX19 + PEX3	0,2	0,3	ND	ND	ND	ND	NEG	NEG	9,8	9,8	28,5	3,8	26,5	6,5	POS	POS	POS	POS	hPRS
PPP3CA + PPP3R1	59,4	59,5	33,7	1,5	37,3	5,8	POS	POS	NA	NA	NA	NA	NA	NA	IP	IP	POS	POS	hPRS
PRKAR2A + VIL2	8,1	2,2	4,6	0,8	ND	ND	POS	NEG	0,2		ND	ND			NEG	PREY	POS	NEG	hPRS
PSMD4 + RAD23A	1,8	2,5	ND	ND	ND	ND	NEG	NEG	0,3	0,3	ND	ND	ND	ND	NEG	NEG	NEG	NEG	hPRS
PTK2 + SRC	4,1	3,8	6,5	0,4	6,6	1,3	POS	POS							NC	NC	POS	POS	hPRS
PTPN11 + FRS2	1,6	1,5	ND	ND	ND	ND	NEG	NEG							NC	NC	NEG	NEG	hPRS
RAC1 + ARFIP2	1,7	1,7	ND	ND	ND	ND	NEG	NEG	2,5	1,7	ND	ND	ND	ND	NEG	NEG	NEG	NEG	hPRS
RAF1 + RAP1A	0,7	0,2	ND	ND	ND	ND	NEG	NEG	NA	NA	NA	NA	NA	NA	PREY	PREY	NEG	NEG	hPRS
RCC1 + RAN	4,1	4,7	1,2	0,1	1,5	0,1	NEG	NEG	0,5	0,5	ND	ND	ND	ND	NEG	NEG	NEG	NEG	hPRS

Interaction	set a								set b								set a+b		Set
	ICR Exp1	ICR Exp2	mean cNIR Exp1	sem cNIR Exp1	mean cNIR Exp2	sem cNIR Exp2	result Exp1	result Exp2	ICR Exp1	ICR Exp2	mean cNIR Exp1	sem cNIR Exp1	mean cNIR Exp2	sem cNIR Exp2	result Exp1	result Exp2	result Exp1	result Exp2	
RET + FRS2	1,8	3,1	ND	ND	1,2	0,0	NEG	NEG							NC	NC	NEG	NEG	hPRS
RHOA + ARHGAP1							NC	NC	1,0	1,2	ND	ND	ND	ND	NEG	NEG	NEG	NEG	hPRS
RIPK2 + CARD4	1,4	0,8	ND	ND	ND	ND	NEG	NEG	0,7	0,6	ND	ND	ND	ND	NEG	NEG	NEG	NEG	hPRS
RPA2 + RPA3							NC	NC	0,7	0,6	ND	ND	ND	ND	NEG	NEG	NEG	NEG	hPRS
S100A1 + S100B	175,3	90,9	91,5	3,2	96,8	14,3	POS	POS	162,9	168,2	20,5	1,6	20,7	1,4	POS	POS	POS	POS	hPRS
S100A6 + S100B	2,7	2,5	ND	ND	ND	ND	NEG	NEG	2,6	3,0	ND	ND	0,3	0,0	NEG	NEG	NEG	NEG	hPRS
SKP1A + SKP2							NC	NC	0,1	0,1	ND	ND	ND	ND	NEG	NEG	NEG	NEG	hPRS
SMAD1 + SMAD4	NA	NA	NA	NA	NA	NA	PREY	NEG							NC	NC	NEG	NEG	hPRS
SMAD3 + SMAD4	0,4	0,4	ND	ND	ND	ND	NEG	NEG	NA	NA	NA	NA	NA	NA	PREY	PREY	NEG	NEG	hPRS
SMAD4 + DCP1A	1,5	1,0	ND	ND	ND	ND	NEG	NEG	NA	NA	NA	NA	NA	NA	PREY	NEG	NEG	NEG	hPRS
TNFSF10 + TNFRSF10B							NC	NC	1,5	1,2	ND	ND	ND	ND	NEG	NEG	NEG	NEG	hPRS
TP53 + UBE2I	2,2	1,6	ND	ND	ND	ND	NEG	NEG	2,7	3,0	ND	ND	ND	ND	NEG	NEG	NEG	NEG	hPRS
APOD + MUC7	0,2	0,2	ND	ND	ND	ND	NEG	NEG	NA	NA	NA	NA	NA	NA	IP	IP	NEG	NEG	hRRS
ARSA + DBN1	1,1	1,1	ND	ND	ND	ND	NEG	NEG	0,3	0,2	-0,4	0,0	-0,4	0,0	NEG	NEG	NEG	NEG	hRRS
ASS + FLJ13912	0,4	0,6	ND	ND	ND	ND	NEG	NEG	2,8	2,3	9,1	1,5	5,8	1,2	NEG	NEG	NEG	NEG	hRRS
ATP5O + CLEC2D	NA	NA	NA	NA	NA	NA	IP	IP	0,3	0,7	-0,2	0,0	-0,1	0,0	NEG	NEG	NEG	NEG	hRRS
BAD + FGF18	0,8	0,8	ND	ND	ND	ND	NEG	NEG	0,8	1,1	0,7	0,5	1,2	0,1	NEG	NEG	NEG	NEG	hRRS
BMP5 + C10orf119	NA	NA	NA	NA	NA	NA	PREY	PREY	0,7	0,7	0,1	0,1	0,1	0,0	NEG	NEG	NEG	NEG	hRRS
BTC + KIAA0515	0,4	0,6	ND	ND	ND	ND	NEG	NEG	1,5	1,2	0,1	0,1	0,0	0,1	NEG	NEG	NEG	NEG	hRRS
BYSL + KIAA0907	1,0	0,9	ND	ND	ND	ND	NEG	NEG	0,9	0,7	3,4	1,1	0,8	0,2	NEG	NEG	NEG	NEG	hRRS
CA2 + PTPRS	4,3	4,8	1,7	0,2	1,2	0,1	NEG	NEG	1,1	1,3	0,4	0,4	0,1	0,2	NEG	NEG	NEG	NEG	hRRS
CD151 + WDR41	NA	3,9	NA	NA	0,4	0,0	PREY	NEG							NC	NC	NEG	NEG	hRRS
CD34 + SNX21	0,8	0,7	ND	ND	ND	ND	NEG	NEG							NC	NC	NEG	NEG	hRRS
CD81 + NPC2	1,0	NA	ND	ND	NA	NA	NEG	PREY	0,4	0,5	-0,6	0,2	-0,6	0,2	NEG	NEG	NEG	NEG	hRRS
CENPA + PPIL3	0,7	0,5	ND	ND	ND	ND	NEG	NEG	0,6	0,4	0,0	0,0	0,0	0,0	NEG	NEG	NEG	NEG	hRRS
CKB + HBZ	2,0	3,3	ND	ND	0,0	0,0	NEG	NEG	1,2	1,5	0,2	0,1	0,3	0,1	NEG	NEG	NEG	NEG	hRRS
CLPTM1 + L3MBTL2	0,3	0,2	ND	ND	ND	ND	NEG	NEG	NA	NA	NA	NA	NA	NA	IP	IP	NEG	NEG	hRRS
COPB1 + HPCAL4	1,5	1,5	ND	ND	ND	ND	NEG	NEG	NA	NA	NA	NA	NA	NA	PREY	PREY	NEG	NEG	hRRS
DEFA1 + TSTD2	1,8	1,3	ND	ND	ND	ND	NEG	NEG	0,3	0,5	-1,0	0,0	-1,5	0,0	NEG	NEG	NEG	NEG	hRRS
DLX4 + RAB3IP	0,4	0,4	ND	ND	ND	ND	NEG	NEG	1,9	2,1	3,8	0,8	3,0	0,9	NEG	NEG	NEG	NEG	hRRS
DUT + C19orf40	0,3	NA	ND	ND	NA	NA	NEG	PREY							NC	NC	NEG	NEG	hRRS
EMD + ARMC1	0,3	0,3	ND	ND	ND	ND	NEG	NEG	0,8	0,9	1,1	1,5	1,0	1,0	NEG	NEG	NEG	NEG	hRRS
ERBB3 + C3orf38	0,7	1,0	ND	ND	ND	ND	NEG	NEG	2,9	2,6	0,9	0,6	1,1	0,7	NEG	NEG	NEG	NEG	hRRS
ETF1 + LIMR	2,2	2,5	ND	ND	ND	ND	NEG	NEG	2,1	1,4	0,2	0,1	0,2	0,0	NEG	NEG	NEG	NEG	hRRS
FABP4 + GCG	1,0	1,2	ND	ND	ND	ND	NEG	NEG	0,9	1,0	0,3	0,2	0,1	0,1	NEG	NEG	NEG	NEG	hRRS
FABP7 + STX5A	NA	NA	NA	NA	NA	NA	PREY	PREY	1,2	1,2	0,4	0,1	0,6	0,1	NEG	NEG	NEG	NEG	hRRS
FAS + LSM3	1,9	1,8	ND	ND	ND	ND	NEG	NEG	5,5	3,1	1,6	0,3	1,5	0,2	NEG	NEG	NEG	NEG	hRRS
FIGF + ZNF46	3,7	2,9	20,8	8,0	ND	ND	POS	NEG	0,6	NA	-6,1	0,4	NA	NA	NEG	IP	POS	NEG	hRRS
FKBP3 + NQO2	2,6	2,7	ND	ND	ND	ND	NEG	NEG	1,7	1,7	0,1	0,1	0,0	0,0	NEG	NEG	NEG	NEG	hRRS
GABRA2 + PSTPIP2	0,9	1,0	ND	ND	ND	ND	NEG	NEG	NA	NA	NA	NA	NA	NA	IP	IP	NEG	NEG	hRRS
GALK1 + MCCC1	3,4	3,7	2,9	0,4	2,3	0,6	NEG	NEG	5,4	4,9	4,7	1,4	3,4	0,6	POS	POS	POS	POS	hRRS
GCDH + ZCCHC9	1,0	1,0	ND	ND	ND	ND	NEG	NEG	0,3	NA	0,0	0,3	NA	NA	NEG	PREY	NEG	NEG	hRRS
GPD2 + BOP	1,2	1,0	ND	ND	ND	ND	NEG	NEG	0,6	0,5	-0,2	0,0	-0,1	0,0	NEG	NEG	NEG	NEG	hRRS
GPR18 + HNRPLL	0,8	0,5	ND	ND	ND	ND	NEG	NEG	0,3	0,3	-0,2	0,0	-0,2	0,0	NEG	NEG	NEG	NEG	hRRS
GRIK2 + ARL6IP6	0,6	0,7	ND	ND	ND	ND	NEG	NEG	NA	NA	NA	NA	NA	NA	PREY	PREY	NEG	NEG	hRRS
HCLS1 + SALL2	0,7	0,6	ND	ND	ND	ND	NEG	NEG							NC	NC	NEG	NEG	hRRS
HIST1H1C + NPDC1							NC	NC	0,9	0,7	22,2	4,5	27,7	13,4	NEG	NEG	NEG	NEG	hRRS
HLA-DMB + PSEN2	1,5	1,7	ND	ND	ND	ND	NEG	NEG	NA	3,5	NA	NA	0,4	0,0	PREY	NEG	NEG	NEG	hRRS
HLA-DQB1 + ATOH7	0,6	0,6	ND	ND	ND	ND	NEG	NEG							NC	NC	NEG	NEG	hRRS
HMGB1 + TEAD4	1,9	1,8	ND	ND	ND	ND	NEG	NEG	0,6	0,5	-0,7	0,0	-0,4	0,1	NEG	NEG	NEG	NEG	hRRS
HNRPM + TNFSF10	0,5	0,7	ND	ND	ND	ND	NEG	NEG	1,8	2,2	56,5	15,9	16,5	2,0	NEG	NEG	NEG	NEG	hRRS
INPP1 + UBLCP1							NC	NC	0,7	0,7	0,9	0,3	0,8	0,1	NEG	NEG	NEG	NEG	hRRS
ITPA + WDR62	3,1	3,3	1,2	0,1	0,8	0,1	NEG	NEG	1,5	1,3	0,3	0,1	0,3	0,0	NEG	NEG	NEG	NEG	hRRS
ITPK1 + TMEM22	1,4	1,2	ND	ND	ND	ND	NEG	NEG	0,7	0,9	-0,1	0,1	0,3	0,1	NEG	NEG	NEG	NEG	hRRS
JAK3 + ATP6V1D	1,0	0,7	ND	ND	ND	ND	NEG	NEG							NC	NC	NEG	NEG	hRRS
LAMP2 + UBE2G2	0,8	1,1	ND	ND	ND	ND	NEG	NEG	0,6	NA	0,0	0,2	NA	NA	NEG	PREY	NEG	NEG	hRRS
LUM + UGGT2	1,1	1,3	ND	ND	ND	ND	NEG	NEG	NA	NA	NA	NA	NA	NA	PREY	PREY	NEG	NEG	hRRS
MAOB + CTCF	1,0	0,5	ND	ND	ND	ND	NEG	NEG	0,7	0,3	-0,3	0,1	-0,2	0,1	NEG	NEG	NEG	NEG	hRRS
MCM2 + PLXNA4	1,0	1,9	ND	ND	ND	ND	NEG	NEG	2,8	3,1	2,0	0,3	1,6	0,5	NEG	NEG	NEG	NEG	hRRS
MNAT1 + GMPPA							NC	NC	0,8	0,7	0,3	0,2	0,2	0,0	NEG	NEG	NEG	NEG	hRRS
MOBP + MRPS25							NC	NC	2,3	1,5	1,1	0,4	0,4	0,1	NEG	NEG	NEG	NEG	hRRS
MX2 + NUP37	3,4	4,3	0,9	0,1	1,4	0,1	NEG	NEG							NC	NC	NEG	NEG	hRRS
MYBL2 + ENOX1	1,2	1,2	ND	ND	ND	ND	NEG	NEG	NA	0,1	NA	NA	-0,1	0,1	PREY	NEG	NEG	NEG	hRRS
NAT2 + DNAJA1	1,3	1,4	ND	ND	ND	ND	NEG	NEG							NC	NC	NEG	NEG	hRRS
NDP + NUDT4	2,1	2,7	ND	ND	ND	ND	NEG	NEG							NC	NC	NEG	NEG	hRRS
NFIB + TIRAP	NA	NA	NA	NA	NA	NA	PREY	PREY	0,1	0,0	-1,0	0,0	-1,2	0,0	NEG	NEG	NEG	NEG	hRRS
NKX2-5 + CSGALNACT2	0,2	0,2	ND	ND	ND	ND	NEG	NEG	1,2	0,6	5,0	3,4	3,1	2,6	NEG	NEG	NEG	NEG	hRRS
NONO + VMD2	0,1	NA	ND	ND	NA	NA	NEG	PREY	NA	NA	NA	NA	NA	NA	IP	IP	NEG	NEG	hRRS
NUDT2 + MIIP	1,9	2,2	ND	ND	ND	ND	NEG	NEG	NA	NA	NA	NA	NA	NA	PREY	PREY	NEG	NEG	hRRS
OSM + LOC146542							NC	NC	0,8	0,6	0,9	0,7	0,5	0,4	NEG	NEG	NEG	NEG	hRRS
P2RY6 + TRIM26							NC	NC	0,8	1,2	-0,2	0,1	0,0	0,0	NEG	NEG	NEG	NEG	hRRS
PBX2 + VILL	2,1	2,7	ND	ND	ND	ND	NEG	NEG	2,3	3,0	1,6	0,6	1,3	0,2	NEG	NEG	NEG	NEG	hRRS
PDE9A + FLJ38964	NA	NA	NA	NA	NA	NA	PREY	PREY	2,1	2,0	0,3	0,0	0,2	0,0	NEG	NEG	NEG	NEG	hRRS
PDGFRA + NDFIP1	1,9	2,2	ND	ND	ND	ND	NEG	NEG	NA	NA	NA	NA	NA	NA	IP	IP	NEG	NEG	hRRS

Interaction	set a								set b								set a+b		Set
	ICR Exp1	ICR Exp2	mean cNIR Exp1	sem cNIR Exp1	mean cNIR Exp2	sem cNIR Exp2	result Exp1	result Exp2	ICR Exp1	ICR Exp2	mean cNIR Exp1	sem cNIR Exp1	mean cNIR Exp2	sem cNIR Exp2	result Exp1	result Exp2	result Exp1	result Exp2	
PDHB + ZC3HC1	1,8	3,0	ND	ND	1,3	0,2	NEG	NEG	1,2	3,4	0,2	0,2	2,0	0,6	NEG	NEG	NEG	NEG	hRRS
PMCH + RIC3	NA	NA	NA	NA	NA	NA	IP	IP	0,4	0,6	-0,2	0,0	-0,1	0,0	NEG	NEG	NEG	NEG	hRRS
PML + SGK3	0,3	0,4	ND	ND	ND	ND	NEG	NEG	1,0	0,7	101,7	23,7	42,2	16,0	NEG	NEG	NEG	NEG	hRRS
PPP1R12B + ZKSCAN4							NC	NC	0,9	0,8	3,1	0,4	2,9	0,2	NEG	NEG	NEG	NEG	hRRS
PPP1R1A + MGC33692	0,4	0,6	ND	ND	ND	ND	NEG	NEG	0,7	0,9	-0,4	0,1	-0,4	0,1	NEG	NEG	NEG	NEG	hRRS
PPP6C + ZNF350	0,6	0,6	ND	ND	ND	ND	NEG	NEG	1,2	1,1	2,5	0,6	1,9	0,3	NEG	NEG	NEG	NEG	hRRS
PROS1 + STK25	0,9	1,1	ND	ND	ND	ND	NEG	NEG	1,9	3,0	0,9	0,1	1,0	0,1	NEG	NEG	NEG	NEG	hRRS
PSMD12 + CRIPT	0,7	1,0	ND	ND	ND	ND	NEG	NEG	1,0	0,8	-0,1	0,1	-0,1	0,0	NEG	NEG	NEG	NEG	hRRS
PSMD5 + SLC22A15	0,3	0,3	ND	ND	ND	ND	NEG	NEG	0,4	0,3	-0,1	0,0	-0,1	0,0	NEG	NEG	NEG	NEG	hRRS
PSMD5 + SYCE1	1,4	1,3	ND	ND	ND	ND	NEG	NEG	0,2	0,2	-0,3	0,0	-0,3	0,0	NEG	NEG	NEG	NEG	hRRS
RAB3B + BOC	0,2	0,1	ND	ND	ND	ND	NEG	NEG	1,5	1,6	0,5	0,6	1,2	0,8	NEG	NEG	NEG	NEG	hRRS
RBM3 + SF3A1							NC	NC	0,4	1,3	-0,1	0,0	0,0	0,0	NEG	NEG	NEG	NEG	hRRS
RGR + ABCF3	1,0	1,5	ND	ND	ND	ND	NEG	NEG	0,9	0,8	0,0	0,0	0,0	0,0	NEG	NEG	NEG	NEG	hRRS
RHOC + NUP62CL	1,2	0,7	ND	ND	ND	ND	NEG	NEG	0,7	0,7	-0,1	0,0	-0,1	0,0	NEG	NEG	NEG	NEG	hRRS
RXRB + CXCL11	0,3	0,6	ND	ND	ND	ND	NEG	NEG	0,9	NA	-0,8	1,0	NA	NA	NEG	IP	NEG	NEG	hRRS
SCARB1 + PHF21B							NC	NC	1,0	0,9	0,2	0,1	-0,1	0,0	NEG	NEG	NEG	NEG	hRRS
SERPINB3 + DCTN6	1,6	2,2	ND	ND	ND	ND	NEG	NEG	0,4	0,4	-1,3	0,0	-2,2	0,0	NEG	NEG	NEG	NEG	hRRS
SHMT2 + STAC3	0,6	0,7	ND	ND	ND	ND	NEG	NEG	0,8	0,7	-0,1	0,0	-0,1	0,1	NEG	NEG	NEG	NEG	hRRS
SLC25A6 + ZNF213	1,5	1,7	ND	ND	ND	ND	NEG	NEG	0,7	0,8	-10,9	0,1	-3,3	0,1	NEG	NEG	NEG	NEG	hRRS
SLC6A1 + TM4SF4	18,5	24,4	7,9	0,3	8,3	0,7	POS	POS	6,6	6,6	9,6	2,2	8,1	1,0	POS	POS	POS	POS	hRRS

Table 5: DULIP results from the Y2H-PRS, HI-PRS and Y2H-RRS. ICR: internal control ratio; cNIR: corrected normalized interaction ratio; Exp: Experiment; NA: not available (no expression/immunoprecipitation); PREY: no prey expression; IP: no immunoprecipitation; NC: not constructed; ND: not determined.

	set a								set b								set a+b		
Interaction	ICR Exp1	ICR Exp2	mean cNIR Exp1	sem cNIR Exp1	mean cNIR Exp2	sem cNIR Exp2	result Exp1	result Exp2	ICR Exp1	ICR Exp2	mean cNIR Exp1	sem cNIR Exp1	mean cNIR Exp2	sem cNIR Exp2	result Exp1	result Exp2	result Exp1	result Exp2	Set
ACTN4 + MYOZ1	6,9	5,6	0,4	0,1	0,1	0,3	NEG	NEG	21,4	19,3	19,9	0,6	17,7	5,3	POS	POS	POS	POS	Y2H-PRS
AP2B1 + THAP1	1,2	1,2	ND	ND	ND	ND	NEG	NEG	ND	ND	ND	ND	ND	ND	PREY	PREY	NEG	NEG	Y2H-PRS
AES + SH3GL3	0,3	0,3	ND	ND	ND	ND	NEG	NEG	0,4	0,3	ND	ND	ND	ND	NEG	NEG	NEG	NEG	Y2H-PRS
APEH + KIAA0174	10,1	13	3,1	0,3	2,6	0,1	POS	NEG	7,5	8,3	31,6	1,6	40,8	3,2	POS	POS	POS	POS	Y2H-PRS
APLP1 + GDF9	ND	ND	ND	ND	ND	ND	IP	IP	ND	ND	ND	ND	ND	ND	PREY	PREY	ND	ND	Y2H-PRS
ARR3 + DVL2	3,2	2,7	6,1	0,9	ND	ND	POS	NEG							NC	NC	POS	NEG	Y2H-PRS
BNIP3L + RINT1	5,4	5,5	0,4	0	0,4	0	NEG	NEG	2,2	1,9	ND	ND	ND	ND	NEG	NEG	NEG	NEG	Y2H-PRS
CASP8 + TFCP2	0,8	0,7	ND	ND	ND	ND	NEG	NEG	0,1	0,1	ND	ND	ND	ND	NEG	NEG	NEG	NEG	Y2H-PRS
CCND3 + EFEMP2	0,2	0,3	ND	ND	ND	ND	NEG	NEG	3,6	3,5	30,1	2,7	28,6	6,9	POS	POS	POS	POS	Y2H-PRS
CDKN1A + FLAD1	1,1	1,4	ND	ND	ND	ND	NEG	NEG	1,1	1	ND	ND	ND	ND	NEG	NEG	NEG	NEG	Y2H-PRS
AP2S1 + AP2A1	ND	ND	ND	ND	ND	ND	IP	IP							NC	NC	NEG	NEG	Y2H-PRS
COPB1 + TRIM37	ND	ND	ND	ND	ND	ND	IP	IP							NC	NC	NEG	NEG	Y2H-PRS
CSTF2 + IMMT	2,7	2,4	ND	ND	ND	ND	NEG	NEG	1,2	1,6	ND	ND	ND	ND	NEG	NEG	NEG	NEG	Y2H-PRS
CTBP1 + LCORL	34,9	28,4	4,2	0,4	4,4	0,1	POS	POS	18,4	12,9	17	2,3	15,4	2,2	POS	POS	POS	POS	Y2H-PRS
CTBP2 + TGIF1	23,8	28,5	10,6	1,3	14	1,1	POS	POS	3,3	3,6	6,2	0,9	5,8	0,1	POS	POS	POS	POS	Y2H-PRS
DAO + PRKAB2							NC	NC	1,5	2,6	ND	ND	ND	ND	NEG	NEG	NEG	NEG	Y2H-PRS
GADD45A + DCTN2	0,6	0,6	ND	ND	ND	ND	NEG	NEG	1,1	0,9	ND	ND	ND	ND	NEG	NEG	NEG	NEG	Y2H-PRS
DOM3Z + FLOT2	ND	ND	ND	ND	ND	ND	PREY	PREY	2	1,6	ND	ND	ND	ND	NEG	NEG	NEG	NEG	Y2H-PRS
DVL2 + ZBTB8A							NC	NC	1,9	2,7	ND	ND	ND	ND	NEG	NEG	NEG	NEG	Y2H-PRS
EWSR1 + NDUFB1	2,2	2,8	ND	ND	ND	ND	NEG	NEG	1,2	1,1	ND	ND	ND	ND	NEG	NEG	NEG	NEG	Y2H-PRS
FABP4 + VIM	0,7	0,7	ND	ND	ND	ND	NEG	NEG	4,5	4,3	3	0,1	2,8	0,5	POS	NEG	POS	NEG	Y2H-PRS
FLT1 + PTPN11	1,7	1,3	ND	ND	ND	ND	NEG	NEG							NC	NC	NEG	NEG	Y2H-PRS
GAPDH + TK1	2,9	3,5	ND	ND	1,7	0,2	NEG	NEG	1,9	1,7	ND	ND	ND	ND	NEG	NEG	NEG	NEG	Y2H-PRS
HNRNPC + KPNA3	ND	ND	ND	ND	ND	ND	PREY	PREY	ND	ND	ND	ND	ND	ND	IP	IP	ND	ND	Y2H-PRS
HNRNPK + RBM42	1,8	2,6	ND	ND	ND	ND	NEG	NEG	3	2,2	0,7	0,1	ND	ND	NEG	NEG	NEG	NEG	Y2H-PRS
PRMT1 + NOL4	7,8	6,6	0,9	0,1	0,7	0,1	NEG	NEG	2,3	2,9	ND	ND	ND	ND	NEG	NEG	NEG	NEG	Y2H-PRS
HSPA5 + PSME3	6	7,3	2,6	0,6	3,3	0,2	NEG	POS	0,8	0,8	ND	ND	ND	ND	NEG	NEG	NEG	POS	Y2H-PRS
IL2RG + CAPNS1	1,6	1,7	ND	ND	ND	ND	NEG	NEG	ND	ND	ND	ND	ND	ND	PREY	PREY	NEG	NEG	Y2H-PRS
KPNA1 + LMO4	2,7	3,4	ND	ND	5,6	1,2	NEG	POS	ND	ND	ND	ND	ND	ND	PREY	PREY	NEG	POS	Y2H-PRS
KPNA3 + FAM50B	ND	ND	ND	ND	ND	ND	IP	IP	ND	ND	ND	ND	ND	ND	PREY	PREY	ND	ND	Y2H-PRS
KRT15 + WAC	ND	ND	ND	ND	ND	ND	IP	IP	ND	ND	ND	ND	ND	ND	IP	IP	ND	ND	Y2H-PRS
KRT19 + C10orf10	1,5	1,7	ND	ND	ND	ND	NEG	NEG	3,3	2,9	22,3	1,8	ND	ND	POS	NEG	POS	NEG	Y2H-PRS
SMAD1 + AP2A2	0,8	0,6	ND	ND	ND	ND	NEG	NEG	1,7	0,8	ND	ND	ND	ND	NEG	NEG	NEG	NEG	Y2H-PRS
SMAD4 + GPNMB	0,2	0,1	ND	ND	ND	ND	NEG	NEG	0,8	0,7	ND	ND	ND	ND	NEG	NEG	NEG	NEG	Y2H-PRS
SMAD5 + BCAT1	0,8	0,9	ND	ND	ND	ND	NEG	NEG	1,3	1,1	ND	ND	ND	ND	NEG	NEG	NEG	NEG	Y2H-PRS
MAGEA11 + TRMT1	1,1	0,6	ND	ND	ND	ND	NEG	NEG	4,2	4,4	5,3	0,8	4,5	0,6	POS	POS	POS	POS	Y2H-PRS
MDFI + DHRS1	5,2	5,3	4,4	0,5	3,9	0,5	POS	POS	3,8	4,2	12,8	1,3	12,1	1,1	POS	POS	POS	POS	Y2H-PRS
MDK + RPL18A	2	2	ND	ND	ND	ND	NEG	NEG	ND	ND	ND	ND	ND	ND	IP	IP	NEG	NEG	Y2H-PRS
MEOX2 + RND2	1,7	1,7	ND	ND	ND	ND	NEG	NEG	3,4	4,1	2	0,5	2	0,4	NEG	NEG	NEG	NEG	Y2H-PRS
TRIM37 + MCM10							NC	NC	1,1	1,3	ND	ND	ND	ND	NEG	NEG	NEG	NEG	Y2H-PRS
OAT + C2orf18	0,1	0,1	ND	ND	ND	ND	NEG	NEG	0,4	0,4	ND	ND	ND	ND	NEG	NEG	NEG	NEG	Y2H-PRS
ORC1 + MCM7							NC	NC	2,5	2,9	ND	ND	ND	ND	NEG	NEG	NEG	NEG	Y2H-PRS
PDCL + PSMC5	53,8	47,6	10,9	0,6	10,7	1,4	POS	POS	4,5	4,6	4,6	0,8	4,6	0,3	POS	POS	POS	POS	Y2H-PRS
PIN1 + SOCS3	1	1	ND	ND	ND	ND	NEG	NEG	1,4	0,5	ND	ND	ND	ND	NEG	NEG	NEG	NEG	Y2H-PRS
PLSCR1 + NTN4	13,8	13,5	6	0,6	6,9	0,1	POS	POS	14,9	11,4	45,7	8	44,4	2,2	POS	POS	POS	POS	Y2H-PRS
PPP1CA + RANBP9	0,6	0,8	ND	ND	ND	ND	NEG	NEG	1	1,1	ND	ND	ND	ND	NEG	NEG	NEG	NEG	Y2H-PRS
PPP1CC + NEK2	2,2	1,9	ND	ND	ND	ND	NEG	NEG	1,5	1,6	ND	ND	ND	ND	NEG	NEG	NEG	NEG	Y2H-PRS
PSMA1 + PSMB9	6,5	6,8	1,1	0,2	1,7	0,3	NEG	NEG	6	6,6	2,3	0,2	2,1	0,2	NEG	NEG	NEG	NEG	Y2H-PRS
PTN + SAT1	ND	ND	ND	ND	ND	ND	IP	IP	0,5	0,6	ND	ND	ND	ND	NEG	NEG	NEG	NEG	Y2H-PRS
RAP1GDS1 + KRAS	3,2	3,8	0,8	0,1	0,7	0	NEG	NEG	4	4	1	0,1	0,3	0,2	NEG	NEG	NEG	NEG	Y2H-PRS
RAP2B + RUNDC3A	14	13,9	6,2	0,5	6,4	0,9	POS	POS	6,6	5,3	3,7	0,5	3,2	0,3	POS	POS	POS	POS	Y2H-PRS
REG1B + BAT3	3,6	2,8	1	0,2	ND	ND	NEG	NEG	1,6	1,7	ND	ND	ND	ND	NEG	NEG	NEG	NEG	Y2H-PRS
TRIM27 + KCTD15	0,6	0,4	ND	ND	ND	ND	NEG	NEG	8,4	7,4	4,3	0,4	4,9	0,8	POS	POS	POS	POS	Y2H-PRS
RGS2 + DYNLL1	1,6	1,5	ND	ND	ND	ND	NEG	NEG	1,8	2,1	ND	ND	ND	ND	NEG	NEG	NEG	NEG	Y2H-PRS
RPS6 + RPL6	2,4	5,2	ND	ND	7,8	0,6	NEG	POS	7,9	3,7	5	0,1	4,8	0,5	POS	POS	POS	POS	Y2H-PRS
SRSF2 + U2AF1	3,3	3,3	10,1	0,1	8,8	0,3	POS	POS	1,7	1,9	ND	ND	ND	ND	NEG	NEG	POS	POS	Y2H-PRS
SMN1 + UNC119	3,4	3,8	0,8	0,1	0,8	0,2	NEG	NEG	3,5	3,8	0,6	0,2	1	0,1	NEG	NEG	NEG	NEG	Y2H-PRS
SPP1 + CTNNBL1	0,5	0,5	ND	ND	ND	ND	NEG	NEG	0,9	0,9	ND	ND	ND	ND	NEG	NEG	NEG	NEG	Y2H-PRS
SULT2B1 + ALS2CR12	41,7	34,6	11,4	1,1	10,9	0,5	POS	POS	37,4	30,3	288,1	40,4	228,2	20,2	POS	POS	POS	POS	Y2H-PRS
TADA2A + TADA3	186,2	185,5	122	13,3	127,1	3,9	POS	POS	310,9	286,9	108,5	7,7	113,4	6,9	POS	POS	POS	POS	Y2H-PRS
TDO2 + ASMTL	0,2	0,2	ND	ND	ND	ND	NEG	NEG	29,7	63,5	10,7	1	6,5	3,2	POS	POS	POS	POS	Y2H-PRS
TGFB1I1 + NR3C1	2,7	2	ND	ND	ND	ND	NEG	NEG	2	1,2	ND	ND	ND	ND	NEG	NEG	NEG	NEG	Y2H-PRS
TK1 + CRMP1	7,5	6,1	1,6	0,2	1,1	0,2	NEG	NEG	1,9	1,7	ND	ND	ND	ND	NEG	NEG	NEG	NEG	Y2H-PRS
TP53 + LAMA4	3,8	3,3	0,4	0,1	0,5	0,1	NEG	NEG	4,5	3,4	17,4	1,1	4,8	2,5	POS	POS	POS	POS	Y2H-PRS
TRAF2 + IRF4	2,1	1,8	ND	ND	ND	ND	NEG	NEG	2,7	2,2	ND	ND	ND	ND	NEG	NEG	NEG	NEG	Y2H-PRS
TTR + FEZ1	5,7	4,2	1,3	0,1	1,2	0,3	NEG	NEG	2	2,7	ND	ND	ND	ND	NEG	NEG	NEG	NEG	Y2H-PRS
TUBB2A + RIC8A	1,4	1,3	ND	ND	ND	ND	NEG	NEG	2,3	2,6	ND	ND	ND	ND	NEG	NEG	NEG	NEG	Y2H-PRS
UBE2D3 + MEX3B	ND	ND	ND	ND	ND	ND	IP	IP	0,3	0,4	ND	ND	ND	ND	NEG	NEG	NEG	NEG	Y2H-PRS
UGP2 + ARIH2	3,3	3,2	1,7	0,3	1,6	0,2	NEG	NEG	3,3	3,4	2,2	0,3	2,5	0,5	NEG	NEG	NEG	NEG	Y2H-PRS
VIL1 + TEX11	1,5	1,5	ND	ND	ND	ND	NEG	NEG	1,9	2,2	ND	ND	ND	ND	NEG	NEG	NEG	NEG	Y2H-PRS

	set a								set b								set a+b		
Interaction	ICR Exp1	ICR Exp2	mean cNIR Exp1	sem cNIR Exp1	mean cNIR Exp2	sem cNIR Exp2	result Exp1	result Exp2	ICR Exp1	ICR Exp2	mean cNIR Exp1	sem cNIR Exp1	mean cNIR Exp2	sem cNIR Exp2	result Exp1	result Exp2	result Exp1	result Exp2	Set
VIM + HMG20B	3,9	3,7	1,1	0,3	1	0,2	NEG	NEG	0,8	0,7	ND	ND	ND	ND	NEG	NEG	NEG	NEG	Y2H-PRS
YY1 + FKBP1A	3,4	3,1	0,1	0,1	0,1	0,1	NEG	NEG	2,2	1,9	ND	ND	ND	ND	NEG	NEG	NEG	NEG	Y2H-PRS
YWHAG + TERF1	0,7	0,8	ND	ND	ND	ND	NEG	NEG	2	2,3	ND	ND	ND	ND	NEG	NEG	NEG	NEG	Y2H-PRS
ZBTB25 + SORBS3	1,4	1	ND	ND	ND	ND	NEG	NEG	64,7	114,2	15,2	1,7	7,8	3,9	POS	POS	POS	POS	Y2H-PRS
AIMP2 + FHL3	9,6	14,1	5	0,6	5,7	0,3	POS	POS	4,1	3,5	9,8	1,1	8,9	0,5	POS	POS	POS	POS	Y2H-PRS
ANP32A + NSFL1C	0,8	1	ND	ND	ND	ND	NEG	NEG	0,5	0,5	ND	ND	ND	ND	NEG	NEG	NEG	NEG	Y2H-PRS
NME5 + DYDC2	108,7	100,5	11,6	0,3	9,8	1,1	POS	POS							NC	NC	POS	POS	Y2H-PRS
NCK2 + CPSF6	2,2	1,5	ND	ND	ND	ND	NEG	NEG	1,6	1,5	ND	ND	ND	ND	NEG	NEG	NEG	NEG	Y2H-PRS
PIAS1 + ESR1							NC	NC	5,8	4,3	1	0	0,8	0,3	NEG	NEG	NEG	NEG	Y2H-PRS
DENR + MCTS1	0,1	0,1	ND	ND	ND	ND	NEG	NEG	14,1	12,5	79,3	4,8	70,8	4,7	POS	POS	POS	POS	Y2H-PRS
USO1 + C1orf94	5,5	7	6,9	1	6	0,5	POS	POS	3,7	3,4	5,2	1,4	3,6	0,7	POS	POS	POS	POS	Y2H-PRS
EIF3H + ABI3	0,4	0,4	ND	ND	ND	ND	NEG	NEG	1,2	1,4	ND	ND	ND	ND	NEG	NEG	NEG	NEG	Y2H-PRS
RAB11A + DTNBP1	3,4	3,3	-0,1	0	0	0	NEG	NEG	1,2	1,2	ND	ND	ND	ND	NEG	NEG	NEG	NEG	Y2H-PRS
TSC22D1 + CCDC90B	0,5	0,4	ND	ND	ND	ND	NEG	NEG	0,6	0,7	ND	ND	ND	ND	NEG	NEG	NEG	NEG	Y2H-PRS
LDB1 + SSBP2							NC	NC	28	31,9	60,2	4	53,8	4,2	POS	POS	POS	POS	Y2H-PRS
PRC1 + USHBP1	2,1	1,8	ND	ND	ND	ND	NEG	NEG	0,8	0,6	ND	ND	ND	ND	NEG	NEG	NEG	NEG	Y2H-PRS
USP2 + BEND5	1,3	1,2	ND	ND	ND	ND	NEG	NEG	1,6	2,5	ND	ND	ND	ND	NEG	NEG	NEG	NEG	Y2H-PRS
AIFM1 + SETDB1	13,5	11,5	3,5	0,2	3,3	0,3	POS	POS	7,4	6,4	7,8	1,3	7	0,6	POS	POS	POS	POS	Y2H-PRS
SRSF11 + ETS1	1,8	3	ND	ND	0	0	NEG	NEG	1,2	0,8	ND	ND	ND	ND	NEG	NEG	NEG	NEG	Y2H-PRS
TRIP13 + PPP2CA	15,3	15,7	3,1	0,2	3,7	0,3	POS	POS	11,9	12,4	27,4	1,6	26,4	6,3	POS	POS	POS	POS	Y2H-PRS
RAB33A + RABAC1	0,6	0,5	ND	ND	ND	ND	NEG	NEG	0,7	0,6	ND	ND	ND	ND	NEG	NEG	NEG	NEG	Y2H-PRS
HOMER1 + C1orf116	10,6	10	2,7	0,5	2,6	0,3	NEG	NEG	25,2	23	16,7	0,9	18,2	0,5	POS	POS	POS	POS	Y2H-PRS
TR_HOMER1 + C1orf116	10,6	10	2,7	0,5	2,6	0,3	NEG	NEG	25,2	23	16,7	0,9	18,2	0,5	POS	POS	POS	POS	Y2H-PRS
FHL5 + FHL2							NC	NC	11,3	9,6	8,6	0,9	7,5	0,2	POS	POS	POS	POS	Y2H-PRS
FXR2 + KIAA1217	4,8	6,1	2,4	0,4	2,2	0,4	NEG	NEG	4,6	3,9	8,9	1,5	9,4	1	POS	POS	POS	POS	Y2H-PRS
LITAF + RADIL	ND	ND	ND	ND	ND	ND	IP	IP	ND	ND	ND	ND	ND	ND	PREY	PREY	ND	ND	Y2H-PRS
DAZAP2 + AATF	1,4	0,7	ND	ND	ND	ND	NEG	NEG	0,8	0,9	ND	ND	ND	ND	NEG	NEG	NEG	NEG	Y2H-PRS
POM121 + CEP55	ND	ND	ND	ND	ND	ND	IP	IP	ND	ND	ND	ND	ND	ND	PREY	PREY	ND	ND	Y2H-PRS
PDCD6IP + GRB2	0,5	0,4	ND	ND	ND	ND	NEG	NEG	3,7	3,6	3,2	0,7	2,7	0,2	POS	NEG	POS	NEG	Y2H-PRS
SF3B4 + ILF3	5,5	4,6	1,3	0,2	1,6	0,1	NEG	NEG	3	2,4	0,6	0,1	ND	ND	NEG	NEG	NEG	NEG	Y2H-PRS
MCRS1 + LSM6	0,3	0,3	ND	ND	ND	ND	NEG	NEG	1,4	0,4	ND	ND	ND	ND	NEG	NEG	NEG	NEG	Y2H-PRS
MAD2L2 + ADAM15	ND	ND	ND	ND	ND	ND	PREY	PREY	ND	ND	ND	ND	ND	ND	IP	IP	ND	ND	Y2H-PRS
TADA3 + CCDC101	129,6	162,3	80,3	4,2	77,7	1,2	POS	POS	249,6	246,5	87,5	5,9	80	3,1	POS	POS	POS	POS	Y2H-PRS
PRDX4 + NR4A1	1	1	ND	ND	ND	ND	NEG	NEG	0,8	0,7	ND	ND	ND	ND	NEG	NEG	NEG	NEG	Y2H-PRS
RABAC1 + RAB7A	0,1	0,1	ND	ND	ND	ND	NEG	NEG	0,6	0,6	ND	ND	ND	ND	NEG	NEG	NEG	NEG	Y2H-PRS
PDLIM5 + PRKCE							NC	NC	2,1	0,1	ND	ND	ND	ND	NEG	NEG	NEG	NEG	Y2H-PRS
SPAG5 + SNAPIN	62,4	70,2	27,7	5,5	37,8	2,4	POS	POS	56,4	72,3	25,3	0,9	22,1	0,4	POS	POS	POS	POS	Y2H-PRS
STAMBP + CHMP4A	3,4	6	3,6	0,2	5,2	1	POS	POS	1,7	1,1	ND	ND	ND	ND	NEG	NEG	POS	POS	Y2H-PRS
SIX2 + AES	6,7	10,8	2,8	0,8	4,5	1	NEG	POS	10,3	12,3	4,1	0,3	5,5	0,4	POS	POS	POS	POS	Y2H-PRS
GADD45G + PTPRK	0,1	0,1	ND	ND	ND	ND	NEG	NEG	3,4	4	43,6	5,5	55,6	7,1	POS	POS	POS	POS	Y2H-PRS
COPS5 + HAND2	4,2	4,9	1,6	0,3	2	0,4	NEG	NEG	2,2	2,4	ND	ND	ND	ND	NEG	NEG	NEG	NEG	Y2H-PRS
IMMT + CCDC113	14,2	17,1	20,4	5,1	22,4	3,3	POS	POS	2	1,5	ND	ND	ND	ND	NEG	NEG	POS	POS	Y2H-PRS
CCDC85B + PRC1	0,6	0,7	ND	ND	ND	ND	NEG	NEG	0,6	0,8	ND	ND	ND	ND	NEG	NEG	NEG	NEG	Y2H-PRS
RBPMS + ZNF581	1,9	1,6	ND	ND	ND	ND	NEG	NEG	2,2	2,3	ND	ND	ND	ND	NEG	NEG	NEG	NEG	Y2H-PRS
MID2 + DYDC1	3,1	3,8	0,7	0,1	0,8	0,1	NEG	NEG	11,8	5,1	25,9	0,7	3,2	4,1	POS	POS	POS	POS	Y2H-PRS
CPSF6 + ARMC7	2,5	1,9	ND	ND	ND	ND	NEG	NEG	2	1,6	ND	ND	ND	ND	NEG	NEG	NEG	NEG	Y2H-PRS
XRN2 + TOLLIP	2	2,7	ND	ND	ND	ND	NEG	NEG	1,8	0	ND	ND	ND	ND	NEG	NEG	NEG	NEG	Y2H-PRS
GGA2 + ARF3	0,7	0,4	ND	ND	ND	ND	NEG	NEG	2,8	2,3	ND	ND	ND	ND	NEG	NEG	NEG	NEG	Y2H-PRS
SF3B3 + EFTUD2	7,2	6,9	2,9	0,2	3,5	0,5	NEG	POS	4,6	5,2	3,2	0,4	3,2	0,7	POS	POS	POS	POS	Y2H-PRS
LDOC1 + NRIP1	8,3	7,5	5,3	0,4	4,1	0	POS	POS	ND	ND	ND	ND	ND	ND	IP	IP	POS	POS	Y2H-PRS
RAD54B + CCDC33	1,6	1,5	ND	ND	ND	ND	NEG	NEG	1,9	1,5	ND	ND	ND	ND	NEG	NEG	NEG	NEG	Y2H-PRS
SUMF2 + ZFYVE9	7,6	7,5	-1,3	0,2	0,5	0,1	NEG	NEG	2	2	ND	ND	ND	ND	NEG	NEG	NEG	NEG	Y2H-PRS
RNF11 + PDCD6IP	4,7	4,4	3,4	0,5	2,3	0	POS	NEG	1,3	0,7	ND	ND	ND	ND	NEG	NEG	POS	NEG	Y2H-PRS
TUBGCP4 + FBF1	1,5	1,5	ND	ND	ND	ND	NEG	NEG	7,1	5,7	4,7	0,1	5,5	0,1	POS	POS	POS	POS	Y2H-PRS
LSM1 + UXT	6,4	5,7	0,5	0,1	0,6	0,1	NEG	NEG	1,6	1,4	ND	ND	ND	ND	NEG	NEG	NEG	NEG	Y2H-PRS
CHMP4A + SYT17	1	1	ND	ND	ND	ND	NEG	NEG	2,4	2,7	ND	ND	ND	ND	NEG	NEG	NEG	NEG	Y2H-PRS
NME7 + TNIP1	5	5	8,7	1,4	7,7	0,3	POS	POS	1,4	1,1	ND	ND	ND	ND	NEG	NEG	POS	POS	Y2H-PRS
EFEMP2 + ZNF426	2,2	2,7	ND	ND	ND	ND	NEG	NEG	0,1	0,1	ND	ND	ND	ND	NEG	NEG	NEG	NEG	Y2H-PRS
CXXC5 + SMAD3							NC	NC	1,7	1,8	ND	ND	ND	ND	NEG	NEG	NEG	NEG	Y2H-PRS
MBIP + PLEKHF2	1,2	1,1	ND	ND	ND	ND	NEG	NEG	0,4	0,4	ND	ND	ND	ND	NEG	NEG	NEG	NEG	Y2H-PRS
LUC7L2 + KIAA1377	3,2	4,6	0,3	0,2	0,3	0,1	NEG	NEG	0,9	0,7	ND	ND	ND	ND	NEG	NEG	NEG	NEG	Y2H-PRS
SUFU + HMGA1	2	1	ND	ND	ND	ND	NEG	NEG	0,6	0,5	ND	ND	ND	ND	NEG	NEG	NEG	NEG	Y2H-PRS
SYT17 + TSC22D4	1,1	0,7	ND	ND	ND	ND	NEG	NEG	0,8	0,9	ND	ND	ND	ND	NEG	NEG	NEG	NEG	Y2H-PRS
EXOSC4 + DOM3Z	1,8	2,1	ND	ND	ND	ND	NEG	NEG	1,3	1,3	ND	ND	ND	ND	NEG	NEG	NEG	NEG	Y2H-PRS
NECAB2 + GTPBP10	3,4	2,9	0,7	0	ND	ND	NEG	NEG	3,1	4,3	14,8	2,7	21,9	3,7	POS	POS	POS	POS	Y2H-PRS
RNF111 + UBE2D1	ND	ND	ND	ND	ND	ND	IP	IP	2,3	2,1	ND	ND	ND	ND	NEG	NEG	NEG	NEG	Y2H-PRS
WDYHV1 + PLDN	0,9	0,9	ND	ND	ND	ND	NEG	NEG	1,6	1,4	ND	ND	ND	ND	NEG	NEG	NEG	NEG	Y2H-PRS
THAP1 + ZCCHC10	7,9	7,3	3,5	0,8	3,1	0,6	POS	POS	6,9	10,1	61,8	8,8	67,8	7	POS	POS	POS	POS	Y2H-PRS
UBE2W + XIAP	2,8	2,7	ND	ND	ND	ND	NEG	NEG	2	2,3	ND	ND	ND	ND	NEG	NEG	NEG	NEG	Y2H-PRS
DDX19A + MIF4GD							NC	NC	12,7	4,1	1,8	0,3	0,3	0,5	NEG	NEG	NEG	NEG	Y2H-PRS
FAM46A + KEAP1	3,8	4,4	6,1	1,5	4,7	0,3	POS	POS	2,4	2,7	ND	ND	ND	ND	NEG	NEG	POS	POS	Y2H-PRS
LUC7L + GADD45G	1,1	1,2	ND	ND	ND	ND	NEG	NEG	3	3,3	0,3	0,1	0,2	0,2	NEG	NEG	NEG	NEG	Y2H-PRS
RCOR3 + KIAA0182	81,7	92,2	41,5	3,3	38,8	1,7	POS	POS	145,2	146,6	156,9	15,8	143,4	13,1	POS	POS	POS	POS	Y2H-PRS
TEX11 + RIBC2	2,5	2,3	ND	ND	ND	ND	NEG	NEG	4,3	4,6	2,1	0,3	2,2	0,4	NEG	NEG	NEG	NEG	Y2H-PRS
EXOSC5 + CDK5RAP1	2,9	3,7	ND	ND	2,3	0,2	NEG	NEG	3	7	4,9	0,6	6,8	0,8	POS	POS	POS	POS	Y2H-PRS

	set a								set b								set a+b		
Interaction	ICR Exp1	ICR Exp2	mean cNIR Exp1	sem cNIR Exp1	mean cNIR Exp2	sem cNIR Exp2	result Exp1	result Exp2	ICR Exp1	ICR Exp2	mean cNIR Exp1	sem cNIR Exp1	mean cNIR Exp2	sem cNIR Exp2	result Exp1	result Exp2	result Exp1	result Exp2	Set
CHMP1B + CHMP1A	11,9	10,7	3,6	0,4	4,3	0,8	POS	POS	13,5	14,1	7,3	0,1	7,1	0,9	POS	POS	POS	POS	Y2H-PRS
KLHDC5 + RCN3	4,4	4,4	3,3	0,8	2,8	0,1	POS	NEG	2,4	5,5	ND	ND	3,5	2,1	NEG	POS	POS	POS	Y2H-PRS
BEGAIN + CATSPER1	19,4	22,4	5,2	0,9	5,2	0,4	POS	POS	1,6	1,8	ND	ND	ND	ND	NEG	NEG	POS	POS	Y2H-PRS
C1orf114 + PPP1CA	9,1	6,4	2,2	0,2	2	0,1	NEG	NEG	12,2	13,6	3	0,2	3	0,3	POS	POS	POS	POS	Y2H-PRS
KLHL12 + SNX20	4,9	5	2,1	0,3	1,9	0,2	NEG	NEG	9,8	7,9	7	1,2	7,8	2,1	POS	POS	POS	POS	Y2H-PRS
NIF3L1 + CUTC	2,4	2,9	ND	ND	ND	ND	NEG	NEG	0,5	0,6	ND	ND	ND	ND	NEG	NEG	NEG	NEG	Y2H-PRS
SNIP1 + SP100	5,3	13,2	2,2	0,3	2,4	0,6	NEG	NEG	2,2	1,6	ND	ND	ND	ND	NEG	NEG	NEG	NEG	Y2H-PRS
CCDC33 + KHDRBS3	40,7	34,5	73,1	7,9	76,9	15,4	POS	POS	1	1	ND	ND	ND	ND	NEG	NEG	POS	POS	Y2H-PRS
CLPB + SMAD9	2,3	1,8	ND	ND	ND	ND	NEG	NEG	0,6	0,5	ND	ND	ND	ND	NEG	NEG	NEG	NEG	Y2H-PRS
KRTAP4-12 + ZNF250	3,5	2,8	10,6	0,3	ND	ND	POS	NEG	1,3	1,4	ND	ND	ND	ND	NEG	NEG	POS	NEG	Y2H-PRS
MYCBPAP + PRKAR2A							NC	NC	3,9	2,4	2,4	0,6	ND	ND	NEG	NEG	NEG	NEG	Y2H-PRS
TRIM63 + TCAP	1,9	2,4	ND	ND	ND	ND	NEG	NEG	0,3	0,4	ND	ND	ND	ND	NEG	NEG	NEG	NEG	Y2H-PRS
GTPBP3 + PARP11	8,1	5,7	3,8	0,4	2,4	0,1	POS	NEG	5,3	4,7	19,9	5,7	17,4	2,9	POS	POS	POS	POS	Y2H-PRS
C1orf94 + MAPK1IP1L	2,6	3,6	ND	ND	1	0,3	NEG	NEG	3,4	2,5	11,9	3,5	ND	ND	POS	NEG	POS	NEG	Y2H-PRS
FBF1 + FAS	ND	ND	ND	ND	ND	ND	PREY	PREY	ND	ND	ND	ND	ND	ND	IP	IP	ND	ND	Y2H-PRS
FATE1 + TRAF2	3,5	2,7	3,2	0,2	ND	ND	POS	NEG	3,7	3,2	3,1	0,4	-5,5	0,6	POS	NEG	POS	NEG	Y2H-PRS
CCDC120 + CEP170P1							NC	NC	8,1	12,8	2,7	0,3	3,5	0,4	NEG	POS	NEG	POS	Y2H-PRS
RHEBL1 + TXNL4A	2,8	3,2	ND	ND	0,2	0	NEG	NEG	3,8	3,6	1,3	0,1	1,1	0,1	NEG	NEG	NEG	NEG	Y2H-PRS
DPPA2 + MOAP1	1,7	1	ND	ND	ND	ND	NEG	NEG	1,3	1,5	ND	ND	ND	ND	NEG	NEG	NEG	NEG	Y2H-PRS
C1orf65 + PDLIM7							NC	NC	ND	ND	ND	ND	ND	ND	IP	IP	NEG	NEG	Y2H-PRS
KCNRG + CCNK	1,1	0,7	ND	ND	ND	ND	NEG	NEG	0,1	0,1	ND	ND	ND	ND	NEG	NEG	NEG	NEG	Y2H-PRS
AES + EAF1	4,0	3,5	4,7	0,9	4,5	1,1	POS	POS	4,3	3,3	1,7	0,5	1,7	0,5	NEG	NEG	POS	POS	HI-PRS
ALAS1 + KLHL35	2,0	2,3	ND	ND	ND	ND	NEG	NEG	3,8	4,0	10,7	1,5	8,9	0,6	POS	POS	POS	POS	HI-PRS
XIAP + CKS1B	0,3	0,3	ND	ND	ND	ND	NEG	NEG	0,7	1,0	ND	ND	ND	ND	NEG	NEG	NEG	NEG	HI-PRS
AQP1 + CRTAC1	1,2	1,4	ND	ND	ND	ND	NEG	NEG	0,1	0,0	ND	ND	ND	ND	NEG	NEG	NEG	NEG	HI-PRS
TRIM23 + RSRC2	0,9	0,8	ND	ND	ND	ND	NEG	NEG	0,4	0,4	ND	ND	ND	ND	NEG	NEG	NEG	NEG	HI-PRS
ARL2 + PDE6D	8,6	11,9	5,4	0,7	7,4	1,3	POS	POS	1,9	2,2	ND	ND	ND	ND	NEG	NEG	POS	POS	HI-PRS
ARR3 + ZNF496	3,3	3,0	27,2	1,7	23,6	2,5	POS	POS	2,0	1,8	ND	ND	ND	ND	NEG	NEG	POS	POS	HI-PRS
BCL6 + BLZF1	11,9	9,8	16,7	2,8	13,3	0,6	POS	POS	5,8	5,7	36,7	3,2	43,7	5,5	POS	POS	POS	POS	HI-PRS
CAMK2B + C13orf1	0,4	0,3	ND	ND	ND	ND	NEG	NEG	1,9	2,3	ND	ND	ND	ND	NEG	NEG	NEG	NEG	HI-PRS
CCND3 + CDK6	114,1	101,4	38,2	2,7	37,2	3,9	POS	POS	43,4	39,2	20,9	4,3	17,4	2,7	POS	POS	POS	POS	HI-PRS
CDC42 + CDC42EP2	5,7	8,1	4,2	0,1	5,8	0,4	POS	POS	5,6	4,7	2,1	0,1	3,6	0,5	NEG	POS	POS	POS	HI-PRS
CDR2 + SMARCE1	0,9	1,1	ND	ND	ND	ND	NEG	NEG	0,5	0,9	ND	ND	ND	ND	NEG	NEG	NEG	NEG	HI-PRS
CRX + SOX5	8,1	8,0	71,1	6,2	67,9	7,1	POS	POS	14,9	9,3	4,7	0,2	5,5	1,2	POS	POS	POS	POS	HI-PRS
CTBP1 + HOXB5	0,5	1,0	ND	ND	ND	ND	NEG	NEG	1,3	2,6	ND	ND	ND	ND	NEG	NEG	NEG	NEG	HI-PRS
CTBP2 + ZNF750	10,7	12,4	11,3	1,8	14,5	2,0	POS	POS	13,9	24,8	70,8	6,6	86,0	6,1	POS	POS	POS	POS	HI-PRS
DDIT3 + FOSL2	7,3	6,5	20,0	0,7	22,5	1,0	POS	POS	2,5	3,2	ND	ND	5,3	0,4	NEG	POS	POS	POS	HI-PRS
FABP3 + NUP62	1,9	1,3	ND	ND	ND	ND	NEG	NEG	0,4	0,4	ND	ND	ND	ND	NEG	NEG	NEG	NEG	HI-PRS
GCSH + SFI1	ND	ND	ND	ND	ND	ND	PREY	PREY	ND	ND	ND	ND	ND	ND	IP	IP	ND	ND	HI-PRS
GOLGA2 + RIBC1	2,5	2,1	ND	ND	ND	ND	NEG	NEG	1,5	0,8	ND	ND	ND	ND	NEG	NEG	NEG	NEG	HI-PRS
HSPA8 + BAG3							NC	NC	3,0	5,8	1,7	0,1	1,8	0,1	NEG	NEG	NEG	NEG	HI-PRS
KIF2A + MRPL53	1,2	0,9	ND	ND	ND	ND	NEG	NEG	2,3	3,4	ND	ND	2,4	0,3	NEG	NEG	NEG	NEG	HI-PRS
KRTAP5-9 + ZNF581	1,0	0,8	ND	ND	ND	ND	NEG	NEG	ND	ND	ND	ND	ND	ND	PREY	PREY	NEG	NEG	HI-PRS
LGALS3 + PPIG	1,1	0,5	ND	ND	ND	ND	NEG	NEG	0,6	1,4	ND	ND	ND	ND	NEG	NEG	NEG	NEG	HI-PRS
MAGEA11 + PHF16	8,1	7,6	18,1	2,2	23,1	5,6	POS	POS	6,4	6,9	29,0	0,4	30,3	1,6	POS	POS	POS	POS	HI-PRS
MAGOH + RBM8A	142,5	160,1	54,3	5,0	64,8	3,8	POS	POS	42,6	54,0	60,5	2,2	76,3	9,4	POS	POS	POS	POS	HI-PRS
MDFI + PDIA5	3,1	3,0	16,0	3,2	17,9	1,5	POS	NEG	3,5	4,9	34,1	2,7	37,5	0,8	POS	POS	POS	POS	HI-PRS
MEOX1 + RANBP3	1,6	1,5	ND	ND	ND	ND	NEG	NEG	4,2	2,7	2,9	0,4	ND	ND	NEG	NEG	NEG	NEG	HI-PRS
MFAP1 + ZFP64	0,9	1,1	ND	ND	ND	ND	NEG	NEG	5,5	4,6	2,6	0,8	2,6	0,2	NEG	NEG	NEG	NEG	HI-PRS
CTAGE5 + MAGEB18	0,9	1,2	ND	ND	ND	ND	NEG	NEG	3,0	3,8	0,4	0,0	0,6	0,2	NEG	NEG	NEG	NEG	HI-PRS
NME1 + PID1	0,2	0,2	ND	ND	ND	ND	NEG	NEG	3,5	3,5	6,6	1,1	6,5	0,7	POS	POS	POS	POS	HI-PRS
PCBD1 + FXR2	0,2	1,1	ND	ND	ND	ND	NEG	NEG	1,6	1,6	ND	ND	ND	ND	NEG	NEG	NEG	NEG	HI-PRS
PLSCR1 + GDPD5	0,2	0,3	ND	ND	ND	ND	NEG	NEG	0,5	0,5	ND	ND	ND	ND	NEG	NEG	NEG	NEG	HI-PRS
PTPN3 + DIP2A	ND	ND	ND	ND	ND	ND	IP	IP	ND	ND	ND	ND	ND	ND	PREY	PREY	ND	ND	HI-PRS
REL + TRIM74	2,6	2,6	ND	ND	ND	ND	NEG	NEG	1,0	2,1	ND	ND	ND	ND	NEG	NEG	NEG	NEG	HI-PRS
RPLP0 + CCNDBP1	87,1	80,8	154,6	18,0	140,1	10,4	POS	POS	16,6	15,3	45,1	2,6	40,5	5,1	POS	POS	POS	POS	HI-PRS
SDCBP + CT45A5	0,4	0,3	ND	ND	ND	ND	NEG	NEG	1,7	1,6	ND	ND	ND	ND	NEG	NEG	NEG	NEG	HI-PRS
SIAH1 + DNALI1	0,8	1,0	ND	ND	ND	ND	NEG	NEG	0,9	0,9	ND	ND	ND	ND	NEG	NEG	NEG	NEG	HI-PRS
SKP1 + FBXO28	44,8	43,8	24,8	0,0	21,9	1,2	POS	POS	50,5	65,0	50,4	2,9	66,3	4,8	POS	POS	POS	POS	HI-PRS
TCF12 + NEUROG3	9,3	10,2	148,0	0,6	149,1	25,9	POS	POS	3,2	4,7	0,5	0,1	0,5	0,1	NEG	NEG	POS	POS	HI-PRS
SUMO1 + ZMYM5	1,9	1,9	ND	ND	ND	ND	NEG	NEG	1,2	1,3	ND	ND	ND	ND	NEG	NEG	NEG	NEG	HI-PRS
SDPR + A1CF							NC	NC	1,9	1,5	ND	ND	ND	ND	NEG	NEG	NEG	NEG	HI-PRS
NCK2 + RBM26	0,6	0,6	ND	ND	ND	ND	NEG	NEG	2,3	1,7	ND	ND	ND	ND	NEG	NEG	NEG	NEG	HI-PRS
CADPS + C19orf66	2,8	2,3	ND	ND	ND	ND	NEG	NEG	1,8	1,5	ND	ND	ND	ND	NEG	NEG	NEG	NEG	HI-PRS
EIF2B2 + C9orf72	3,0	3,0	0,9	0,1	0,8	0,1	NEG	NEG	3,9	2,7	1,4	0,0	ND	ND	NEG	NEG	NEG	NEG	HI-PRS
FXR2 + CDKL3	1,4	1,3	ND	ND	ND	ND	NEG	NEG	1,2	2,6	ND	ND	ND	ND	NEG	NEG	NEG	NEG	HI-PRS
HDAC4 + EFEMP2	0,2	0,1	ND	ND	ND	ND	NEG	NEG	ND	ND	ND	ND	ND	ND	IP	IP	NEG	NEG	HI-PRS
POM121 + PAXIP1	ND	ND	ND	ND	ND	ND	IP	IP	ND	ND	ND	ND	ND	ND	PREY	PREY	ND	ND	HI-PRS
PDCD6IP + CEP55	34,9	37,0	20,9	2,8	18,4	2,5	POS	POS	5,8	3,2	23,2	3,6	18,3	2,0	POS	POS	POS	POS	HI-PRS
RABAC1 + ADCK3	0,7	0,7	ND	ND	ND	ND	NEG	NEG	1,1	1,7	ND	ND	ND	ND	NEG	NEG	NEG	NEG	HI-PRS
RBPMS + RDH12	1,1	1,1	ND	ND	ND	ND	NEG	NEG	1,4	1,4	ND	ND	ND	ND	NEG	NEG	NEG	NEG	HI-PRS
EXOSC8 + COL23A1	0,2	0,2	ND	ND	ND	ND	NEG	NEG	5,3	4,1	6,2	0,8	5,8	1,1	POS	POS	POS	POS	HI-PRS
GABARAPL2 + TSR2	3,9	3,5	0,1	0,0	0,1	0,0	NEG	NEG	0,4	0,4	ND	ND	ND	ND	NEG	NEG	NEG	NEG	HI-PRS
PUF60 + SAP30BP	3,1	3,0	0,7	0,1	0,9	0,0	NEG	NEG	10,3	8,6	6,4	0,8	4,9	0,4	POS	POS	POS	POS	HI-PRS
TRIM32 + PTCD2	2,1	2,3	ND	ND	ND	ND	NEG	NEG	ND	ND	ND	ND	ND	ND	IP	IP	NEG	NEG	HI-PRS

	set a								set b								set a+b		
Interaction	ICR Exp1	ICR Exp2	mean cNIR Exp1	sem cNIR Exp1	mean cNIR Exp2	sem cNIR Exp2	result Exp1	result Exp2	ICR Exp1	ICR Exp2	mean cNIR Exp1	sem cNIR Exp1	mean cNIR Exp2	sem cNIR Exp2	result Exp1	result Exp2	result Exp1	result Exp2	Set
CCNDBP1 + ZNF627	5,3	5,2	3,1	0,4	3,0	0,3	POS	POS	ND	ND	ND	ND	ND	ND	IP	IP	POS	POS	HI-PRS
LDOC1 + FAM90A1	0,9	1,1	ND	ND	ND	ND	NEG	NEG	0,7	0,9	ND	ND	ND	ND	NEG	NEG	NEG	NEG	HI-PRS
ARFIP2 + MAL2	2,5	3,1	ND	ND	0,5	0,1	NEG	NEG	3,7	6,0	0,6	0,0	0,9	0,0	NEG	NEG	NEG	NEG	HI-PRS
TFIP11 + LOC729862	0,8	0,7	ND	ND	ND	ND	NEG	NEG	ND	ND	ND	ND	ND	ND	IP	IP	NEG	NEG	HI-PRS
CBY1 + CCDC11	4,3	2,2	8,2	1,3	ND	ND	POS	NEG	0,7	0,7	ND	ND	ND	ND	NEG	NEG	POS	NEG	HI-PRS
TUBGCP4 + RNF146	2,0	2,1	ND	ND	ND	ND	NEG	NEG	1,7	1,1	ND	ND	ND	ND	NEG	NEG	NEG	NEG	HI-PRS
UBQLN1 + ZNF343	0,3	0,4	ND	ND	ND	ND	NEG	NEG	0,2	0,3	ND	ND	ND	ND	NEG	NEG	NEG	NEG	HI-PRS
C21orf45 + ZNF471	4,6	4,1	2,1	0,2	2,3	0,3	NEG	NEG	8,0	7,1	22,4	3,1	22,2	2,7	POS	POS	POS	POS	HI-PRS
KCTD9 + FAM124B	0,3	0,4	ND	ND	ND	ND	NEG	NEG	1,3	1,3	ND	ND	ND	ND	NEG	NEG	NEG	NEG	HI-PRS
PRMT6 + KIF9	4,2	4,2	3,7	1,2	4,7	1,2	POS	POS	1,8	1,8	ND	ND	ND	ND	NEG	NEG	POS	POS	HI-PRS
VAC14 + CDRT4	1,5	1,8	ND	ND	ND	ND	NEG	NEG	1,7	2,0	ND	ND	ND	ND	NEG	NEG	NEG	NEG	HI-PRS
CTNNBL1 + C2orf62	1,5	1,9	ND	ND	ND	ND	NEG	NEG	0,7	0,6	ND	ND	ND	ND	NEG	NEG	NEG	NEG	HI-PRS
LXN + GSG1L	ND	ND	ND	ND	ND	ND	PREY	PREY	0,8	0,4	ND	ND	ND	ND	NEG	NEG	NEG	NEG	HI-PRS
NIF3L1 + C15orf38	0,9	0,7	ND	ND	ND	ND	NEG	NEG	0,8	0,6	ND	ND	ND	ND	NEG	NEG	NEG	NEG	HI-PRS
GRAMD3 + NAPRT1	0,7	0,8	ND	ND	ND	ND	NEG	NEG	4,8	3,7	3,5	0,9	1,8	0,7	POS	NEG	POS	NEG	HI-PRS
BOLL + ZNF385C	5,1	5,2	12,0	1,0	12,5	0,7	POS	POS	1,4	1,6	ND	ND	ND	ND	NEG	NEG	POS	POS	HI-PRS
AAGAB + AP1S3	2,7	2,5	ND	ND	ND	ND	NEG	NEG	11,5	12,6	7,9	0,4	7,2	0,9	POS	POS	POS	POS	HI-PRS
NDEL1 + ZNF572	5,1	11,3	66,5	10,3	64,7	4,2	POS	POS	3,5	2,9	29,9	1,6	ND	ND	POS	NEG	POS	POS	HI-PRS
PIH1D2 + DPH3	0,8	0,7	ND	ND	ND	ND	NEG	NEG	2,4	2,6	ND	ND	ND	ND	NEG	NEG	NEG	NEG	HI-PRS
KLC3 + CENPP	2,9	2,4	ND	ND	ND	ND	NEG	NEG	2,5	2,2	ND	ND	ND	ND	NEG	NEG	NEG	NEG	HI-PRS
ZNF483 + ZSCAN22	15,9	13,5	29,4	0,8	22,1	1,2	POS	POS	0,1	0,1	ND	ND	ND	ND	NEG	NEG	POS	POS	HI-PRS
C19orf46 + C10orf35	3,1	3,0	0,7	0,0	0,5	0,1	NEG	NEG	0,5	0,3	ND	ND	ND	ND	NEG	NEG	NEG	NEG	HI-PRS
ACTG1 + TMPRSS4							NC	NC	0,8	0,7	ND	ND	ND	ND	NEG	NEG	NEG	NEG	Y2H-RRS
AP2A1 + C1orf103	0,5	0,6	ND	ND	ND	ND	NEG	NEG	ND	ND	ND	ND	ND	ND	PREY	PREY	NEG	NEG	Y2H-RRS
AGT + RHEBL1	1,2	1,3	ND	ND	ND	ND	NEG	NEG	0,6	0,8	ND	ND	ND	ND	NEG	NEG	NEG	NEG	Y2H-RRS
APBB2 + RPL6	0,8	0,8	ND	ND	ND	ND	NEG	NEG	0,8	0,7	ND	ND	ND	ND	NEG	NEG	NEG	NEG	Y2H-RRS
AQP1 + HIST1H3H	0,7	0,3	ND	ND	ND	ND	NEG	NEG	0,2	0,1	ND	ND	ND	ND	NEG	NEG	NEG	NEG	Y2H-RRS
ARF3 + ARHGDIB	0,8	0,5	ND	ND	ND	ND	NEG	NEG	0,3	0,2	ND	ND	ND	ND	NEG	NEG	NEG	NEG	Y2H-RRS
RHOA + GOSR1	1,3	1,8	ND	ND	ND	ND	NEG	NEG	1	1,9	ND	ND	ND	ND	NEG	NEG	NEG	NEG	Y2H-RRS
ATIC + MEOX1	1,5	1	ND	ND	ND	ND	NEG	NEG	0,4	0,6	ND	ND	ND	ND	NEG	NEG	NEG	NEG	Y2H-RRS
BGN + TTBK2	0,7	1	ND	ND	ND	ND	NEG	NEG	2,5	2,2	ND	ND	ND	ND	NEG	NEG	NEG	NEG	Y2H-RRS
CAPNS1 + FOXR1	0,5	0,4	ND	ND	ND	ND	NEG	NEG	1,1	1,2	ND	ND	ND	ND	NEG	NEG	NEG	NEG	Y2H-RRS
CASP8 + TTR	0,3	0,3	ND	ND	ND	ND	NEG	NEG	0,1	0,1	ND	ND	ND	ND	NEG	NEG	NEG	NEG	Y2H-RRS
CDC42 + YWHAG	0,2	0,2	ND	ND	ND	ND	NEG	NEG	0,6	0,5	ND	ND	ND	ND	NEG	NEG	NEG	NEG	Y2H-RRS
CDK6 + EXOSC4	2,6	3,3	ND	ND	0,6	0,1	NEG	NEG	1,5	1,8	ND	ND	ND	ND	NEG	NEG	NEG	NEG	Y2H-RRS
CSK + ALS2CR12	3,6	3,3	-0,9	0,1	-0,2	0	NEG	NEG	1,5	1,3	ND	ND	ND	ND	NEG	NEG	NEG	NEG	Y2H-RRS
CSNK1D + ARFIP2	1,5	2,5	ND	ND	ND	ND	NEG	NEG	1,2	1,4	ND	ND	ND	ND	NEG	NEG	NEG	NEG	Y2H-RRS
DBH + KHDRBS3	0,5	0,4	ND	ND	ND	ND	NEG	NEG	0,9	0,6	ND	ND	ND	ND	NEG	NEG	NEG	NEG	Y2H-RRS
DOM3Z + APBB2	0,6	0,6	ND	ND	ND	ND	NEG	NEG	0,7	0,8	ND	ND	ND	ND	NEG	NEG	NEG	NEG	Y2H-RRS
EEF1D + FBXW7	2	3	ND	ND	0,1	0	NEG	NEG	2,1	2,5	ND	ND	ND	ND	NEG	NEG	NEG	NEG	Y2H-RRS
EWSR1 + RGS2	2,7	1,4	ND	ND	ND	ND	NEG	NEG	0,2	0,7	ND	ND	ND	ND	NEG	NEG	NEG	NEG	Y2H-RRS
GJA5 + CSNK1D	0,7	0,6	ND	ND	ND	ND	NEG	NEG	0,5	0,9	ND	ND	ND	ND	NEG	NEG	NEG	NEG	Y2H-RRS
GNB2 + EIF3H							NC	NC	2,4	2,9	ND	ND	ND	ND	NEG	NEG	NEG	NEG	Y2H-RRS
GRIN2C + SMAD1	0,8	1,1	ND	ND	ND	ND	NEG	NEG	0,7	0,7	ND	ND	ND	ND	NEG	NEG	NEG	NEG	Y2H-RRS
GSN + AP1S3	1,5	1,8	ND	ND	ND	ND	NEG	NEG	1,2	1,2	ND	ND	ND	ND	NEG	NEG	NEG	NEG	Y2H-RRS
BRF1 + ANP32A	0,3	0,2	ND	ND	ND	ND	NEG	NEG	0,2	0,4	ND	ND	ND	ND	NEG	NEG	NEG	NEG	Y2H-RRS
HTT + RIC8A	1,9	2,2	ND	ND	ND	ND	NEG	NEG	1,7	1,2	ND	ND	ND	ND	NEG	NEG	NEG	NEG	Y2H-RRS
IRF4 + CEP70	2	2,6	ND	ND	ND	ND	NEG	NEG	0,6	0,7	ND	ND	ND	ND	NEG	NEG	NEG	NEG	Y2H-RRS
KLRC1 + ZMYM5							NC	NC	1,2	1	ND	ND	ND	ND	NEG	NEG	NEG	NEG	Y2H-RRS
MAX + ILF3	1,9	2,1	ND	ND	ND	ND	NEG	NEG	1,3	1,6	ND	ND	ND	ND	NEG	NEG	NEG	NEG	Y2H-RRS
MDK + APBB1	0,5	0,8	ND	ND	ND	ND	NEG	NEG	0,8	0,8	ND	ND	ND	ND	NEG	NEG	NEG	NEG	Y2H-RRS
MFAP1 + BLZF1	0,9	0,9	ND	ND	ND	ND	NEG	NEG	0,6	1,4	ND	ND	ND	ND	NEG	NEG	NEG	NEG	Y2H-RRS
MXI1 + PKN1	2,3	1,9	ND	ND	ND	ND	NEG	NEG	1,3	1,3	ND	ND	ND	ND	NEG	NEG	NEG	NEG	Y2H-RRS
NACA + WDYHV1	1,4	1,9	ND	ND	ND	ND	NEG	NEG	2,3	2,6	ND	ND	ND	ND	NEG	NEG	NEG	NEG	Y2H-RRS
NDUFB1 + GTF2A2	0,8	0,8	ND	ND	ND	ND	NEG	NEG	0,1	0,1	ND	ND	ND	ND	NEG	NEG	NEG	NEG	Y2H-RRS
NDUFV2 + CDA							NC	NC	0,7	0,9	ND	ND	ND	ND	NEG	NEG	NEG	NEG	Y2H-RRS
NGF + ZNF331	ND	ND	ND	ND	ND	ND	IP	IP	1,1	1,1	ND	ND	ND	ND	NEG	NEG	NEG	NEG	Y2H-RRS
ORC5 + ADSSL1	1,5	1,8	ND	ND	ND	ND	NEG	NEG	1,4	1,8	ND	ND	ND	ND	NEG	NEG	NEG	NEG	Y2H-RRS
PHYH + BTBD1	1,1	1,2	ND	ND	ND	ND	NEG	NEG	0,6	0,6	ND	ND	ND	ND	NEG	NEG	NEG	NEG	Y2H-RRS
POLR2L + IPO4	1,8	1,4	ND	ND	ND	ND	NEG	NEG	2	1,9	ND	ND	ND	ND	NEG	NEG	NEG	NEG	Y2H-RRS
PSAP + RPL21	1,2	1,2	ND	ND	ND	ND	NEG	NEG	0,2	0,4	ND	ND	ND	ND	NEG	NEG	NEG	NEG	Y2H-RRS
PSMB9 + ASB3	1,6	2,7	ND	ND	ND	ND	NEG	NEG	1,5	2	ND	ND	ND	ND	NEG	NEG	NEG	NEG	Y2H-RRS
PTPN11 + GLE1	1,2	1,5	ND	ND	ND	ND	NEG	NEG	2,1	1,9	ND	ND	ND	ND	NEG	NEG	NEG	NEG	Y2H-RRS
PTS + RCOR3	0,5	0,4	ND	ND	ND	ND	NEG	NEG	0,9	0,9	ND	ND	ND	ND	NEG	NEG	NEG	NEG	Y2H-RRS
ABCD3 + FKBP1A	1,2	1,1	ND	ND	ND	ND	NEG	NEG							NC	NC	NEG	NEG	Y2H-RRS
RAP2B + SYF2	1,6	2	ND	ND	ND	ND	NEG	NEG	3,3	2,4	8	0,8	ND	ND	POS	NEG	POS	NEG	Y2H-RRS
RFC3 + ACTN4							NC	NC	0,2	0,2	ND	ND	ND	ND	NEG	NEG	NEG	NEG	Y2H-RRS
RFC4 + SDSL	2,1	2,2	ND	ND	ND	ND	NEG	NEG	1,2	1,2	ND	ND	ND	ND	NEG	NEG	NEG	NEG	Y2H-RRS
TRIM27 + TYMS	0,7	0,9	ND	ND	ND	ND	NEG	NEG							NC	NC	NEG	NEG	Y2H-RRS
RPS6KB1 + GDAP1	1,9	1,1	ND	ND	ND	ND	NEG	NEG							NC	NC	NEG	NEG	Y2H-RRS
S100B + EAF1	1,3	0,9	ND	ND	ND	ND	NEG	NEG	0,8	0,6	ND	ND	ND	ND	NEG	NEG	NEG	NEG	Y2H-RRS
SKP1 + CSK	1,1	1,2	ND	ND	ND	ND	NEG	NEG	1,5	1,2	ND	ND	ND	ND	NEG	NEG	NEG	NEG	Y2H-RRS
SQLE + HDAC4	0,8	0,9	ND	ND	ND	ND	NEG	NEG	0,2	0,3	ND	ND	ND	ND	NEG	NEG	NEG	NEG	Y2H-RRS
MLX + VSX2	1,2	2,7	ND	ND	ND	ND	NEG	NEG	0,5	2	ND	ND	ND	ND	NEG	NEG	NEG	NEG	Y2H-RRS
TGFBR2 + C2orf62	3,4	3,8	13,6	1,6	19,4	5,8	POS	POS	0,2	0,2	ND	ND	ND	ND	NEG	NEG	POS	POS	Y2H-RRS

	set a								set b								set a+b		
Interaction	ICR Exp1	ICR Exp2	mean cNIR Exp1	sem cNIR Exp1	mean cNIR Exp2	sem cNIR Exp2	result Exp1	result Exp2	ICR Exp1	ICR Exp2	mean cNIR Exp1	sem cNIR Exp1	mean cNIR Exp2	sem cNIR Exp2	result Exp1	result Exp2	result Exp1	result Exp2	Set
UBE2V1 + SOX7	0,3	0,2	ND	ND	ND	ND	NEG	NEG	2	1,8	ND	ND	ND	ND	NEG	NEG	NEG	NEG	Y2H-RRS
CDC7 + PRC1	1,6	0,5	ND	ND	ND	ND	NEG	NEG							NC	NC	NEG	NEG	Y2H-RRS
HIST1H3H + ADRB2							NC	NC	0,8	1,8	ND	ND	ND	ND	NEG	NEG	NEG	NEG	Y2H-RRS
BLZF1 + ZBTB8A	1	1,7	ND	ND	ND	ND	NEG	NEG	0,8	1,3	ND	ND	ND	ND	NEG	NEG	NEG	NEG	Y2H-RRS
PIAS1 + FAM90A1	1,6	1,3	ND	ND	ND	ND	NEG	NEG	1,2	1,3	ND	ND	ND	ND	NEG	NEG	NEG	NEG	Y2H-RRS
TCAP + MBIP	0,4	0,4	ND	ND	ND	ND	NEG	NEG	1,2	1,1	ND	ND	ND	ND	NEG	NEG	NEG	NEG	Y2H-RRS
CDC23 + PDHB	2,9	2,8	ND	ND	ND	ND	NEG	NEG	13,7	11,2	-1,5	1,2	-14,2	1,7	NEG	NEG	NEG	NEG	Y2H-RRS
TSC22D1 + RAD54B	1,5	1,4	ND	ND	ND	ND	NEG	NEG	0,9	0,7	ND	ND	ND	ND	NEG	NEG	NEG	NEG	Y2H-RRS
CDK5R1 + VIL1	1,2	0,9	ND	ND	ND	ND	NEG	NEG	0,6	0,5	ND	ND	ND	ND	NEG	NEG	NEG	NEG	Y2H-RRS
SQSTM1 + EIF3G	0,8	1	ND	ND	ND	ND	NEG	NEG	2,9	3,1	ND	ND	1,6	0,5	NEG	NEG	NEG	NEG	Y2H-RRS
UNC119 + YY1	2,7	2	ND	ND	ND	ND	NEG	NEG							NC	NC	NEG	NEG	Y2H-RRS
RAB33A + ATL1	2	2	ND	ND	ND	ND	NEG	NEG							NC	NC	NEG	NEG	Y2H-RRS
HOMER1 + SARS	0,4	0,4	ND	ND	ND	ND	NEG	NEG	2,2	2,9	ND	ND	ND	ND	NEG	NEG	NEG	NEG	Y2H-RRS
TR_HOMER1 + SARS	0,4	0,4	ND	ND	ND	ND	NEG	NEG	2,2	2,9	ND	ND	ND	ND	NEG	NEG	NEG	NEG	Y2H-RRS
HAND2 + BRWD1	7,7	5,3	2,6	0,2	2,8	0	NEG	NEG	2,6	2,1	ND	ND	ND	ND	NEG	NEG	NEG	NEG	Y2H-RRS
FXR2 + CRX	1,3	2,8	ND	ND	ND	ND	NEG	NEG	0,4	1	ND	ND	ND	ND	NEG	NEG	NEG	NEG	Y2H-RRS
SEC24C + GTF2H1	0,4	0,8	ND	ND	ND	ND	NEG	NEG	0,7	0,7	ND	ND	ND	ND	NEG	NEG	NEG	NEG	Y2H-RRS
KIAA0141 + DCTN2							NC	NC	1,4	1,2	ND	ND	ND	ND	NEG	NEG	NEG	NEG	Y2H-RRS
PDCD6IP + ACTA1	1,2	1,6	ND	ND	ND	ND	NEG	NEG	0,8	0,9	ND	ND	ND	ND	NEG	NEG	NEG	NEG	Y2H-RRS
DHRS9 + PCNA	0,3	0,5	ND	ND	ND	ND	NEG	NEG							NC	NC	NEG	NEG	Y2H-RRS
ZNHIT1 + SAP30BP	1,3	1,1	ND	ND	ND	ND	NEG	NEG							NC	NC	NEG	NEG	Y2H-RRS
FBLN5 + TSC22D4	3,5	2,4	4,2	1,3	ND	ND	POS	NEG	3,1	3,2	1,4	0,2	1,3	0,1	NEG	NEG	POS	NEG	Y2H-RRS
KAT5 + BRPF3	0,6	0,6	ND	ND	ND	ND	NEG	NEG	1,1	0,7	ND	ND	ND	ND	NEG	NEG	NEG	NEG	Y2H-RRS
STAMBP + MOCOS	6,2	5,1	5,9	0,3	6,4	0,7	POS	POS							NC	NC	POS	POS	Y2H-RRS
EXOC5 + FOSL2	0,9	0,8	ND	ND	ND	ND	NEG	NEG							NC	NC	NEG	NEG	Y2H-RRS
KHDRBS3 + RPS6	1,2	1,4	ND	ND	ND	ND	NEG	NEG	1,1	0,7	ND	ND	ND	ND	NEG	NEG	NEG	NEG	Y2H-RRS
GIPC1 + MCRS1	2	0,9	ND	ND	ND	ND	NEG	NEG	0,3	0,3	ND	ND	ND	ND	NEG	NEG	NEG	NEG	Y2H-RRS
RUVBL2 + FUT2	0,6	0,6	ND	ND	ND	ND	NEG	NEG							NC	NC	NEG	NEG	Y2H-RRS
TXNL4A + TRIM54	2,1	2,8	ND	ND	ND	ND	NEG	NEG	1	0,7	ND	ND	ND	ND	NEG	NEG	NEG	NEG	Y2H-RRS
SUB1 + KLHL35	1,2	1,1	ND	ND	ND	ND	NEG	NEG	1,3	1,6	ND	ND	ND	ND	NEG	NEG	NEG	NEG	Y2H-RRS
PDIA5 + MMP3	0,6	0,7	ND	ND	ND	ND	NEG	NEG	2,9	5	ND	ND	4,2	0,3	NEG	POS	NEG	POS	Y2H-RRS
MID2 + PLDN	1,2	1,1	ND	ND	ND	ND	NEG	NEG	0,7	1	ND	ND	ND	ND	NEG	NEG	NEG	NEG	Y2H-RRS
C10orf10 + IQUB	0,7	1	ND	ND	ND	ND	NEG	NEG	0,7	0,5	ND	ND	ND	ND	NEG	NEG	NEG	NEG	Y2H-RRS
EXOSC8 + KLHDC5	1,7	0,9	ND	ND	ND	ND	NEG	NEG	2	2,7	ND	ND	ND	ND	NEG	NEG	NEG	NEG	Y2H-RRS
PAXIP1 + TWIST2	1,5	1	ND	ND	ND	ND	NEG	NEG	1,2	1,2	ND	ND	ND	ND	NEG	NEG	NEG	NEG	Y2H-RRS
NUP62 + NDC80							NC	NC	9,2	13,3	108,3	17,8	81,4	6,6	POS	POS	POS	POS	Y2H-RRS
TFIP11 + FMR1	1,2	1,1	ND	ND	ND	ND	NEG	NEG	1,7	0,8	ND	ND	ND	ND	NEG	NEG	NEG	NEG	Y2H-RRS
RAD54B + GDPD5							NC	NC	0,7	0,8	ND	ND	ND	ND	NEG	NEG	NEG	NEG	Y2H-RRS
BRP44 + GDI1	1	1	ND	ND	ND	ND	NEG	NEG	0,3	0,3	ND	ND	ND	ND	NEG	NEG	NEG	NEG	Y2H-RRS
SEC22A + DCTN1	0,5	0,5	ND	ND	ND	ND	NEG	NEG	0,2	0,2	ND	ND	ND	ND	NEG	NEG	NEG	NEG	Y2H-RRS
RNF11 + RCN3	0,6	0,8	ND	ND	ND	ND	NEG	NEG	0,6	0,8	ND	ND	ND	ND	NEG	NEG	NEG	NEG	Y2H-RRS
ZBTB32 + ZSCAN22	2,8	1,9	ND	ND	ND	ND	NEG	NEG	1	0,9	ND	ND	ND	ND	NEG	NEG	NEG	NEG	Y2H-RRS
SNX12 + DOM3Z	1	0,7	ND	ND	ND	ND	NEG	NEG	0,5	0,7	ND	ND	ND	ND	NEG	NEG	NEG	NEG	Y2H-RRS
ASB3 + GATA2	1	0,9	ND	ND	ND	ND	NEG	NEG	1,3	1,3	ND	ND	ND	ND	NEG	NEG	NEG	NEG	Y2H-RRS
CDKL3 + LMO3	ND	ND	ND	ND	ND	ND	IP	IP	1,3	1,1	ND	ND	ND	ND	NEG	NEG	NEG	NEG	Y2H-RRS
KLF3 + PRMT6	0,5	0,8	ND	ND	ND	ND	NEG	NEG	0,5	0,4	ND	ND	ND	ND	NEG	NEG	NEG	NEG	Y2H-RRS
LUC7L2 + PPP1CC	1,1	0,6	ND	ND	ND	ND	NEG	NEG	0,8	0,9	ND	ND	ND	ND	NEG	NEG	NEG	NEG	Y2H-RRS
BRWD1 + SEC22A	0,4	0,4	ND	ND	ND	ND	NEG	NEG	0,6	0,5	ND	ND	ND	ND	NEG	NEG	NEG	NEG	Y2H-RRS
NECAB2 + PRPF19							NC	NC	1,5	1,7	ND	ND	ND	ND	NEG	NEG	NEG	NEG	Y2H-RRS
RBFOX1 + MAX	0,5	0,5	ND	ND	ND	ND	NEG	NEG	2,1	3,3	ND	ND	3,8	0,5	NEG	POS	NEG	POS	Y2H-RRS
PIGG + MFAP1	0,7	1,6	ND	ND	ND	ND	NEG	NEG	0,4	0,7	ND	ND	ND	ND	NEG	NEG	NEG	NEG	Y2H-RRS
MCM10 + RAP1GDS1	0,8	0,2	ND	ND	ND	ND	NEG	NEG	0,6	0,5	ND	ND	ND	ND	NEG	NEG	NEG	NEG	Y2H-RRS
PEX26 + KBTBD7	0,6	0,5	ND	ND	ND	ND	NEG	NEG	1,4	1,3	ND	ND	ND	ND	NEG	NEG	NEG	NEG	Y2H-RRS
VPS11 + CHMP7	1,9	1,2	ND	ND	ND	ND	NEG	NEG	0,3	0,4	ND	ND	ND	ND	NEG	NEG	NEG	NEG	Y2H-RRS
TEX11 + ROBLD3							NC	NC	1,1	1,7	ND	ND	ND	ND	NEG	NEG	NEG	NEG	Y2H-RRS
JPH3 + SDCBP	2,3	1,8	ND	ND	ND	ND	NEG	NEG	1,2	1	ND	ND	ND	ND	NEG	NEG	NEG	NEG	Y2H-RRS
SPC25 + FAM50B	1	1,6	ND	ND	ND	ND	NEG	NEG	0,7	0,9	ND	ND	ND	ND	NEG	NEG	NEG	NEG	Y2H-RRS
MYOZ1 + UNC119							NC	NC	1,2	1,4	ND	ND	ND	ND	NEG	NEG	NEG	NEG	Y2H-RRS
KLHL12 + ANKRD44	3,1	2,8	3,2	0,5	ND	ND	POS	NEG	3,3	4,5	12,5	2,1	10,2	1,3	POS	POS	POS	POS	Y2H-RRS
ARMC7 + ATXN1	3	3,3	0,6	0,2	1,1	0,3	NEG	NEG	1,7	1,2	ND	ND	ND	ND	NEG	NEG	NEG	NEG	Y2H-RRS
IPO4 + SUB1	3,5	2,4	0,6	0,1	ND	ND	NEG	NEG	0,7	0,9	ND	ND	ND	ND	NEG	NEG	NEG	NEG	Y2H-RRS
ZNF750 + NR3C1	0,9	0,5	ND	ND	ND	ND	NEG	NEG	0,3	0,4	ND	ND	ND	ND	NEG	NEG	NEG	NEG	Y2H-RRS
GDPD5 + GSN	0,6	1,6	ND	ND	ND	ND	NEG	NEG							NC	NC	NEG	NEG	Y2H-RRS
DIAPH3 + TRAPPC2	1,1	1,4	ND	ND	ND	ND	NEG	NEG	1,5	2,5	ND	ND	ND	ND	NEG	NEG	NEG	NEG	Y2H-RRS
SOX7 + TK1	0,5	0,4	ND	ND	ND	ND	NEG	NEG	0,2	0,3	ND	ND	ND	ND	NEG	NEG	NEG	NEG	Y2H-RRS
MAGT1 + HMGA1	0,4	0,3	ND	ND	ND	ND	NEG	NEG	1	0,7	ND	ND	ND	ND	NEG	NEG	NEG	NEG	Y2H-RRS
DTNBP1 + MCM3	0,6	0,5	ND	ND	ND	ND	NEG	NEG	1,2	1,5	ND	ND	ND	ND	NEG	NEG	NEG	NEG	Y2H-RRS
MEX3B + EXOSC8	1,5	3,1	ND	ND	0	0,1	NEG	NEG	1,4	1,3	ND	ND	ND	ND	NEG	NEG	NEG	NEG	Y2H-RRS
SYT3 + GTPBP10	1	1,2	ND	ND	ND	ND	NEG	NEG	0,5	0,5	ND	ND	ND	ND	NEG	NEG	NEG	NEG	Y2H-RRS
GTPBP3 + KRAS	2,7	1,5	ND	ND	ND	ND	NEG	NEG	1,4	1,6	ND	ND	ND	ND	NEG	NEG	NEG	NEG	Y2H-RRS
FBF1 + STIP1	1,4	1,5	ND	ND	ND	ND	NEG	NEG	1,3	1,6	ND	ND	ND	ND	NEG	NEG	NEG	NEG	Y2H-RRS
DPP9 + ARL2	1,2	1,3	ND	ND	ND	ND	NEG	NEG	1,9	1,3	ND	ND	ND	ND	NEG	NEG	NEG	NEG	Y2H-RRS
BOD1 + ABCD3							NC	NC	1,3	1,4	ND	ND	ND	ND	NEG	NEG	NEG	NEG	Y2H-RRS
COL23A1 + ATP6V1B1	0,6	0,5	ND	ND	ND	ND	NEG	NEG							NC	NC	NEG	NEG	Y2H-RRS
TWIST2 + GARS	1,3	1,1	ND	ND	ND	ND	NEG	NEG	1	1,3	ND	ND	ND	ND	NEG	NEG	NEG	NEG	Y2H-RRS

	set a								set b								set a+b		
Interaction	ICR Exp1	ICR Exp2	mean cNIR Exp1	sem cNIR Exp1	mean cNIR Exp2	sem cNIR Exp2	result Exp1	result Exp2	ICR Exp1	ICR Exp2	mean cNIR Exp1	sem cNIR Exp1	mean cNIR Exp2	sem cNIR Exp2	result Exp1	result Exp2	result Exp1	result Exp2	Set
TRAPPC5 + CBX2							NC	NC	0,9	1	ND	ND	ND	ND	NEG	NEG	NEG	NEG	Y2H-RRS
ALS2CR12 + RAD23A	1,8	1,7	ND	ND	ND	ND	NEG	NEG	5,1	3,7	0,9	0,2	1,7	0,3	NEG	NEG	NEG	NEG	Y2H-RRS
EMID2 + MEOX2	0,4	2	ND	ND	ND	ND	NEG	NEG	1,6	1,3	ND	ND	ND	ND	NEG	NEG	NEG	NEG	Y2H-RRS
ZNF483 + BEND5	1	0,8	ND	ND	ND	ND	NEG	NEG	0,3	0,2	ND	ND	ND	ND	NEG	NEG	NEG	NEG	Y2H-RRS
ZNF296 + ARNT	1,9	2,1	ND	ND	ND	ND	NEG	NEG	0,7	0,6	ND	ND	ND	ND	NEG	NEG	NEG	NEG	Y2H-RRS
C10orf35 + KLC3	ND	ND	ND	ND	ND	ND	IP	IP	1,7	0,5	ND	ND	ND	ND	NEG	NEG	NEG	NEG	Y2H-RRS
KIF6 + XIAP	1,1	0,9	ND	ND	ND	ND	NEG	NEG	1,1	1,3	ND	ND	ND	ND	NEG	NEG	NEG	NEG	Y2H-RRS
C2orf62 + GCSH	0,7	0,8	ND	ND	ND	ND	NEG	NEG	1	1	ND	ND	ND	ND	NEG	NEG	NEG	NEG	Y2H-RRS
KRTAP10-3 + RNF11	ND	ND	ND	ND	ND	ND	IP	IP	0,3	0,2	ND	ND	ND	ND	NEG	NEG	NEG	NEG	Y2H-RRS
CT45A5 + MCM10	1,7	1,4	ND	ND	ND	ND	NEG	NEG	0,9	0,8	ND	ND	ND	ND	NEG	NEG	NEG	NEG	Y2H-RRS
C22orf41 + IL18RAP							NC	NC	ND	ND	ND	ND	ND	ND	IP	IP	NEG	NEG	Y2H-RRS

Table 6: DULIP results from the AIRS. ICR: internal control ratio; cNIR: corrected normalized interaction ratio; Exp: Experiment; NA: not available (no expression/immunoprecipitation); PREY: no prey expression; IP: no immunoprecipitation; NC: not constructed; ND: not determined.

Interaction	Kd (nM)	Set a								Set b								Set a+b	
		ICR Exp1	ICR Exp2	mean cNIR Exp1	sem cNIR Exp1	mean cNIR Exp2	sem cNIR Exp2	result Exp1	result Exp2	ICR Exp1	ICR Exp2	mean cNIR Exp1	sem cNIR Exp1	mean cNIR Exp2	sem cNIR Exp2	result Exp1	result Exp2	result Exp1	result Exp2
NCK2 + LIMS1	3000000	3,2	3,5	0,1	0,1	0,1	0	NEG	NEG	1,7	2	ND	ND	ND	ND	NEG	NEG	NEG	NEG
CALR + CD8A	126000	0,9	0,8	ND	ND	ND	ND	NEG	NEG	0,7	0,7	ND	ND	ND	ND	NEG	NEG	NEG	NEG
TNNI3 + TNNC1	31000	4,5	5	0,3	0,2	0,9	0,1	NEG	NEG	12	13,5	0,7	0,1	0,8	0,2	NEG	NEG	NEG	NEG
RAC2 + PLCG2	21900	0,8	0,8	ND	ND	ND	ND	NEG	NEG	0,8	0,7	ND	ND	ND	ND	NEG	NEG	NEG	NEG
ARF1 + AP1S3	20000	1,1	1	ND	ND	ND	ND	NEG	NEG	0,4	0,5	ND	ND	ND	ND	NEG	NEG	NEG	NEG
FUBP1 + PUF60	14000	0,9	1,4	ND	ND	ND	ND	NEG	NEG	0,7	0,8	ND	ND	ND	ND	NEG	NEG	NEG	NEG
S100B + FGF2	10000	1,4	1,2	ND	ND	ND	ND	NEG	NEG	0,4	0,3	ND	ND	ND	ND	NEG	NEG	NEG	NEG
HLA-C + KPNA2	9500	0,7	1,5	ND	ND	ND	ND	NEG	NEG	NA	NA	NA	NA	NA	NA	PREY	PREY	NEG	NEG
RAB4A + ZFYVE20	7700	2,5	1,7	ND	ND	ND	ND	NEG	NEG	1,6	NA	ND	NA	ND	NA	NEG	PREY	NEG	NEG
PAK1 + ARHGEF7	7500	12	7,6	3,3	0,7	3,1	0,2	POS	POS	2,6	1,9	ND	ND	ND	ND	NEG	NEG	POS	POS
HSPBP1 + HSPA1A	6500	11,7	15,5	7,6	1,6	6,6	0,7	POS	POS	65,9	49,2	8,2	1	6,6	0,1	POS	POS	POS	POS
PLCB2 + RAC1	5300	0,9	0,7	ND	ND	ND	ND	NEG	NEG	0,2	0,2	ND	ND	ND	ND	NEG	NEG	NEG	NEG
MTA1 + HDAC1	5000	1,5	1,4	ND	ND	ND	ND	NEG	NEG	0,9	1,1	ND	ND	ND	ND	NEG	NEG	NEG	NEG
XRCC4 + NHEJ1	4100	NA	NA	NA	NA	NA	NA	PREY	PREY	0,3	0,4	ND	ND	ND	ND	NEG	NEG	NEG	NEG
ENAH + TES	3600	NA	NA	NA	NA	NA	NA	PREY	PREY	2,1	2,5	ND	ND	ND	ND	NEG	NEG	NEG	NEG
IPO13 + EIF1AX	3000	0,4	0,4	ND	ND	ND	ND	NEG	NEG							NC	NC	NEG	NEG
RAC1 + ARFIP2	3000	0,4	0,3	ND	ND	ND	ND	NEG	NEG	4,3	3,7	4	0,8	4	0,3	POS	POS	POS	POS
CD3E + CD3G	2730	NA	NA	NA	NA	NA	NA	PREY	PREY	0,6	1,2	ND	ND	ND	ND	NEG	NEG	NEG	NEG
RAC1 + NCF2	2700	2	2,2	ND	ND	ND	ND	NEG	NEG	1,6	1,1	ND	ND	ND	ND	NEG	NEG	NEG	NEG
OSBP + VAPA	2100	44,8	37,3	96,5	9,2	123,2	3,6	POS	POS	NA	NA	NA	NA	NA	NA	PREY	PREY	POS	POS
MAPK1 + RPS6KA1	2000	7,6	9,7	2,2	0,3	2,1	0,1	NEG	NEG	0,6	0,6	ND	ND	ND	ND	NEG	NEG	NEG	NEG
PRPF4 + PPIH	1970	1,8	1,5	ND	ND	ND	ND	NEG	NEG	4,7	6	0,8	0,2	1	0,2	NEG	NEG	NEG	NEG
TIMP1 + MMP14	1530	3,2	3,7	24,1	6,2	18,5	0,9	POS	POS	NA	NA	NA	NA	NA	NA	PREY	PREY	POS	POS
MAPRE1 + MAPRE3	1500	NA	NA	NA	NA	NA	NA	PREY	PREY	10	14,2	9,3	3,3	9,3	1,7	POS	POS	POS	POS
HIRA + ASF1A	1300	0,5	0,7	ND	ND	ND	ND	NEG	NEG	0,7	1,4	ND	ND	ND	ND	NEG	NEG	NEG	NEG
MIF + RPS19	1300	1,2	1,1	ND	ND	ND	ND	NEG	NEG	0,2	0,3	ND	ND	ND	ND	NEG	NEG	NEG	NEG
BANF1 + EMD	590	1	1,4	ND	ND	ND	ND	NEG	NEG							NC	NC	NEG	NEG
RNF31 + RBCK1	520	0,6	0,4	ND	ND	ND	ND	NEG	NEG	14,9	22,6	43,8	2,9	62,9	8,2	POS	POS	POS	POS
BCL9 + TCF7L2	459	2,3	2,2	ND	ND	ND	ND	NEG	NEG	0,6	0,3	ND	ND	ND	ND	NEG	NEG	NEG	NEG
SPAG9 + ARF6	420	NA	NA	NA	NA	NA	NA	IP	IP	0,8	1	ND	ND	ND	ND	NEG	NEG	NEG	NEG
RAB11A + RAB11FIP2	250	38,7	25,1	3,4	1,2	3,9	0,3	POS	POS	12,6	21,8	2,4	0,1	4,8	0,3	NEG	POS	POS	POS
CDC42 + ARHGAP1	239	0,6	0,4	ND	ND	ND	ND	NEG	NEG	1,6	1,7	ND	ND	ND	ND	NEG	NEG	NEG	NEG
STAMBP + CHMP3	113	1,8	1,9	ND	ND	ND	ND	NEG	NEG	1,8	2,3	ND	ND	ND	ND	NEG	NEG	NEG	NEG
MBP + HLADRB5	100	0,1	0,1	ND	ND	ND	ND	NEG	NEG	1,5	2	ND	ND	ND	ND	NEG	NEG	NEG	NEG
HBA2 + AHSP	93	NA	NA	NA	NA	NA	NA	PREY	PREY	1,3	2,3	ND	ND	ND	ND	NEG	NEG	NEG	NEG
AIMP2 + KARS	90	139,9	124,9	59,9	9,2	49,2	10,6	POS	POS	34,2	32,3	22,4	1,3	29,1	5,9	POS	POS	POS	POS
U2AF2 + SF1	84	0,9	0,5	ND	ND	ND	ND	NEG	NEG	NA	NA	NA	NA	NA	NA	IP	IP	NEG	NEG
CDK2 + CKS1B	77	9,3	8,6	1,5	0,3	1	0,1	NEG	NEG	2,1	5,4	ND	ND	0,6	0,2	NEG	NEG	NEG	NEG
PFN1 + VASP	57	5	5	2	0,6	2,8	0,6	NEG	NEG	2,3	2,3	ND	ND	ND	ND	NEG	NEG	NEG	NEG
SRSF1 + SRPK1	50	NA	NA	NA	NA	NA	NA	PREY	PREY	2,6	1,3	ND	ND	ND	ND	NEG	NEG	NEG	NEG
WASL + BAIAP2L1	40	2,9	2,9	ND	ND	ND	ND	NEG	NEG	1,9	2	ND	ND	ND	ND	NEG	NEG	NEG	NEG
BCAR1 + SH2D3C	30	3,4	3,3	2	0,3	2,8	0,4	NEG	NEG	NA	NA	NA	NA	NA	NA	IP	IP	NEG	NEG
S100A10 + AHNAK	30	0,4	0,2	ND	ND	ND	ND	NEG	NEG	0,7	0,9	ND	ND	ND	ND	NEG	NEG	NEG	NEG
EIF4A3 + CWC22	28,4	3,8	5,2	3,5	0,3	8,2	1,6	POS	POS	1,1	2,6	ND	ND	ND	ND	NEG	NEG	POS	POS
SOCS2 + CUL5	28,1	2	2,8	ND	ND	ND	ND	NEG	NEG	26,3	35,9	6,3	0,6	9,1	0,7	POS	POS	POS	POS
ARL2 + ARL2BP	20	4,3	4,7	0,5	0	0,7	0	NEG	NEG	2,4	2	ND	ND	ND	ND	NEG	NEG	NEG	NEG
TERF2 + TERF2IP	16,5	NA	NA	NA	NA	NA	NA	PREY	PREY	0,9	0,8	ND	ND	ND	ND	NEG	NEG	NEG	NEG
CASP9 + XIAP	13	1,9	1,7	ND	ND	ND	ND	NEG	NEG	7,2	4,5	1,3	0,1	0,8	0,2	NEG	NEG	NEG	NEG
CSNK2B + CSNK2A1	12,6	122,8	110,1	177,2	8,9	118,4	11,6	POS	POS	31,5	17,2	60	5,7	40,5	1,1	POS	POS	POS	POS
GATAD2A + MBD2	12,4	6,8	7,8	5	1	6,1	1,4	POS	POS	NA	NA	NA	NA	NA	NA	IP	IP	POS	POS
MMP2 + TIMP2	5,2	0,5	0,5	ND	ND	ND	ND	NEG	NEG	3,2	4,5	1,8	0,3	1,6	0,2	NEG	NEG	NEG	NEG
RMI2 + RMI1	4,5	2,6	2	ND	ND	ND	ND	NEG	NEG	2,7	1,9	ND	ND	ND	ND	NEG	NEG	NEG	NEG
SMN1 + SMN2	3,3	92,4	59,5	81	10,1	53,5	6,6	POS	POS	115,6	119,1	91,4	7,1	127,3	17	POS	POS	POS	POS
USH1G + USH1C	1	219,9	206,3	88,6	3,1	90,6	13,9	POS	POS	187,2	202,3	36,5	4	41,9	2,8	POS	POS	POS	POS
MAGOH + RBM8A	0,7	36,4	29,8	17	0,8	24,2	1,9	POS	POS	111,6	88	58,6	5,8	40,6	1,9	POS	POS	POS	POS
EPO + EPOR	0,0037	NA	NA	NA	NA	NA	NA	PREY	PREY	1,5	2,2	ND	ND	ND	ND	NEG	NEG	NEG	NEG
RNASE1 + RNH1	0,0000003	157,5	192,7	75,8	9,2	67,2	5	POS	POS	NA	NA	NA	NA	NA	NA	PREY	PREY	POS	POS

Table 7: Constructs used for systematic BRIP interaction screening. PA: ProteinA; NL: NanoLuc luciferase; GW: gateway cassette; X: Donor/Prey; Y: Acceptor/Bait.

Plasmid	Fusion protein	Symbol	Gene ID	Uniprot ID
pcmyc-NL-GW	NanoLuc-X			
pGW-NL-cmyc	X-NanoLuc			
pPA-mCit-GW	ProteinA-mCitrine-Y			
pGW-mCit-PA	Y-mCitrine-ProteinA			
pPA-mCit-NL	ProteinA-mCitrine-NanoLuc			
pPA-mCit	ProteinA-mCitrine			
pNL	NanoLuc			
pPA-NL	ProteinA-NanoLuc			
pPA-mCit-BAD	ProteinA-mCit-BAD	BAD	572	Q92934
pcmyc-NL-BCL2L1	NanoLuc-BCL2L1	BCL2L1	598	Q07817
pcmyc-BCL2L1	BCL2L1	BCL2L1	598	Q07817
pPA-mCit-Syntaxin-1	ProteinA-mCitrine-Syntaxin-1	STX1A	6804	Q16623
pcmyc-NL-Munc18	NanoLuc-Munc18	STXBP1	25558	P61765
pcmyc-NL-Munc18 K46E	NanoLuc-Munc18 K46E	STXBP1	25558	P61765
pcmyc-NL-Munc18 E59K	NanoLuc-Munc18 E59K	STXBP1	25558	P61765
pcmyc-NL-Munc18 K46E/E59K	NanoLuc-Munc18 K46E/E59K	STXBP1	25558	P61765
pcmyc-NL-MDM2	NanoLuc-MDM2	MDM2	4193	Q00987
pPA-mCit-p53	ProteinA-mCitrine-p53	TP53	7157	P04637
pcmyc-NL-FKBP12	NanoLuc-FKBP12	FKBP1A	2280	P62942
pPA-mCit-FRB	ProteinA-mCitrine-MTOR (2021-2113aa)	MTOR	2475	P42345

Table 8: In-cell BRET and cell-free co-IP results from the BRIP assay for the hPRS and hRRS. Displayed are the BRET ratios and co-IP efficiencies from two independent experiments and their mean + sd. All interactions were screened as donor/acceptor (set a) and acceptor/donor (set b) combinations. Exp: Experiment; SD: standart deviation.

			Set a								Set b							
			in-cell BRET				cell-free co-IP				in-cell BRET				cell-free co-IP			
ID	Interaction	Set	Exp1	Exp2	Mean	SD	Exp1	Exp2	Mean	SD	Exp1	Exp2	Mean	SD	Exp1	Exp2	Mean	SD
1	AKT1 + PDPK1	hPRS	0,017	-0,001	0,008	0,013	0,1%	0,3%	0,2%	0,1%	0,021	0,012	0,016	0,007	0,7%	0,7%	0,7%	0,0%
2	AKT1 + TCL1A	hPRS	0,026	0,007	0,016	0,014	0,0%	0,1%	0,1%	0,0%	0,016	0,025	0,021	0,007	0,1%	0,3%	0,2%	0,1%
3	BIRC4 + CASP3	hPRS	0,045	0,005	0,025	0,028	0,1%	0,3%	0,2%	0,2%	0,017	0,008	0,012	0,006	0,2%	0,6%	0,4%	0,3%
4	BIRC4 + CASP7	hPRS	-0,001	0,004	0,001	0,003	0,2%	0,2%	0,2%	0,0%	-0,003	-0,003	-0,003	0,000	0,0%	NA	0,0%	
5	BIRC4 + CASP9	hPRS	0,036	0,046	0,041	0,007	0,9%	1,0%	0,9%	0,1%	-0,003	0,000	-0,002	0,003	NA	NA		
6	ARF1 + ARFIP2	hPRS	-0,005	-0,002	-0,004	0,002	0,0%	0,0%	0,0%	0,0%	-0,007	-0,013	-0,010	0,004	0,0%	0,0%	0,0%	0,0%
7	RHOA + ARHGAP1	hPRS	0,002	0,002	0,002	0,000	0,0%	0,0%	0,0%	0,0%	0,001	0,000	0,001	0,001	0,0%	0,0%	0,0%	0,0%
8	ARHGAP1 + BNIP2	hPRS	-0,003	0,002	-0,001	0,003	0,1%	0,1%	0,1%	0,0%	0,020	0,014	0,017	0,004	1,6%	1,5%	1,5%	0,0%
9	ATF3 + DDIT3	hPRS	0,086	0,067	0,077	0,014	4,4%	2,7%	3,5%	1,2%	0,160	0,079	0,119	0,057	11,2%	13,4%	12,3%	1,5%
10	B2M + HLA-A	hPRS	-0,001	0,002	0,000	0,002	0,0%	0,0%	0,0%	0,0%	0,003	-0,003	0,000	0,005	0,0%	0,1%	0,1%	0,0%
11	B2M + HLA-B	hPRS	-0,003	0,002	-0,001	0,004	0,0%	0,0%	0,0%	0,0%	0,016	0,027	0,022	0,008	0,0%	-1,5%	-0,8%	1,1%
12	B2M + HLA-C	hPRS	0,001	0,007	0,004	0,004	0,1%	0,0%	0,1%	0,1%	0,001	-0,001	0,000	0,001	0,1%	0,5%	0,3%	0,3%
13	BAD + BCL2L1	hPRS	0,216	0,138	0,177	0,055	56,7%	64,2%	60,5%	5,3%	NC	NC	NC	NC	NC	NC	NC	NC
14	BAK1 + BCL2L1	hPRS	NC	NC	NC	NC	NC	NC	NC	NC	NC	NC	NC	NC	NC	NC	NC	NC
15	BDNF + NTF5	hPRS	0,087	0,041	0,064	0,033	1,7%	4,0%	2,8%	1,6%	0,123	0,073	0,098	0,036	5,1%	6,4%	5,7%	0,9%
16	CASP2 + CRADD	hPRS	0,002	0,004	0,003	0,001	1,9%	3,5%	2,7%	1,1%	0,003	0,001	0,002	0,001	1,3%	1,7%	1,5%	0,3%
17	CBLB + GRB2	hPRS	0,131	0,154	0,142	0,016	0,1%	1,7%	0,9%	1,1%	0,002	-0,001	0,001	0,002	0,0%	0,0%	0,0%	0,0%
18	CCND3 + CDK6	hPRS	0,156	0,129	0,142	0,019	27,9%	4,6%	16,3%	16,5%	0,062	0,055	0,059	0,004	12,1%	6,7%	9,4%	3,8%
19	CD2 + CD58	hPRS	-0,006	-0,003	-0,005	0,003	0,0%	0,1%	0,0%	0,0%	0,018	0,015	0,016	0,002	-1,4%	-1,7%	-1,5%	0,3%
20	CDK2 + CKS1B	hPRS	0,082	0,050	0,066	0,023	0,1%	0,1%	0,1%	0,0%	0,160	0,170	0,165	0,007	0,0%	0,0%	0,0%	0,0%
21	CDKN1A + CCNA1	hPRS	0,055	0,048	0,052	0,005	14,7%	11,7%	13,2%	2,2%	0,067	0,046	0,056	0,015	20,9%	20,1%	20,5%	0,6%
22	CDKN1B + CCNA1	hPRS	0,039	0,037	0,038	0,001	5,7%	7,9%	6,8%	1,6%	0,084	0,063	0,073	0,015	31,9%	32,6%	32,2%	0,5%
23	CEBPG + FOS	hPRS	0,011	0,019	0,015	0,005	0,0%	0,1%	0,0%	0,1%	0,008	0,009	0,009	0,001	0,1%	0,1%	0,1%	0,0%
24	CGA + CGB5	hPRS	-0,001	0,008	0,003	0,006	0,2%	0,2%	0,2%	0,0%	0,003	0,003	0,003	0,001	0,4%	0,5%	0,5%	0,0%
25	RCC1 + RAN	hPRS	0,003	0,016	0,009	0,010	4,4%	1,0%	2,7%	2,4%	0,003	0,005	0,004	0,001	3,3%	1,4%	2,3%	1,3%
26	CRK + PDGFRB	hPRS	-0,013	-0,006	-0,010	0,005	0,0%	NA	0,0%		0,252	0,251	0,252	0,001	0,7%	-1,2%	-0,2%	1,3%
27	GADD45A + PCNA	hPRS	0,005	0,011	0,008	0,004	5,4%	1,8%	3,6%	2,5%	-0,004	0,002	-0,001	0,004	0,2%	0,1%	0,1%	0,0%
28	DDIT3 + FOS	hPRS	0,031	0,028	0,029	0,002	1,5%	1,7%	1,6%	0,1%	0,006	0,008	0,007	0,002	0,9%	1,1%	1,0%	0,1%
29	DR1 + DRAP1	hPRS	0,243	0,254	0,249	0,008	91,9%	51,4%	71,7%	28,6%	0,195	0,206	0,200	0,007	50,3%	44,0%	47,1%	4,5%
30	ERBB3 + NRG1	hPRS	-0,016	0,022	0,003	0,027	0,0%	NA	0,0%		0,017	0,004	0,010	0,009	4,0%	4,0%	4,0%	0,0%
31	FABP5 + S100A7	hPRS	NC	NC	NC	NC	NC	NC	NC	NC	NC	NC	NC	NC	NC	NC	NC	NC
32	FANCA + FANCC	hPRS	NC	NC	NC	NC	NC	NC	NC	NC	NC	NC	NC	NC	NC	NC	NC	NC
33	FANCA + FANCG	hPRS	NC	NC	NC	NC	NC	NC	NC	NC	NC	NC	NC	NC	NC	NC	NC	NC
34	FEN1 + PCNA	hPRS	0,068	0,092	0,080	0,017	0,0%	0,0%	0,0%	0,0%	0,005	0,011	0,008	0,004	0,1%	0,1%	0,1%	0,0%
35	FGF1 + FGFR1	hPRS	-0,011	0,025	0,007	0,025	1,3%	0,5%	0,9%	0,6%	-0,001	0,001	0,000	0,001	0,3%	0,4%	0,3%	0,1%
36	GRB2 + PTK2	hPRS	NC	NC	NC	NC	NC	NC	NC	NC	NC	NC	NC	NC	NC	NC	NC	NC
37	GRB2 + VAV1	hPRS	-0,007	0,000	-0,004	0,005	0,0%	0,0%	0,0%	0,0%	0,024	0,020	0,022	0,003	0,1%	0,2%	0,1%	0,0%
38	GRB2 + LAT	hPRS	NC	NC	NC	NC	NC	NC	NC	NC	-0,004	-0,001	-0,002	0,002	0,0%	0,0%	0,0%	0,0%
39	NR3C1 + HSPCA	hPRS	-0,005	0,007	0,001	0,008	0,1%	0,0%	0,0%	0,0%	-0,006	-0,003	-0,004	0,002	0,0%	0,1%	0,0%	0,0%
40	NR3C1 + RELA	hPRS	-0,004	0,001	-0,002	0,003	-0,1%	0,1%	0,0%	0,1%	-0,005	-0,005	-0,005	0,001	0,1%	0,1%	0,1%	0,0%
41	CXCL1 + IL8RB	hPRS	0,050	0,090	0,070	0,029	-0,1%	-3,1%	-1,6%	2,1%	-0,007	-0,002	-0,005	0,004	0,1%	0,1%	0,1%	0,0%
42	GTF2F1 + GTF2F2	hPRS	NC	NC	NC	NC	NC	NC	NC	NC	NC	NC	NC	NC	NC	NC	NC	NC
43	HBA2 + HBB	hPRS	0,232	0,235	0,234	0,002	0,0%	1,7%	0,8%	1,2%	0,239	0,279	0,259	0,028	4,4%	2,9%	3,7%	1,1%
44	HDAC1 + RB1	hPRS	-0,008	-0,002	-0,005	0,004	0,1%	0,2%	0,2%	0,0%	-0,004	-0,002	-0,003	0,002	0,5%	0,0%	0,2%	0,4%
45	HDAC1 + ZBTB16	hPRS	-0,005	0,003	-0,001	0,005	5,6%	3,6%	4,6%	1,5%	-0,003	0,001	-0,001	0,003	10,9%	13,3%	12,1%	1,7%
46	HIF1A + TP53	hPRS	NC	NC	NC	NC	NC	NC	NC	NC	NC	NC	NC	NC	NC	NC	NC	NC
47	IFIT1 + EIF3S6	hPRS	0,006	0,006	0,006	0,000	0,0%	0,1%	0,0%	0,0%	-0,002	0,001	-0,001	0,002	0,0%	0,0%	0,0%	0,0%
48	IGF2 + IGFBP4	hPRS	-0,014	-0,006	-0,010	0,005	0,2%	0,2%	0,2%	0,0%	-0,002	0,002	0,000	0,003	0,9%	-1,8%	-0,5%	1,9%
49	JUNB + BATF	hPRS	0,062	0,075	0,068	0,010	13,9%	10,9%	12,4%	2,1%	0,100	0,084	0,092	0,011	23,7%	20,9%	22,3%	2,0%
50	LCP2 + NCK1	hPRS	0,006	-0,002	0,002	0,006	0,1%	0,1%	0,1%	0,0%	0,015	0,010	0,013	0,003	0,3%	0,3%	0,3%	0,0%
51	LCP2 + VAV1	hPRS	0,003	-0,004	0,000	0,005	0,0%	0,0%	0,0%	0,0%	0,020	0,011	0,015	0,006	0,2%	0,3%	0,2%	0,1%
52	LCP2 + GRAP2	hPRS	0,056	0,054	0,055	0,001	8,2%	9,4%	8,8%	0,9%	0,026	0,028	0,027	0,001	12,5%	19,5%	16,0%	4,9%
53	LGALS3 + LGALS3BP	hPRS	-0,002	-0,003	-0,003	0,001	0,6%	0,1%	0,4%	0,3%	0,004	0,004	0,004	0,000	0,4%	1,4%	0,9%	0,7%
54	LMNA + LMNB1	hPRS	0,049	0,035	0,042	0,010	56,9%	20,2%	38,6%	25,9%	0,009	0,005	0,007	0,003	5,9%	6,1%	6,0%	0,2%
55	LMNA + RB1	hPRS	-0,001	-0,005	-0,003	0,003	2,0%	2,0%	2,0%	0,1%	0,010	0,007	0,008	0,002	1,2%	2,3%	1,7%	0,8%
56	MAD2L1 + MAD1L1	hPRS	0,112	0,109	0,110	0,002	76,5%	48,0%	62,3%	20,1%	0,077	0,070	0,073	0,006	31,0%	37,7%	34,3%	4,7%
57	SMAD1 + SMAD4	hPRS	0,001	-0,001	0,000	0,001	0,2%	0,2%	0,2%	0,0%	0,008	0,004	0,006	0,003	1,0%	0,8%	0,9%	0,1%
58	SMAD3 + SMAD4	hPRS	0,000	-0,002	-0,001	0,001	0,0%	0,0%	0,0%	0,0%	0,023	0,021	0,022	0,002	0,9%	1,6%	1,2%	0,5%
59	SMAD4 + DCP1A	hPRS	0,011	0,015	0,013	0,003	0,2%	0,2%	0,2%	0,0%	0,003	0,002	0,002	0,001	0,5%	0,5%	0,5%	0,0%
60	MAFG + NFE2L1	hPRS	NC	NC	NC	NC	NC	NC	NC	NC	0,044	0,035	0,039	0,006	1,4%	3,5%	2,4%	1,5%
61	MCM2 + MCM3	hPRS	0,000	-0,003	-0,001	0,002	0,0%	0,0%	0,0%	0,0%	0,003	0,001	0,002	0,002	0,0%	0,0%	0,0%	0,0%
62	MCM2 + MCM5	hPRS	NC	NC	NC	NC	NC	NC	NC	NC	0,003	0,002	0,002	0,001	0,2%	0,2%	0,2%	0,0%
63	NCBP1 + NCBP2	hPRS	0,160	0,148	0,154	0,009	7,4%	20,9%	14,2%	9,6%	0,058	0,064	0,061	0,004	21,2%	22,6%	21,9%	1,0%
64	NF2 + HGS	hPRS	0,056	0,029	0,043	0,019	6,1%	3,7%	4,9%	1,7%	0,018	0,017	0,017	0,000	1,7%	4,2%	3,0%	1,8%
65	ORC2L + ORC4L	hPRS	-0,002	0,000	-0,001	0,001	0,9%	5,9%	3,4%	3,5%	0,015	0,007	0,011	0,006	16,8%	6,5%	11,6%	7,3%
66	ORC2L + MCM10	hPRS	0,003	0,005	0,004	0,001	0,0%	-0,7%	-0,3%	0,5%	0,012	0,004	0,008	0,006	0,1%	0,0%	0,1%	0,1%
67	PDE4D + GNB2L1	hPRS	-0,003	-0,003	-0,003	0,001	0,0%	0,1%	0,1%	0,1%	0,000	0,001	0,000	0,000	0,0%	0,0%	0,0%	0,0%
68	PDGFRB + PTPN11	hPRS	NA	NA			0,4%	22,6%	11,5%	15,7%	-0,001	0,001	0,000	0,001	0,2%	1,2%	0,7%	0,8%

			Set a								Set b							
			in-cell BRET				cell-free co-IP				in-cell BRET				cell-free co-IP			
ID	Interaction	Set	Exp1	Exp2	Mean	SD	Exp1	Exp2	Mean	SD	Exp1	Exp2	Mean	SD	Exp1	Exp2	Mean	SD
69	PEX14 + PEX19	hPRS	0,063	0,044	0,053	0,013	0,2%	0,1%	0,1%	0,1%	0,114	0,073	0,093	0,029	0,0%	0,0%	0,0%	0,0%
70	PPP3CA + PPP3R1	hPRS	NC	NC	NC	NC	NC	NC	NC	NC	NC	NC	NC	NC	NC	NC	NC	NC
71	PRKAR2A + VIL2	hPRS	0,005	0,002	0,003	0,002	0,1%	0,1%	0,1%	0,0%	0,010	0,010	0,010	0,001	0,0%	0,0%	0,0%	0,0%
72	MAPK7 + MAP2K5	hPRS	NC	NC	NC	NC	NC	NC	NC	NC	NC	NC	NC	NC	NC	NC	NC	NC
73	PSMD4 + RAD23A	hPRS	0,070	0,062	0,066	0,006	0,2%	0,2%	0,2%	0,0%	0,005	0,010	0,007	0,004	NA	0,0%	0,0%	
74	PTK2 + SRC	hPRS	NC	NC	NC	NC	NC	NC	NC	NC	NC	NC	NC	NC	NC	NC	NC	NC
75	PTPN11 + FRS2	hPRS	0,006	0,001	0,003	0,003	NA	0,1%	0,1%		0,240	0,204	0,222	0,026	NA	-1,4%	-1,4%	
76	PEX19 + PEX3	hPRS	0,015	0,011	0,013	0,003	1,0%	0,6%	0,8%	0,3%	0,025	0,036	0,030	0,008	0,7%	0,7%	0,7%	0,0%
77	PEX19 + PEX11B	hPRS	0,031	0,020	0,025	0,008	0,3%	0,1%	0,2%	0,1%	0,087	0,096	0,092	0,006	1,1%	1,0%	1,1%	0,1%
78	PEX19 + PEX16	hPRS	0,052	0,049	0,050	0,002	0,8%	0,7%	0,8%	0,1%	0,103	0,111	0,107	0,005	1,4%	2,4%	1,9%	0,7%
79	RAC1 + ARFIP2	hPRS	0,001	-0,003	-0,001	0,003	0,1%	0,0%	0,1%	0,0%	-0,019	-0,010	-0,014	0,006	0,0%	0,1%	0,1%	0,1%
80	RAF1 + RAP1A	hPRS	0,003	0,000	0,001	0,002	0,8%	0,9%	0,8%	0,1%	-0,003	0,005	0,001	0,006	0,5%	0,7%	0,6%	0,2%
81	RET + FRS2	hPRS	NC	NC	NC	NC	NC	NC	NC	NC	NC	NC	NC	NC	NC	NC	NC	NC
82	RPA2 + RPA3	hPRS	0,001	-0,003	-0,001	0,003	0,0%	0,0%	0,0%	0,0%	0,003	0,008	0,005	0,004	0,5%	0,8%	0,7%	0,2%
83	S100A1 + S100B	hPRS	NA	NA			0,4%	120,5%	60,5%	84,9%	0,411	0,457	0,434	0,033	41,3%	40,6%	41,0%	0,5%
84	S100A6 + S100B	hPRS	NA	NA			0,0%	2,5%	1,3%	1,8%	0,023	0,024	0,024	0,001	0,2%	0,2%	0,2%	0,0%
85	SKP1A + SKP2	hPRS	0,006	0,000	0,003	0,004	0,6%	0,6%	0,6%	0,0%	0,054	0,060	0,057	0,004	2,6%	3,2%	2,9%	0,5%
86	SKP1A + BTRC	hPRS	0,024	0,016	0,020	0,006	32,8%	17,8%	25,3%	10,6%	-0,006	0,003	-0,002	0,006	NA	0,1%	0,1%	
87	TP53 + UBE2I	hPRS	NC	NC	NC	NC	NC	NC	NC	NC	NC	NC	NC	NC	NC	NC	NC	NC
88	TRAF6 + TAB3	hPRS	NC	NC	NC	NC	NC	NC	NC	NC	NC	NC	NC	NC	NC	NC	NC	NC
89	TNFSF10 + TNFRSF10B	hPRS	NC	NC	NC	NC	NC	NC	NC	NC	NC	NC	NC	NC	NC	NC	NC	NC
90	RIPK2 + CARD4	hPRS	0,131	0,105	0,118	0,019	1,2%	18,4%	9,8%	12,2%	-0,009	0,002	-0,004	0,008	NA	4,3%	4,3%	
91	GRAP2 + LAT	hPRS	0,424	0,166	0,295	0,183	0,1%	35,7%	17,9%	25,2%	-0,011	0,002	-0,004	0,010	0,1%	0,1%	0,1%	0,0%
92	LSM3 + LSM2	hPRS	0,503	0,563	0,533	0,042	73,3%	38,8%	56,1%	24,4%	0,463	0,439	0,451	0,017	53,3%	55,3%	54,3%	1,4%
1	NAT2 + DNAJA1	hRRS	0,028	0,025	0,027	0,002	0,4%	0,17%	0,3%	0,2%	-0,001	0,005	0,002	0,004	NA	0,1%	0,1%	
2	ACVR1 + CWF19L1	hRRS	0,025	0,032	0,028	0,005	-0,3%	-0,43%	-0,4%	0,1%	NC	NC	NC	NC	NC	NC	NC	NC
3	SLC25A6 + ZNF213	hRRS	0,006	0,008	0,007	0,001	1,0%	0,46%	0,7%	0,4%	0,004	0,001	0,002	0,002	NA	NA		
4	NUDT2 + MIIP	hRRS	0,010	0,015	0,013	0,004	3,1%	1,30%	2,2%	1,3%	0,000	0,003	0,001	0,002	2,7%	1,0%	1,8%	1,2%
5	APOD + MUC7	hRRS	NA	NA			0,0%	-0,04%	0,0%	0,0%	0,001	0,012	0,006	0,008	-0,8%	-1,5%	-1,1%	0,5%
6	FAS + LSM3	hRRS	0,002	0,005	0,003	0,002	-0,4%	-0,36%	-0,4%	0,0%	-0,004	-0,001	-0,003	0,002	-0,1%	0,0%	-0,1%	0,0%
7	RHOC + NUP62CL	hRRS	0,007	0,006	0,007	0,000	0,0%	0,05%	0,0%	0,0%	-0,002	0,001	0,000	0,002	0,0%	0,0%	0,0%	0,0%
8	ARSA + DBN1	hRRS	0,004	0,002	0,003	0,002	-0,7%	-0,57%	-0,6%	0,1%	-0,004	-0,002	-0,003	0,002	NA	NA		
9	ASS + FLJ13912	hRRS	0,000	0,000	0,000	0,000	0,2%	0,08%	0,1%	0,1%	0,003	0,004	0,003	0,001	0,0%	0,0%	0,0%	0,0%
10	ATP5O + CLEC2D	hRRS	0,007	0,007	0,007	0,000	-1,2%	-1,54%	-1,4%	0,2%	-0,004	-0,002	-0,003	0,001	-0,1%	0,0%	0,0%	0,0%
11	BAD + FGF18	hRRS	NC	NC	NC	NC	NC	NC	NC	NC	NC	NC	NC	NC	NC	NC	NC	NC
12	BMP5 + C10orf119	hRRS	-0,003	0,002	-0,001	0,003	-0,3%	-0,56%	-0,4%	0,2%	0,000	0,000	0,000	0,000	0,0%	0,0%	0,0%	0,0%
13	BTC + KIAA0515	hRRS	0,004	-0,002	0,001	0,004	-0,1%	-0,08%	-0,1%	0,0%	-0,002	0,002	0,000	0,003	0,0%	0,0%	0,0%	0,1%
14	BYSL + KIAA0907	hRRS	NC	NC	NC	NC	NC	NC	NC	NC	NC	NC	NC	NC	NC	NC	NC	NC
15	CA2 + PTPRS	hRRS	NC	NC	NC	NC	NC	NC	NC	NC	NC	NC	NC	NC	NC	NC	NC	NC
16	CANX + ARHGEF15	hRRS	0,002	0,000	0,001	0,002	0,0%	-0,07%	0,0%	0,1%	-0,003	-0,002	-0,002	0,000	0,1%	0,0%	0,0%	0,0%
17	CANX + ATAD2	hRRS	NC	NC	NC	NC	NC	NC	NC	NC	NC	NC	NC	NC	NC	NC	NC	NC
18	CD34 + C20orf161	hRRS	0,009	NA	0,009	NA	-2,6%	-2,09%	-2,3%	0,3%	-0,003	-0,001	-0,002	0,002	0,3%	0,2%	0,2%	0,0%
19	SCARB1 + PHF21B	hRRS	-0,004	-0,005	-0,004	0,001	2,1%	0,42%	1,2%	1,2%	-0,005	-0,001	-0,003	0,003	1,3%	0,8%	1,1%	0,4%
20	CD81 + NPC2	hRRS	-0,002	-0,003	-0,003	0,001	0,1%	0,00%	0,0%	0,1%	-0,008	-0,003	-0,005	0,003	-0,3%	-0,3%	-0,3%	0,0%
21	CD151 + WDR41	hRRS	-0,002	-0,003	-0,002	0,001	1,4%	0,66%	1,1%	0,5%	-0,001	0,001	0,000	0,001	4,9%	1,2%	3,0%	2,6%
22	CENPA + PPIL3	hRRS	0,002	-0,002	0,000	0,003	0,8%	0,59%	0,7%	0,2%	0,008	0,005	0,006	0,002	10,6%	7,5%	9,1%	2,2%
23	CHC1 + KLHL6	hRRS	0,001	-0,001	0,000	0,001	0,1%	0,07%	0,1%	0,0%	0,001	0,001	0,001	0,000	1,9%	1,9%	1,9%	0,0%
24	CKB + HBZ	hRRS	-0,003	-0,001	-0,002	0,001	0,0%	0,01%	0,0%	0,0%	0,002	0,004	0,003	0,001	0,0%	0,0%	0,0%	0,0%
25	CLPTM1 + L3MBTL2	hRRS	0,004	0,003	0,003	0,001	0,9%	NA	0,9%		-0,001	-0,004	-0,003	0,002	NA	NA		
26	CNN1 + FRAG1	hRRS	NC	NC	NC	NC	NC	NC	NC	NC	0,003	-0,002	0,000	0,003	NA	NA		
27	COPB1 + SLC39A14	hRRS	0,003	0,007	0,005	0,003	1,3%	NA	1,3%		0,003	0,004	0,004	0,000	NA	NA		
28	COPB1 + HPCAL4	hRRS	0,004	0,000	0,002	0,003	1,9%	2,82%	2,4%	0,7%	-0,003	0,000	-0,001	0,002	0,1%	0,0%	0,1%	0,0%
29	NKX2-5 + GALNACT-2	hRRS	-0,002	-0,004	-0,003	0,001	0,6%	0,30%	0,4%	0,2%	0,009	0,009	0,009	0,000	0,0%	0,1%	0,1%	0,0%
30	DEFA1 + C9orf97	hRRS	-0,008	-0,012	-0,010	0,002	0,1%	0,10%	0,1%	0,0%	-0,002	0,000	-0,001	0,001	0,0%	0,1%	0,0%	0,1%
31	DLX4 + RAB3IP	hRRS	-0,002	-0,002	-0,002	0,000	0,2%	0,14%	0,2%	0,0%	0,004	NA	0,004		0,0%	0,4%	0,2%	0,3%
32	DUT + C19orf40	hRRS	0,000	0,001	0,001	0,001	0,1%	0,08%	0,1%	0,0%	0,000	-0,001	-0,001	0,001	0,0%	0,0%	0,0%	0,0%
33	EMD + ARMC1	hRRS	0,018	0,013	0,015	0,004	0,7%	0,68%	0,7%	0,0%	0,007	0,005	0,006	0,001	1,0%	0,8%	0,9%	0,1%
34	ERBB3 + C3orf38	hRRS	-0,007	-0,010	-0,009	0,002	0,0%	0,05%	0,0%	0,0%	-0,004	-0,002	-0,003	0,001	0,9%	0,2%	0,6%	0,5%
35	ETF1 + LIMR	hRRS	0,000	0,000	0,000	0,000	0,2%	0,22%	0,2%	0,0%	0,004	0,001	0,002	0,002	0,5%	0,3%	0,4%	0,2%
36	FABP4 + GCG	hRRS	-0,002	-0,001	-0,002	0,001	0,0%	0,00%	0,0%	0,0%	-0,011	-0,011	-0,011	0,000	0,0%	0,0%	0,0%	0,1%
37	FABP7 + STX5A	hRRS	0,001	-0,005	-0,002	0,004	0,2%	0,09%	0,2%	0,1%	0,002	0,004	0,003	0,001	0,6%	0,6%	0,6%	0,0%
38	FIGF + ZNF46	hRRS	-0,003	-0,006	-0,005	0,002	0,1%	0,03%	0,0%	0,0%	0,011	0,005	0,008	0,004	0,0%	1,0%	0,5%	0,7%
39	FKBP3 + NQO2	hRRS	0,001	0,000	0,001	0,000	0,0%	0,00%	0,0%	0,0%	0,004	0,002	0,003	0,002	0,0%	0,0%	0,0%	0,0%
40	GABRA2 + PSTPIP2	hRRS	NC	NC	NC	NC	NC	NC	NC	NC	NC	NC	NC	NC	NC	NC	NC	NC
41	GALK1 + MCCC1	hRRS	-0,003	-0,004	-0,003	0,001	0,1%	0,05%	0,1%	0,0%	0,027	NA	0,027		0,0%	5,4%	2,7%	3,8%
42	GCDH + ZCCHC9	hRRS	0,000	-0,001	0,000	0,000	0,0%	0,01%	0,0%	0,0%	0,000	0,001	0,001	0,001	0,2%	1,7%	0,9%	1,0%
43	GP1BA + PVRL2	hRRS	0,040	0,033	0,036	0,005	20,5%	9,42%	15,0%	7,8%	-0,003	-0,001	-0,002	0,002	1,5%	1,6%	1,5%	0,0%
44	GPD2 + BOP	hRRS	NC	NC	NC	NC	NC	NC	NC	NC	-0,003	-0,004	-0,004	0,001	0,0%	0,0%	0,0%	0,0%
45	GPR18 + HNRPLL	hRRS	0,006	-0,008	-0,001	0,010	0,0%	-0,05%	0,0%	0,0%	-0,005	-0,002	-0,004	0,002	0,0%	NA	0,0%	
46	GRIK2 + ARL6IP6	hRRS	0,154	0,040	0,097	0,081	0,3%	1,23%	0,7%	0,7%	NC	NC	NC	NC	NC	NC	NC	NC
47	HIST1H1C + NPDC1	hRRS	0,001	-0,001	0,000	0,001	0,2%	0,09%	0,1%	0,1%	0,000	0,001	0,000	0,001	0,1%	0,1%	0,1%	0,0%
48	HCLS1 + SALL2	hRRS	0,000	-0,002	-0,001	0,001	0,0%	0,01%	0,0%	0,0%	0,004	0,005	0,005	0,001	0,1%	0,1%	0,1%	0,0%
49	HLA-DMB + PSEN2	hRRS	0,058	0,039	0,049	0,014	0,2%	0,23%	0,2%	0,0%	0,008	-0,001	0,004	0,006	0,0%	0,0%	0,0%	0,0%
50	HLA-DQB1 + ATOH7	hRRS	NC	NC	NC	NC	NC	NC	NC	NC	-0,005	0,000	-0,002	0,004	0,0%	0,0%	0,0%	0,0%
51	HMGB1 + TEAD4	hRRS	0,002	-0,006	-0,002	0,006	0,0%	0,00%	0,0%	0,0%	NC	NC	NC	NC	NC	NC	NC	NC

			Set a								Set b							
			in-cell BRET				cell-free co-IP				in-cell BRET				cell-free co-IP			
ID	Interaction	Set	Exp1	Exp2	Mean	SD	Exp1	Exp2	Mean	SD	Exp1	Exp2	Mean	SD	Exp1	Exp2	Mean	SD
52	INPP1 + UBLCP1	hRRS	-0,001	-0,004	-0,002	0,002	0,0%	0,00%	0,0%	0,0%	0,006	0,000	0,003	0,004	0,0%	-0,2%	-0,1%	0,1%
53	ITPA + C19orf14	hRRS	0,000	-0,005	-0,002	0,004	0,0%	0,01%	0,0%	0,0%	0,008	0,006	0,007	0,001	0,8%	0,6%	0,7%	0,1%
54	ITPK1 + TMEM22	hRRS	NC	NC	NC	NC	NC	NC	NC	NC	-0,002	0,000	-0,001	0,001	0,9%	0,3%	0,6%	0,4%
55	JAK3 + ATP6V1D	hRRS	NC	NC	NC	NC	NC	NC	NC	NC	NC	NC	NC	NC	NC	NC	NC	NC
56	LAMP2 + UBE2G2	hRRS	0,002	-0,003	0,000	0,003	0,1%	-0,34%	-0,1%	0,3%	0,001	-0,002	-0,001	0,002	0,0%	0,0%	0,0%	0,0%
57	LUM + UGCGL2	hRRS	-0,003	-0,008	-0,006	0,003	-0,1%	-0,39%	-0,2%	0,2%	-0,001	0,000	0,000	0,001	0,0%	-0,2%	-0,1%	0,1%
58	MAOB + CTCF	hRRS	NC	NC	NC	NC	NC	NC	NC	NC	0,001	-0,001	0,000	0,002	0,0%	-0,1%	0,0%	0,1%
59	MCM2 + PLXNA4	hRRS	0,002	-0,004	-0,001	0,004	0,0%	0,00%	0,0%	0,0%	0,002	-0,002	0,000	0,002	0,0%	0,0%	0,0%	0,0%
60	MNAT1 + GMPPA	hRRS	0,003	-0,004	0,000	0,005	0,0%	0,00%	0,0%	0,0%	0,004	0,002	0,003	0,001	7,8%	3,6%	5,7%	3,0%
61	MOBP + MRPS25	hRRS	0,000	-0,002	-0,001	0,001	0,8%	1,15%	1,0%	0,2%	0,001	0,001	0,001	0,000	0,9%	0,3%	0,6%	0,4%
62	MX2 + NUP37	hRRS	-0,004	0,026	0,011	0,021	0,0%	-0,02%	0,0%	0,0%	0,003	0,003	0,003	0,000	1,4%	0,0%	0,7%	1,0%
63	MYBL2 + ENOX1	hRRS	0,007	0,005	0,006	0,001	0,1%	-0,02%	0,0%	0,1%	-0,001	-0,001	-0,001	0,001	0,4%	0,1%	0,3%	0,2%
64	PPP1R12B + ZNF307	hRRS	NC	NC	NC	NC	NC	NC	NC	NC	NC	NC	NC	NC	NC	NC	NC	NC
65	HNRPM + TNFSF10	hRRS	-0,001	-0,007	-0,004	0,004	0,1%	0,13%	0,1%	0,0%	NC	NC	NC	NC	NC	NC	NC	NC
66	NDP + NUDT4	hRRS	-0,004	-0,011	-0,008	0,005	0,8%	0,39%	0,6%	0,3%	-0,003	-0,002	-0,002	0,001	0,0%	0,0%	0,0%	0,0%
67	NFIB + TIRAP	hRRS	0,000	-0,002	-0,001	0,002	1,6%	0,61%	1,1%	0,7%	-0,001	-0,004	-0,002	0,002	7,9%	1,2%	4,6%	4,8%
68	NONO + VMD2	hRRS	-0,002	-0,008	-0,005	0,004	0,1%	0,04%	0,1%	0,1%	-0,001	0,001	0,000	0,001	0,0%	0,0%	0,0%	0,0%
69	NT5E + TAB3	hRRS	NC	NC	NC	NC	NC	NC	NC	NC	NC	NC	NC	NC	NC	NC	NC	NC
70	OSM + LOC146542	hRRS	NC	NC	NC	NC	NC	NC	NC	NC	NC	NC	NC	NC	NC	NC	NC	NC
71	P2RY6 + TRIM26	hRRS	0,009	0,005	0,007	0,003	1,3%	-0,70%	0,3%	1,4%	-0,002	0,001	-0,001	0,002	NA	0,0%	0,0%	
72	PBX2 + VILL	hRRS	0,006	0,001	0,004	0,003	1,1%	0,57%	0,8%	0,4%	0,004	0,006	0,005	0,001	2,7%	1,8%	2,2%	0,6%
73	PDE9A + FLJ38964	hRRS	NC	NC	NC	NC	NC	NC	NC	NC	NC	NC	NC	NC	NC	NC	NC	NC
74	PDGFRA + NDFIP1	hRRS	NC	NC	NC	NC	NC	NC	NC	NC	0,009	0,006	0,007	0,002	0,8%	0,3%	0,6%	0,4%
75	PDHB + ZC3HC1	hRRS	0,003	0,000	0,002	0,002	0,3%	0,53%	0,4%	0,2%	0,003	0,000	0,001	0,003	0,3%	0,2%	0,2%	0,1%
76	PFDN2 + ZNF440	hRRS	-0,002	-0,004	-0,003	0,002	0,0%	0,01%	0,0%	0,0%	-0,003	-0,004	-0,003	0,001	10,4%	2,0%	6,2%	5,9%
77	PMCH + RIC3	hRRS	0,005	0,002	0,003	0,002	0,1%	0,07%	0,1%	0,1%	-0,002	-0,003	-0,003	0,001	0,0%	-0,1%	0,0%	0,1%
78	PML + SGKL	hRRS	0,001	-0,001	0,000	0,002	3,5%	0,82%	2,2%	1,9%	-0,002	0,002	0,000	0,003	0,5%	0,7%	0,6%	0,2%
79	PPP1R1A + DENND6B	hRRS	0,001	-0,002	-0,001	0,002	0,0%	0,00%	0,0%	0,0%	NC	NC	NC	NC	NC	NC	NC	NC
80	PPP6C + ZNF350	hRRS	0,001	-0,002	-0,001	0,002	0,6%	0,67%	0,6%	0,1%	0,002	0,003	0,002	0,001	0,7%	2,3%	1,5%	1,1%
81	PROS1 + STK25	hRRS	NC	NC	NC	NC	NC	NC	NC	NC	-0,002	-0,001	-0,002	0,000	0,1%	-0,1%	0,0%	0,1%
82	PSMD5 + SLC22A15	hRRS	-0,001	-0,003	-0,002	0,001	0,0%	0,00%	0,0%	0,0%	-0,001	-0,003	-0,002	0,001	0,5%	0,1%	0,3%	0,2%
83	PSMD5 + C10orf94	hRRS	0,000	-0,002	-0,001	0,001	0,0%	0,01%	0,0%	0,0%	0,002	0,002	0,002	0,000	0,0%	-0,1%	0,0%	0,0%
84	PSMD12 + CRIPT	hRRS	0,005	-0,003	0,001	0,005	0,1%	-0,08%	0,0%	0,1%	-0,002	-0,001	-0,001	0,001	0,0%	0,0%	0,0%	0,0%
85	RAB3B + BOC	hRRS	0,000	-0,003	-0,002	0,002	0,0%	0,03%	0,0%	0,0%	-0,006	-0,009	-0,008	0,002	0,0%	0,0%	0,0%	0,0%
86	RBM3 + SF3A1	hRRS	NC	NC	NC	NC	NC	NC	NC	NC	NC	NC	NC	NC	NC	NC	NC	NC
87	RFX3 + SEMA4G	hRRS	0,003	-0,003	0,000	0,005	0,0%	0,02%	0,0%	0,0%	0,003	NA	0,003	#DIV/0!	0,1%	-7,8%	-3,9%	5,6%
88	RGR + ABCF3	hRRS	0,001	-0,003	-0,001	0,002	0,2%	0,09%	0,1%	0,1%	-0,003	-0,004	-0,004	0,001	0,1%	0,0%	0,1%	0,1%
89	RXRB + CXCL11	hRRS	-0,001	-0,004	-0,002	0,002	0,0%	0,00%	0,0%	0,0%	-0,007	-0,011	-0,009	0,003	0,0%	-5,5%	-2,8%	3,9%
90	SERPINB3 + DCTN6	hRRS	0,003	-0,002	0,000	0,003	0,0%	0,00%	0,0%	0,0%	-0,001	0,001	0,000	0,001	0,0%	-0,1%	-0,1%	0,1%
91	SHMT2 + STAC3	hRRS	0,001	-0,004	-0,002	0,004	0,0%	0,01%	0,0%	0,0%	0,013	0,007	0,010	0,005	0,0%	-0,2%	-0,1%	0,1%
92	SLC6A1 + TM4SF4	hRRS	0,014	0,008	0,011	0,004	6,7%	3,16%	4,9%	2,5%	NC	NC	NC	NC	NC	NC	NC	NC

Table 9: In-cell BRET and cell-free co-IP results from the BRIP assay for the AIRSv2. Displayed are the BRET ratios and co-IP efficiencies from two independent experiments and their mean + SD. All interactions were screened as donor/acceptor (set a) and acceptor/donor (set b) combinations. Exp: Experiment; SD: standart deviation.

		Set a								Set b							
		in-cell BRET				cell-free co-IP				in-cell BRET				cell-free co-IP			
Interaction	Kd (nM)	Exp 1	Exp 2	Mean	SD	Exp 1	Exp 2	Mean	SD	Exp 1	Exp 2	Mean	SD	Exp 1	Exp 2	Mean	SD
NCK2 + LIMS1	3000000	-0,001	-0,015	-0,008	0,010	0,0%	0,0%	0,0%	0,0%	0,016	0,012	0,014	0,003	0,1%	0,2%	0,1%	0,1%
CALR + CD8A	126000	0,004	-0,003	0,000	0,005	0,3%	0,3%	0,3%	0,0%	0,002	0,013	0,007	0,008	0,6%	0,7%	0,7%	0,1%
TNNI3 + TNNC1	31000	0,158	0,143	0,151	0,011	11,8%	-0,1%	5,8%	8,4%	0,026	-0,005	0,011	0,022	0,0%	0,0%	0,0%	0,0%
CLINT1 + VTI1B	22000	0,063	0,049	0,056	0,010	2,0%	0,5%	1,3%	1,1%	0,013	0,003	0,008	0,007	0,1%	0,4%	0,2%	0,2%
RAC2 + PLCG2	21900	0,000	0,007	0,004	0,005	0,2%	0,0%	0,1%	0,1%	0,007	0,004	0,005	0,002	0,1%	0,4%	0,3%	0,2%
ARF1 + AP1S3	20000	-0,001	0,002	0,001	0,002	0,0%	0,0%	0,0%	0,0%	0,012	0,024	0,018	0,009	0,8%	0,9%	0,8%	0,0%
FUBP1 + PUF60	14000	0,018	0,018	0,018	0,000	0,1%	0,1%	0,1%	0,0%	0,004	-0,016	-0,006	0,015	0,2%	0,2%	0,2%	0,0%
HLA-DQA1 + HLA-DQB1	11400	1,112	1,087	1,100	0,018	24,1%	15,6%	19,8%	6,0%	0,080	0,034	0,057	0,033	5,0%	2,1%	3,5%	2,1%
S100B + FGF2	10000	0,006	-0,007	-0,001	0,009	0,0%	0,0%	0,0%	0,0%	0,004	-0,006	-0,001	0,008	0,0%	0,0%	0,0%	0,0%
RAB4A + ZFYVE20	7700	-0,002	0,002	0,000	0,003	8,5%	0,3%	4,4%	5,8%	0,018	0,031	0,025	0,009	0,8%	0,0%	0,4%	0,6%
PAK1 + ARHGEF7	7500	0,007	0,009	0,008	0,002	0,0%	0,1%	0,1%	0,1%	0,052	0,016	0,034	0,026	12,9%	16,9%	14,9%	2,9%
HSPBP1 + HSPA1A	6500	0,005	-0,013	-0,004	0,012	0,0%	0,0%	0,0%	0,0%	0,015	-0,011	0,002	0,018	0,0%	0,0%	0,0%	0,0%
PLCB2 + RAC1	5300	0,017	0,011	0,014	0,004	30,9%	0,9%	15,9%	21,2%	0,002	0,003	0,002	0,001	0,1%	0,2%	0,1%	0,1%
MTA1 + HDAC1	5000	0,002	-0,007	-0,002	0,007	0,1%	0,0%	0,0%	0,0%	-0,001	0,021	0,010	0,015	4,2%	4,1%	4,2%	0,1%
XRCC4 + NHEJ1	4100	0,060	0,059	0,060	0,001	0,0%	0,0%	0,0%	0,0%	0,038	-0,005	0,016	0,030	0,0%	0,0%	0,0%	0,0%
ENAH + TES	3600	0,012	0,001	0,006	0,007	-1,4%	-0,3%	-0,9%	0,8%	0,003	0,010	0,006	0,005	0,0%	0,0%	0,0%	0,0%
RAC1 + ARFIP2	3000	0,017	0,033	0,025	0,011	0,4%	0,1%	0,3%	0,2%	0,014	0,006	0,010	0,006	0,0%	0,1%	0,1%	0,0%
IPO13 + EIF1AX	3000	0,010	-0,002	0,004	0,008	0,6%	0,3%	0,4%	0,2%	0,007	0,008	0,008	0,001	0,0%	0,0%	0,0%	0,0%
ICAM1 + ITGAL	3000	0,025	0,009	0,017	0,012	1,8%	0,6%	1,2%	0,9%	-0,002	0,006	0,002	0,005	0,8%	0,3%	0,5%	0,4%
CD3E + CD3G	2730	0,012	0,009	0,011	0,002	1,3%	1,0%	1,1%	0,2%	-0,001	0,010	0,005	0,008	0,2%	0,2%	0,2%	0,0%
RAC1 + NCF2	2700	0,004	0,012	0,008	0,006	0,3%	0,7%	0,5%	0,2%	0,002	0,016	0,009	0,010	0,8%	3,2%	2,0%	1,7%
OSBP + VAPA	2100	0,054	0,048	0,051	0,005	-0,8%	-1,1%	-0,9%	0,2%	0,004	-0,011	-0,004	0,010	0,0%	0,0%	0,0%	0,0%
MAPK1 + RPS6KA1	2000	0,031	0,027	0,029	0,003	0,0%	0,0%	0,0%	0,0%	0,040	0,005	0,022	0,025	0,5%	1,5%	1,0%	0,7%
PRPF4 + PPIH	1970	0,028	0,015	0,021	0,009	0,2%	0,1%	0,2%	0,0%	0,003	-0,010	-0,004	0,009	0,1%	0,3%	0,2%	0,1%
CHMP6 + VPS25	1800	0,006	0,000	0,003	0,004	0,5%	1,5%	1,0%	0,7%	0,003	0,023	0,013	0,014	1,1%	0,5%	0,8%	0,5%
TIMP1 + MMP14	1530	0,025	-0,013	0,006	0,027	2,2%	-0,1%	1,0%	1,6%	0,000	0,017	0,008	0,012	0,4%	1,5%	0,9%	0,8%
MAPRE1 + MAPRE3	1500	0,067	0,039	0,053	0,020	10,5%	11,8%	11,2%	0,9%	0,078	0,095	0,087	0,012	8,4%	15,7%	12,0%	5,2%
MIF + RPS19	1300	-0,003	-0,004	-0,003	0,000	0,0%	0,0%	0,0%	0,0%	0,002	0,012	0,007	0,007	0,0%	0,0%	0,0%	0,0%
RBP4 + TTR	800	0,018	-0,005	0,007	0,016	1,4%	0,9%	1,2%	0,3%	0,047	0,013	0,030	0,024	3,8%	4,0%	3,9%	0,1%
RNF31 + RBCK1	520	0,196	0,214	0,205	0,013	4,0%	1,8%	2,9%	1,5%	0,474	0,122	0,298	0,249	46,9%	141,4%	94,2%	66,9%
BCL9 + TCF7L2	459	0,021	0,006	0,014	0,010	-0,1%	-0,2%	-0,2%	0,1%	0,000	0,014	0,007	0,010	0,3%	0,4%	0,3%	0,1%
SPAG9 + ARF6	420	0,010	0,010	0,010	0,000	1,0%	0,2%	0,6%	0,6%	0,000	0,001	0,001	0,001	0,5%	0,6%	0,5%	0,1%
PRIM1 + PRIM2	250	1,079	0,229	0,654	0,601	-20,1%	4,6%	-7,7%	17,5%	-0,016	0,130	0,057	0,103	0,0%	78,8%	39,4%	55,7%
RAB11A + RAB11FIP2	250	-0,001	0,001	0,000	0,001	0,1%	0,0%	0,1%	0,0%	0,010	0,024	0,017	0,010	7,2%	13,3%	10,3%	4,3%
CDC42 + ARHGAP1	239	0,005	0,011	0,008	0,004	0,0%	0,1%	0,1%	0,0%	0,005	0,005	0,005	0,000	0,0%	0,0%	0,0%	0,0%
RALB + RALBP1	184	0,001	0,001	0,001	0,000	1,9%	0,1%	1,0%	1,3%	0,006	0,013	0,010	0,005	0,1%	2,7%	1,4%	1,8%
SERPIND1 + F2	115	0,003	-0,020	-0,008	0,016	0,7%	0,5%	0,6%	0,1%	0,004	0,008	0,006	0,003	0,9%	0,7%	0,8%	0,2%
STAMBP + CHMP3	113	0,123	0,147	0,135	0,017	0,1%	0,1%	0,1%	0,0%	0,004	0,021	0,013	0,012	0,5%	0,3%	0,4%	0,1%
MBP + HLA-DRB5	100	0,001	-0,014	-0,007	0,011	0,0%	0,1%	0,0%	0,0%	0,010	0,011	0,010	0,000	0,1%	0,1%	0,1%	0,0%
HBA2 + AHSP	93	0,004	0,005	0,004	0,000	0,0%	0,1%	0,0%	0,0%	0,009	0,009	0,009	0,000	0,0%	0,0%	0,0%	0,0%
AIMP2 + KARS	90	0,015	0,003	0,009	0,008	2,5%	2,2%	2,4%	0,2%	0,025	0,004	0,015	0,015	3,5%	3,9%	3,7%	0,3%
U2AF2 + SF1	84	0,014	0,007	0,010	0,004	0,1%	0,1%	0,1%	0,1%	0,015	0,011	0,013	0,003	0,0%	1,0%	0,5%	0,7%
CDK2 + CKS1B	77	0,023	0,035	0,029	0,008	0,2%	0,2%	0,2%	0,0%	0,398	0,003	0,201	0,279	0,0%	0,0%	0,0%	0,0%
PFN1 + VASP	57	0,003	0,001	0,002	0,001	0,0%	0,0%	0,0%	0,0%	0,008	-0,005	0,001	0,010	0,0%	0,0%	0,0%	0,0%
SRSF1 + SRPK1	50	0,000	0,001	0,001	0,001	0,0%	0,0%	0,0%	0,0%	0,003	0,013	0,008	0,007	0,2%	0,5%	0,4%	0,2%
PEX19 + PEX3	40,8	0,005	0,008	0,006	0,002	0,6%	0,0%	0,3%	0,4%	0,077	0,061	0,069	0,011	4,1%	50,2%	27,1%	32,6%
WASL + BAIAP2L1	40	0,003	0,004	0,004	0,000	0,1%	0,1%	0,1%	0,0%	-0,003	0,013	0,005	0,011	0,2%	0,2%	0,2%	0,0%
S100A10 + AHNAK	30	0,007	0,007	0,007	0,000	0,2%	0,0%	0,1%	0,1%	0,002	0,002	0,002	0,000	0,1%	0,1%	0,1%	0,0%
EIF4A3 + CWC22	28,4	0,025	0,018	0,022	0,005	0,1%	0,1%	0,1%	0,0%	0,001	0,010	0,006	0,006	0,4%	0,3%	0,3%	0,1%
SOCS2 + CUL5	28,1	0,062	0,054	0,058	0,005	1,6%	1,5%	1,5%	0,1%	0,131	0,020	0,076	0,078	13,7%	12,3%	13,0%	1,0%
BTLA + TNFRSF14	25	0,001	0,002	0,002	0,001	0,4%	-0,1%	0,2%	0,4%	0,002	0,007	0,005	0,003	-0,6%	-1,7%	-1,2%	0,7%
ARL2 + ARL2BP	20	0,067	0,085	0,076	0,013	0,0%	0,1%	0,1%	0,1%	0,608	0,011	0,310	0,423	0,5%	0,7%	0,6%	0,2%
TERF2 + TERF2IP	16,5	0,005	0,005	0,005	0,000	0,0%	0,0%	0,0%	0,0%	0,003	0,004	0,003	0,000	0,0%	0,0%	0,0%	0,0%
CASP9 + XIAP	13	0,023	0,022	0,023	0,000	3,3%	0,8%	2,1%	1,8%	0,024	0,006	0,015	0,013	0,9%	0,5%	0,7%	0,3%
CSNK2B + CSNK2A1	12,6	0,068	0,079	0,074	0,008	16,0%	22,0%	19,0%	4,2%	0,180	0,112	0,146	0,048	12,6%	25,0%	18,8%	8,8%
CGB + CGB5	10	-0,005	0,004	-0,001	0,006	0,5%	0,6%	0,5%	0,1%	0,002	0,011	0,007	0,007	1,2%	1,3%	1,3%	0,1%
CCNC + CDK8	7,05	0,048	0,095	0,071	0,033	8,0%	5,0%	6,5%	2,2%	0,057	0,064	0,060	0,005	12,1%	12,9%	12,5%	0,5%
VWF + GP1BA	5,8	0,011	-0,017	-0,003	0,019	1,0%	0,6%	0,8%	0,3%	0,005	0,016	0,010	0,008	0,5%	0,5%	0,5%	0,0%
MMP2 + TIMP2	5,2	0,003	0,005	0,004	0,001	0,3%	0,1%	0,2%	0,2%	-0,001	0,002	0,001	0,002	0,1%	0,1%	0,1%	0,0%
RMI2 + RMI1	4,5	-0,003	0,001	-0,001	0,003	0,6%	0,8%	0,7%	0,1%	0,017	0,013	0,015	0,002	1,3%	7,9%	4,6%	4,6%
PPP3R1 + PPP3CA	4	-0,003	0,011	0,004	0,010	3,2%	2,3%	2,7%	0,7%	-0,002	0,016	0,007	0,012	1,4%	2,8%	2,1%	1,0%
SMN1 + SMN2	3,3	0,189	0,136	0,162	0,038	19,9%	9,9%	14,9%	7,1%	0,305	0,047	0,176	0,182	28,8%	68,5%	48,6%	28,0%
IL12B + IL23A	2	0,079	0,078	0,079	0,000	5,0%	0,6%	2,8%	3,1%		0,012	0,012		0,1%	0,3%	0,2%	0,1%
USH1G + USH1C	1	0,027	0,023	0,025	0,003	1,4%	-0,2%	0,6%	1,1%	0,190	0,032	0,111	0,112	43,1%	72,4%	57,7%	20,8%
VTN + SERPINE1	1	-0,004	0,001	-0,001	0,003	0,3%	0,1%	0,2%	0,1%	NC	NC	NC	NC	NC	NC	NC	NC
IL6 + IL6R	0,8	0,001	-0,010	-0,005	0,008	0,9%	0,1%	0,5%	0,6%	0,027	0,016	0,021	0,008	0,2%	0,3%	0,2%	0,1%
MAGOH + RBM8A	0,7	0,368	0,330	0,349	0,027	19,5%	21,8%	20,6%	1,6%	0,315	0,014	0,164	0,213	49,6%	89,4%	69,5%	28,2%

		Set a								Set b							
		in-cell BRET				cell-free co-IP				in-cell BRET				cell-free co-IP			
Interaction	Kd (nM)	Exp 1	Exp 2	Mean	SD	Exp 1	Exp 2	Mean	SD	Exp 1	Exp 2	Mean	SD	Exp 1	Exp 2	Mean	SD
MMP1 + TIMP1	0,4	0,003	-0,004	0,000	0,005	1,6%	0,7%	1,2%	0,6%	0,003	0,008	0,006	0,004	1,4%	0,6%	1,0%	0,6%
NTF4 + NTRK2	0,26	0,028	0,018	0,023	0,008	11,7%	-0,1%	5,8%	8,3%	0,038	0,042	0,040	0,003	3,6%	18,9%	11,3%	10,8%
EPO + EPOR	0,0037	0,002	-0,015	-0,006	0,012	0,4%	0,3%	0,4%	0,1%	0,007	0,009	0,008	0,002	2,9%	2,9%	2,9%	0,0%
RNASE1 + RNH1	0,00000029	-0,005	-0,007	-0,006	0,001	2,8%	3,3%	3,0%	0,4%	0,000	0,018	0,009	0,013	3,6%	11,3%	7,5%	5,5%

9. References

1. Hegyi, H., Kalmar, L., Horvath, T. & Tompa, P. Verification of alternative splicing variants based on domain integrity, truncation length and intrinsic protein disorder. *Nucleic Acids Res* **39,** 1208–1219 (2011).
2. Kim, M.-S. *et al.* A draft map of the human proteome. *Nature* **509,** 575–581 (2014).
3. Braun, P. & Gingras, A.-C. History of protein-protein interactions: from egg-white to complex networks. *Proteomics* **12,** 1478–1498 (2012).
4. Venkatesan, K. *et al.* An empirical framework for binary interactome mapping. *Nat. Methods* **6,** 83–90 (2009).
5. Stumpf, M. P. H. *et al.* Estimating the size of the human interactome. **105,** 6959–6964 (2008).
6. Sahni, N. *et al.* Edgotype: a fundamental link between genotype and phenotype. *Current Opinion in Genetics & Development* **23,** 649–657 (2013).
7. Sahni, N. *et al.* Widespread macromolecular interaction perturbations in human genetic disorders. *Cell* **161,** 647–660 (2015).
8. 1000 Genomes Project Consortium *et al.* A global reference for human genetic variation. *Nature* **526,** 68–74 (2015).
9. Goehler, H. *et al.* A protein interaction network links GIT1, an enhancer of huntingtin aggregation, to Huntington's disease. *Mol. Cell* **15,** 853–865 (2004).
10. Stelzl, U. *et al.* A human protein-protein interaction network: a resource for annotating the proteome. *Cell* **122,** 957–968 (2005).
11. Rual, J.-F. *et al.* Towards a proteome-scale map of the human protein-protein interaction network. **437,** 1173–1178 (2005).
12. Rolland, T. *et al.* A proteome-scale map of the human interactome network. *Cell* **159,** 1212–1226 (2014).
13. Rajagopala, S. V. *et al.* The binary protein-protein interaction landscape of Escherichia coli. *Nat Biotechnol* **32,** –290 (2014).
14. Huttlin, E. L. *et al.* The BioPlex Network: A Systematic Exploration of the Human Interactome. *Cell* **162,** 425–440 (2015).
15. Hakhverdyan, Z. *et al.* Rapid, optimized interactomic screening. *Nat. Methods* **12,** 553–560 (2015).
16. Yu, H. *et al.* High-quality binary protein interaction map of the yeast interactome network. *Science* **322,** 104–110 (2008).
17. Arabidopsis Interactome Mapping Consortium. Evidence for network evolution in an Arabidopsis interactome map. *Science* **333,** 601–607 (2011).
18. Hosp, F. *et al.* Quantitative interaction proteomics of neurodegenerative disease proteins. *CellReports* **11,** 1134–1146 (2015).
19. Vinayagam, A. *et al.* A Directed Protein Interaction Network for Investigating Intracellular Signal Transduction. *Science Signaling* **4,** rs8–rs8 (2011).
20. Hegele, A. *et al.* Dynamic protein-protein interaction wiring of the human spliceosome. **45,** 567–580 (2012).
21. Meyer, K. & Selbach, M. Quantitative affinity purification mass spectrometry: a versatile technology to study protein-protein interactions. *Front. Genet.* **6,** 237 (2015).
22. Taipale, M. *et al.* Quantitative analysis of HSP90-client interactions reveals principles of substrate recognition. *Cell* **150,** 987–1001 (2012).
23. Trepte, P. *et al.* DULIP: A Dual Luminescence-Based Co-Immunoprecipitation Assay for Interactome Mapping in Mammalian Cells. *Journal of Molecular Biology* **427,** 3375–3388 (2015).
24. Chavez, J. D. *et al.* Quantitative interactome analysis reveals a chemoresistant

edgotype. *Nature Communications* **6,** 7928 (2015).
25. Nooren, I. M. A. & Thornton, J. M. Diversity of protein-protein interactions. *EMBO J* **22,** 3486–3492 (2003).
26. Jones, S. & Thornton, J. M. Principles of protein-protein interactions. *Proceedings of the National Academy of Sciences* **93,** 13–20 (1996).
27. Perkins, J. R., Diboun, I., Dessailly, B. H., Lees, J. G. & Orengo, C. Transient protein-protein interactions: structural, functional, and network properties. *Structure* **18,** 1233–1243 (2010).
28. Finzel, B. C., Weber, P. C., Hardman, K. D. & Salemme, F. R. Structure of ferricytochrome c' from Rhodospirillum molischianum at 1.67 A resolution. *Journal of Molecular Biology* **186,** 627–643 (1985).
29. Kastritis, P. L. & Bonvin, A. M. J. J. On the binding affinity of macromolecular interactions: daring to ask why proteins interact. *J R Soc Interface* **10,** 20120835–20120835 (2013).
30. Olsson, T. S. G., Williams, M. A., Pitt, W. R. & Ladbury, J. E. The thermodynamics of protein-ligand interaction and solvation: insights for ligand design. *Journal of Molecular Biology* **384,** 1002–1017 (2008).
31. Pierce, M. M., Raman, C. S. & Nall, B. T. Isothermal titration calorimetry of protein-protein interactions. *METHODS* **19,** 213–221 (1999).
32. Nooren, I. M. A. & Thornton, J. M. Structural characterisation and functional significance of transient protein-protein interactions. *Journal of Molecular Biology* **325,** 991–1018 (2003).
33. Mohan, A. *et al.* Analysis of molecular recognition features (MoRFs). *Journal of Molecular Biology* **362,** 1043–1059 (2006).
34. Singh, G. P., Ganapathi, M. & Dash, D. Role of intrinsic disorder in transient interactions of hub proteins. *Proteins* **66,** 761–765 (2007).
35. Dyson, H. J. & Wright, P. E. Intrinsically unstructured proteins and their functions. *Nat. Rev. Mol. Cell Biol.* **6,** 197–208 (2005).
36. Li, Y.-C. *et al.* A Versatile Platform to Analyze Low-Affinity and Transient Protein-Protein Interactions in Living Cells in Real Time. *CellReports* **9,** 1946–1958 (2014).
37. Hodson, C. *et al.* Structural analysis of human FANCL, the E3 ligase in the Fanconi anemia pathway. **286,** 32628–32637 (2011).
38. Machida, Y. J. *et al.* UBE2T is the E2 in the Fanconi anemia pathway and undergoes negative autoregulation. **23,** 589–596 (2006).
39. Hodson, C., Purkiss, A., Miles, J. A. & Walden, H. Structure of the human FANCL RING-Ube2T complex reveals determinants of cognate E3-E2 selection. *Structure* **22,** 337–344 (2014).
40. Barclay, J. W. *et al.* Phosphorylation of Munc18 by protein kinase C regulates the kinetics of exocytosis. **278,** 10538–10545 (2003).
41. Söllner, T. *et al.* SNAP receptors implicated in vesicle targeting and fusion. *Nature* **362,** 318–324 (1993).
42. Söllner, T., Bennett, M. K., Whiteheart, S. W., Scheller, R. H. & Rothman, J. E. A protein assembly-disassembly pathway in vitro that may correspond to sequential steps of synaptic vesicle docking, activation, and fusion. *Cell* **75,** 409–418 (1993).
43. Fernández-Chacón, R. *et al.* The synaptic vesicle protein CSP alpha prevents presynaptic degeneration. *Neuron* **42,** 237–251 (2004).
44. Rizo, J. & Südhof, T. C. The membrane fusion enigma: SNAREs, Sec1/Munc18 proteins, and their accomplices--guilty as charged? *Annu. Rev. Cell Dev. Biol.* **28,** 279–308 (2012).
45. Hata, Y. & Südhof, T. C. A novel ubiquitous form of Munc-18 interacts with multiple syntaxins. Use of the yeast two-hybrid system to study interactions between proteins involved in membrane traffic. *J Biol Chem* **270,** 13022–13028 (1995).
46. Rizo, J. & Südhof, T. C. Snares and Munc18 in synaptic vesicle fusion. *Nat Rev*

Neurosci **3,** 641–653 (2002).
47. de Vries, K. J. *et al.* Dynamics of munc18-1 phosphorylation/dephosphorylation in rat brain nerve terminals. *Eur J Neurosci* **12,** 385–390 (2000).
48. Hedin, S. G. Trypsin and Antitrypsin. *Biochem J* **1,** 474–483 (1906).
49. Fields, S. & Song, O. A novel genetic system to detect protein-protein interactions. **340,** 245–246 (1989).
50. Karas, M. & Hillenkamp, F. Laser desorption ionization of proteins with molecular masses exceeding 10,000 daltons. *Anal Chem* **60,** 2299–2301 (1988).
51. Fenn, J. B., Mann, M., Meng, C. K., Wong, S. F. & Whitehouse, C. M. Electrospray ionization for mass spectrometry of large biomolecules. *Science* **246,** 64–71 (1989).
52. Goffeau, A. *et al.* Life with 6000 genes. *Science* **274,** 546–563–7 (1996).
53. Uetz, P. *et al.* A comprehensive analysis of protein-protein interactions in Saccharomyces cerevisiae. **403,** 623–627 (2000).
54. McPherson, J. D. *et al.* A physical map of the human genome. *Nature* **409,** 934–941 (2001).
55. Lander, E. S. *et al.* Initial sequencing and analysis of the human genome. *Nature* **409,** 860–921 (2001).
56. Venter, J. C. *et al.* The sequence of the human genome. *Science* **291,** 1304–1351 (2001).
57. Ho, Y. *et al.* Systematic identification of protein complexes in Saccharomyces cerevisiae by mass spectrometry. *Nature* **415,** 180–183 (2002).
58. Gavin, A.-C. *et al.* Functional organization of the yeast proteome by systematic analysis of protein complexes. *Nature* **415,** 141–147 (2002).
59. Dragulescu-Andrasi, A., Chan, C. T., De, A., Massoud, T. F. & Gambhir, S. S. Bioluminescence resonance energy transfer (BRET) imaging of protein-protein interactions within deep tissues of living subjects. **108,** 12060–12065 (2011).
60. Sadaie, W., Harada, Y., Matsuda, M. & Aoki, K. Quantitative in vivo fluorescence cross-correlation analyses highlight the importance of competitive effects in the regulation of protein-protein interactions. *Mol Cell Biol* **34,** 3272–3290 (2014).
61. Gräslund, S. *et al.* Protein production and purification. *Nat Meth* **5,** 135–146 (2008).
62. Velazquez-Campoy, A., Leavitt, S. A. & Freire, E. Characterization of protein-protein interactions by isothermal titration calorimetry. *Methods Mol Biol* **1278,** 183–204 (2015).
63. Liedberg, B., Nylander, C. & Lundström, I. Biosensing with surface plasmon resonance--how it all started. *Biosens Bioelectron* **10,** i–ix (1995).
64. Nedelkov, D. & Nelson, R. W. Surface plasmon resonance mass spectrometry: recent progress and outlooks. *Trends Biotechnol* **21,** 301–305 (2003).
65. Patching, S. G. Surface plasmon resonance spectroscopy for characterisation of membrane protein-ligand interactions and its potential for drug discovery. *Biochim Biophys Acta* **1838,** 43–55 (2014).
66. Krone, J. R., Nelson, R. W., Dogruel, D., Williams, P. & Granzow, R. BIA/MS: interfacing biomolecular interaction analysis with mass spectrometry. *Anal Biochem* **244,** 124–132 (1997).
67. Madeira, A. *et al.* Coupling surface plasmon resonance to mass spectrometry to discover novel protein-protein interactions. *Nature Protocols* **4,** 1023–1037 (2009).
68. Vidal, M. & Fields, S. The yeast two-hybrid assay: still finding connections after 25 years. *Nat. Methods* **11,** 1203–1206 (2014).
69. Petschnigg, J. *et al.* The mammalian-membrane two-hybrid assay (MaMTH) for probing membrane-protein interactions in human cells. *Nat. Methods* **11,** 585–592 (2014).
70. Lievens, S. *et al.* Kinase Substrate Sensor (KISS), a mammalian in situ protein interaction sensor. *Mol Cell Proteomics* **13,** 3332–3342 (2014).
71. Stynen, B., Tournu, H., Tavernier, J. & Van Dijck, P. Diversity in genetic in vivo methods for protein-protein interaction studies: from the yeast two-hybrid system to the

mammalian split-luciferase system. *Microbiol Mol Biol Rev* **76,** 331–382 (2012).
72. LaCount, D. J. *et al.* A protein interaction network of the malaria parasite Plasmodium falciparum. **438,** 103–107 (2005).
73. Boxem, M. *et al.* A protein domain-based interactome network for C. elegans early embryogenesis. *Cell* **134,** 534–545 (2008).
74. Braun, P. *et al.* An experimentally derived confidence score for binary protein-protein interactions. *Nat. Methods* **6,** 91–97 (2009).
75. Chen, Y.-C., Rajagopala, S. V., Stellberger, T. & Uetz, P. Exhaustive benchmarking of the yeast two-hybrid system. *Nat. Methods* **7,** 667–8– author reply 668 (2010).
76. Huang, H., Jedynak, B. M. & Bader, J. S. Where have all the interactions gone? Estimating the coverage of two-hybrid protein interaction maps. *PLoS Comput Biol* **3,** e214 (2007).
77. Huang, H. & Bader, J. S. Precision and recall estimates for two-hybrid screens. *Bioinformatics* **25,** 372–378 (2009).
78. Rajagopala, S. V. & Uetz, P. Analysis of protein-protein interactions using high-throughput yeast two-hybrid screens. *Methods Mol Biol* **781,** 1–29 (2011).
79. Dittmar, J. C., Reid, R. J. & Rothstein, R. ScreenMill: a freely available software suite for growth measurement, analysis and visualization of high-throughput screen data. *BMC Bioinformatics* **11,** 353 (2010).
80. Möckli, N. & Auerbach, D. Quantitative beta-galactosidase assay suitable for high-throughput applications in the yeast two-hybrid system. *Biotech* **36,** 872–876 (2004).
81. Ruusuvuori, P. *et al.* Quantitative analysis of colony morphology in yeast. *Biotech* **56,** 18–27 (2014).
82. Han, G. A. *et al.* Munc18-1 domain-1 controls vesicle docking and secretion by interacting with syntaxin-1 and chaperoning it to the plasma membrane. *Mol Biol Cell* **22,** 4134–4149 (2011).
83. Johnsson, N. & Varshavsky, A. Split ubiquitin as a sensor of protein interactions in vivo. **91,** 10340–10344 (1994).
84. Remy, I. & Michnick, S. W. Clonal selection and in vivo quantitation of protein interactions with protein-fragment complementation assays. *Proceedings of the National Academy of Sciences* **96,** 5394–5399 (1999).
85. Ghosh, I., Hamilton, A. D. & Regan, L. Antiparallel Leucine Zipper-Directed Protein Reassembly: Application to the Green Fluorescent Protein. *J Am Chem Soc* **122,** 5658–5659 (2000).
86. Morell, M., Ventura, S. & Avilés, F. X. Protein complementation assays: approaches for the in vivo analysis of protein interactions. *FEBS LETTERS* **583,** 1684–1691 (2009).
87. Chen, C.-D., Oh, S.-Y., Hinman, J. D. & Abraham, C. R. Visualization of APP dimerization and APP-Notch2 heterodimerization in living cells using bimolecular fluorescence complementation. *Journal of Neurochemistry* **97,** 30–43 (2006).
88. Tarassov, K. *et al.* An in vivo map of the yeast protein interactome. *Science* **320,** 1465–1470 (2008).
89. Sung, M.-K. *et al.* Genome-wide bimolecular fluorescence complementation analysis of SUMO interactome in yeast. *Genome Research* **23,** –746 (2013).
90. Miller, K. E., Kim, Y., Huh, W.-K. & Park, H.-O. Bimolecular Fluorescence Complementation (BiFC) Analysis: Advances and Recent Applications for Genome-Wide Interaction Studies. *Journal of Molecular Biology* **427,** 2039–2055 (2015).
91. Kodama, Y. & Hu, C.-D. An improved bimolecular fluorescence complementation assay with a high signal-to-noise ratio. *Biotech* **49,** 793–805 (2010).
92. Ohashi, K., Kiuchi, T., Shoji, K., Sampei, K. & Mizuno, K. Visualization of cofilin-actin and Ras-Raf interactions by bimolecular fluorescence complementation assays using a new pair of split Venus fragments. *Biotech* **52,** 45–50 (2012).
93. Ciruela, F., Vilardaga, J.-P. & Fernández-Dueñas, V. Lighting up multiprotein complexes: lessons from GPCR oligomerization. *Trends Biotechnol* **28,** 407–415

(2010).
94. Paulmurugan, R., Umezawa, Y. & Gambhir, S. S. Noninvasive imaging of protein-protein interactions in living subjects by using reporter protein complementation and reconstitution strategies. *Proceedings of the National Academy of Sciences* **99,** 15608–15613 (2002).
95. Paulmurugan, R. & Gambhir, S. S. Monitoring protein-protein interactions using split synthetic renilla luciferase protein-fragment-assisted complementation. *Anal Chem* **75,** 1584–1589 (2003).
96. Remy, I. & Michnick, S. W. A highly sensitive protein-protein interaction assay based on Gaussia luciferase. *Nat Meth* **3,** 977–979 (2006).
97. Zhao, J., Nelson, T. J., Vu, Q., Truong, T. & Stains, C. I. Self-Assembling NanoLuc Luciferase Fragments as Probes for Protein Aggregation in Living Cells. *ACS Chem Biol* acschembio.5b00758 (2015). doi:10.1021/acschembio.5b00758
98. Stefan, E. *et al.* Quantification of dynamic protein complexes using Renilla luciferase fragment complementation applied to protein kinase A activities in vivo. *Proceedings of the National Academy of Sciences* **104,** 16916–16921 (2007).
99. Kaihara, A., Kawai, Y., Sato, M., Ozawa, T. & Umezawa, Y. Locating a protein-protein interaction in living cells via split Renilla luciferase complementation. *Anal Chem* **75,** 4176–4181 (2003).
100. Kato, N. Luciferase and Bioluminescence Microscopy for Analyses of Membrane Dynamics in Living Cells. *J Membra Sci Technol* **02,** 1–2 (2012).
101. Nickerson, A., Huang, T., Lin, L.-J. & Nan, X. Photoactivated localization microscopy with bimolecular fluorescence complementation (BiFC-PALM) for nanoscale imaging of protein-protein interactions in cells. *PLoS ONE* **9,** e100589 (2014).
102. Liu, Z. *et al.* Super-resolution imaging and tracking of protein-protein interactions in sub-diffraction cellular space. *Nature Communications* **5,** 4443 (2014).
103. Hu, C.-D. & Kerppola, T. K. Simultaneous visualization of multiple protein interactions in living cells using multicolor fluorescence complementation analysis. *Nat Biotechnol* **21,** 539–545 (2003).
104. Cabantous, S. *et al.* A new protein-protein interaction sensor based on tripartite split-GFP association. *Sci. Rep.* **3,** 2854 (2013).
105. Morell, M., Espargaro, A., Avilés, F. X. & Ventura, S. Detection of transient protein-protein interactions by bimolecular fluorescence complementation: the Abl-SH3 case. *Proteomics* **7,** 1023–1036 (2007).
106. Sung, M.-K. & Huh, W.-K. In vivo quantification of protein-protein interactions in Saccharomyces cerevisiae using bimolecular fluorescence complementation assay. *J. Microbiol. Methods* **83,** 194–201 (2010).
107. Lane, D. P. & Crawford, L. V. T antigen is bound to a host protein in SV40-transformed cells. *Nature* **278,** 261–263 (1979).
108. Barrios-Rodiles, M. *et al.* High-throughput mapping of a dynamic signaling network in mammalian cells. *Science* **307,** 1621–1625 (2005).
109. Miller, B. W. *et al.* Application of an integrated physical and functional screening approach to identify inhibitors of the Wnt pathway. *Molecular Systems Biology* **5,** 315 (2009).
110. Jia, S. *et al.* Relative quantification of protein-protein interactions using a dual luciferase reporter pull-down assay system. *PLoS ONE* **6,** e26414 (2011).
111. Ellis, J. D. *et al.* Tissue-specific alternative splicing remodels protein-protein interaction networks. **46,** 884–892 (2012).
112. Shalgi, R. *et al.* Widespread regulation of translation by elongation pausing in heat shock. **49,** 439–452 (2013).
113. Taipale, M. *et al.* Chaperones as thermodynamic sensors of drug-target interactions reveal kinase inhibitor specificities in living cells. *Nat Biotechnol* **31,** 630–637 (2013).
114. Taipale, M. *et al.* A quantitative chaperone interaction network reveals the architecture

of cellular protein homeostasis pathways. *Cell* **158,** 434–448 (2014).
115. Xu, G. *et al.* Novel protein interactions with endoglin and activin receptor-like kinase 1: potential role in vascular networks. *Mol Cell Proteomics* **13,** 489–502 (2014).
116. Beckett, D., Kovaleva, E. & Schatz, P. J. A minimal peptide substrate in biotin holoenzyme synthetase-catalyzed biotinylation. *Protein Sci* **8,** 921–929 (1999).
117. Chapman-Smith, A. & Cronan, J. E. The enzymatic biotinylation of proteins: a post-translational modification of exceptional specificity. *Trends Biochem Sci* **24,** 359–363 (1999).
118. Cario, G. & Franck, J. Über Zerlegung von Wasserstoffmolekülen durch angeregte Quecksilberatome. *Z. Physik* **11,** 161–166 (1922).
119. Cario, G. & Franck, J. Über sensibilisierte Fluoreszenz von Gasen. *Z. Physik* **17,** 202–212 (1923).
120. Förster, T. Zwischenmolekulare Energiewanderung und Fluoreszenz. *Annalen der Physik* **437,** 55–75 (1948).
121. Vogel, S. S., Thaler, C. & Koushik, S. V. Fanciful FRET. *Sci STKE* **2006,** re2–re2 (2006).
122. Stryer, L. & Haugland, R. P. Energy transfer: a spectroscopic ruler. *Proceedings of the National Academy of Sciences* **58,** 719–726 (1967).
123. Shimomura, O., Johnson, F. H. & Saiga, Y. Extraction, Purification and Properties of Aequorin, a Bioluminescent Protein from the Luminous Hydromedusan, Aequorea. *Journal of Cellular and Comparative Physiology* **59,** 223–239 (1962).
124. Chalfie, M., Tu, Y., Euskirchen, G., Ward, W. W. & Prasher, D. C. Green fluorescent protein as a marker for gene expression. *Science* **263,** 802–805 (1994).
125. Tsien, R. Y. The green fluorescent protein. *Annu Rev Biochem* **67,** 509–544 (1998).
126. Shaner, N. C., Steinbach, P. A. & Tsien, R. Y. A guide to choosing fluorescent proteins. *Nat Meth* **2,** 905–909 (2005).
127. Heim, R. & Tsien, R. Y. Engineering green fluorescent protein for improved brightness, longer wavelengths and fluorescence resonance energy transfer. *Curr Biol* **6,** 178–182 (1996).
128. Mitra, R. D., Silva, C. M. & Youvan, D. C. Fluorescence resonance energy transfer between blue-emitting and red-shifted excitation derivatives of the green fluorescent protein. *Gene* **173,** 13–17 (1996).
129. Miyawaki, A. *et al.* Fluorescent indicators for Ca2+ based on green fluorescent proteins and calmodulin. *Nature* **388,** 882–887 (1997).
130. Mahajan, N. P. *et al.* Bcl-2 and Bax interactions in mitochondria probed with green fluorescent protein and fluorescence resonance energy transfer. *Nat Biotechnol* **16,** 547–552 (1998).
131. Pollok, B. Using GFP in FRET-based applications. *Trends Cell Biol* **9,** 57–60 (1999).
132. Piston, D. W. & Kremers, G.-J. Fluorescent protein FRET: the good, the bad and the ugly. *Trends Biochem Sci* **32,** 407–414 (2007).
133. Bastiaens, P. I. & Jovin, T. M. Microspectroscopic imaging tracks the intracellular processing of a signal transduction protein: fluorescent-labeled protein kinase C beta I. *Proceedings of the National Academy of Sciences* **93,** 8407–8412 (1996).
134. Hoppe, A., Christensen, K. & Swanson, J. A. Fluorescence resonance energy transfer-based stoichiometry in living cells. *Biophys J* **83,** 3652–3664 (2002).
135. Elder, A. D. *et al.* A quantitative protocol for dynamic measurements of protein interactions by Förster resonance energy transfer-sensitized fluorescence emission. *Journal of The Royal Society Interface* **6,** S59–S81 (2009).
136. Chen, W. *et al.* A method to quantify FRET stoichiometry with phasor plot analysis and acceptor lifetime ingrowth. *Biophys J* **108,** 999–1002 (2015).
137. Morin, J. G. & Hastings, J. W. Energy transfer in a bioluminescent system. *J. Cell. Physiol.* **77,** 313–318 (1971).
138. Shimomura, O. The discovery of aequorin and green fluorescent protein. *J Microsc* **217,** 1–15 (2005).

139. Xu, Y., Piston, D. W. & Johnson, C. H. A bioluminescence resonance energy transfer (BRET) system: application to interacting circadian clock proteins. *Proceedings of the National Academy of Sciences* **96,** 151–156 (1999).
140. Bacart, J., Corbel, C., Jockers, R., Bach, S. & Couturier, C. The BRET technology and its application to screening assays. *Biotechnol. J.* **3,** 311–324 (2008).
141. Nakatani, N., Hasegawa, J.-Y. & Nakatsuji, H. Red Light in Chemiluminescence and Yellow-Green Light in Bioluminescence: Color-Tuning Mechanism of Firefly, Photinus pyralis, Studied by the Symmetry-Adapted Cluster–Configuration Interaction Method. *J Am Chem Soc* **129,** 8756–8765 (2007).
142. Bertrand, L. *et al.* The BRET2/arrestin assay in stable recombinant cells: a platform to screen for compounds that interact with G protein-coupled receptors (GPCRS). *J. Recept. Signal Transduct. Res.* **22,** 533–541 (2002).
143. Arai, R., Nakagawa, H., Kitayama, A., Ueda, H. & Nagamune, T. Detection of protein-protein interaction by bioluminescence resonance energy transfer from firefly luciferase to red fluorescent protein. *J. Biosci. Bioeng.* **94,** 362–364 (2002).
144. Li, F. *et al.* Buffer enhanced bioluminescence resonance energy transfer sensor based on Gaussia luciferase for in vitro detection of protease. *Anal. Chim. Acta* **724,** 104–110 (2012).
145. Machleidt, T. *et al.* NanoBRET-A Novel BRET Platform for the Analysis of Protein-Protein Interactions. *ACS Chem Biol* **10,** 1797–1804 (2015).
146. Dacres, H., Michie, M., Wang, J., Pfleger, K. D. G. & Trowell, S. C. Effect of enhanced Renilla luciferase and fluorescent protein variants on the Förster distance of Bioluminescence resonance energy transfer (BRET). *Biochemical and Biophysical Research Communications* **425,** 625–629 (2012).
147. Borroto-Escuela, D. O., Flajolet, M., Agnati, L. F., Greengard, P. & Fuxe, K. Bioluminescence resonance energy transfer methods to study G protein-coupled receptor-receptor tyrosine kinase heteroreceptor complexes. *Methods Cell Biol.* **117,** 141–164 (2013).
148. So, M.-K., Xu, C., Loening, A. M., Gambhir, S. S. & Rao, J. Self-illuminating quantum dot conjugates for in vivo imaging. *Nat Biotechnol* **24,** 339–343 (2006).
149. Xiong, L., Shuhendler, A. J. & Rao, J. Self-luminescing BRET-FRET near-infrared dots for in vivo lymph-node mapping and tumour imaging. *Nature Communications* **3,** 1193 (2012).
150. Reck-Peterson, S. L. *et al.* Single-molecule analysis of dynein processivity and stepping behavior. *Cell* **126,** 335–348 (2006).
151. De, A., Ray, P., Loening, A. M. & Gambhir, S. S. BRET3: a red-shifted bioluminescence resonance energy transfer (BRET)-based integrated platform for imaging protein-protein interactions from single live cells and living animals. *FASEB J* **23,** 2702–2709 (2009).
152. Mo, X.-L. *et al.* Enabling systematic interrogation of protein-protein interactions in live cells with a versatile ultra-high-throughput biosensor platform. *Journal of Molecular Cell Biology* (2015). doi:10.1093/jmcb/mjv064
153. Pfleger, K. D. G. *et al.* Extended bioluminescence resonance energy transfer (eBRET) for monitoring prolonged protein-protein interactions in live cells. *Cell Signal* **18,** 1664–1670 (2006).
154. De, A., Loening, A. M. & Gambhir, S. S. An improved bioluminescence resonance energy transfer strategy for imaging intracellular events in single cells and living subjects. *Cancer Res* **67,** 7175–7183 (2007).
155. Yao, H., Zhang, Y., Xiao, F., Xia, Z. & Rao, J. Quantum dot/bioluminescence resonance energy transfer based highly sensitive detection of proteases. *Angew. Chem. Int. Ed. Engl.* **46,** 4346–4349 (2007).
156. Pfleger, K. D. G. & Eidne, K. A. Illuminating insights into protein-protein interactions using bioluminescence resonance energy transfer (BRET). *Nat Meth* **3,** 165–174 (2006).
157. Wallrabe, H. & Periasamy, A. Imaging protein molecules using FRET and FLIM

microscopy. *Current Opinion in Biotechnology* **16,** 19–27 (2005).
158. Wood, K. V. The Bioluminescence Advantage. *Promega Notes* 3–5 (2007). at <https://www.promega.de/resources/pubhub/promega-notes-2007/the-bioluminescence-advantage/>
159. Coulon, V. *et al.* Subcellular imaging of dynamic protein interactions by bioluminescence resonance energy transfer. *Biophys J* **94,** 1001–1009 (2008).
160. Ando, Y. *et al.* Firefly bioluminescence quantum yield and colour change by pH-sensitive green emission. *Nature Photon* **2,** 44–47 (2007).
161. Inouye, S., Watanabe, K., Nakamura, H. & Shimomura, O. Secretional luciferase of the luminous shrimp Oplophorus gracilirostris: cDNA cloning of a novel imidazopyrazinone luciferase(1). *FEBS LETTERS* **481,** 19–25 (2000).
162. Shimomura, O., Masugi, T., Johnson, F. H. & Haneda, Y. Properties and reaction mechanism of the bioluminescence system of the deep-sea shrimp Oplophorus gracilorostris. *Biochemistry* **17,** 994–998 (1978).
163. Hall, M. P. *et al.* Engineered luciferase reporter from a deep sea shrimp utilizing a novel imidazopyrazinone substrate. *ACS Chem Biol* **7,** 1848–1857 (2012).
164. Stoddart, L. A. *et al.* Application of BRET to monitor ligand binding to GPCRs. *Nat. Methods* **12,** 661–663 (2015).
165. Schaub, F. X. *et al.* Fluorophore-NanoLuc BRET Reporters Enable Sensitive In Vivo Optical Imaging and Flow Cytometry for Monitoring Tumorigenesis. *Cancer Res* 1–37 (2015). doi:10.1158/0008-5472.CAN-14-3538
166. Pfleger, K. D. G., Seeber, R. M. & Eidne, K. A. Bioluminescence resonance energy transfer (BRET) for the real-time detection of protein-protein interactions. *Nature Protocols* **1,** 337–345 (2006).
167. Hamdan, F. F., Percherancier, Y., Breton, B. & Bouvier, M. Monitoring protein-protein interactions in living cells by bioluminescence resonance energy transfer (BRET). *Curr Protoc Neurosci* **Chapter 5,** Unit 5.23 (2006).
168. Drinovec, L., Kubale, V., Nøhr Larsen, J. & Vrecl, M. Mathematical models for quantitative assessment of bioluminescence resonance energy transfer: application to seven transmembrane receptors oligomerization. *Front. Endocrin.* **3,** 104 (2012).
169. Martínez-Muñoz, L. *et al.* CCR5/CD4/CXCR4 oligomerization prevents HIV-1 gp120IIIB binding to the cell surface. *Proc. Natl. Acad. Sci. U.S.A.* **111,** E1960–9 (2014).
170. Gersbach, C. A. Genome engineering: the next genomic revolution. *Nat. Methods* **11,** 1009–1011 (2014).
171. Sudmant, P. H. *et al.* An integrated map of structural variation in 2,504 human genomes. *Nature* **526,** 75–81 (2015).
172. Mouse Genome Sequencing Consortium *et al.* Initial sequencing and comparative analysis of the mouse genome. *Nature* **420,** 520–562 (2002).
173. Chimpanzee Sequencing and Analysis Consortium. Initial sequence of the chimpanzee genome and comparison with the human genome. *Nature* **437,** 69–87 (2005).
174. Howe, K. *et al.* The zebrafish reference genome sequence and its relationship to the human genome. *Nature* **496,** 498–503 (2013).
175. Ewing, R. M. *et al.* Large-scale mapping of human protein-protein interactions by mass spectrometry. *Molecular Systems Biology* **3,** 89 (2007).
176. Havugimana, P. C. *et al.* A census of human soluble protein complexes. *Cell* **150,** 1068–1081 (2012).
177. Coffill, C. R. *et al.* Mutant p53 interactome identifies nardilysin as a p53R273H-specific binding partner that promotes invasion. *EMBO Rep.* **13,** 638–644 (2012).
178. Arkin, M. R., Tang, Y. & Wells, J. A. Small-molecule inhibitors of protein-protein interactions: progressing toward the reality. *Chemistry & Biology* **21,** 1102–1114 (2014).
179. Wells, J. A. & McClendon, C. L. Reaching for high-hanging fruit in drug discovery at

protein-protein interfaces. **450,** 1001–1009 (2007).
180. Liang, X., Peng, L., Baek, C.-H. & Katzen, F. Single step BP/LR combined Gateway reactions. *Biotech* **55,** 265–268 (2013).
181. Rajan, S. *et al.* Structural transition in Bcl-xL and its potential association with mitochondrial calcium ion transport. *Sci. Rep.* 1–12 (2015). doi:10.1038/srep10609
182. Gordon, G. W., Berry, G., Liang, X. H., Levine, B. & Herman, B. Quantitative fluorescence resonance energy transfer measurements using fluorescence microscopy. *Biophys J* **74,** 2702–2713 (1998).
183. Schaefer, M. H. *et al.* HIPPIE: Integrating Protein Interaction Networks with Experiment Based Quality Scores. *PLoS ONE* **7,** e31826 (2012).
184. Smialowski, P. *et al.* The Negatome database: a reference set of non-interacting protein pairs. *Nucleic Acids Res* **38,** D540–4 (2010).
185. Wang, R., Fang, X., Lu, Y. & Wang, S. The PDBbind database: collection of binding affinities for protein-ligand complexes with known three-dimensional structures. *J Med Chem* **47,** 2977–2980 (2004).
186. Kastritis, P. L. *et al.* A structure-based benchmark for protein-protein binding affinity. *Protein Sci* **20,** 482–491 (2011).
187. Meijer, M. *et al.* Munc18-1 mutations that strongly impair SNARE-complex binding support normal synaptic transmission. **31,** 2156–2168 (2012).
188. Walhout, A. J. *et al.* Protein interaction mapping in C. elegans using proteins involved in vulval development. *Science* **287,** 116–122 (2000).
189. Jaeger, W. C., Armstrong, S. P., Hill, S. J. & Pfleger, K. D. G. Biophysical Detection of Diversity and Bias in GPCR Function. *Front. Endocrin.* **5,** 26 (2014).
190. Szalai, B. *et al.* Improved methodical approach for quantitative BRET analysis of G Protein Coupled Receptor dimerization. *PLoS ONE* **9,** e109503 (2014).
191. Oltersdorf, T. *et al.* An inhibitor of Bcl-2 family proteins induces regression of solid tumours. *Nature* **435,** 677–681 (2005).
192. Tse, C. *et al.* ABT-263: a potent and orally bioavailable Bcl-2 family inhibitor. *Cancer Res* **68,** 3421–3428 (2008).
193. Wendt, M. D. Discovery of ABT-263, a Bcl-family protein inhibitor: observations on targeting a large protein-protein interaction. *Expert Opin Drug Discov* **3,** 1123–1143 (2008).
194. Vassilev, L. T. *et al.* In vivo activation of the p53 pathway by small-molecule antagonists of MDM2. *Science* **303,** 844–848 (2004).
195. Wade, M., Li, Y.-C. & Wahl, G. M. MDM2, MDMX and p53 in oncogenesis and cancer therapy. *Nat Rev Cancer* **13,** 83–96 (2013).
196. Nero, T. L., Morton, C. J., Holien, J. K., Wielens, J. & Parker, M. W. Oncogenic protein interfaces: small molecules, big challenges. *Nature Publishing Group* **14,** 248–262 (2014).
197. McNicholas, S., Potterton, E., Wilson, K. S. & Noble, M. E. M. Presenting your structures: the CCP4mg molecular-graphics software. *Acta Crystallogr D Biol Crystallogr* **67,** 386–394 (2011).
198. Chen, J., Zheng, X. F., Brown, E. J. & Schreiber, S. L. Identification of an 11-kDa FKBP12-rapamycin-binding domain within the 289-kDa FKBP12-rapamycin-associated protein and characterization of a critical serine residue. *Proceedings of the National Academy of Sciences* **92,** 4947–4951 (1995).
199. Choi, J., Chen, J., Schreiber, S. L. & Clardy, J. Structure of the FKBP12-rapamycin complex interacting with the binding domain of human FRAP. *Science* **273,** 239–242 (1996).
200. Vézina, C., Kudelski, A. & Sehgal, S. N. Rapamycin (AY-22,989), a new antifungal antibiotic. I. Taxonomy of the producing streptomycete and isolation of the active principle. *J. Antibiot.* **28,** 721–726 (1975).
201. Heitman, J., Movva, N. R. & Hall, M. N. Targets for cell cycle arrest by the

immunosuppressant rapamycin in yeast. *Science* **253,** 905–909 (1991).
202. Blohm, P. *et al.* Negatome 2.0: a database of non-interacting proteins derived by literature mining, manual annotation and protein structure analysis. *Nucleic Acids Res* **42,** D396–400 (2014).
203. Estojak, J., Brent, R. & Golemis, E. A. Correlation of two-hybrid affinity data with in vitro measurements. *Mol Cell Biol* **15,** 5820–5829 (1995).
204. Brückner, A., Polge, C., Lentze, N., Auerbach, D. & Schlattner, U. Yeast two-hybrid, a powerful tool for systems biology. *IJMS* **10,** 2763–2788 (2009).
205. Vinayagam, A., Stelzl, U. & Wanker, E. E. Repeated two-hybrid screening detects transient protein–protein interactions. *Theor Chem Acc* **125,** 613–619 (2010).
206. Deplus, R. *et al.* TET2 and TET3 regulate GlcNAcylation and H3K4 methylation through OGT and SET1/COMPASS. *EMBO J* **32,** 645–655 (2013).
207. Bleichert, F., Botchan, M. R. & Berger, J. M. Crystal structure of the eukaryotic origin recognition complex. *Nature* **519,** 321–326 (2015).
208. Ostlund, C., Bonne, G., Schwartz, K. & Worman, H. J. Properties of lamin A mutants found in Emery-Dreifuss muscular dystrophy, cardiomyopathy and Dunnigan-type partial lipodystrophy. *Journal of Cell Science* **114,** 4435–4445 (2001).
209. Gross, A., McDonnell, J. M. & Korsmeyer, S. J. BCL-2 family members and the mitochondria in apoptosis. *Genes & Development* **13,** 1899–1911 (1999).
210. Brunelle, J. K. & Letai, A. Control of mitochondrial apoptosis by the Bcl-2 family. *Journal of Cell Science* **122,** 437–441 (2009).
211. Sacksteder, K. A. *et al.* PEX19 Binds Multiple Peroxisomal Membrane Proteins, Is PredominantlyCytoplasmic, and Is Required for Peroxisome Membrane Synthesis. *The Journal of Cell Biology* **148,** 1–14 (2000).
212. Yokote, K. *et al.* Identification of Tyr-762 in the platelet-derived growth factor alpha-receptor as the binding site for Crk proteins. *Oncogene* **16,** 1229–1239 (1998).
213. Lee, J. *et al.* Characterization of two high affinity human interleukin-8 receptors. *Journal of Biological Chemistry* **267,** 16283–16287 (1992).
214. Donovan, J. A., Ota, Y., Langdon, W. Y. & Samelson, L. E. Regulation of the association of p120cbl with Grb2 in Jurkat T cells. *Journal of Biological Chemistry* **271,** 26369–26374 (1996).
215. Vasilescu, J., Guo, X. & Kast, J. Identification of protein-protein interactions using in vivo cross-linking and mass spectrometry. *Proteomics* **4,** 3845–3854 (2004).
216. Tagwerker, C. *et al.* A tandem affinity tag for two-step purification under fully denaturing conditions: application in ubiquitin profiling and protein complex identification combined with in vivocross-linking. *Mol Cell Proteomics* **5,** 737–748 (2006).
217. Grünberg, R. *et al.* Engineering of weak helper interactions for high-efficiency FRET probes. *Nature Methods* **10,** 1021–1027 (2013).
218. Wang, X. *et al.* Three-dimensional reconstruction of protein networks provides insight into human genetic disease. *Nat Biotechnol* **30,** 159–164 (2012).
219. Schlüter, K., Schleicher, M. & Jockusch, B. M. Effects of single amino acid substitutions in the actin-binding site on the biological activity of bovine profilin I. *Journal of Cell Science* **111 (Pt 22),** 3261–3273 (1998).
220. Peltomäki, P. & Vasen, H. F. Mutations predisposing to hereditary nonpolyposis colorectal cancer: database and results of a collaborative study. The International Collaborative Group on Hereditary Nonpolyposis Colorectal Cancer. *Gastroenterology* **113,** 1146–1158 (1997).
221. Hata, Y., Slaughter, C. A. & Südhof, T. C. Synaptic vesicle fusion complex contains unc-18 homologue bound to syntaxin. *Nature* **366,** 347–351 (1993).
222. Vu, B. *et al.* Discovery of RG7112: A Small-Molecule MDM2 Inhibitor in Clinical Development. *ACS Med Chem Lett* **4,** 466–469 (2013).
223. Gandhi, L. *et al.* Phase I study of Navitoclax (ABT-263), a novel Bcl-2 family inhibitor,

in patients with small-cell lung cancer and other solid tumors. *J. Clin. Oncol.* **29,** 909–916 (2011).
224. Saunders, R. N., Metcalfe, M. S. & Nicholson, M. L. Rapamycin in transplantation: a review of the evidence. *Kidney Int.* **59,** 3–16 (2001).
225. Meier, C., Cairns-Smith, S. & Schulze, U. Can emerging drug classes improve R&D productivity? *Drug Discovery Today* **18,** 607–609 (2013).
226. Chatr-Aryamontri, A. *et al.* The BioGRID interaction database: 2015 update. *Nucleic Acids Res* **43,** D470–8 (2015).
227. Schaefer, M. H. *et al.* Adding protein context to the human protein-protein interaction network to reveal meaningful interactions. *PLoS Comput Biol* **9,** e1002860 (2013).
228. Stroedicke, M. *et al.* Systematic interaction network filtering identifies CRMP1 as a novel suppressor of huntingtin misfolding and neurotoxicity. *Genome Research* **25,** 701–713 (2015).
229. Kamburov, A., Stelzl, U. & Herwig, R. IntScore: a web tool for confidence scoring of biological interactions. *Nucleic Acids Res* **40,** –W146 (2012).
230. Aitchison, J. D. & Rout, M. P. The interactome challenge. *The Journal of Cell Biology* **7,** 120–4 (2015).
231. Palidwor, G. A. *et al.* Detection of alpha-rod protein repeats using a neural network and application to huntingtin. *PLoS Comput Biol* **5,** e1000304 (2009).
232. Thévenaz, P., Ruttimann, U. E. & Unser, M. A pyramid approach to subpixel registration based on intensity. *IEEE Trans Image Process* **7,** 27–41 (1998).

10. Contributions

- **Fig. 7a:** N-terminal DULIP destination vectors were created by Dr. Ulrich Stelzl, Molecular Interaction Networks group, Max-Planck-Institute for Molecular Genetics (MPIMG); C-terminal DULIP destination vectors were created by Dr. Alexander Buntru and Christopher Secker, Neuroproteomics group, Max-Delbrück-Center for Molecular Medicine (MDC)
- **Fig. 10a and b:** Y2H assays were performed by Konrad Klockmeier, Neuroproteomics group, Max-Delbrück-Center for Molecular Medicine (MDC)
- **Fig. 10c:** FRET assays were performed by Dr. Alexander Buntru and Lydia Brusendorf, Neuroproteomics group, Max-Delbrück-Center for Molecular Medicine (MDC)
- **Fig. 18d and e:** Y2H assays were performed by Konrad Klockmeier, Neuroproteomics group, Max-Delbrück-Center for Molecular Medicine (MDC)
- **Fig. 18f:** FRET assays were performed by Dr. Alexander Buntru and Lydia Brusendorf, Neuroproteomics group, Max-Delbrück-Center for Molecular Medicine (MDC)
- **Fig. 30f:** Bioluminescence imaging was performed by Sheila Hoffmann, Synaptopathy group, German Center for Neurodegenerative Diseases (DZNE)

11. Relevant Publications

- Trepte, P. *et al.* DULIP: A Dual Luminescence-Based Co-Immunoprecipitation Assay for Interactome Mapping in Mammalian Cells. *Journal of Molecular Biology* **427,** 3375–3388 (2015). http://dx.doi.org/10.1016/j.jmb.2015.08.003

12. Acknowledgements

First of all, I would like to thank Erich who put responsibility but also great faith in me and my work. He allowed me to pursue my ideas with great freedom, a lot of help but also to work very independently on this practice-oriented PhD project. This allowed me to develop my scientific ambition, interest, critical thinking and leadership qualities. At the same time, he provided guidance, resources and critical appraisal of my work, which all helped me to become a better and confident scientist. I am very grateful to him that I could pursue my work in his lab and enjoyed the time very much.

Of cause, I would also like to thank so many people in the lab, because without them the work would have been impossible. Alex and Konrad helped me with great discussions in the "Denkerstube" about planning experiments, data analysis and of cause also with drinking beer (after work). But without the help from Martina and Sabrina probably no idea would have been realizable, who I thank a lot for their great help in performing all the experiments in an amazing quality. I am very grateful to Lindsay, who helped to develop an R-based script for the semi-automated data analysis of DULIP results. I would also like to thank Kirstin, Alexandra, Chris and Lydia as well as Anne and Anne for their great technical help and all the other members in the group for discussions and support.
Thanks also go to Craig and Sheila. Craig, who gave his approval to perform the imaging experiments, and especially to Sheila who realized them and put so much work into it. I hope we continue with this fruitful collaboration.

I also had a lot of help with writing my thesis. Here, I would like to thank again Erich who helped me to put structure into chaos. Alex, Konrad, Loni and my parents who proof-read my thesis and helped me to find bigger and smaller mistakes.

Most importantly, I would like to thank Greta, but also the rest of my family and of cause my friends. Thanks for the fun, support and for not talking to much about work for the past five years.